Controlled chemical functionalization of graphene oxide

Isabella Anna Vacchi

UNIVERSITÉ DE STRASBOURG

EDSC
École Doctorale des Sciences Chimiques

Université de Strasbourg

ECOLE DOCTORALE DES SCIENCES CHIMIQUES

Controlled chemical functionalization of graphene oxide

by

Isabella Anna Vacchi

Thesis submitted for the degree of Doctor of Philosophy in Chemistry

20th September 2017

Supervisor: **Dr. Alberto Bianco**

Co-supervisor: **Dr. Cécilia Ménard-Moyon**

Members of the jury: **Prof. Siegfried Eigler**

Dr. Giuliano Giambastiani

UNIVERSITÉ DE STRASBOURG

ÉCOLE DOCTORALE DES SCIENCES CHIMIQUES

THÈSE présentée par :

Isabella Anna VACCHI

soutenue le : **20 septembre 2017**

pour obtenir le grade de : **Docteur de l'université de Strasbourg**

Discipline/ Spécialité : Chimie

Fonctionnalisation chimique contrôlée de l'oxyde de graphène

THÈSE dirigée par :

M. BIANCO Alberto	**Directeur de recherche**, CNRS
Mme. MÉNARD-MOYON Cécilia	**Chargée de recherche,** CNRS

RAPPORTEURS :

M. EIGLER Siegfried	Professeur, Institute of Chemistry and Biochemistry of Berlin
M. GIAMBASTIANI Giuliano	Senior researcher, Institute of Chemistry of OrganoMetallic Compounds of Florence

Isabella Anna VACCHI

Fonctionnalisation chimique contrôlée de l'oxyde de graphène

Résumé

L'oxyde de graphène est un nanomatériau prometteur grâce à ses caractéristiques physico-chimiques. Cependant, jusqu'à aujourd'hui, sa composition exacte reste encore inconnue. Ceci est dû à la complexité et au caractère non-stœchiométrique de ce matériau.

Nous avons commencé par étudier sa composition de surface et sa réactivité. Nous avons utilisé des échantillons synthétisés de manière différente pour explorer la relation entre la méthode de synthèse et la composition de surface. En outre, nous avons préparé un dérivé fonctionnalisé avec un agent chélatant de radionucléides pour étudier sa biodistribution et l'impact de la taille latérale.

Par la suite, nous avons essayé plusieurs stratégies de multi-fonctionnalisation. L'avantage est de pouvoir combiner différentes propriétés. Nous avons observé que, souvent après la fonctionnalisation, la dispersabilité de l'oxyde de graphène diminue. Ainsi, nous avons développé un échantillon fonctionnalisé par un polymère soluble dans l'eau.

Enfin, nous avons exploré et amélioré les méthodes de caractérisation de l'oxyde de graphène. Une caractérisation approfondie par différentes techniques est fondamentale pour comprendre les modifications que le matériau a subies.

Mot clé : oxyde de graphène, composition de surface, fonctionnalisation, multi-fonctionnalisation, biodistribution, dispersabilité, caractérisation.

Résumé en anglais

Graphene oxide is a promising nanomaterial thanks to its physicochemical characteristics. However, until today its exact composition remains still unknown. This is due to the complexity and non-stoichiometric character of this material.

We started by investigating the surface composition of graphene oxide and its reactivity. We used differently synthesized samples to explore the relationship between the synthesis method and the surface composition. Furthermore, we functionalized graphene oxide with a chelating agent of radionuclides to study its biodistribution, and the impact of the lateral size.

Afterwards, we tried different strategies for multifunctionalization with the aim to combine different properties. We observed that the dispersibility of graphene oxide often decreased after functionalization. Thus, we developed a highly water-stable graphene oxide sample by grafting a water-soluble polymer on its surface.

Finally, we explored and improved the characterization methods for graphene oxide. A thorough investigation using different characterization techniques is fundamental to understand the modifications that the material underwent.

Keywords: Graphene oxide, surface composition, functionalization, multifunctionalization, biodistribution, dispersibility, characterization.

Acknowledgements

I would like to thank Dr. Alberto Bianco, my supervisor, for giving me the possibility to do my PhD in his research group, in a friendly and scientifically stimulating environment. I would also like to thank him for the chance to join different conferences, schools and the internship at the laboratory of Prof. Komatsu, in Japan.

I'm really grateful to Dr. Cécilia Ménard-Moyon, my co-supervisor, for the support she gave to me, all the suggestions and help. She has been my reference in this three years, by being both a friend and a boss in her kind and pleasant way.

I'm also grateful to prof. Siegfried Eigler and Dr. Giuliano Giambastiani, for accepting to be members of my defense commission and reading this manuscript.

I wish to thank as well Prof. Sylviane Muller for accepting me within the UPR 3572, an interdisciplinary department with a lot of positive and helpful persons.

Afterwards, I would like also to thank Prof. Naoki Komatsu for having accepted me in his group, for my 3 months stay in Japan. I want also to express my gratitude to Prof. Kostas Kostarelos, for the collaboration on the biodistibution project.

I want to acknowledge as well all the people who helped me with the XPS: Fanny Richard for the formation to use the XPS apparatus, Dr. David Morgan for the help in the interpretation of the C KLL Auger spectra, Dr. Mark Biesinger and Dr. Neal Farley for the help in the improvement of the analysis of carbon nanomaterials and for making available tools and lessons to interpret XPS data. I would like to thank on this subject also Thomas Cottineau, Andrea Vacchi, Giacomo Reina and other persons for the nice discussions about electric charging and other XPS problematics, and Ilario Ferigutti, for helping me doing a statistically valid graph with the binding energy values collected from the literature.

I want to acknowledge also Dr. Jésus Raya for all the MAS NMR experiments on my samples.

Some of my samples have also been analyzed in the analytical platforms of the University of Strasbourg and I wish to thank all the technicians that performed them.

I would like to thank my colleagues and ex-colleagues, for the nice moments spent together and the help in case of need (Fengjuan, Giacomo, Adriano, Quyen, Matteo, Diane, Raji, Dinesh, Matthieu, Somnya, Ilaria, Gloria, Laura, Maxim, Olga, Mélanie, Julie and all the others)

I want to express my gratitude also to Fengjuan, Thomas, Andrea, and Giacomo for having helped me with the correction of some of the chapters of the thesis (or of some parts of them) and Jérôme for the correction of the first draft of the French résume.

I would like to express a big "thank you" to all my family for being always there for me.

I'm really grateful as well to Jérôme, my boyfriend, for the patience and support that was really important in this last month.

I'm really thankful also to all my friends, for the great moment spent together and support when needed:

- *From north Italy: Mainly Giulia, Alessandra and David and many others*
- *From Bologna and nearby: Federica and Licia*
- *From Strasbourg: Fengjuan, Giacomo and all the others*
- *From Japan (or who I met in Japan): Orsola, Naoko, Sebastian, Joel, Jenny, Salama, Charlie, Jeff and Sibilla. Thanks to you my stay In Japan became really unforgettable.*

If I forgot someone, as you know, is not with intent, I'm really thankful to all the people I had the luck to meet.

Finally, during the redaction of this these I unfortunately lost a very important companion, Kira, the dog of my family. I have a lot of great memory with her, and I did not have the chance to spend the last moments with her because I prioritized the thesis. Thus, I wanted to dedicate this few lines to her and to all the people who will read these lines to help to remember that family and friends should come always before work, because without them we are a shell without a soul.

THANKS TO ALL OF YOU!

Abstract

Doctoral Thesis

by Isabella Anna Vacchi

Graphene family nanomaterials are very attractive thanks to their unique chemical and physical properties. Graphene oxide (GO) is especially studied in the biomedical field due its water dispersibility that makes it suitable for applications in nanomedicine. The first important step to exploit GO in this field is to fully characterize its surface through analytical techniques and chemical investigations. Indeed, until now, the precise chemical composition of GO is still unknown and debated, also because it is strongly related to the synthetic procedure to obtain this material. The second important step, instead, is the functionalization of GO that allows to conjugate molecules for specific applications. In particular, the multifunctionalization is very promising to endow GO with imaging and therapeutic properties.

In this context, the purpose of my PhD work was the chemical investigation of GO and its reactivity towards different covalent functionalization reactions and the development of a strategy of multifunctionalization. The investigation of the composition of GO is essential to control its functionalization for future applications. For this purpose, we chose a series of selective reactions for the derivatization of the different oxygen-containing functions supposed to be present on the surface of GO. Due to their high reactivity, several reactions may occur concomitantly. For this reason, a thorough investigation with control reactions has been performed. Moreover, differently synthesized GO samples were examined to study the relationship between the synthesis procedure and the surface composition. Once we established which are the main functional groups on GO and their reactivity, we started to study a multi-functionalization strategy. For the multifunctionalization we decided to use amino terminated chains, because amino groups can be easily further functionalized in physiological conditions. Thus, to control each chain independently orthogonal protecting groups were selected. By trying different strategies of multifunctionalization, we noticed that, often, the water dispersibility of the sample was decreasing after functionalization. To solve this aspect, we produced a highly water stable GO derivative, by grafting a water-soluble polymer on its surface. On this sample, an additional multifunctionalization strategy was investigated.

Due to the complexity of GO chemical structure, much work remains to be done in developing reliable characterization methods that will aid to obtain an unambiguous structural identification. In this context, we explored the X-ray photoelectron spectroscopy and solid state nuclear magnetic resonance to improve the characterization of GO. Because of the complexity of this material, a good understanding of its pristine form and of the modification it underwent after functionalization is fundamental to avoid misinterpretations.

Index

Acronyms and Abbreviations

a.u.	arbitrary unit
ADME	administration, distribution, metabolism, excretion
AFM	atomic force microscopy
BMPs	bone morphogenetic proteins
Boc	di-*tert*-butyloxycarbonyl group
Boc_2O	di-*tert*-butyl dicarbonate
DMAP	4-(Dimethylamino)pyridine
EDC	1-(ethyl-3-(3-dimethylaminopropyl)carbodiimide
f-GO	functionalized GO
FSLG-HETCOR	frequency-switched Lee Goldburg heteronuclear correlation
FT-IR	Fourier transform IR
FWHM	full width at half maximum
GIC	graphite intercalated compound
GO	graphene oxide
GO-Ant	GO from Antolin
GO-Jp	GO from Japan
GO-K	GO from Manchester
GO-NI	GO from NanoInnova Technologies
HOBt	*N*-hydroxybenzotriazole
HPPH	2-(1-hexyloethyl)-2-devinyl pyropheophorbide-alpha
HRTEM	high resolution TEM
IR	infrared spectroscopy
KHMDS	potassium bis(trimethylsilyl)amide
MAS	magic angle spinning NMR
MS	mass spectrometry
NGO	nanoGO

NMR	nuclear magnetic resonance
NVOC	4,5-dimethoxy-2-nitrobenzyl protecting group
NVOC-Cl	4,5-dimethoxy-2-nitrobenzyl chloroformate
PAMAM	polyamidoamine
PEG	polyethyleneglycol
PEI	polyethyleneimine
PG-GO	polyglycidol-covered GO conjugate
PPS	poly(sodium 4-styrenesulfonate)
RES	reticuloendothelial system
rGO	reduced GO
ROS	reactive oxygen species
SEM	scanning electron microscopy
siRNA	small interfering ribonucleic acid
SP	substance P
SS MAS NMR	solid state magic angle spinning nuclear magnetic resonance
ssDNA	single stranded deoxyribonucleic acid
SSNMR	solid state NMR
Stat3	signal transducer and activator of transcription 3
TEM	transmission electron microscopy
TGA	thermogravimetric analysis
TIS	triisopropylsilane
UV-Vis	ultraviolet-visible spectroscopy
XPS	X-ray photoelectron spectroscopy
XRD	X-ray diffraction

Résume de thèse

Chapitre 1 : Introduction

Le graphène est un nanomatériau très prometteur et largement étudié du fait de ses caractéristiques uniques, chimiques et physiques.[1]

Le graphène répond aujourd'hui à beaucoup de besoins pour des applications dans les domaines de la nanoélectronique, du photovoltaïque, en science des matériaux et en ingénierie.[2] Sa forme oxydée, l'oxyde de graphène (GO), mieux dispersée dans les milieux physiologiques, est actuellement étudiée dans le domaine biologique pour créer des biocapteurs, pour diagnostiquer des maladies, comme agent antibactérien et antiviral, pour le ciblage du cancer et pour la thérapie photothermique.[3–9]

La surface du GO présente différents groupements fonctionnels incluant des groupements hydroxyles, époxydes et carbonyles (Fig. 1).[10,11] Mais, jusqu'à aujourd'hui, la composition exacte est encore inconnue et beaucoup discutée, aussi parce qu'elle est fortement liée au procédé de synthèse du GO. De plus, la structure du GO est très complexe, et pour cette raison, beaucoup de travail reste à faire : i) pour trouver des méthodes de caractérisation qui aideraient à obtenir une identification structurelle sans équivoque, ii) pour développer des méthodes de synthèse qui donneraient des produits uniformes.

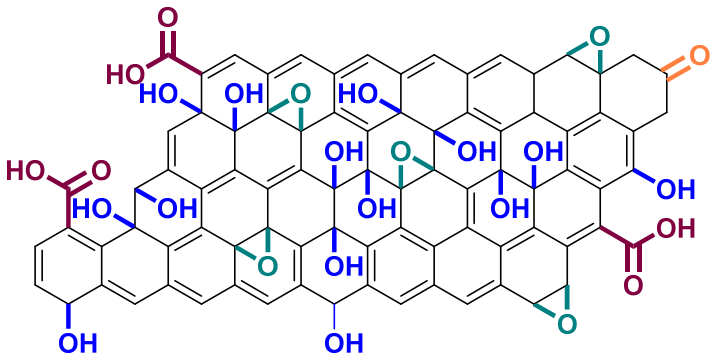

Figure 1 Structure simplifiée du GO.

La première étape pour exploiter le GO pour des applications biomédicales est de bien connaître sa composition de surface. Il est donc nécessaire de le caractériser en utilisant différentes techniques analytiques et chimiques. Une fois cette étape accomplie, l'étape suivante est de modifier la surface du GO par fonctionnalisation covalente pour lui conférer des caractéristiques spécifiques en fonction de l'application visée. La fonctionnalisation du GO permet de conjuguer différentes molécules. En particulier, la multi-fonctionnalisation est prometteuse pour donner au GO plusieurs propriétés, comme par exemple d'imagerie et thérapeutique.

Par conséquent, mon projet se développe autour de ces différents axes :

- étude de la composition de surface du GO par fonctionnalisation covalente et comparaison d'échantillons de GO obtenus par différents procédés de synthèse.
- multi-fonctionnalisation covalente du GO.
- étude pour trouver des méthodes analytiques fiables pour caractériser le GO, par exemple par spectroscopie photoélectronique par rayons X (XPS) et par spectroscopie RMN en phase solide.

Chapitre 2 : Étude de la composition de surface de l'oxyde de graphène

Afin d'étudier la composition de la surface du GO, nous avons choisi des réactions sélectives pour dérivatiser les différents groupements oxygénés supposés être présents sur le GO.

Nous avons effectué une réaction d'éthérification (réaction de Williamson) et d'estérification sur les groupements hydroxyles (Fig. 2).

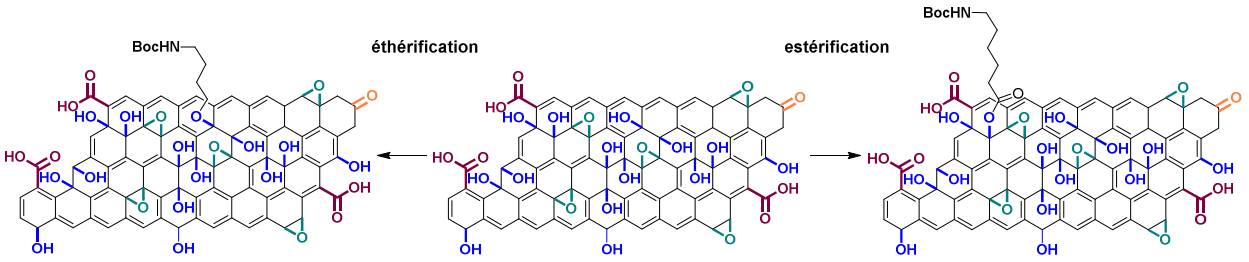

Figure 2 Schématisation simplifiée des réactions sur les groupements hydroxyles.

Nous avons accompli une réaction d'amidation et d'estérification sur les acides carboxyliques (Fig. 3). Il s'avère que dans ce cas les taux de fonctionnalisation sont faibles, ce qui indique l'absence d'un nombre significatif d'acides carboxyliques réactifs.

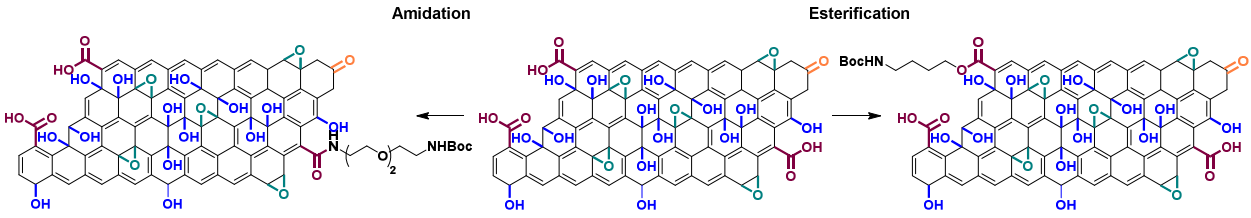

Figure 3 Schématisation simplifiée des réactions sur les groupements carboxyliques.

Nous avons réalisé la réaction de Wittig sur les groupements carbonyles (Fig. 4). Aussi dans ce cas, les taux de fonctionnalisation étant négligeables, nous en avons déduit l'absence de ce groupe en quantité significative.

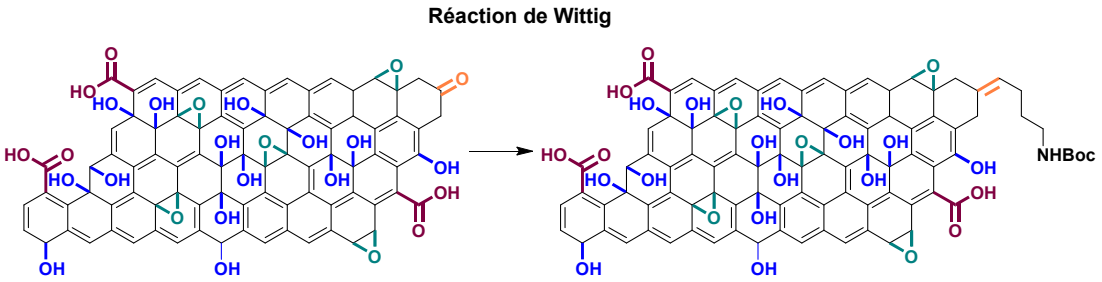

Figure 4 Schématisation simplifiée de la réaction de Wittig sur les groupements carbonyles.

Nous avons effectué l'ouverture des époxydes avec une chaîne aminée. Cette fonction chimique s'avère être majoritaire sur la surface du GO au vu des taux de fonctionnalisation élevés que nous avons obtenus (Fig. 5).

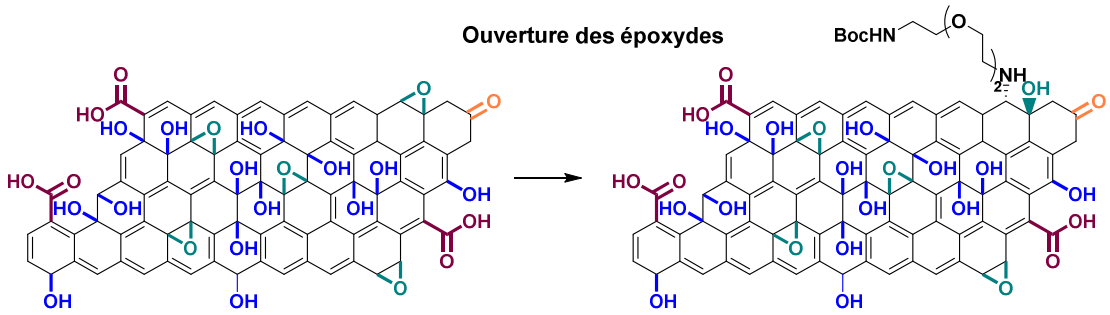

Figure 5 Schématisation simplifiée de la réaction d'ouverture des époxydes par un dérivé aminé.

En conclusion, les groupements que nous avons constaté être présents sur le GO sont principalement les époxydes et les hydroxyles, et en quantité minoritaire les acides carboxyliques et les carbonyles.

Nous avons répété les mêmes réactions sur deux échantillons différents de GO, l'un obtenu par coupage et exfoliation de nanofibres de carbone et l'autre par la méthode de Hummers qui est fréquemment utilisée. Nous avons pu constater que les groupements fonctionnels sont les mêmes, par contre leur pourcentage varie. Ces résultats ont été confirmés par des moyens analytiques tels que la RMN en phase solide (Fig. 6).[12] En accord avec les données rapportées dans la littérature, les pics à 60.9 ppm et 70.8 ppm peuvent être attribués respectivement aux groupes époxydes et hydroxyles.[13,14] Le pic situé à 129.4 ppm est attribué aux doubles liaisons C=C, tandis que le pic large et faible autour de 90-100 ppm pourrait être attribué aux lactols.[15,16] Par contre, les pics correspondant aux groupes carbonyles sont plutôt localisés autour de 160-190 ppm.[17]

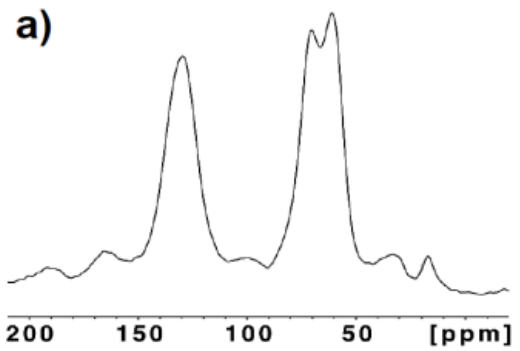

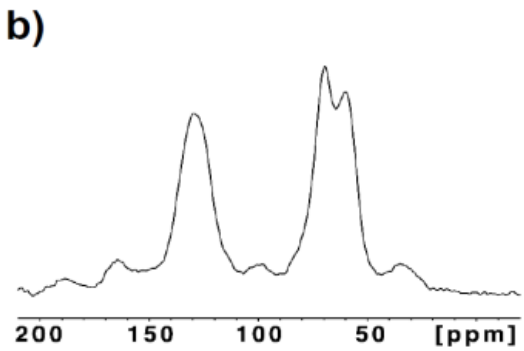

δ (ppm)	%
16.5	3.8
58.9	29.7
69.7	30.5
102.2	2.4
129.3	30.2
189.6	3.5

δ (ppm)	%
59.1	15.3
69.8	34.1
97.6	5.3
128.3	42.9
186.8	2.5

Figure 6 RMN quantitative ^{13}C en phase solide de GO synthétisé a) par la méthode de Hummers et b) par exfoliation de nanofibres de carbone, et pourcentages respectifs des différents pics (les déplacements chimiques assignés aux groupements carbonyles sont signalés en rouge).

Chaque échantillon a été caractérisé par spectroscopie FT-IR, analyse thermogravimétrique (ATG), spectroscopie Raman, XPS, microscopie électronique à transmission et par un test colorimétrique (test de Kaiser).

Pour chaque réaction (mono-fonctionnalisation ou multi-fonctionnalisation), des réactions contrôles ont été effectuées. Une réaction contrôle est une réaction effectuée dans les mêmes conditions réactionnelles, mais en l'absence d'un des réactifs. Ces réactions sont indispensables en raison de la grande réactivité des groupements oxygénés qui peuvent provoquer des réactions secondaires et aussi en raison du risque d'adsorption des molécules sur la surface du GO *via* des interactions non-covalentes.

Ensuite, pour étudier la biodistribution du GO, nous avons exploité l'ouverture des époxydes pour greffer sur sa surface un agent chélatant de radionucléotides (DOTA) (Fig. 7). Trois échantillons de GO avec des dimensions latérales différentes ont été testés pour établir la relation entre la taille latérale et la biodistribution. Les résultats ont montré une distribution dans les organes différente selon les échantillons, mais tous ont été éliminés principalement dans les urines, et aussi dans les excréments.

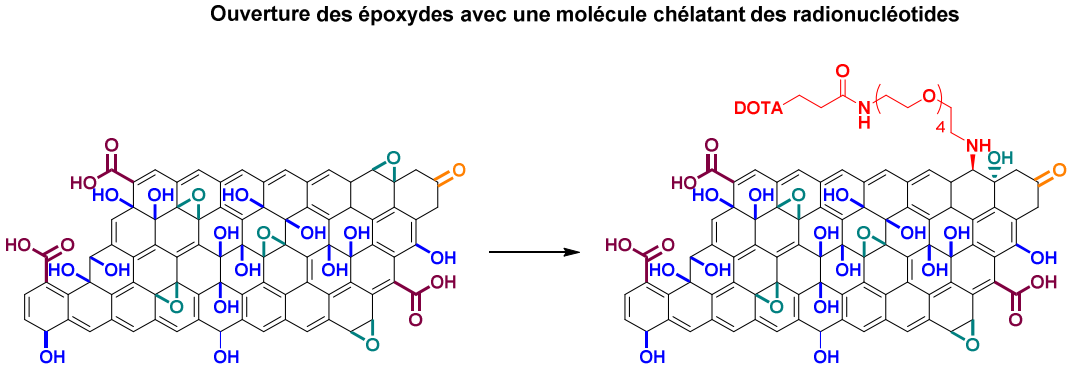

Figure 7 Schématisation simplifiée de l'ouverture des époxydes avec une molécule chélatant des radionucléides.

Chapitre 3 : Double fonctionnalisation de l'oxyde de graphène

Une fois établie la composition de surface du GO, nous avons combiné des réactions déjà testées pour développer une stratégie de multi-fonctionnalisation. Nous avons choisi les réactions qui ont donné les taux de fonctionnalisation les plus importants. Par conséquent, nous avons décidé de focaliser notre attention sur les groupements époxydes et hydroxyles, et spécifiquement sur la réaction d'ouverture des époxydes avec une molécule aminée et sur la réaction d'éthérification et d'estérification des hydroxyles.

Pour la multi-fonctionnalisation, nous avons choisi des chaînes aminées car les fonctions amines sont très réactives et peuvent être facilement dérivatisées avec des molécules biologiquement actives. Ainsi, pour contrôler les deux chaînes d'une façon indépendante, nous avons utilisé des groupements protecteurs orthogonaux en considérant la sensibilité du GO face à des températures élevées et des conditions réductrices. Nous avons choisi de combiner le groupement Boc avec un groupement photoclivable, le α-methyl *o*-nitrobenzyl ester (Fig. 8). Ensuite, nous avons optimisé les conditions pour la réaction de photoclivage.

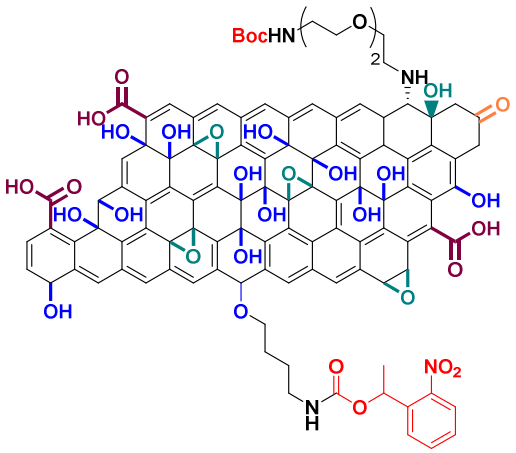

Figure 8 Multi-fonctionnalisation avec des chaînes aminées protégées par des groupements orthogonaux (en rouge).

Pour la multi-fonctionnalisation, nous avons testé différentes combinaisons. Nous avons essayé l'ouverture des époxydes avant l'éthérification (Fig. 9). Ce choix était le plus logique vu que l'ouverture des époxydes augmente le taux d'hydroxyles sur la surface du GO. Cependant, les résultats de l'éthérification n'étaient pas satisfaisants, le taux de fonctionnalisation étant inférieur à celui de la mono-fonctionnalisation par éthérification.

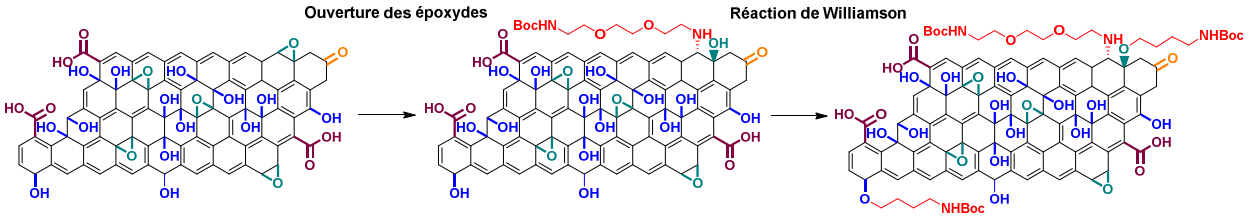

Figure 9 Schématisation simplifiée de la stratégie de multi-fonctionnalisation par ouverture des époxydes suivie de la réaction de Williamson.

Probablement que cette différence est due à une instabilité des groupements hydroxyles après l'ouverture des époxydes. Pour cette raison, nous avons essayé une stratégie "one-pot" en effectuant simultanément les deux réactions (Fig. 10). Néanmoins, le taux de fonctionnalisation par éthérification reste relativement faible.

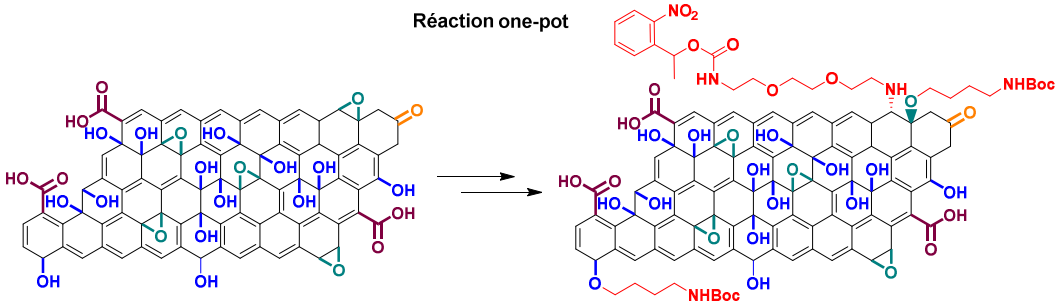

Figure 10 Schématisation simplifiée de la stratégie de multi-fonctionnalisation "one-pot".

Nous avons donc inversé les deux réactions en procédant dans l'ordre à l'éthérification puis à l'ouverture des époxydes (Fig. 11). Le résultat n'était encore pas satisfaisant, le taux de fonctionnalisation par ouverture des époxydes n'étant pas aussi élevé que par mono-fonctionnalisation. Le faible taux de fonctionnalisation de la deuxième réaction est peut-être du à un encombrement stérique.

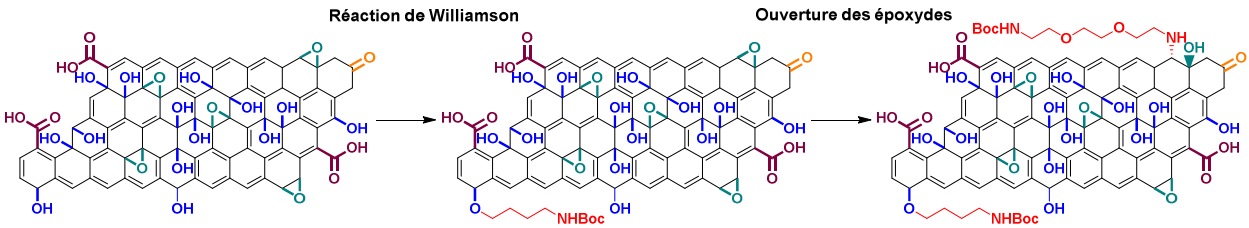

Figure 11 Schématisation simplifiée de la stratégie de multi-fonctionnalisation par réaction de Williamson suivie de l'ouverture des époxydes.

Nous avons donc testé une approche différente en effectuant une estérification des groupements hydroxyles après l'ouverture des époxydes (Fig. 12). Le rendement de la réaction d'estérification est plus important par rapport aux essais précédents, mais n'atteint toujours pas les taux de fonctionnalisation attendus d'après les valeurs obtenues par mono-fonctionnalisation. Ainsi, il est très possible que cela soit dû à un encombrement stérique. En effet, il a été montré dans la littérature que les groupes fonctionnels sont localisés à une forte densité sur certaines zones de la surface du GO.[18] En conséquence, une fois que la première molécule est attachée à la surface du GO, la deuxième molécule ne peut pas être introduite au-delà d'une certaine quantité en raison de l'encombrement stérique du à la présence de la première molécule introduite. En outre, nous avons observé que souvent après fonctionnalisation, la dispersabilité des dérivés diminue. Il est possible que cela affecte aussi le rendement final de la seconde réaction.

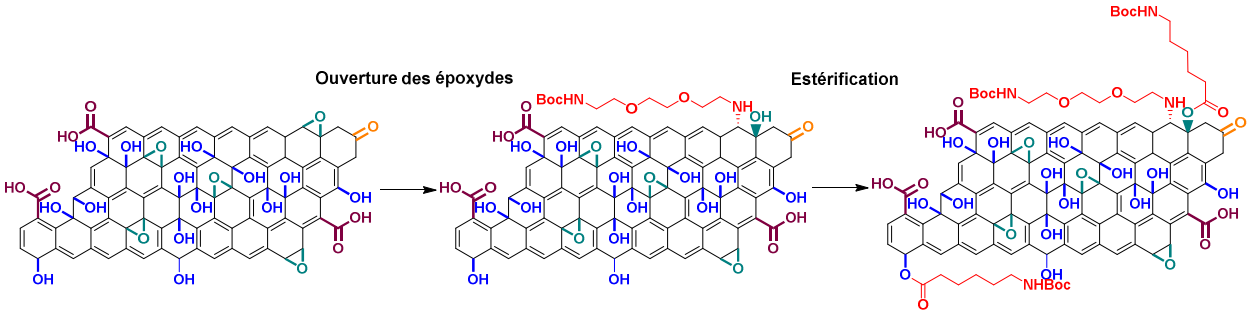

Figure 12 Schématisation simplifiée de la stratégie de multi-fonctionnalisation par ouverture des époxydes suivie de l'estérification.

Un aspect important à considérer pour utiliser des dérivés de GO pour des applications biomédicales est leur dispersabilité dans les milieux physiologiques. Souvent, après fonctionnalisation la dispersabilité dans l'eau diminue. Ceci peut être expliqué par le fait que la quantité et le type de groupements oxygénés change après fonctionnalisation et par conséquent la charge de surface change aussi, ce qui peut induire l'agrégation des feuillets de graphène. La dispersabilité dans l'eau et dans les milieux physiologiques est indispensable afin de minimiser toute toxicité potentielle. Pour résoudre ce problème, nous avons décidé d'augmenter la dispersabilité du GO dans l'eau en modifiant la surface du GO avec un polymère (le polyglycidol) qui a une solubilité aqueuse élevée (Fig. 13).[19] Ce travail a été réalisé dans le Laboratoire du Professeur Naoki Komatsu à l'Université de Kyoto (Japon).

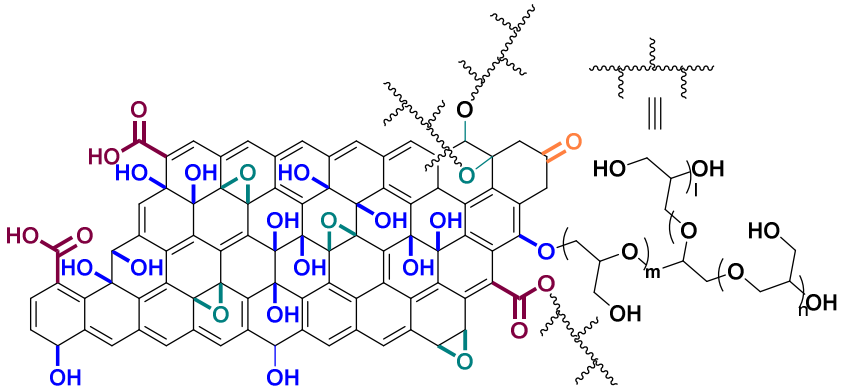

Figure 13 Structure simplifiée du GO fonctionnalisé avec le polyglycidol.

Nous avons essayé différentes conditions pour la polymérisation du glycidol *in situ* avec le GO afin d'obtenir un taux de fonctionnalisation élevé avec une modification mineure du GO.

Nous avons testé la réaction à trois températures différentes : température ambiante, 80°C et 140°C. Le taux de fonctionnalisation pour la réaction à température ambiante est plus faible comparé aux deux autres conditions. Vu que la réaction à 140°C induit une réduction partielle du GO, le meilleur résultat a été obtenu à 80°C. La réduction du GO à 140°C a été confirmée par ATG sur des échantillons contrôles de GO.

En parallèle, nous avons testé la réaction à température ambiante en ajoutant des bases comme catalyseur (Et_3N et NaOH), ce qui a permis d'obtenir des taux de fonctionnalisation importants, mais plus faibles par rapport à la réaction à 80°C.[20]

Ensuite, nous avons étudié la stabilité des différents échantillons dans l'eau et nous avons observé qu'elle est meilleure après fonctionnalisation avec le polymère. Les échantillons traités à 80°C et à température ambiante avec Et_3N montrent une stabilité plus importante dans l'eau.

Une fois ce complexe GO-polymère obtenu avec une stabilité élevée dans l'eau, nous avons développé une stratégie de multi-fonctionnalisation.

Vu que la surface du GO est recouverte de polyglycidol, la meilleure option est de modifier la surface du polymère. Le polyglycidol est constitué d'un nombre élevé de groupements hydroxyles. Dans un premier temps, nous avons partiellement modifié les hydroxyles en azotures qui présentent l'avantage de pouvoir être facilement utilisés pour des réactions "click". Les fonctions hydroxyles restantes peuvent être ensuite modifiées par estérification pour obtenir un GO multifonctionnel. Dans un premier temps, nous avons modifié les azides par la réaction click avec un peptide ciblant les reins (Fig. 14). L'introduction de ce peptide a été confirmée par XPS et FT-IR. L'objectif était de conjuguer un peptide de ciblage et une molécule pour faire de l'imagerie, comme le DOTA, un agent chélatant de radionucléides, ou un fluorophore. Malheureusement, en raison du manque de temps, la deuxième étape de la multi-fonctionnalisation n'a pas pu être effectuée.

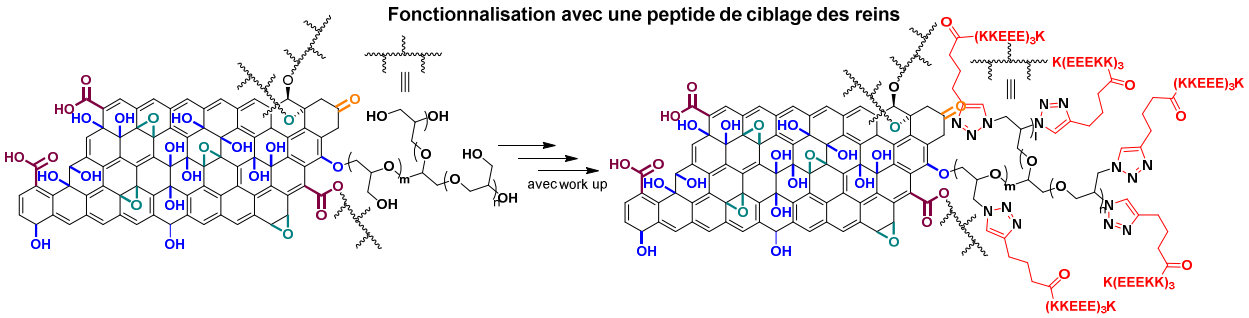

Figure 14 Schématisation simplifiée de la fonctionnalisation du GO avec un peptide de ciblage sur les groupements hydroxyles.

Par conséquent nous avons obtenu des dérivés de GO très stables dans l'eau, fonctionnalisés avec un polymère biocompatible qui peut facilement être modifié par multi-fonctionnalisation.

Chapitre 4 : Comment améliorer l'analyse XPS et l'interprétation des données pour étudier l'oxyde de graphene et autres nanomatériaux

La caractérisation du GO est une étape très importante et délicate. A cause de la complexité structurelle du GO, sa caractérisation est très difficile du fait de l'absence de techniques analytiques suffisamment sensibles. Il faut donc utiliser plusieurs techniques en même temps et conserver un esprit critique. Les meilleures techniques jusqu'à aujourd'hui sont la RMN en phase solide et l'XPS. La RMN donne de très bons résultats qui peuvent être quantitatifs en choisissant certaines configurations, mais cela prend beaucoup de temps. L'analyse d'un échantillon peut prendre d'une journée jusqu'à une semaine. Par conséquent, cette technique ne peut pas être utilisée pour tous les échantillons. Par contre, l'XPS donne une réponse plus immédiate, mais les données sont plus difficiles à interpréter. Il faut donc être rigoureux dans l'analyse des données.

L'XPS est une technique très précise quand on analyse des échantillons conducteurs. Toutefois, le GO est un nanomatériau isolant. Il a donc fallu optimiser les conditions d'analyse pour limiter ou diminuer au maximum l'erreur dans l'analyse causée par le chargement des échantillons pendant l'analyse.

La première étape pour accomplir cela était d'améliorer les paramètres d'analyse, pour voir si la qualité et la résolution des spectres pouvaient être améliorées.

L'étape suivante était de choisir le meilleur substrat pour prendre les mesures. Il y a deux aspects importants dans la préparation des échantillons : le type de substrat et le dépôt de l'échantillon sur le substrat. Dans le premier cas, il faut décider si le substrat doit être conducteur ou isolant. Dans le deuxième cas, il faut trouver un moyen de déposer les échantillons d'une manière très uniforme, très compacte et stable dans l'ultravide. Nous avons ainsi essayé différents substrats et diverses méthodes de préparation des échantillons pour l'analyse.

Une fois établie la méthode de préparation des échantillons, les conditions d'analyse sont également très importantes. Parmi tous les réglages, il y a trois aspects à considérer : choisir une espèce

chimique comme référence en cas de besoin de correction de la charge, répéter l'analyse plusieurs fois et prendre les spectres de tous les éléments présents pour collecter le plus d'informations possible.

La nécessité de répéter l'analyse est expliquée par le fait que les nanomatériaux à base de carbone sont très inhomogènes. En outre, nous avons observé que la référence utilisée pour la correction du décalage de charge et l'échantillon analysé ne subissent pas toujours le même décalage de charge. Ainsi, utiliser une référence externe n'est pas toujours utile. Cependant, nous avons établi qu'il est possible de calculer le rapport C sp^2 et sp^3 à partir de la première dérivée du spectre C KLL Auger. Cette valeur peut être utilisée pour appliquer la correction de décalage de charge appropriée aux spectres.

Le GO est très difficile à analyser par XPS de par son caractère isolant et sa complexité due à une quantité élevée des différents groupements fonctionnels qui donnent un nombre important de signaux superposés dans les spectres.

Chapitre 5 : Conclusions et perspectives

En conclusion, pendant ma thèse, nous avons établi que la surface du GO est composée principalement de groupements époxydes et hydroxyles, et que la différence entre deux échantillons de GO obtenus par des procédés de synthèse différents est liée principalement au pourcentage des groupements fonctionnels. Nous avons amélioré les conditions d'analyse par XPS pour caractériser avec précision la surface du GO. Nous avons augmenté la dispersabilité du GO dans les milieux aqueux en conjuguant un polymère, le polyglycidol. Enfin, nous avons développé et étudié des stratégies de multi-fonctionnalisation.

Comme perspectives, nous continuerons à explorer différentes approches de double fonctionnalisation. Il serait notamment intéressant de pouvoir localiser les groupements fonctionnels introduits à la surface du GO. Cette étude aidera à comprendre s'il y a un problème d'encombrement stérique qui limite le taux de fonctionnalisation du GO dans le cas de stratégies de double fonctionnalisation. De plus, il est prévu d'évaluer le GO fonctionnalisé avec le peptide de ciblage et la molécule d'imagerie *in vitro* et *in vivo* afin d'exploiter les propriétés du GO pour des applications thérapeutiques.

Bibliographie

1. Novoselov KS, Geim AK, Morozov SV, et al. Electric Field Effect in Atomically Thin Carbon Films. Science 2004;306(5696):666–9.

2. Huang X, Yin Z, Wu S, et al. Graphene-Based Materials: Synthesis, Characterization, Properties, and Applications. Small 2011;7(14):1876–1902.

3. Kuila T, Bose S, Khanra P, Mishra AK, Kim NH, Lee JH. Recent advances in graphene-based biosensors. Biosens Bioelectron 2011;26(12):4637–48.

4. Shao Y, Wang J, Wu H, Liu J, Aksay IA, Lin Y. Graphene Based Electrochemical Sensors and Biosensors: A Review. Electroanalysis 2010;22(10):1027–1036.

5. Mohanty N, Berry V. Graphene-Based Single-Bacterium Resolution Biodevice and DNA Transistor: Interfacing Graphene Derivatives with Nanoscale and Microscale Biocomponents. Nano Lett 2008;8(12):4469–76.

6. Akhavan O, Ghaderi E. Toxicity of Graphene and Graphene Oxide Nanowalls Against Bacteria. ACS Nano 2010;4(10):5731–6.

7. Akhavan O, Choobtashani M, Ghaderi E. Protein Degradation and RNA Efflux of Viruses Photocatalyzed by Graphene–Tungsten Oxide Composite Under Visible Light Irradiation. J Phys Chem C 2012;116(17):9653–9.

8. Yang K, Zhang S, Zhang G, Sun X, Lee S-T, Liu Z. Graphene in Mice: Ultrahigh In Vivo Tumor Uptake and Efficient Photothermal Therapy. Nano Lett 2010;10(9):3318–23.

9. Yang K, Wan J, Zhang S, Tian B, Zhang Y, Liu Z. The influence of surface chemistry and size of nanoscale graphene oxide on photothermal therapy of cancer using ultra-low laser power. Biomaterials 2012;33(7):2206–14.

10. Dreyer DR, Park S, Bielawski CW, Ruoff RS. The chemistry of graphene oxide. Chem Soc Rev 2009;39(1):228–40.

11. Szabó T, Berkesi O, Forgó P, et al. Evolution of Surface Functional Groups in a Series of Progressively Oxidized Graphite Oxides. Chem Mater 2006;18(11):2740–9.

12. Vacchi IA, Spinato C, Raya J, Bianco A, Ménard-Moyon C. Chemical reactivity of graphene oxide towards amines elucidated by solid-state NMR. Nanoscale 2016;8(28):13714–21.

13. Lerf A, He H, Forster M, Klinowski J. Structure of Graphite Oxide Revisited. J Phys Chem B 1998;102(23):4477–82.

14. He H, Riedl T, Lerf A, Klinowski J. Solid-State NMR Studies of the Structure of Graphite Oxide. J Phys Chem 1996;100(51):19954–8.

15. Cai W, Piner RD, Stadermann FJ, et al. Synthesis and Solid-State NMR Structural Characterization of ^{13}C-Labeled Graphite Oxide. Science 2008;321(5897):1815–7.

16. Dimiev AM, Alemany LB, Tour JM. Graphene Oxide. Origin of Acidity, Its Instability in Water, and a New Dynamic Structural Model. ACS Nano 2013;7(1):576–88.

17. Gao W, Alemany LB, Ci L, Ajayan PM. New insights into the structure and reduction of graphite oxide. Nat Chem 2009;1(5):403–8.

18. Hunt A, Dikin DA, Kurmaev EZ, et al. Epoxide Speciation and Functional Group Distribution in Graphene Oxide Paper-Like Materials. Adv Funct Mater 2012;22(18):3950–7.

19. Zhao L, Nakae Y, Qin H, et al. Polyglycerol-functionalized nanodiamond as a platform for gene delivery: Derivatization, characterization, and hybridization with DNA. Beilstein J Org Chem 2014;10:707–13.

20. Sandler SR, Berg FR. Room temperature polymerization of glycidol. J Polym Sci [A1] 1966;4(5):1253–9.

CHAPTER 1: INTRODUCTION

1.1 Introduction: Graphene oxide and its biomedical applications

Graphene and its oxidized form graphene oxide (GO) are emerging nanomaterials studied in several fields including materials science, chemistry, physics, biology, medicine, nanotechnology.

GO was discovered in 1859 by Brodie, long before graphene, but only recently its properties started to be fully exploited and studied. After Brodie's finding, other procedures to obtain GO from graphite were developed by Staudenmaier and Hummers.[1–3]

GO is a two dimensional material made of sp^2 and sp^3 hybridized carbon atoms arranged in a hexagonal honeycomb pattern and of oxygen atoms present in the form of different functional groups (Figure 1.1). The type and amount of oxygenated species is still highly discussed today. This is due to a lack of sufficiently sensitive analytical techniques and to the amorphous and berthollide character of this material.

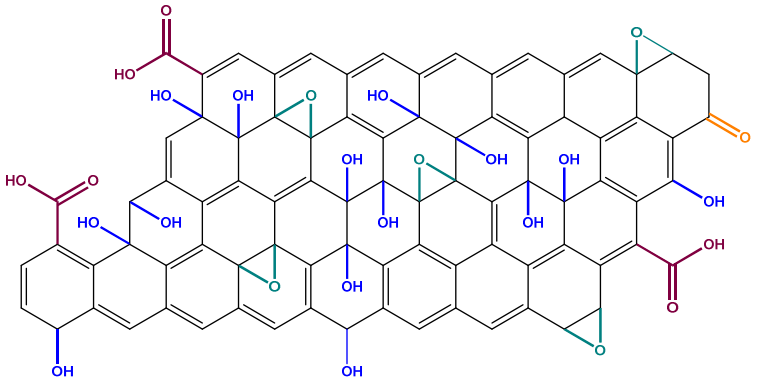

Figure 1.1 Schematized representation of GO

The shape of GO sheets is typically irregular. Their lateral size can be tuned from few nm to mm. This aspect depends on the starting graphite, the oxidation time and the oxidation procedure used, and can be easily modified by sonication.[4,5] An accurate post-sonication, centrifugation and filtration procedure is required to obtain size-sorted GO suspensions.[4–6] But until today it is still not possible to totally control the size of this material.[7]

GO, opposite to its non-oxidized form graphene, is an insulating material due to the highly disrupted sp^2 plane and, thanks to the oxygenated functional groups, it is very hydrophilic. GO is more chemically reactive due to the presence of defects. It shows a higher optical transmittance than graphene because of the different electronic structure, but also lower mechanical properties.[8] GO can be easily reduced to graphene and this is really interesting because then all the characteristics of graphene can be acquired, as for example, the thermal and electrical conductivity and a higher mechanical strength. However, graphene, when obtained by reduction from GO, often contains a high number of defects and hence the electrical performance is not as high as it is for a “pure” graphene layer.

This carbon nanomaterial, due to its hydrophilic aspect, finds many applications in the biomedical field. It is studied for drug delivery owing to the large surface area that can lead to high drug loading. Drugs and molecules can be covalently attached or can be adsorbed onto the surface of GO. The large surface area of graphene family materials enhances the opportunities also for multi drug delivery or for combined strategies of targeting and imaging. Different studies have been performed already on the delivery of anticancer drugs, genes, and peptides in the last years using graphene materials.[9–13] To mention one interesting example, a GO for electrically controlled drug delivery loaded with dexamethasone has been prepared by Weaver *et al.*, and showed an on-demand local delivery of drug molecules.[14]

Beside drug delivery, GO is investigated for cellular imaging, to develop a cost effective technique for early diagnosis and treatment of diseases. This nanomaterial, indeed, is easy to fabricate, non-toxic and stable compared to other organic dyes or quantum dots.[15] GO is made of small ordered sp^2 clusters within a sp^3 C-O matrix.[16] Because of this configuration π-electrons are confined in this clusters and give rise to fluorescence.[17,18] But, because of its aromatic structure, GO is also a strong quencher of dye molecules adsorbed on its surface, thus making non-exploitable the conjugation of fluorescent species on it.[19]

An additional biomedical application of GO is the photodynamic and photothermal therapy for tumor treatment. These two therapeutic modalities are mainly due to the light absorption capacity in the near-IR-region. In photodynamic therapy the absorbed energy activates photosensitizing agents immobilized onto GO, generating cytotoxic reactive oxygen species (ROS). Meanwhile in photothermal therapy the energy is absorbed by the aromatic areas of this material and released into heat. This released heat is exploited for photoablation of tumors for example. Recently, Rong *et al.* loaded 2-(1-hexyloethyl)-2-devinyl pyropheophorbide-alpha (HPPH) onto GO showing a dramatic improvement in the photodynamic cancer cell kill efficacy of HPPH.[20]

Another growing research field for graphene derivatives is gene therapy. The interest of this 2D carbon nanomaterials is due to the large surface area and the oxygenated species that facilitate the interactions with various polymers to design a non-viral transfection vector.[16] For gene delivery, graphene derivatives have to be modified to rend the surface cationic and to facilitate the electrostatic interactions with anionic oligonucleotides. The main molecules used until now are polyamidoamine (PAMAM), polyethyleneimine (PEI), or PEI combined with polyethyleneglycol (PEG) or PEI combined with poly(sodium 4-styrenesulfonate (PPS).[21–23] Chitosan has been also complexed on GO by Bao *et al.* for simultaneous drug and gene delivery. This complex was found to be perfect for the condensation of plasmid DNA in stable, nanosized complexes.[24]

Graphene family nanomaterials act also as antibacterial agents.[25] This is due to the fact that they cause damage to the bacterial cell membrane and create oxidative stress.

For tissue engineering this nanomaterial plays a promising role thanks to the non-significant toxicity, the cost effectiveness and the excellent thermal and electrical conductivity.[26] For example, La *et al.* preloaded a Ti-GO implant with several bone morphogenetic proteins (BMPs) and substance P (SP) factors and obtained a dual delivery system that induced a rapid formation of bone growth without the typical side effects of BMP-2, such as bone overgrowth, inflammation, and uncontrolled bone formation.[27–30]

Graphene and its derivatives have been investigated also for biosensing.[31] The high electron transport mobility, extraordinary mechanical strength, exceptional thermal and electrical conductivity make them appropriate for this application too. A thrombin biosensor based on GO has been developed.[32] This facilitates the detection of thrombin via non covalent assembly of graphene and the aptamer, exhibiting high sensitivity and selectivity (aptamers are selected single-stranded oligonucleotides specific to proteins, small molecules or ions).[32]

In conclusion, GO, thanks to its characteristics, shows a big potential for a plethora of applications in the biomedical field.

1.2 Main synthesis procedures and structural properties of graphene oxide

GO is mainly synthesized through an oxidative process applied to graphite. As mentioned above, Brodie developed the first production procedure of this material. He treated graphite with an oxidation mixture made of potassium chlorate and fuming nitric acid.[1] This procedure was modified in 1898 by Staudenmaier who added to the oxidation mixture concentrated sulfuric acid, reduced the oxidation cycles to only one and introduced a two-step protocol.[2,33,34] Later, in 1958 this protocol has been further optimized by Hummers and Offeman obtaining a time-efficient synthetic route. They introduced potassium

permanganate as a strong oxidant with sodium nitrate and sulfuric acid.[35] Because of the fact that this technique produces toxic gases during the oxidation, Tour *et al.* replaced sodium nitrate with phosphoric acid, that does not produce such dangerous gases.[36]

Recently, Eigler *et al.* developed an improved method to obtain a better quality GO called oxo-G.[37] They pointed out on the fact that the temperature used during the synthesis of GO is a key factor that influences the structure of this material. They established that the temperature used during the classical synthesis procedures causes over-oxidation and the loss of carbon as CO_2 in extended amount. Thus, the temperature during the synthesis process and the aqueous workup was decreased from 45°C to 10°C. In this oxo-G about every second carbon atom is sp^2 hybridized, and as a result, there is still an important aromatic system next to the oxygenated species. The major functional groups in oxo-G are hydroxyls, epoxides, and organosulfates. This material appears to be of high interest because its reduction produces graphene with a lower amount of defects, thus having a better conductivity.[38]

The synthesis procedure is one of the factors that influences the surface composition of GO. This brought to some discrepancy in the structure models. Some variations in the composition of GO for example are due to the oxidation mixture chosen, permanganate *versus* chlorate mixtures or, as we just mentioned above, to the temperature applied during the oxidation process.

Eng *et al.* performed a voltammetry analysis study of the surface composition of a sample of GO obtained using a permanganate oxidation mixture and another one obtained using the chlorate oxidation mixture (Figure 1.2).[39] They discovered that the permanganate mixture produced a majority of *ortho*-quinones followed by ketones. Only a small quantity of carboxyl groups was found, consistent with the latest reports. The main components of permanganate oxidized GO were found to be the epoxides and a minor presence of hydroxyl groups. The same authors pointed on the fact that hydroxyls can congregate in densely oxidized regions and there could be a contribution of steric effects, which brings to a low proportion of hydroxyls detected.[40] They found out that chlorate oxidation mixture produces instead GO with a more uniform distribution but lower total amount of oxygenated functional groups, and that these are mainly ketones. No carboxylic acids at all were detected. The same amount of hydroxyl groups was found for both GO samples, meanwhile no further information was given by the authors on the epoxide amount in the chlorate oxidized GO. Due to the lack of carboxyl groups in both types of GO, the acidity of this material has been explained by the presence of vinylogous acids.[41]

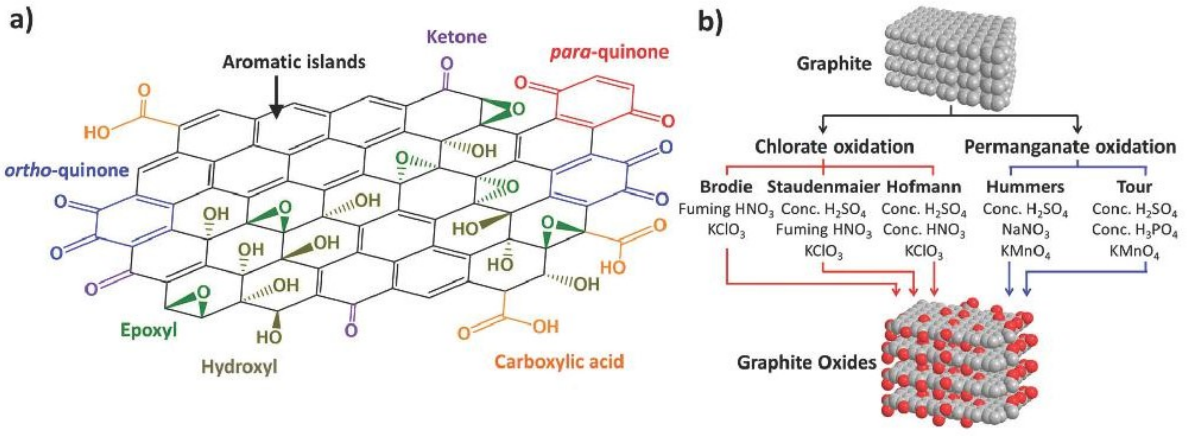

Figure 1.2 a) Schematized GO structure established by Eng *et al.*[39]; b) Schematization of the synthesis procedures of GO. Adapted from reference 39.

Recently, due to the strong relation between the structure of GO and its synthesis procedure, the researchers spent more time studying the formation process of GO from graphite. Dimiev and Tour

distinguished three steps in this oxidation process.[42] The first one is the conversion of graphite into a sulfuric acid intercalated graphite. The second is the conversion into oxidized graphite that happens by adding $KMnO_4$. The third and last step is connected with the water addition and brings to the formation of GO. They also observed that the oxidation progresses from the edge to the center, thus larger graphite takes more time to be oxidized compared to small size graphite. Moreover, crystallinity matters too: highly crystalline graphite samples were converted into oxidized graphite slower than disordered graphite.
Last year, Morimoto *et al.* carefully studied the oxidation of graphite understanding which factors and components play a key role in the synthesis of GO.[43] They established that the pre-oxidation often used is not necessary, neither the use of additives, such as $NaNO_3$ or H_3PO_4. They optimized the reaction conditions, and the best resulted to be 35°C for two hours with a $KMnO_4$/graphite mass ratio <3. Before, Nishina *et al.* reported that the oxygen content is correlated to the amount of $KMnO_4$ used, and it is well known that an excess of $KMnO_4$ causes an overoxidation.[44,45] The temperature, as also established by Eigler *et al.*, causes the formation of defective GO and loss of CO_2 if too high.[37] Thus, determining the correct temperature and amount of $KMnO_4$ is important. Quenching the reaction with water prior to purification is instead fundamental to convert insoluble Mn(III) to soluble Mn(II) species, to be able to eliminate manganese completely from GO during the purification steps (Figure 1.3). H_2O_2 has the role to increase the solubility of certain Mn species, but other compounds such as mild reducing agents can also be used.[43]

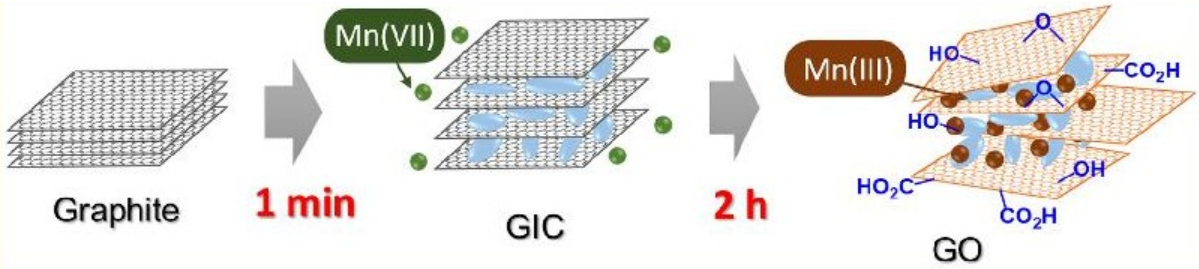

Figure 1.3 Schematized synthesis procedure mechanism established by Morimoto *et al* (GIC=graphite intercalated compound).[43]

By looking at the studies just mentioned, the importance of the factors influencing the structure composition becomes more and more clear. This is also a reason why since the discovery of GO we can find many different models trying to explain its structure.

1.3 Why is the determination of GO structure so difficult? Theoretical structures and instability of graphene oxide

As already mentioned in the previous paragraph, there are different factors that influence the surface composition of GO: the synthesis procedure, the starting material used (for example expanded graphene or natural graphite flakes),[46] the type of workup (aqueous or in organic media),[47] the impurities potentially present and the storage conditions. Indeed, GO is metastable and the size of sp^2 hybridized clusters increases with time.[48] Moreover, GO shows a high sorption capability for various ions on its surface, a crucial aspect in the development of GO filtration membranes. But, for example, elements of the d-block (such as iron, chromium, vanadium, manganese and mercury), which have different oxidation states, possess enough redox potential to induce modifications in the chemical composition of GO.[49] This is due to the instability of some oxygen functionalities such as epoxides. Thus, the presence of some ion contaminants has always to be considered as well as their use during the synthesis or modification of GO.
Furthermore, GO is sensitive to thermal treatment and to harsh chemical conditions (strong basic and reducing conditions). In a study published in 2013 Eigler *et al.* have shown how a treatment using NaOH affects the structure of GO causing rupture of the carbon framework if performed at 40°C.[45]

The decomposition of GO due to heating starts at 50°C with the formation of CO_2 and the creation and increase of vacancies. At higher temperatures the release of water, CO_2 and CO can be monitored by thermogravimetric analysis combined with mass spectrometry (TGA-MS) and thermogravimetric analysis combined with infrared spectroscopy (TGA-IR) analysis.[50] It seems that rearrangement reactions with hydrate intermediates lead to the formation of carboxylic acids that are then released as CO_2.

Other factors that can strongly affect the surface composition of GO are ultrasonication processes and laser irradiations. A prolonged ultrasonication process can cause the introduction of more defects in GO and a reduction of the size. Moreover, if combined with heating at a temperature higher than 50°C it can also reduce GO.[51,52] Laser irradiation causes instead local heating with consequent local reduction of this nanomaterial. This is often exploited in electronics for the formation of local micropatterns of reduced GO.[53,54] Laser irradiation reduces GO also *via* a photochemical effect.[55]

Another controversial aspect is the presence of oxidative carbonaceous debris adsorbed on the surface after the oxidation process and not washed away during workup.[56] These features, if present, can also bring to some degree of misinterpretation of the structure of GO.

For all these reasons and because of the complexity of GO and the lack of sufficiently sensitive analytical techniques for characterization, there are many different GO models in the literature. In this paragraph the main models will be described.

The first model is the one proposed by Hofmann and Holst in 1939. In their structure GO presents repeating units of 1,2-epoxides on the entire sp^2-hybridized structure (Figure 1.4a).[57]

The second model was suggested in 1946 by Ruess. This GO structure contains 1,3-epoxide and hydroxyl groups on a mainly sp^3-hybridized wrinkled carbon sheet composed of *trans* linked cyclohexane chairs (Figure 1.4b).[58]

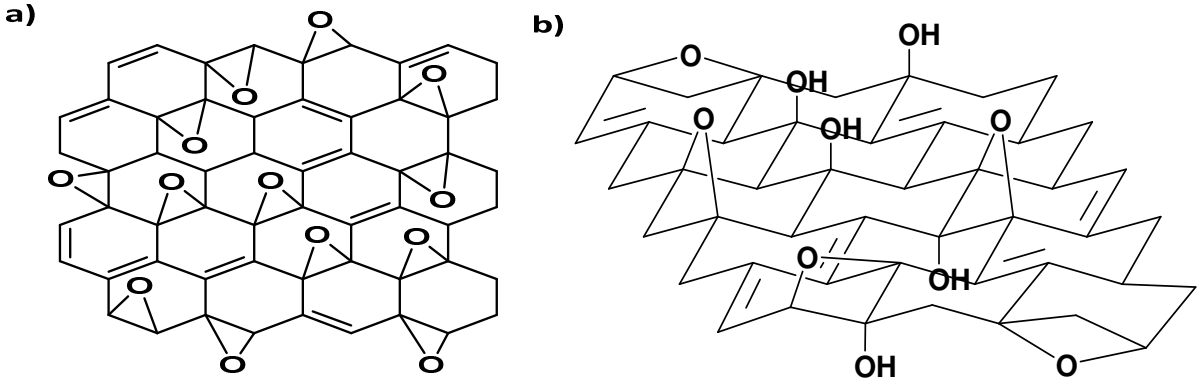

Figure 1.4 Schematic representation of a) the model proposed by Hofmann and Holst and b) the model proposed by Ruess. Adapted from references 57 and 58, respectively.

In 1969, Sholz and Boehm published the third theoretical structure of GO, in which there are hydroxyls and ketones on a corrugated carbon layer (Figure 1.5a).[59]

The fourth model was presented by Nakajima and Matsuo in 1994.[60] By studying two types of GO, obtained through modified Staudenmaier method and electrochemical method, they established that the first step of the synthesis of GO is the formation of a stage two GIC. Moreover, they proposed, after a fluorination study of GO, a similar structure to poly(dicarbon monofluoride) $(C_2F)_n$ (Figure 1.5b).

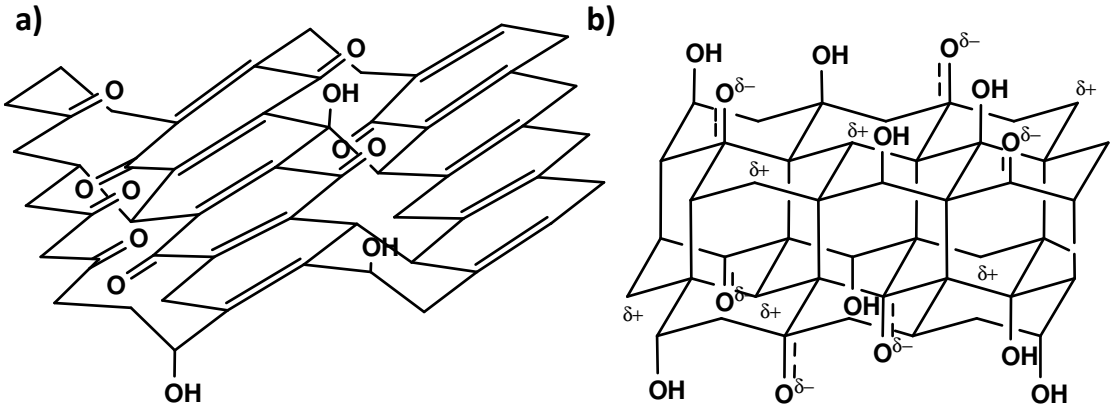

Figure 1.5 Schematic representation of a) the model proposed by Sholz and Boehm and b) the model proposed by Nakajima and Matsuo.[59,60]

All these models were mostly obtained through characterization by elemental composition, chemical reactions and X-ray diffraction analysis.[61]

Until today the most accepted model is the fifth one. This was proposed in 1998 by Lerf and Klinowski after a nuclear magnetic resonance (NMR) study. In this case, the main functional groups are epoxides and hydroxyl groups on the basal plane and carboxylic acids at the edges (Figure 1.6).[62] They were the first suggesting a random distribution of flat aromatic regions and wrinkled regions of sp^3 carbon atoms bearing oxygenated functional groups.

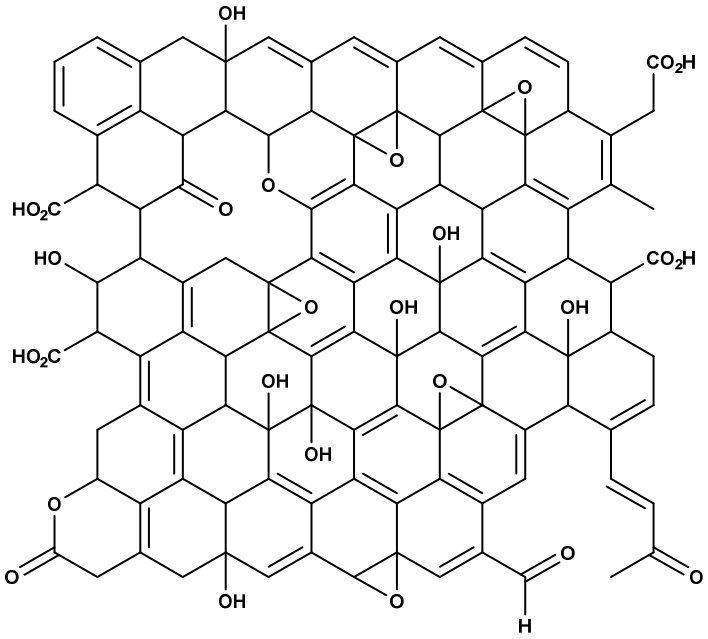

Figure 1.6 Schematic representation of the model proposed by Lerf and Klinowski. Adapted from reference 62.

In 2006 a sixth model was proposed by Dékány *et al.* after NMR, X-ray diffraction (XRD), transmission electron microscopy (TEM), electron spin resonance, Fourier Transform IR (FT-IR), elemental analysis and X-ray photoelectron spectroscopy (XPS) investigation. In this model, GO consists of two distinct zones with *trans*-linked cyclohexane chairs and corrugate hexagon ribbons. The first domain consists of epoxides and hydroxyls meanwhile the second one of ketones and quinones (Figure 1.7a). Phenolic groups are also mentioned to explain the acidity of GO.[63]

Ajayan and coworkers proposed the seventh GO model in 2009 through a thorough magic angle spinning (MAS) NMR study. In this model, beside a majority of hydroxyls and epoxides, a minor

contribution of other functional groups is also considered, such as five- and six-membered ring lactols and ketones (Figure 1.7b).[64]

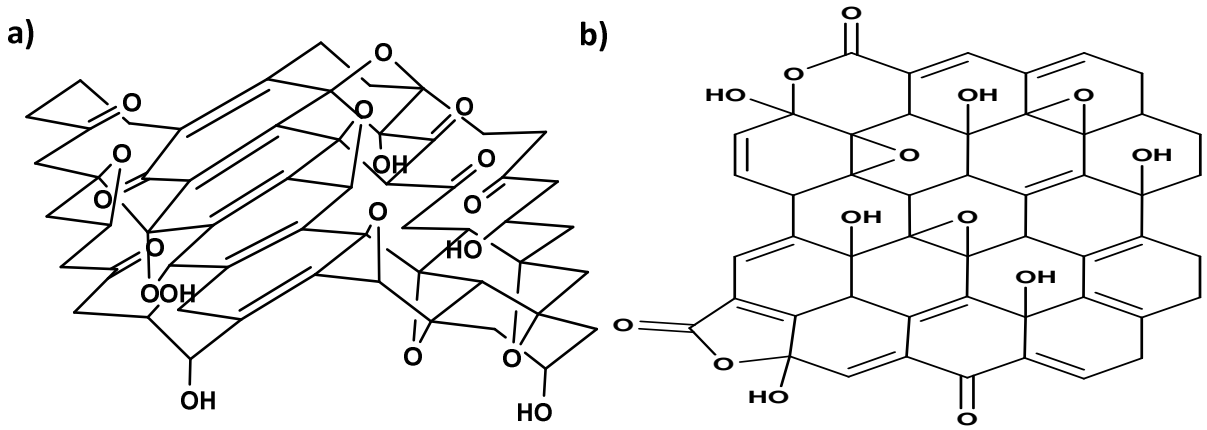

Figure 1.7 Schematic representation of a) the model proposed by Dékány *et al.* and b) the model proposed by Ajayan *et al*. Adapted from references 63 and 64, respectively.

The latest model of GO has been suggested by Tour and coworkers. They proposed a dynamic structure with an undefined set of functional groups. This structure constantly evolves in aqueous solvents. The driving force of the constant surface transformation appears to be an accumulation of negative charges on GO. The acidity of this structure is due to carbonyls associated with hydroxyls in form of vinylogous acids. Prolonged exposure to water degrades gradually GO, a process that appears to be slower in acidic conditions. This model explains also the reduction of GO under strong alkaline conditions, resulting in the formation of CO_2 and vacancies.[41]

Even if there are many different models proposed in the literature, until today the precise structure of GO is still unknown.

1.4 Functionalization and characterization of graphene oxide

Once GO is obtained from the strong oxidative process, it can be functionalized on the oxygen functionalities created all over its surface or onto the aromatic system that is left intact. Functionalization is often used in biomedical field to conjugate functional molecules, impart targeting capacity, or enhance the dispersibility of the final complex. The functionalization can be both covalent and non-covalent. In the first case a covalent bond is formed, in the second instead different weak interactions coexist.

It has to be noted that GO is often covalently or non-covalently functionalized prior reduction or it is reduced at the same time to restore the conductivity of the graphene structure. This is done to recover and exploit the thermal and electrical conductivity of this material.

1.4.1 Covalent functionalization and multifunctionalization

Thanks to the presence of different types of oxygenated functional groups on GO, there are many possibilities of derivatization of this material. GO is more reactive compared to graphene towards functionalization, but considering its highly oxidized surface, many side reactions can happen. It is really difficult to obtain a good degree of selectivity due to the elevated number of groups. For this reason, it is strongly suggested to always perform control reactions. These are reactions performed in the same conditions, only by avoiding to add a fundamental reagent.

The principal groups already studied in the literature for GO functionalization are the epoxides, the hydroxyls and carboxylic acids. The hydroxyl groups are mainly localized on the core surface of GO. This group can undergo different reactions, such as silanization[65], etherification[66], phosphorylation[67] and the

Ritter reaction.[68] Silanes are very reactive toward protic groups. For example, *N*-[(3-trimethoxysilyl)propyl]ethylenediamine triacetic acid has been attached onto GO through silanization to prepare an antimicrobial system. The final compound showed a higher antimicrobial activity that could be due to a synergistic activity of both GO and the ethylenediamine triacetic acid moiety.[69] It is believed that the silanization is a two-step reaction. The first step is the hydrolysis of the trialkoxy groups of the silane followed by the reaction between the Si-OH groups and the hydroxyl groups of GO (Scheme 1.1). This reaction has been optimized in time by performing it under microwave irradiation.[70] This optimized procedure allows to perform the reaction in a few minutes.

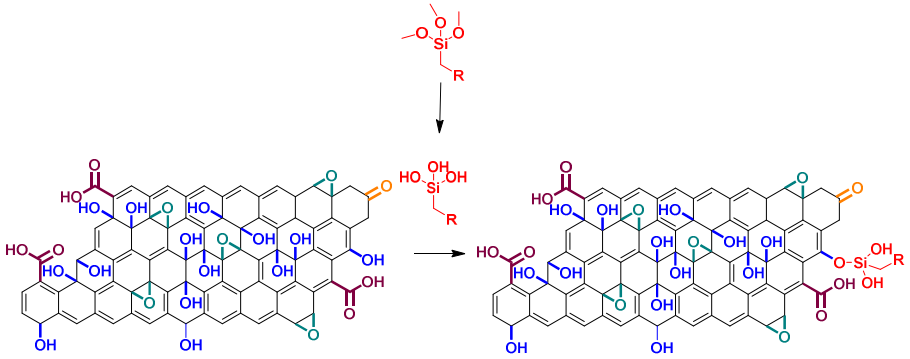

Scheme 1.1 Silanization reaction on GO. (The reaction has been drawn only on one functional group for clarity reasons. Side reactions were not considered).

Another reaction that has been performed on the hydroxyl groups is the Johnson-Claisen rearrangement (Scheme 1.2).[71] This is a modified Claisen reaction in which an allylic alcohol with an orthoester is used. Only the allylic alcohols on GO undergo this reaction. Therefore, not all hydroxyl groups on GO are functionalized.

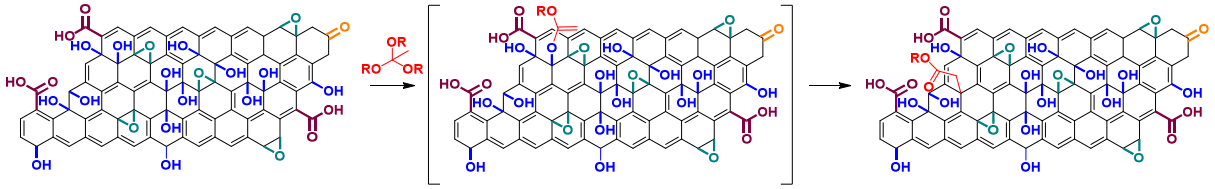

Scheme 1.2 Johnson-Claisen rearrangement on GO. (The reaction has been drawn only on one functional group for clarity reasons. Side reactions were not considered).

More recently, the Ritter reaction has been performed on GO (Scheme 1.3).[68] In this reaction carbocations are produced on the basal plane of GO, which allow a nucleophilic attack by the nitrogen of a nitrile. An amide is formed after hydrolysis. This reaction has been performed with sulfuric acid and acetic acid at 70°C, conditions that brought to the reduction of GO to restore the conductivity of this material.

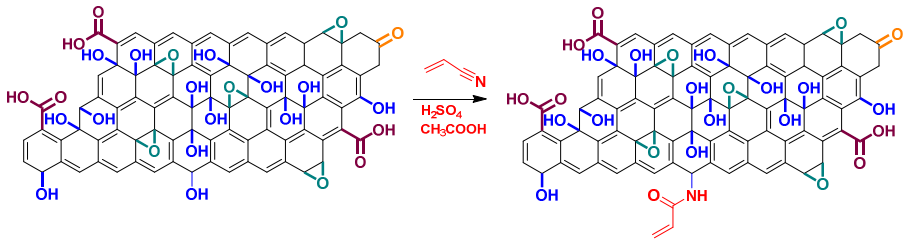

Scheme 1.3 Ritter reaction on GO.[68] (The reaction has been drawn only on one functional group for clarity reasons. Side reactions were not considered).

Another approach recently mentioned to functionalize the hydroxyl groups is the phosphorylation performed to improve the adsorption capability of GO towards uranium (VI) from aqueous solutions.[67] The reaction has been performed by mixing GO with concentrated phosphoric acid at 50°C (Scheme 1.4).

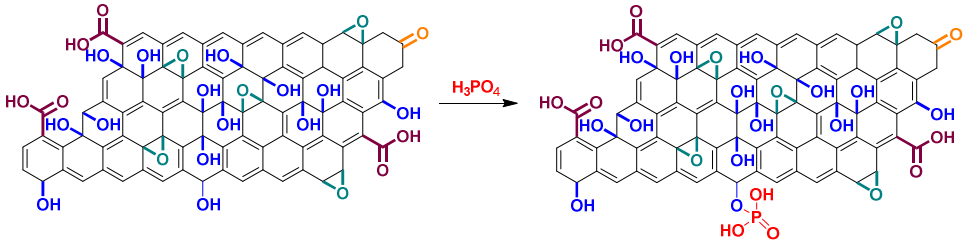

Scheme 1.4 Phosphorylation of GO.[67] (The reaction has been drawn only on one functional group for clarity reasons. Side reactions were not considered).

In most of the approaches mentioned in the literature, the molecules are grafted on the carboxylic acids. These groups are located mainly at the edges, and are commonly activated to form an ester or an amide. The amidation reaction has been performed on GO in both harsh and mild conditions (Scheme 1.5). In the first case the carboxylic acid is activated to acyl chloride using thionyl or oxalyl chloride. In the second case, coupling agents are employed. However, thionyl or oxalyl chloride can also react with the hydroxyl groups, causing side reactions.

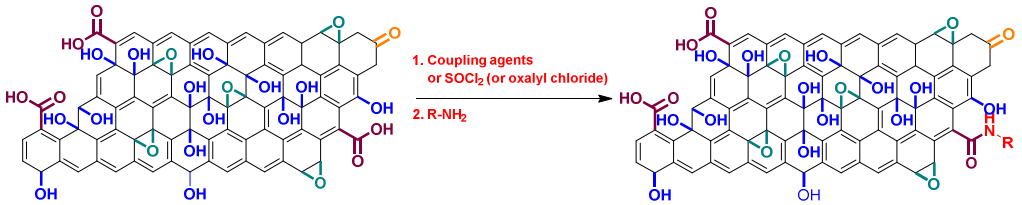

Scheme 1.5 Amidation approaches on GO: with coupling agents and *via* the formation of acyl chlorides. (The reaction has been drawn only on one functional group for clarity reasons. Side reactions were not considered).

The esterification (Scheme 1.6), as the amidation reaction, has been performed using thionyl or oxalyl chloride. In this case, a base was used to deprotonate the alcohol to form the ester bond. Through these conditions a poly(3-hexylthiophene) molecule was grafted to GO, to design heterojunction photovoltaic devices.[72] Alternative conditions are the Steglich esterification in which 1-(ethyl-3-(3-dimethylaminopropyl)carbodiimide (EDC) and 4-(Dimethylamino)pyridine (DMAP) are used as coupling agents. This reaction has been recently used by Mei *et al.* to perform a double functionalization on GO.[73]

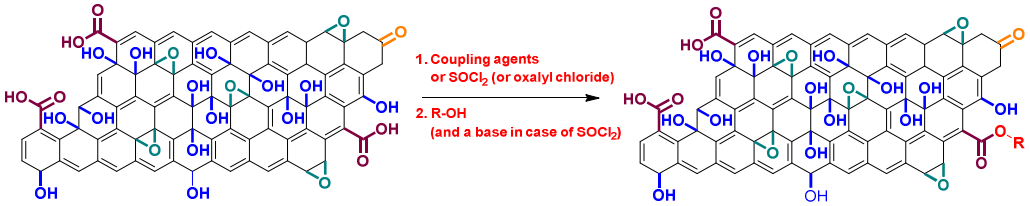

Scheme 1.6 Esterification approaches on GO: the Steglich conditions with coupling agents and the esterification with acyl chlorides. (The reaction has been drawn only on one functional group for clarity reasons. Side reactions were not considered).

A further reaction performed recently on the carboxylic acid group is the Hunsdiecker reaction (Scheme 1.7). This reaction has been performed by Jankovsky *et al.* obtaining brominated graphene.[74] A high concentration of bromine was introduced on GO (bromine concentration of ~20 wt% for the most brominated graphene). Considering the low amount of carboxylic acid initially present on GO, it is possible that side reactions happened. The authors, indeed, mentioned the possibility of a direct bromination of the backbone and also the opening of the epoxides by bromine.

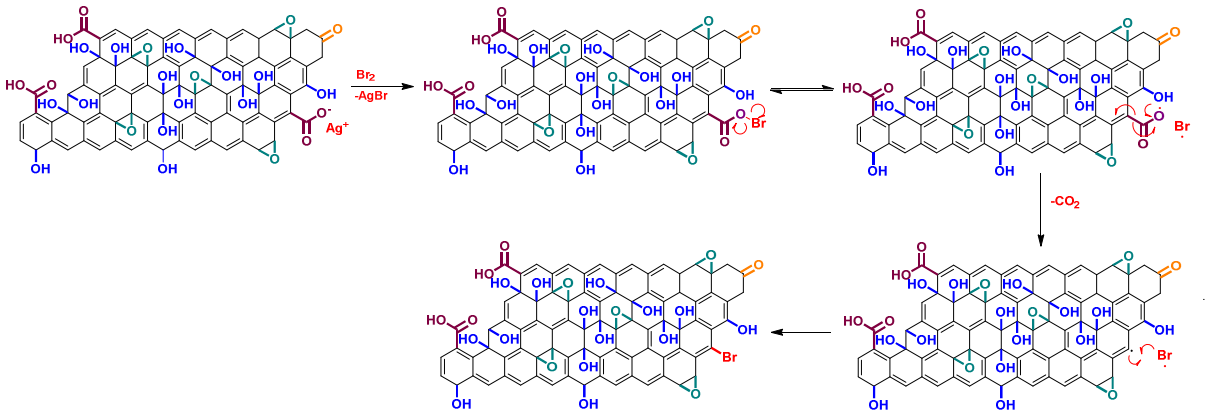

Scheme 1.7 Hunsdiecker reaction on GO. (The reaction has been drawn only on one functional group for clarity reasons. Side reactions were not considered).

The addition of isocyanate compounds has been used in various GO derivatives (Scheme 1.8). Isocyanates can react with both carboxyl and hydroxyl groups with the formation of amides and carbamates, respectively.[75,76] This reaction has been used to get pillared lamellar hybrid porous material.[77]

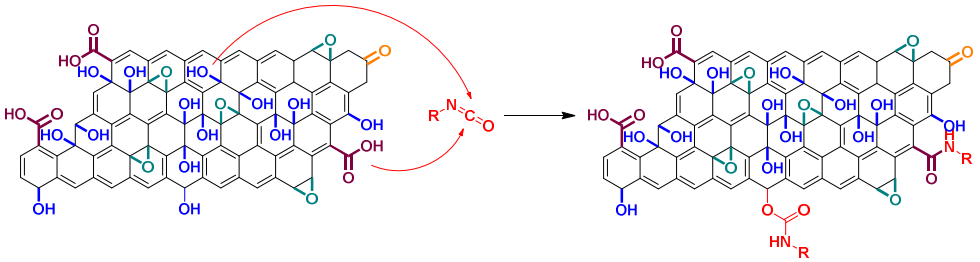

Scheme 1.8 Isocyanate reactions on GO. (The reaction has been drawn only on one functional group for clarity reasons).

Another group on the surface of GO that has been investigated for functionalization is the epoxide. This group is mainly located on the basal plane. The epoxide ring has been mostly opened with amine-terminated molecules or sodium azide (Scheme 1.9). Through this nucleophilic ring-opening chromophores and polymers have been introduced onto GO. Using this strategy, poly-L-lysine has been conjugated to GO to enhance its water dispersibility and biocompatibility.[78] Graphene azide has been synthesized from GO as precursor for click chemistry by Halbig *et al.*[79]

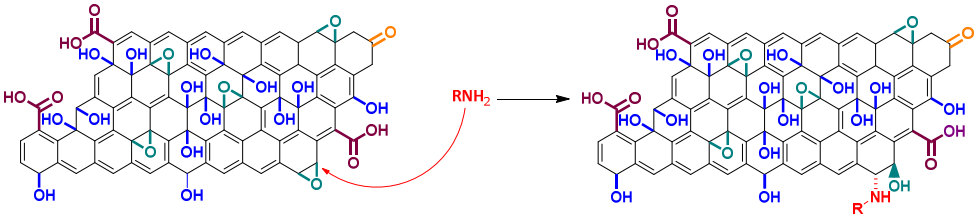

Scheme 1.9 Opening of epoxide ring on GO. (The reaction has been drawn only on one functional group for clarity reasons).

Graphene iodide[80], bromide[81] and chloride[82] were obtained starting from GO. In the first two cases iodine or hydroiodic acid or bromine or hydrobromic acid have been used. In the latter case the chlorination was performed using chlorine atmosphere or plasma assisted exfoliation. For all the three halogenation reactions, GO has been reduced and halogenated functions have been introduced with concomitant removal of the majority of oxygen functionalities.

GO can be functionalized also on its carbon framework. Due to the fact that to interact with the aromatic system stronger conditions often have to be applied, the risk of side reactions is increased. For example, a combination of BuLi and a brominated derivative has been used on GO, leading to alkylation,

etherification and esterification at the same time.[83] The use of highly reactive intermediates, such as diazonium salts[84], carbenes[85] and nitrenes[86] to directly target the basal plane have been mostly applied to reduced GO (rGO) (Scheme 1.10).

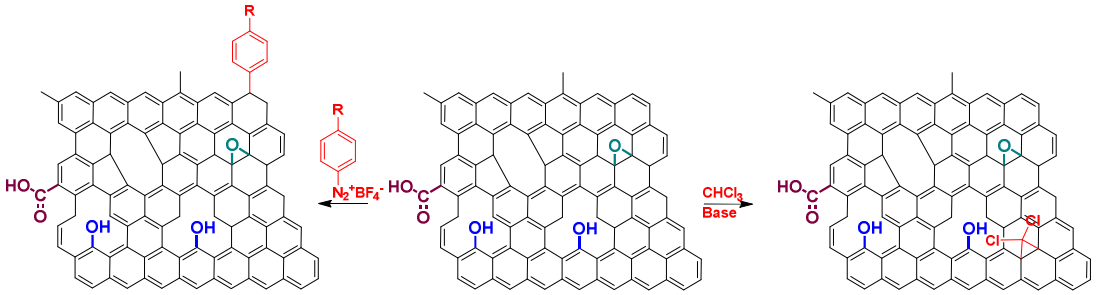

Scheme 1.10 Reaction on rGO with diazonium salts on the left and with carbenes on the right. (The reaction has been drawn only ones for clarity reasons. Side reactions were not considered).

As it is possible to understand, due to its complexity, GO undergoes many different reactions. Thus, a thorough analysis of the final derivative is suggested to understand better the occurrence of the modifications.

1.4.2 Non-covalent functionalization

Non-covalent functionalization of GO occurs through π-π interactions, electrostatic binding, H-bonding, as well as van der Waals, H-π, cation-π and anion-π interactions.[87–90] For example, anticancer drugs were adsorbed onto PEGylated GO nanocarrier.[91] The advantage of this non-covalent approach is that the GO is not modified in its structure nor further defects are introduced in the aromatic system. Moreover, therapeutic molecules can be easier desorbed from the GO surface. On the other hand, the main drawback is that these interactions are less stable than a covalent approach. This is really an important matter in the case of biomedical applications as, for example, the molecules can be desorbed from the surface of GO and released in the blood circulation.

Lu *et al.* immobilized nucleobases and an aromatic dye *via* π-stacking onto GO to obtain a compound for sensing applications.[92] They exploited the quenching effect of GO. Indeed, GO binds the dye-labeled single stranded deoxyribonucleic acid (ssDNA) and quenches the fluorescence of the dye until the binding of this complex is altered due to the presence of a target molecule, resulting in the restoration of the dye fluorescence.

Enzymes instead were immobilized onto GO *via* electrostatic interactions and hydrogen bonds between the oxygen groups of GO and nitrogen groups of the enzymes.[93]

The basal plane of GO, except for the oxygenated functional groups, has a relatively similar structure to graphene. Because of this similarity, van der Waals forces and π-π interactions can be exploited to immobilize molecules. But there are additional interactions from both hydrogen-bond donor and acceptor moieties of the oxygen bearing functional groups. To interact with the surface of GO, a molecule needs a hydrophobic character or/and a highly extended π-system or/and hydrogen-bond donor and acceptor moieties. Π-π Interactions are established if there is a π-system and if the molecule has the good geometry to interact. This last aspect differentiates GO from graphene, indeed, because of the presence of sp^3 carbon atoms there are extended deviations in the planarity of GO. The role of the interactions between a molecule and the structure of GO in some cases can be so important to change the conformation of the molecules.[94]

1.4.3 Main characterization techniques and characterization problematic

Different characterization techniques and analysis methods have been developed to better understand the structure and the behaviour of GO, and the researchers are still looking for new ones.

We can divide the characterization techniques currently used into two groups: the first section determines the morphological characteristics of GO, and the second one establishes the kind and level of functionalization. In the first section we can mention the atomic force microscopy (AFM), TEM, the high resolution TEM (HRTEM) and the scanning electron microscopy (SEM).

The second section comprises the solid state (SS) MAS NMR, TGA, FT-IR and XPS.

Raman spectroscopy and the ultraviolet-visible (UV-Vis) spectroscopy instead are more difficult to classify for the characterization of GO. Indeed, both of them give partial information mainly concerning the degree of oxidation/defects of the GO.

By UV-Vis spectroscopy it is possible to detect two signals for GO. The first is a peak at 300 nm attributed to the n-π* transition of the C=O bonds, meanwhile the second is a peak at 224 nm due to the π-π* transition of the C=C bond (Figure 1.8, left).

Raman spectroscopy is used to define the disorder and the order of the carbon skeleton. Graphene and GO display three main peaks: the D band at 1350 cm^{-1}, the G band at 1580 cm^{-1} and the 2D band at 2700 cm^{-1} (Figure 1.8, center). The G band is related to the sp^2 structure. The D band, instead, is related to the sp^3 carbon atoms, thus it gives information about the defect amount in the aromatic structure, meanwhile the 2D band is related to the number of layers of graphene materials. Considering that modification of GO is done often on the functional groups on its surface and not on the skeleton there is no substantial change in the Raman spectrum.

For GO Raman spectroscopy is often exploited to calculate the I_D/I_G ratio. But, relying on a recent publication this method is not accurate.[95] It seems that in the Raman spectra of GO the G peak is partially wrongly assigned. Apparently this peak at 1580 cm^{-1} is composed of two superposed signals, the G and the D' modes (Figure 1.8, right). The D' peak is proportional to the amount of defects, thus, considering the high defect densities in GO it is expected to contribute significantly to the peak at 1580 cm^{-1}.

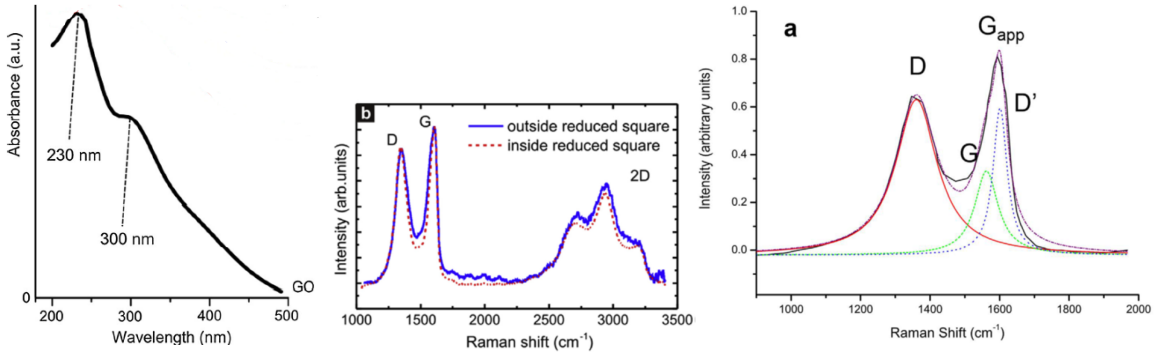

Figure 1.8 UV-Vis spectrum of GO on the left and Raman spectra of GO in the center. On the right a Raman spectrum focused on the 1000-2000 cm^{-1} area with deconvolution to separate the D' from the G peak. Adapted from references 95–97.

Cançado *et al.* recently developed a statistical method to establish the defect density percentage of graphene obtained after reduction of GO by analyzing Raman data.[98] This technique is useful to determine if the produced graphene has still a good conductive sp^2 framework (Figure 1.9), but it is of no interest for GO itself.

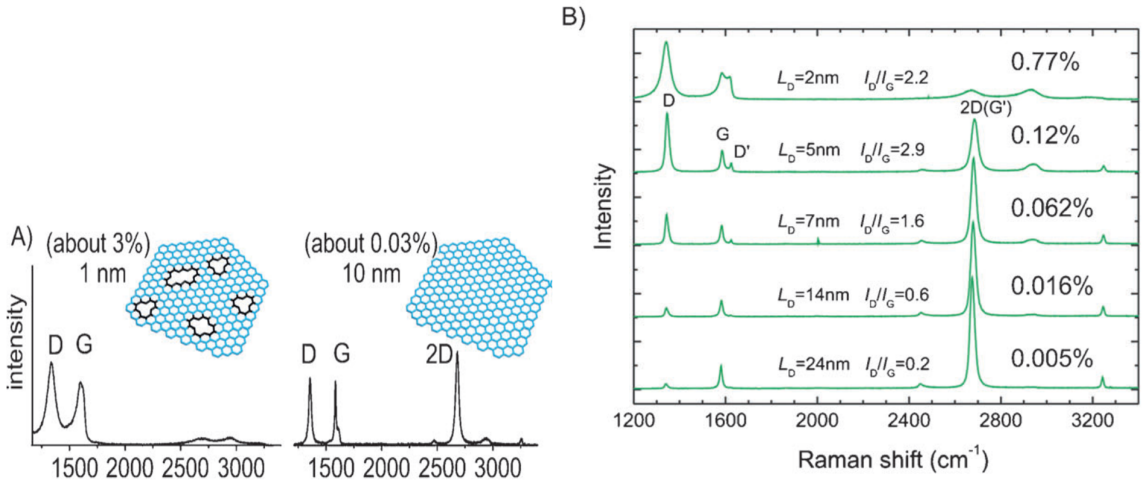

Figure 1.9 A) Raman spectra of rGO (left) and reduced oxoG (right) with simplified structural model and defect density calculated with the method of Cançado *et al.* in percentage and average distance of defects in nm; B) Raman spectra of graphene with L_D (average distance of defects) values between 2 and 24 nm (defect density given in %). Adapted from reference 99.

AFM is a high-resolution method that is used to investigate the surface topology of graphene materials at a nanometer scale in 3D. It gives information about the lateral size and the thickness, thus affording the number of layers.

TEM gives similar morphological information to AFM, but only 2D (Figure 1.10, left). Moreover, this latter method gives also information about the purity of the sample. A HRTEM at atomic resolution provides instead more details on the skeleton of GO. It is possible to see, indeed, patches where oxygenated functions are localized, topological defects, holes, ad-atoms (single atoms lying on a surface), disordered regions and contaminated ones (Figure 1.10, right).[99–101]

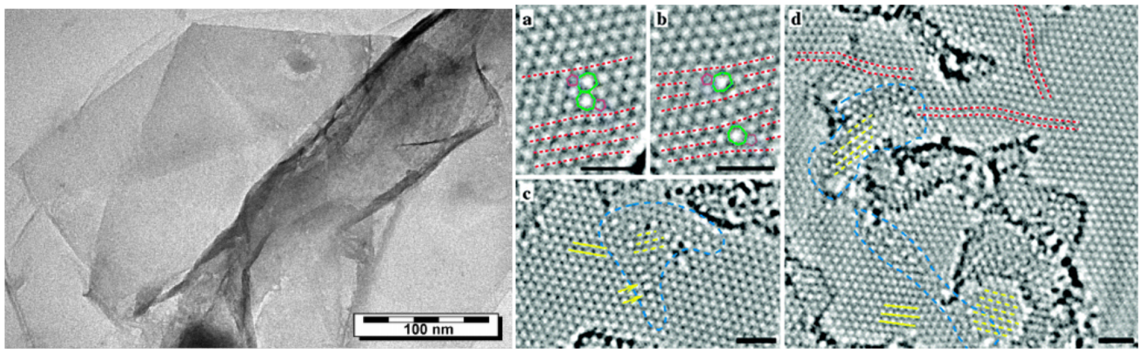

Figure 1.10 Left: TEM image of GO;[63] Right: HRTEM of reduced GO ("**(a, b)** Dislocation dipole observed at two different times (**b)** 2 minutes after **a)**) in the TEM. Each dislocation core consists of a pentagon-heptagon pair. The separation between the dislocation cores has increased, indicating that there is a significant amount of strain present. **(c, d)** Defect cluster, indicated by blue dashed lines. Yellow dashed lines indicate the regions with hexagonal lattice rotated to the dominant orientation (yellow solid lines for comparison). Red dashed lines indicate again distortions in the hexagonal lattice. Yellow arrows in **(c)** indicate strongly elongated carbon polygons. All scale bars are 1 nm"). Adapted from reference 101.

Through FT-IR it is possible to determine the functional groups of GO (Figure 1.11, left). But, due to the presence of adsorbed water on GO there is a strong signal of water in the spectra. The water is difficult to eliminate through thermal treatment because of the thermal instability of this material. In the spectrum of GO we can identify the signal of hydroxyl groups and adsorbed water at 3800-2200 cm^{-1}, the one of the carbonyl group at 1714 cm^{-1}, the skeletal vibration and the signal of oxygen surface compounds or trapped water at 1620 cm^{-1}, the peak assigned to C-O bonds at 1063 cm^{-1} and to the epoxy and ether functionalities at 1266 cm^{-1}.[102]

TGA is often used for the characterization of carbon nanomaterials. It establishes the degree of oxidation or of functionalization, both covalent and non-covalent. Indeed, GO shows a typical thermal profile (Figure 1.11, right). There is a weight loss at low temperatures due to the release of water from GO (below 150°C). At higher temperatures we can see instead the weight loss due to non-covalently adsorbed molecules and labile oxygenated species and above 300°C the one of covalently attached molecules and of the more stable unreacted oxygenated groups. To determine the amount of molecules introduced, it is possible to compare the weight loss of the starting GO from the functionalized one.

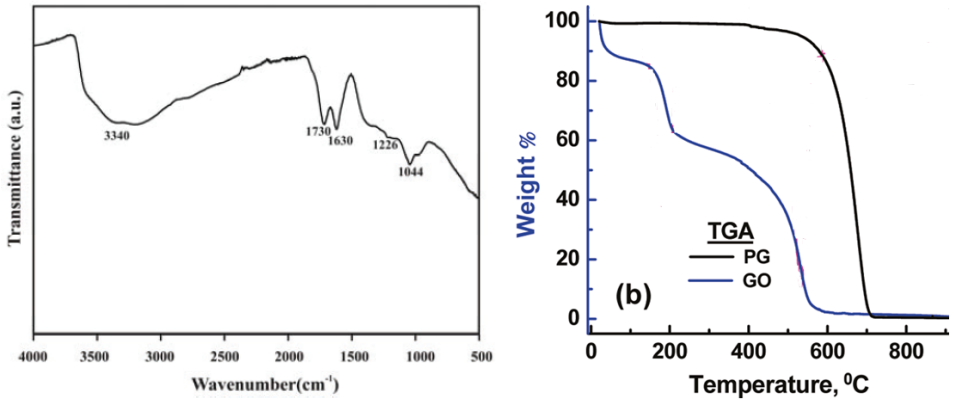

Figure 1.11 On the left the FT-IR spectrum of GO and on the right the TGA of GO and pristine graphite (PG). Adapted from references 103-104, respectively.

By analyzing GO *via* SSNMR it is possible to establish which functional groups are present. In the spectrum the signals at 60.9 ppm, 70.8 ppm and 167 ppm are attributed to the epoxides, the hydroxyls and the carboxylic acids, respectively. The peak at 133 ppm instead corresponds to the C-C double bond (Figure 1.12). The difference between direct ^{13}C SSNMR and ^{1}H-^{13}C cross polarization (CP) SSNMR relays on the fact that in ^{1}H-^{13}C CP SSNMR spectra the polarization of ^{1}H, an abundant nucleus, is transferred to ^{13}C a rarer one.

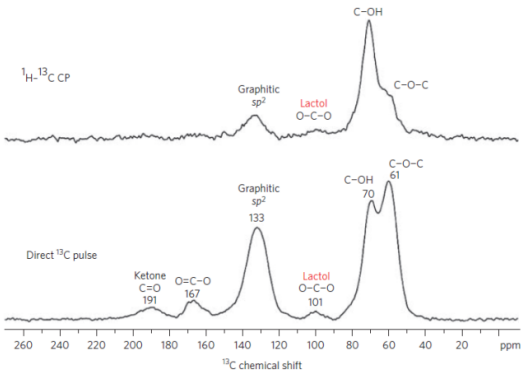

Figure 1.12 Top: ^{1}H–^{13}C CP spectrum; Bottom: direct ^{13}C pulse spectrum of GO. Adapted from reference 64.

XPS is a semi-quantitative spectroscopic technique that measures the kinetic energy and the number of electrons emitted from the material analyzed. This technique gives information about the elemental composition, the empirical formula, the chemical state and the electronic state of the elements in a sample. In the C1s spectral region of GO (Figure 1.13, right) it is possible to detect the signal of sp^2 C-C at 284.5 eV, of sp^3 C-C at 285.2 eV, of hydroxyl, epoxy, carbonyl and carboxylic acid groups at 286.4, 287.1, 288.0 and 289.2 eV, respectively. In the survey instead it is possible to have an overview of all atoms present in the sample (Figure 1.13, left).

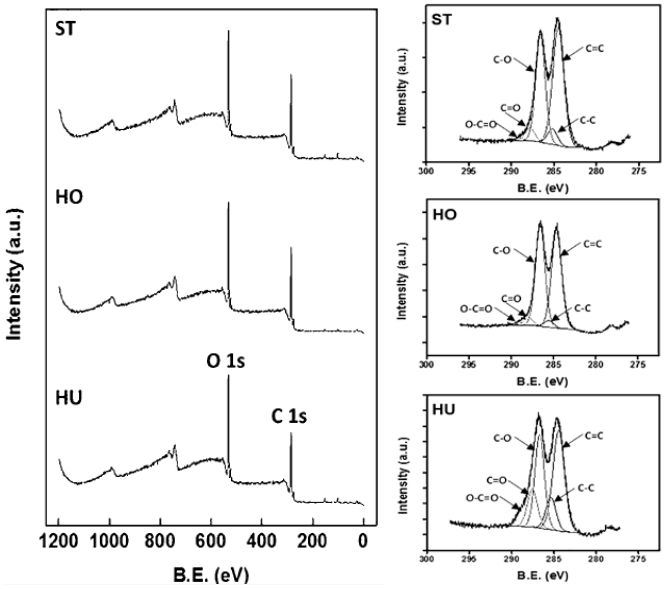

Figure 1.13 On the left the XPS survey spectrum of GO and on the right the carbon high resolution spectrum (ST= Staudenmeier's oxidation procedure; HO=Hofmann's oxidation procedure; HU=Hummers' oxidation procedure). Adapted from reference 105.

Even if, at a first glance, these characterization methods seem enough powerful for GO, there are few difficulties to consider, mainly about the precise determination of the structure before and after modification of this material. The interpretation of the experimental results for GO is often complex and ambiguous. Indeed, the FT-IR spectra are difficult to analyze because of the high amount of signals. Moreover, it does not give a quantitative information. The TGA shows the weight loss of the material, indicating the amount of molecules introduced, but because of the thermal instability of GO and the labile oxygenated species, there are many factors that can influence this weight loss. SSNMR is among all characterization methods the most useful, but it is time consuming, thus it cannot be performed for every sample. The XPS instead takes much less time, but the analysis of the data is quite complex. Attention has to be taken in the deconvolution of the spectra and the analysis conditions.

Moreover, as recently published, GO is highly sensitive to modification that can occur during measurements, such as XPS, Raman and AFM.[96] Thus, a constant verification is required. Heating, X-ray and laser irradiation or current flow can unintentionally affect GO and disturb the chemical and electronic structure.[96] For all these reasons, the combination of several characterization techniques is of fundamental importance to avoid misinterpretation. Moreover, new characterization techniques have still to be developed and the already known ones should be improved.

1.5 Biocompatibility biodegradation and tissue/organ biodistribution

The assessment of the biocompatibility and biodistribution profiles of nanomaterials is a complex topic. The main difficulties are due to the high amounts of variables to consider, such as the nanomaterial surface area, the surface functionalization, the number of layers, the lateral dimension, the purity and the dose.[106] All these factors are highly important to understand the ADME (Administration, Distribution, Metabolism, Excretion) of nanomaterials (Figure 1.14).

Another aspect that is important to underline is that GO, as we know, can have different characteristics depending on the synthesis procedure and on the starting graphite used. This makes it even more difficult to compare studies done by different laboratories.

The surface area plays a key role in the biological interaction of nanomaterials, and because of the high surface area of GO, surface phenomena such as physical adsorption are particularly important. The

number of layers determines instead the bending stiffness. If thin materials are quite deformable by weak forces, a multilayered structure may act as a rigid block when it interacts with cells. The rigidity/deformability and surface composition have an important role also in renal filtration. Lateral dimension is important because it modulates the uptake, renal clearance, blood-brain barrier transport, cell internalization mechanism and other bio-phenomena that are connected to the size. Surface chemistry and charge, like the surface area, strongly affect the biological interactions.[106–108] Das *et al.* prepared GO with different reduction levels to understand the effect of the presence of oxygenated functions on the interaction with cells. They saw that a higher density of these oxygenated groups was associated with increased levels of ROS and with DNA damage within the cells.[109] Moreover, a polar surface has shown a higher influence on hemolytic activity.[110]

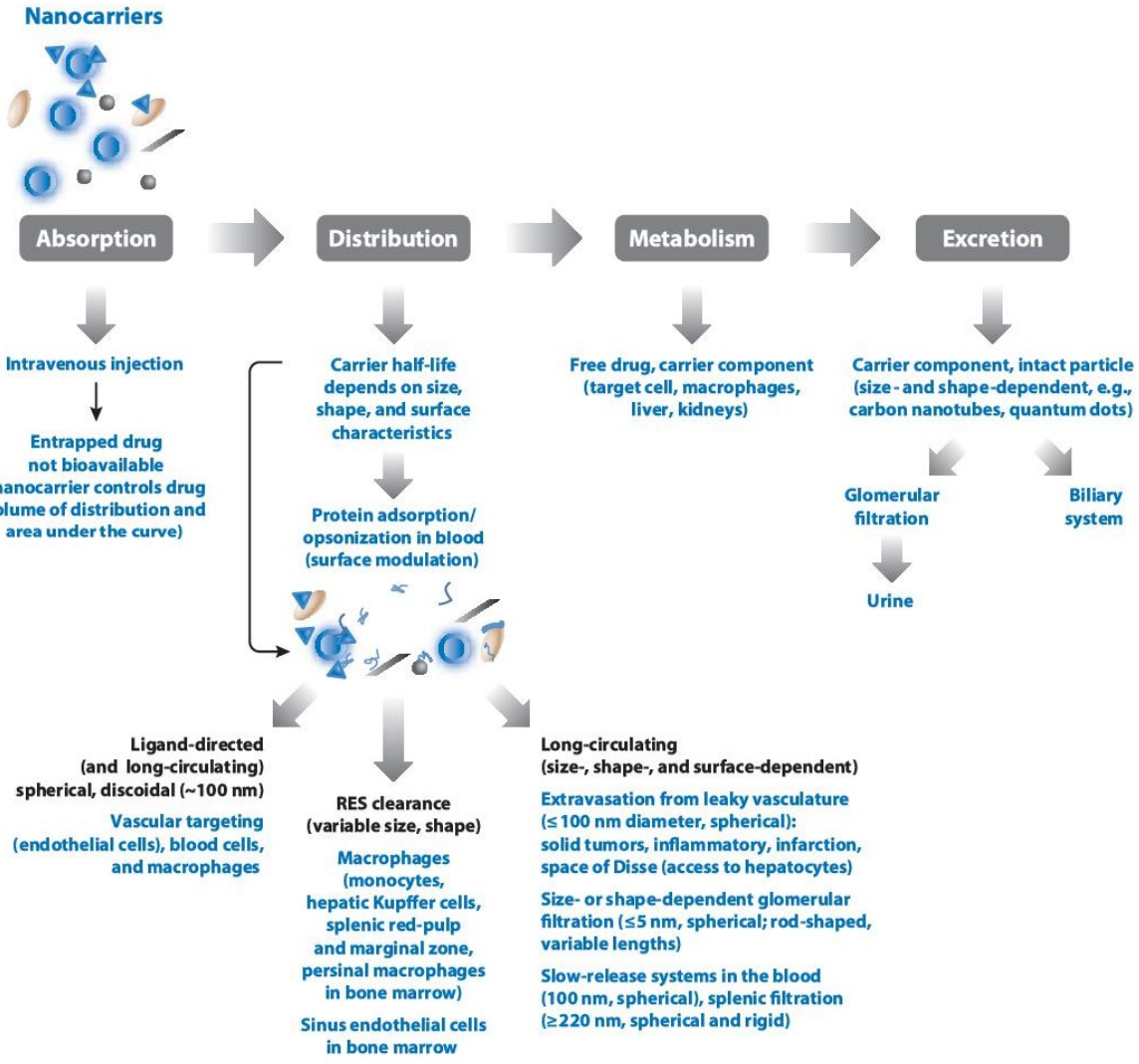

Figure 1.14 "A general overview of the influence of nanoparticle physiochemical characteristics (size, shape, and surface properties) on ADME. Abbreviation: RES, reticuloendothelial system". Adapted from reference 122.

GO, even if stable in aqueous solution, has shown to be less stable in saline or culture medium, a characteristic that can be modulated by functionalization. Studies confirmed that functionalization with PEG, PEGylated poly L-lysine, Pluronic, amines, carboxylates and dextran improved the biocompatibility of graphene family materials.[111–116] Surfactants, such as Tween 80, has been also used to improve the

biocompatibility of GO and avoid aggregation *in vivo*.[117] A good dispersibility can influence also the biodegradation of this material.[118]

The interaction with proteins in blood influences the half-lives and biodistribution of the nanoparticles, it increases their hydrodynamic size, affect their stability and it may induce nanoparticle recognition and clearance by phagocytes or macrophages. Interaction with proteins may also impact on the targetability of nanomedicines. The interaction with proteins is called protein corona formation and it happens as soon as serum proteins adsorb onto the surface of GO. PEG is used to reduce non-specific protein adsorption, but it does not completely prevent this phenomenon.[119] At first, soft coronas are established and later they are replaced through competitive binding with more stable ones.[120] To mitigate the cytotoxicity of GO, Hu *et al.* prepared a GO coated with foetal bovine serum proteins, exploiting the corona effect. They evaluated the toxicity using adenocarcinomic human alveolar epithelial (A549) cells. An exposure to 100 μg/ml showed almost 90% of cell viability with no membrane damage compared with pristine GO that showed a viability of only 50%.[121]

Another key factor is the purity of the material; indeed, it has been shown that toxicity can stem also from some residues left from the strong oxidizing mixture used to synthesize GO, as for example manganese. Moreover, GO may mediate oxidative damages because of its significant catalytic activity.[106]

To analyze the toxicity of GO the best would be to have a well-established common procedure to obtain a biograde pure GO. Considering that until now there are only a lot of studies performed with different kinds of GO, without any standard, the analysis of the results of toxicity studies is still inconclusive.

Moreover, depending on the wished application, different aspects of the biodistribution have to be considered (such as long-term toxicity for tissue engineering applications). For sensing applications only a small quantity of nanomaterial has to be investigated for toxicity, which is opposite to drug delivery and tissue engineering. For tissue engineering long-term toxicity studies are also necessary.[108]

In a recent study Peruzynska *et al.* tested single- and four-layer GO nanoflakes of similar length (1-25 μm) before and after PEGylation on human breast cancer (MCF7) cells. They confirmed that functionalization enhances the dispersibility and stability of the nanomaterial in cell medium, preventing agglomeration and sedimentation. Thus, PEGylated GO showed lower impact in the mitochondrial activity. They observed that GO agglomerates have a higher affinity and attachment to the cells. However, it did not change the morphology of the cells. For PEGylated GO, only at the highest injection (100 μg/ml) the number of metabolically active cells decreased significantly. The number of apoptotic and necrotic cells was, however, negligible. Efficient cellular uptake was observed for both 1-layer and 4-layer GO-PEG. The difference between these two GO-PEG samples was seen only in the production rate of ROS and cell proliferation. Apparently, they observed a decreased oxidation stress in increasing the number of layers. The improved cell proliferation rate of the 4-layer GO-PEG has been explained by a lower adsorption ability and micronutrient depletion from the cell culture medium.[123]

In a recent study, different size GO (lateral size of 89 nm and 277 nm) were tested inside human cervical (HeLa) cells and macrophages at a concentration of 1, 10 and 100 μg/ml.[124] The results suggested a size-dependent toxicity for an incubation time of 12 hours and a concentration-dependent toxicity for a longer incubation time (48 h). Size appeared to have low influence in the reduction of cell viability for longer incubation periods in both cell lines. A reduction in viability was observed in both cell lines after 48 hours at increased concentration. In HeLa cell line the nanoparticles were compartmentalized inside vesicles and appeared to be aggregated. For macrophages, the GO sheets were found inside big vacuoles, and an augmentation in cell size was also noticed.

The important factors that allow GO to pass through cell membranes are the size, shape, coating, charge, hydrodynamic diameter, isoelectric point and pH gradient.[125] To study the cell internalization, protein-

coated GO nanosheets have been prepared. Large and small size GO have been compared (~400 nm and ~800 nm, respectively). A size-dependent cellular uptake has been observed. Large protein-coated GO was mainly internalized by phagocytosis, meanwhile small protein-coated GO by clathrin-mediated endocytosis.[126] This internalization could be also influenced by the coating.

Once inside the cells GO might escape from subcellular compartments, move in the cytoplasm and translocate into the nucleus (GO can insert between the base pairs of the DNA showing a mutagenic effect),[127–129] and it can undergo also oxidative degradation.[130] In recent studies enzymatic degradation of GO resulted possible. Well-dispersed GO has been degraded by both horseradish peroxidase and a human-derived myeloperoxidase in presence of H_2O_2.[118] Degradation of GO samples has been demonstrated to be proportional to its hydrophilic nature and aqueous colloidal stability. Considering the tendency of these 2D carbon nanomaterials to accumulate in the body, this knowledge opens new options in the consideration of the biocompatibility of this type of material.

After internalization, it has been observed that GO with larger lateral size (2 μm) can induce stronger inflammatory response with high release of cytokines.[130] Interestingly, the response of immune cells, depending on the characteristics of graphene materials, such as lateral size, oxidation and functionalization, can be immunoactivating or immunosuppressing.[131] Thus, studying and controlling these parameters is highly important.

Another important cell interaction is the one with erythrocytes. The haemolytic potential of graphene family materials is dependent on their size and aggregation state. GO showed higher haemolysis than graphene, this could be due to the greater surface charge density. In addition, cells can interact with several ROS species that are present on the surface of GO, leading to greater haemolysis. An amino-modified GO (2 μm) has been tested *in vivo* by Singh *et al.* and compared to GO and, opposite to the latter, it does not induce platelet aggregation nor thromboembolism.[115,132] Thus, surface functionalization is an important aspect to avoid haemolysis.

However, GO interaction with cells is different if it is in suspension or in form of a substrate.[133] In many studies of GO as platform for tissue engineering, this material showed to be more biocompatible. In this case GO is used as a solid support and, for example, thanks to the serum proteins adsorption on its hydrophilic surface, a good proliferation and differentiation of stem cells has been demonstrated.[134]

The administration route is another important parameter if we consider the *in vivo* toxicity of this nanomaterial. Tests were performed by administering GO and functionalized GO intravenously, intraperitoneally, orally, pulmonary and intravitreally.[132] Single layer GO with a size of 100-800 nm and a thickness of 1 nm was intravenously injected in 1 and 10 mg/kg dosage.[135] GO exhibited a long circulation time. At low dose the GO did not show pathological changes on kidney, liver, spleen and lungs. On the contrary, at high dose, due to high accumulation and slow clearance, GO accumulated in lungs resulting in pulmonary oedema, granulomatous lesions, inflammatory cell infiltration, and fibrosis. The biodistribution has been assessed by administering ^{188}Re-labelled GO and this was observed to accumulate in the lungs, liver and spleen, and to be internalized by phagocytes in the reticuloendothelial system. In another study of Liu *et al.*, by using two different samples of GO labeled with ^{125}I (1-5 μm and 110-500 nm) in doses of 1 mg/kg and 10 mg/kg, a size-dependent distribution was observed.[136] Large GO accumulated more in the lungs, meanwhile small GO accumulated mainly in the liver but also in the lungs and spleen. This difference was attributed to a different aggregation state. Functionalized GO, though, as for example GO-DOTA, resulted not toxic and to have a different pharmacokinetic profile.[137] The ^{111}In-DOTA-GO, with a size of 50-2000 nm, initially accumulated in the liver and spleen, and later a translocation to the spleen was observed. The sample was eventually extensively eliminated from the body *via* the urine. No organ damage was observed. Another study performed by Li *et al.* compared the biodistribution of nanoGO (NGO) (10-800 nm) with or without PEG after intravenous injection in a dosage of 5 mg/kg.[138] They observed that PEG

coating reduced the retention time in the liver, lung and spleen, and promoted the clearance, meanwhile it prolonged the blood circulation half-life of NGO.

NGO sheet effect on reproduction organs has been studied by Akhavan *et al.* and it seemed to strongly affect spermatozoa and the pregnant functionality of female mice (2 and 4 mg/kg intravenous injection of NGO with lateral size >100 nm).[139] Thus, further studies in this direction have to be performed with functionalized GO.

When GO was administered orally, instead, no accumulation was observed. Meanwhile, when it was administered intraperitoneally an accumulation in the liver and spleen was noticed. This, for example, has been the case in the study of Yang *et al.* who tested ^{125}I-GO and PEG-functionalized nanoGO (PEG-NGO) of a size of 450 and 25 nm, respectively, at a dosage of 50 mg/kg for both of them administered intraperitoneally, and 100 mg/kg for the latter one administered orally.[140] After intraperitoneal administration non-functionalized GO could not be effectively absorbed because of aggregation, opposite to PEG-NGO. The PEG-NGO has been phagocytized in the RES system and, despite a long term retention, no significant toxicity was observed. PEG-NGO administered orally instead could not be absorbed by organs and was rapidly excreted.

Recently, GO administered orally to maternal mice has been proven to seriously damage the gastrointestinal tract at low dose opposite to high dose. The explanation appears to be the agglomeration that happens at high dose, meanwhile at low dose single layers of GO interact with the gastrointestinal surface causing destruction because of the abundant sharp edges.[141]

After pulmonary administration, GO leads to persistent lung injury. Indeed, Li *et al.* have analyzed a GO with a size of 10-800 nm at a dose of 1, 5, 10 mg/kg. They observed thickening of the alveolar septa and oxidative damage.[142] GO permeated through the air blood barrier into the blood and to other organs before being eliminated in urines. However, GO was still localized in the lungs after 3 months, proving an incomplete clearance. Thus, care has to be taken during large-scale production of this material.

No effect was seen instead after intravitreal administration by Yan *et al.* using a GO with a size of 50-500 nm and a dose of 0.1, 0.2, 0.3 mg.[143]

The elimination and degradation of GO and its derivatives are still studied. Until now it seems that pristine GO has a size-dependent excretion between faeces and urine. DOTA-functionalized GO showed instead only urine excretion. Meanwhile, the degradation has been proved to be effective both in *vitro* and in *vivo*. Indeed, *in vivo* degradation conditions of carboxyl functionalized graphene (*f*-G) has been studied by Girish *et al.*[144] They probed the fate of intravenously administered *f*-G material in mice model with the use of confocal Raman microscopy, observing an increase in the I_D/I_G ratio over a period of 8-90 days.

In conclusion, all the studies mentioned used GO samples with different characteristics, thus drawing a real conclusion appears to be a difficult task. Only one thing is sure: other investigations of this material should be performed with a more uniform starting GO. Moreover, functionalized GO seems to be more biocompatible, thus it appears to be promising for biomedical applications.

1.6 Objectives of the Thesis

This work has two main objectives that aim to better understand the structure and reactivity of GO. In particular, the first one is to assess the reactivity and surface composition of differently produced GO samples and the second one is to develop a multifunctionalization procedure on GO for future biomedical applications. In addition, chemical strategies to increase GO dispersibility and the functionalization of GO with DOTA for biodistribution studies have been also investigated.

GO is an emerging nanomaterial in many different fields, but there are still a lot of unsolved questions. GO, depending on the synthesis method, is supposed to have different oxygenated functions on its surface. The high variability of this material is a major issue, even more in the biomedical field. Thus, in

the first study we analyzed two differently synthesized GO to investigate the relation between synthesis method and surface composition. One has been purchased from Nanoinnova technologies (Spain) and the other from Grupo Antolin (Spain). The first one has been obtained through the commonly known Hummers method, meanwhile the second one *via* cutting and exfoliation of carbon nanofibers. Assessing the type and reactivity of the functional groups present is fundamental for further modification for future applications. To accomplish this, we followed in parallel two approaches, an analytical and a chemical one. We improved SSNMR and XPS analysis of GO and performed different selective covalent reactions on the oxygenated groups supposed to be present on the surface of the two GO samples.

The reactions performed (Figure 1.15) are the ring opening of the epoxides with a primary amine, the amidation and esterification for the carboxylic acid groups, the Williamson and the esterification reactions for the hydroxyl groups and the Wittig reaction on the ketones. We discussed the results taking in consideration the difficulties related to the secondary reactions and other effects that could have an influence on the outcome of the reaction. Indeed, because of the high number of functional groups on GO, there are many limitations.

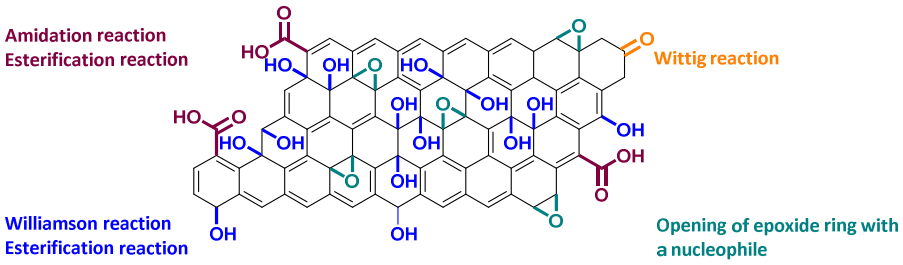

Figure 1.15 Schematization of the reactions performed on GO.

The functionalized GO samples have been characterized by different techniques such as Kaiser test, TGA, FT-IR, XPS and SSNMR.

Subsequently, we used one of the reactions, the opening of epoxides, to covalently attach 1,4,7,10-tetraazacyclododecane-1,4,7,10 tetraacetic acid (DOTA) on three GO samples with a different size. DOTA is a radionuclide chelating agent. The purpose of this study was to better understand the *in vivo* biodistribution of functionalized GO samples with a different lateral size. GO is highly promising for biomedical applications thanks to its high surface area, tuneable conductivity, biodegradability and many other characteristics. But, the biocompatibility and biodistribution of GO have still to be better investigated.

In the second study we exploited the knowledge from the first study to develop a multifunctionalization procedure for GO. Multifunctionalization is a promising approach to design a combined strategy on GO materials for theranostic (combined therapeutic and diagnostic) applications.

To develop the multifunctionalization protocol we investigated different approaches. We combined the reactions that gave the best results in the first study. We tried to perform the opening of the epoxides followed by the Williamson reaction. We tested these two reactions also in the inverse sequence and in one-pot conditions. Next, we performed also the opening of the epoxides followed by the esterification reaction.

After that, we faced another delicate problematic of GO, namely its dispersibility. Indeed, for biomedical applications, it is of fundamental importance to avoid aggregation because this can be a reason of toxicity. Moreover, it is often observed that after functionalization the dispersibility of GO decreases. Thus, to overcome this issue, we polymerized *in situ* on GO the glycidol molecule to obtain a polyglycidol-covered GO conjugate (PG-GO). We chose polyglycidol because it is a highly water soluble and biocompatible polymer.

This PG-GO has been further derivatized with a kidney targeting peptide, and a multifunctionalization strategy is envisaged on this conjugate.

The Thesis is therefore composed of six chapters, as outlined:

Chapter 1 gives an overview on GO, in particular about the production, surface composition, functionalization, characterization, biocompatibility and bioapplications.

Chapter 2 discusses the surface composition and reactivity of differently synthesized GO samples *via* controlled chemical functionalization and different analytical techniques. The synthesis of the DOTA-GO derivatives and the biodistribution studies will be also mentioned in this chapter.

Chapter 3 describes the design of a double functionalization strategy on pristine GO and polymer-coated GO (PG-GO) that has a higher water stability.

Chapter 4 explains how to improve XPS analysis for GO and other nanomaterials. Careful and thorough characterization is indeed important for a good comprehension of nanomaterial characteristics and their functionalization.

Chapter 5 reports general conclusions and perspectives of this thesis work.

Chapter 6 describes all the experimental procedures.

Each chapter is followed by its own references.

1.7 Bibliography

1. Brodie BC. On the Atomic Weight of Graphite. Philos Trans R Soc Lond 1859;149:249–59.

2. Staudenmaier L. Verfahren zur Darstellung der Graphitsäure. Berichte Dtsch Chem Ges 1898;31(2):1481–7.

3. Hummers WS, Offeman RE. Preparation of Graphitic Oxide. J Am Chem Soc 1958;80(6):1339–1339.

4. Pan S, Aksay IA. Factors Controlling the Size of Graphene Oxide Sheets Produced via the Graphite Oxide Route. ACS Nano 2011;5(5):4073–83.

5. Zhang L, Liang J, Huang Y, et al. Size-controlled synthesis of graphene oxide sheets on a large scale using chemical exfoliation. Carbon 2009;47(14):3365–8.

6. Perrozzi F, Prezioso S, Ottaviano L. Graphene oxide: from fundamentals to applications. J Phys Condens Matter 2015;27(1):013002.

7. Walter J, Nacken TJ, Damm C, Thajudeen T, Eigler S, Peukert W. Determination of the lateral dimension of graphene oxide nanosheets using analytical ultracentrifugation. Small Weinh Bergstr Ger 2015;11(7):814–25.

8. Spyrou K, Rudolf P. An Introduction to Graphene. In: Georgakilas V, editor. Functionalization of Graphene. Wiley-VCH Verlag GmbH & Co. KGaA; 2014. p. 1–20.

9. Dembereldorj U, Kim M, Kim S, Ganbold E-O, Lee SY, Joo S-W. A spatiotemporal anticancer drug release platform of PEGylated graphene oxide triggered by glutathione in vitro and in vivo. J Mater Chem 2012;22(45):23845–51.

10. Yang Y, Zhang Y-M, Chen Y, Zhao D, Chen J-T, Liu Y. Construction of a graphene oxide based noncovalent multiple nanosupramolecular assembly as a scaffold for drug delivery. Chem Weinh Bergstr Ger 2012;18(14):4208–15.

11. Yang X, Zhang X, Ma Y, Huang Y, Wang Y, Chen Y. Superparamagnetic graphene oxide–Fe3O4 nanoparticles hybrid for controlled targeted drug carriers. J Mater Chem 2009;19(18):2710–4.

12. Yang X, Wang Y, Huang X, et al. Multi-functionalized graphene oxide based anticancer drug-carrier with dual-targeting function and pH-sensitivity. J Mater Chem 2011;21(10):3448–54.

13. Xu Z, Wang S, Li Y, Wang M, Shi P, Huang X. Covalent Functionalization of Graphene Oxide with Biocompatible Poly(ethylene glycol) for Delivery of Paclitaxel. ACS Appl Mater Interfaces 2014;6(19):17268–76.

14. Weaver CL, LaRosa JM, Luo X, Cui XT. Electrically Controlled Drug Delivery from Graphene Oxide Nanocomposite Films. ACS Nano 2014;8(2):1834–43.

15. Close DM, Xu T, Sayler GS, Ripp S. In vivo bioluminescent imaging (BLI): noninvasive visualization and interrogation of biological processes in living animals. Sensors 2011;11(1):180–206.

16. Nurunnabi M, Parvez K, Nafiujjaman M, et al. Bioapplication of graphene oxide derivatives: drug/gene delivery, imaging, polymeric modification, toxicology, therapeutics and challenges. RSC Adv 2015;5(52):42141–61.

17. Rusli, Robertson J, Amaratunga G a. J. Photoluminescence behavior of hydrogenated amorphous carbon. J Appl Phys 1996;80(5):2998–3003.

18. Ge J, Lan M, Zhou B, et al. A graphene quantum dot photodynamic therapy agent with high singlet oxygen generation. Nat Commun 2014;5:4596.

19. Loh KP, Bao Q, Eda G, Chhowalla M. Graphene oxide as a chemically tunable platform for optical applications. Nat Chem 2010;2(12):1015–24.

20. Rong P, Yang K, Srivastan A, et al. Photosensitizer Loaded Nano-Graphene for Multimodality Imaging Guided Tumor Photodynamic Therapy. Theranostics 2014;4(3):229–39.

21. Chen B, Liu M, Zhang L, Huang J, Yao J, Zhang Z. Polyethylenimine-functionalized graphene oxide as an efficient gene delivery vector. J Mater Chem 2011;21(21):7736–41.

22. Ren T, Li L, Cai X, Dong H, Liu S, Li Y. Engineered polyethylenimine/graphene oxide nanocomposite for nuclear localized gene delivery. Polym Chem 2012;3(9):2561–9.

23. Sarkar K, Madras G, Chatterjee K. Dendron conjugation to graphene oxide using click chemistry for efficient gene delivery. RSC Adv 2015;5(62):50196–211.

24. Bao H, Pan Y, Ping Y, et al. Chitosan-Functionalized Graphene Oxide as a Nanocarrier for Drug and Gene Delivery. Small 2011;7(11):1569–78.

25. He J, Zhu X, Qi Z, et al. The Inhibition Effect of Graphene Oxide Nanosheets on the Development of Streptococcus mutans Biofilms. Part Part Syst Charact 2017;34(5):DOI: 10.1002/ppsc.201700001.

26. Nayak TR, Andersen H, Makam VS, et al. Graphene for Controlled and Accelerated Osteogenic Differentiation of Human Mesenchymal Stem Cells. ACS Nano 2011;5(6):4670–8.

27. Gautschi OP, Frey SP, Zellweger R. Bone morphogenetic proteins in clinical applications. ANZ J Surg 2007;77(8):626–31.

28. Govender S, Csimma C, Genant HK, et al. Recombinant human bone morphogenetic protein-2 for treatment of open tibial fractures: a prospective, controlled, randomized study of four hundred and fifty patients. J Bone Joint Surg Am 2002;84–A(12):2123–34.

29. Termaat MF, Den Boer FC, Bakker FC, Patka P, Haarman HJTM. Bone morphogenetic proteins. Development and clinical efficacy in the treatment of fractures and bone defects. J Bone Joint Surg Am 2005;87(6):1367–78.

30. La W-G, Jin M, Park S, et al. Delivery of bone morphogenetic protein-2 and substance P using graphene oxide for bone regeneration. Int J Nanomedicine 2014;9 Suppl 1:107–16.

31. Shen H, Zhang L, Liu M, Zhang Z. Biomedical Applications of Graphene. Theranostics 2012;2(3):283–94.

32. Chang H, Tang L, Wang Y, Jiang J, Li J. Graphene Fluorescence Resonance Energy Transfer Aptasensor for the Thrombin Detection. Anal Chem 2010;82(6):2341–6.

33. Staudenmaier L. Verfahren zur Darstellung der Graphitsäure. Berichte Dtsch Chem Ges 1899;32(2):1394–9.

34. Staudenmaier L. Untersuchungen über den Graphit. Berichte Dtsch Chem Ges 1899;32(3):2824–34.

35. Hummers WS, Offeman RE. Preparation of Graphitic Oxide. J Am Chem Soc 1958;80(6):1339–1339.

36. Marcano DC, Kosynkin DV, Berlin JM, et al. Improved Synthesis of Graphene Oxide. ACS Nano 2010;4(8):4806–14.

37. Eigler S, Enzelberger-Heim M, Grimm S, et al. Wet Chemical Synthesis of Graphene. Adv Mater 2013;25(26):3583–7.

38. Eigler S, Grimm S, Enzelberger-Heim M, Müller P, Hirsch A. Graphene oxide: efficiency of reducing agents. Chem Commun 2013;49(67):7391–3.

39. Eng AYS, Chua CK, Pumera M. Refinements to the structure of graphite oxide: absolute quantification of functional groups via selective labelling. Nanoscale 2015;7(47):20256–66.

40. Hunt A, Dikin DA, Kurmaev EZ, et al. Epoxide Speciation and Functional Group Distribution in Graphene Oxide Paper-Like Materials. Adv Funct Mater 2012;22(18):3950–7.

41. Dimiev AM, Alemany LB, Tour JM. Graphene Oxide. Origin of Acidity, Its Instability in Water, and a New Dynamic Structural Model. ACS Nano 2013;7(1):576–88.

42. Dimiev AM, Tour JM. Mechanism of Graphene Oxide Formation. ACS Nano 2014;8(3):3060–8.

43. Morimoto N, Suzuki H, Takeuchi Y, et al. Real-Time, in Situ Monitoring of the Oxidation of Graphite: Lessons Learned. Chem Mater 2017;29(5):2150–6.

44. Morimoto N, Kubo T, Nishina Y. Tailoring the Oxygen Content of Graphite and Reduced Graphene Oxide for Specific Applications. Sci Rep 2016;6:srep21715.

45. Eigler S, Grimm S, Hof F, Hirsch A. Graphene oxide: a stable carbon framework for functionalization. J Mater Chem A 2013;1(38):11559–62.

46. Aboutalebi SH, Gudarzi MM, Zheng QB, Kim J-K. Spontaneous Formation of Liquid Crystals in Ultralarge Graphene Oxide Dispersions. Adv Funct Mater 2011;21(15):2978–88.

47. Dimiev A, Kosynkin DV, Alemany LB, Chaguine P, Tour JM. Pristine Graphite Oxide. J Am Chem Soc 2012;134(5):2815–22.

48. Kim S, Zhou S, Hu Y, et al. Room-temperature metastability of multilayer graphene oxide films. Nat Mater 2012;11(6):544–9.

49. Klímová K, Pumera M, Luxa J, et al. Graphene Oxide Sorption Capacity toward Elements over the Whole Periodic Table: A Comparative Study. J Phys Chem C 2016;120(42):24203–12.

50. Eigler S, Dotzer C, Hirsch A, Enzelberger M, Müller P. Formation and Decomposition of CO2 Intercalated Graphene Oxide. Chem Mater 2012;24(7):1276–82.

51. Muthoosamy K, Manickam S. State of the art and recent advances in the ultrasound-assisted synthesis, exfoliation and functionalization of graphene derivatives. Ultrason Sonochem 2017;39:478–93.

52. Halbig CE, Nacken TJ, Walter J, Damm C, Eigler S, Peukert W. Quantitative investigation of the fragmentation process and defect density evolution of oxo-functionalized graphene due to ultrasonication and milling. Carbon 2016;96:897–903.

53. Delle LE, Lanche R, Law JK-Y, et al. Reduced graphene oxide micropatterns as an interface for adherent cells. Phys Status Solidi A 2013;210(5):975–82.

54. Mativetsky JM, Treossi E, Orgiu E, et al. Local Current Mapping and Patterning of Reduced Graphene Oxide. J Am Chem Soc 2010;132(40):14130–6.

55. Trusovas R, Račiukaitis G, Niaura G, Barkauskas J, Valušis G, Pauliukaite R. Recent Advances in Laser Utilization in the Chemical Modification of Graphene Oxide and Its Applications. Adv Opt Mater 2016;4(1):37–65.

56. Naumov A, Grote F, Overgaard M, et al. Graphene Oxide: A One- versus Two-Component Material. J Am Chem Soc 2016;138(36):11445–8.

57. Hofmann U, Holst R. Über die Säurenatur und die Methylierung von Graphitoxyd. Berichte Dtsch Chem Ges B Ser 1939;72(4):754–71.

58. Ruess G. Über das Graphitoxyhydroxyd (Graphitoxyd). Monatshefte Für Chem Verwandte Teile Anderer Wiss 1947;76(3–5):381–417.

59. Scholz W, Boehm HP. Untersuchungen am Graphitoxid. VI. Betrachtungen zur Struktur des Graphitoxids. Z Für Anorg Allg Chem 1969;369(3–6):327–40.

60. Nakajima T, Matsuo Y. Formation process and structure of graphite oxide. Carbon 1994;32(3):469–75.

61. Sen LH, Nainar MAM, Begum S. Model, synthesis and applications of graphene oxide: a review. Nanomater Energy 2014;3(2):61–5.

62. Lerf A, He H, Forster M, Klinowski J. Structure of Graphite Oxide Revisited. J Phys Chem B 1998;102(23):4477–82.

63. Szabó T, Berkesi O, Forgó P, et al. Evolution of Surface Functional Groups in a Series of Progressively Oxidized Graphite Oxides. Chem Mater 2006;18(11):2740–9.

64. Gao W, Alemany LB, Ci L, Ajayan PM. New insights into the structure and reduction of graphite oxide. Nat Chem 2009;1(5):403–8.

65. Xu J, Xu M, Wu J, Wu H, Zhang W-H, Li Y-X. Graphene Oxide Immobilized with Ionic Liquids: Facile Preparation and Efficient Catalysis for Solvent-free Cycloaddition of CO2 to Propylene Carbonate. RSC Adv 2015;5:72360–8.

66. Yu R, Zhang S, Luo Y, Bai R, Zhou J, Song H. Synthetic possibility of polystyrene functionalization based on hydroxyl groups of graphene oxide as nucleophiles. New J Chem 2015;39(7):5096–9.

67. Chen H, Wang Y, Zhao W, et al. Phosphorylation of graphehe oxide to improve adsorption of U(VI) from aquaeous solutions. J Radioanal Nucl Chem 2017;313(1):175–89.

68. de Leon AC, Alonso L, Mangadlao JD, Advincula RC, Pentzer E. Simultaneous Reduction and Functionalization of Graphene Oxide via Ritter Reaction. ACS Appl Mater Interfaces 2017;9(16):14265–72.

69. Mejias Carpio IE, Mangadlao JD, Nguyen HN, Advincula RC, Rodrigues DF. Graphene oxide functionalized with ethylenediamine triacetic acid for heavy metal adsorption and anti-microbial applications. Carbon 2014;77:289–301.

70. Melucci M, Treossi E, Ortolani L, et al. Facile covalent functionalization of graphene oxide using microwaves: bottom-up development of functional graphitic materials. J Mater Chem 2010;20(41):9052–60.

71. Sydlik SA, Swager TM. Functional Graphenic Materials Via a Johnson−Claisen Rearrangement. Adv Funct Mater 2013;23(15):1873–82.

72. Yu D, Yang Y, Durstock M, Baek J-B, Dai L. Soluble P3HT-Grafted Graphene for Efficient Bilayer−Heterojunction Photovoltaic Devices. ACS Nano 2010;4(10):5633–40.

73. Mei K-C, Rubio N, Costa PM, et al. Synthesis of double-clickable functionalised graphene oxide for biological applications. Chem Commun 2015;51(81):14981–4.

74. Jankovsky O, Lojka M, Luxa J, et al. Selective bromination of graphene oxide by Hunsdiecker reaction. Chem – Eur J 2017;23(43):10473–9.

75. Stankovich S, Piner RD, Nguyen ST, Ruoff RS. Synthesis and exfoliation of isocyanate-treated graphene oxide nanoplatelets. Carbon 2006;44(15):3342–7.

76. Wang G, Wang B, Park J, Yang J, Shen X, Yao J. Synthesis of enhanced hydrophilic and hydrophobic graphene oxide nanosheets by a solvothermal method. Carbon 2009;47(1):68–72.

77. Zhang D-D, Zu S-Z, Han B-H. Inorganic–organic hybrid porous materials based on graphite oxide sheets. Carbon 2009;47(13):2993–3000.

78. Shan C, Yang H, Han D, Zhang Q, Ivaska A, Niu L. Water-Soluble Graphene Covalently Functionalized by Biocompatible Poly-l-lysine. Langmuir 2009;25(20):12030–3.

79. Halbig CE, Rietsch P, Eigler S. Towards the Synthesis of Graphene Azide from Graphene Oxide. Mol Basel Switz 2015;20(12):21050–7.

80. Šimek P, Klímová K, Sedmidubský D, Jankovský O, Pumera M, Sofer Z. Towards graphene iodide: iodination of graphite oxide. Nanoscale 2014;7(1):261–70.

81. Jankovský O, Šimek P, Klimová K, et al. Towards graphene bromide: bromination of graphite oxide. Nanoscale 2014;6(11):6065–74.

82. Bouša D, Luxa J, Mazánek V, et al. Toward graphene chloride: chlorination of graphene and graphene oxide. RSC Adv 2016;6(71):66884–92.

83. Huang Y, Yan W, Xu Y, Huang L, Chen Y. Functionalization of Graphene Oxide by Two-Step Alkylation. Macromol Chem Phys 2012;213(10–11):1101–1106.

84. Wei G, Yan M, Dong R, et al. Covalent Modification of Reduced Graphene Oxide by Means of Diazonium Chemistry and Use as a Drug-Delivery System. Chem – Eur J 2012;18(46):14708–16.

85. Ismaili H, Geng D, Sun AX, Kantzas TT, Workentin MS. Light-Activated Covalent Formation of Gold Nanoparticle–Graphene and Gold Nanoparticle–Glass Composites. Langmuir 2011;27(21):13261–8.

86. Xu LQ, Yee YK, Neoh K-G, Kang E-T, Fu GD. Cyclodextrin-functionalized graphene nanosheets, and their host-guest polymer nanohybrids. Polymer 2016;54(9):2264–71.

87. Dougherty DA. The Cation−π Interaction. Acc Chem Res 2013;46(4):885–93.

88. Lee EC, Kim D, Jurečka P, Tarakeshwar P, Hobza P, Kim KS. Understanding of Assembly Phenomena by Aromatic−Aromatic Interactions: Benzene Dimer and the Substituted Systems. J Phys Chem A 2007;111(18):3446–57.

89. Grimme S. On the Importance of Electron Correlation Effects for the π-π Interactions in Cyclophanes. Chem – Eur J 2004;10(14):3423–9.

90. Tarakeshwar P, Choi HS, Kim KS. Olefinic vs Aromatic π−H Interaction: A Theoretical Investigation of the Nature of Interaction of First-row Hydrides with Ethene and Benzene. J Am Chem Soc 2001;123(14):3323–31.

91. Liu Z, Robinson JT, Sun X, Dai H. PEGylated Nanographene Oxide for Delivery of Water-Insoluble Cancer Drugs. J Am Chem Soc 2008;130(33):10876–7.

92. Lu C-H, Yang H-H, Zhu C-L, Chen X, Chen G-N. A Graphene Platform for Sensing Biomolecules. Angew Chem Int Ed 2009;48(26):4785–4787.

93. Zhang J, Zhang F, Yang H, et al. Graphene Oxide as a Matrix for Enzyme Immobilization. Langmuir 2010;26(9):6083–5.

94. Georgakilas V, Tiwari JN, Kemp KC, et al. Noncovalent Functionalization of Graphene and Graphene Oxide for Energy Materials, Biosensing, Catalytic, and Biomedical Applications. Chem Rev 2016;116(9):5464–519.

95. King AAK, Davies BR, Noorbehesht N, et al. A New Raman Metric for the Characterisation of Graphene oxide and its Derivatives. Sci Rep 2016;6:srep19491.

96. Rogala M., Dabrowski P., Kowalczyk P. J., et al. The observer effect in graphene oxide – How the standard measurements affect the chemical and electronic structure. Carbon 2016;103:235–41.

97. Muttaqin, Nakamura T, Nishina Y, Sato S. Chemical surface modification of graphene oxide by femtosecond laser pulse irradiation in aqueous suspensions. J Mater Sci 2017;52(2):749–59.

98. Cançado LG, Jorio A, Martins Ferreira EH, et al. Quantifying Defects in Graphene via Raman Spectroscopy at Different Excitation Energies. Nano Lett 2011;11(8):3190–6.

99. Eigler S, Hirsch A. Chemistry with Graphene and Graphene Oxide—Challenges for Synthetic Chemists. Angew Chem Int Ed 2014;53(30):7720–38.

100. Butz B, Dolle C, Halbig CE, Spiecker E, Eigler S. Highly Intact and Pure Oxo-Functionalized Graphene: Synthesis and Electron-Beam-Induced Reduction. Angew Chem Int Ed 2016;55(51):15771–4.

101. Gómez-Navarro C, Meyer JC, Sundaram RS, et al. Atomic Structure of Reduced Graphene Oxide. Nano Lett 2010;10(4):1144–8.

102. Loryuenyong V, Totepvimarn K, Eimburanapravat P, Boonchompoo W, Buasri A. Preparation and Characterization of Reduced Graphene Oxide Sheets via Water-Based Exfoliation and Reduction Methods. Adv Mater Sci Eng 2013;DOI: 10.1155/2013/923403.

103. Rattana, Chaiyakun S., Witit-anun N., et al. Preparation and characterization of graphene oxide nanosheets. Procedia Eng 2012;32:759–64.

104. Ganguly A, Sharma S, Papakonstantinou P, Hamilton J. Probing the Thermal Deoxygenation of Graphene Oxide Using High-Resolution In Situ X-ray-Based Spectroscopies. J Phys Chem C 2011;115(34):17009–19.

105. Moo JGS, Khezri B, Webster RD, Pumera M. Graphene Oxides Prepared by Hummers', Hofmann's, and Staudenmaier's Methods: Dramatic Influences on Heavy-Metal-Ion Adsorption. ChemPhysChem 2014;15(14):2922–9.

106. Sanchez VC, Jachak A, Hurt RH, Kane AB. Biological Interactions of Graphene-Family Nanomaterials: An Interdisciplinary Review. Chem Res Toxicol 2012;25(1):15–34.

107. Moghimi SM, Hunter AC, Andresen TL. Factors Controlling Nanoparticle Pharmacokinetics: An Integrated Analysis and Perspective. Annu Rev Pharmacol Toxicol 2012;52:481–503.

108. Reina G, González-Domínguez JM, Criado A, Vázquez E, Bianco A, Prato M. Promises, facts and challenges for graphene in biomedical applications. Chem Soc Rev 2017;46(15):4400–16.

109. Das S, Singh S, Singh V, et al. Oxygenated Functional Group Density on Graphene Oxide: Its Effect on Cell Toxicity. Part Part Syst Charact 2013;30(2):148–57.

110. Mc Callion C, Burthem J, Rees-Unwin K, Golovanov A, Pluen A. Graphene in therapeutics delivery: Problems, solutions and future opportunities. Eur J Pharm Biopharm 2016;104:235–50.

111. Yang K, Wan J, Zhang S, Zhang Y, Lee S-T, Liu Z. In Vivo Pharmacokinetics, Long-Term Biodistribution, and Toxicology of PEGylated Graphene in Mice. ACS Nano 2011;5(1):516–22.

112. Zhang W, Wang C, Li Z, et al. Unraveling Stress-Induced Toxicity Properties of Graphene Oxide and the Underlying Mechanism. Adv Mater 2012;24(39):5391–7.

113. Wojtoniszak M, Chen X, Kalenczuk RJ, et al. Synthesis, dispersion, and cytocompatibility of graphene oxide and reduced graphene oxide. Colloids Surf B Biointerfaces 2012;89:79–85.

114. Hu H, Yu J, Li Y, Zhao J, Dong H. Engineering of a novel pluronic F127/graphene nanohybrid for pH responsive drug delivery. J Biomed Mater Res A 2012;100(1):141–8.

115. Singh SK, Singh MK, Kulkarni PP, Sonkar VK, Grácio JJA, Dash D. Amine-Modified Graphene: Thrombo-Protective Safer Alternative to Graphene Oxide for Biomedical Applications. ACS Nano 2012;6(3):2731–40.

116. Zhang S, Yang K, Feng L, Liu Z. In vitro and in vivo behaviors of dextran functionalized graphene. Carbon 2011;49(12):4040–9.

117. Qu G, Wang X, Liu Q, et al. The ex vivo and in vivo biological performances of graphene oxide and the impact of surfactant on graphene oxide's biocompatibility. J Environ Sci China 2013;25(5):873–81.

118. Kurapati R, Russier J, Squillaci MA, et al. Dispersibility-Dependent Biodegradation of Graphene Oxide by Myeloperoxidase. Small 2015;11(32):3985–94.

119. Bhattacharya K, Mukherjee SP, Gallud A, et al. Biological interactions of carbon-based nanomaterials: From coronation to degradation. Nanomedicine Nanotechnol Biol Med 2016;12(2):333–51.

120. Lee YK, Choi E-J, Webster TJ, Kim S-H, Khang D. Effect of the protein corona on nanoparticles for modulating cytotoxicity and immunotoxicity. Int J Nanomedicine 2015;10:97–113.

121. Hu W, Peng C, Lv M, et al. Protein Corona-Mediated Mitigation of Cytotoxicity of Graphene Oxide. ACS Nano 2011;5(5):3693–700.

122. Moghimi SM, Hunter AC, Andresen TL. Factors Controlling Nanoparticle Pharmacokinetics: An Integrated Analysis and Perspective. Annu Rev Pharmacol Toxicol 2012;52:481–503.

123. Peruzynska M, Cendrowski K, Barylak M, et al. Comparative in vitro study of single and four layer graphene oxide nanoflakes — Cytotoxicity and cellular uptake. Toxicol In Vitro 2017;41:205–13.

124. Mendes RG, Koch B, Bachmatiuk A, et al. A size dependent evaluation of the cytotoxicity and uptake of nanographene oxide. J Mater Chem B 2015;3(12):2522–9.

125. Ou L, Song B, Liang H, et al. Toxicity of graphene-family nanoparticles: a general review of the origins and mechanisms. Part Fibre Toxicol 2016;13(1):57.

126. Mu Q, Su G, Li L, et al. Size-Dependent Cell Uptake of Protein-Coated Graphene Oxide Nanosheets. ACS Appl Mater Interfaces 2012;4(4):2259–66.

127. Seabra AB, Paula AJ, de Lima R, Alves OL, Durán N. Nanotoxicity of Graphene and Graphene Oxide. Chem Res Toxicol 2014;27(2):159–68.

128. Liu Y, Luo Y, Wu J, et al. Graphene oxide can induce *in vitro* and *in vivo* mutagenesis. Sci Rep 2013;3:3469.

129. Ren H, Wang C, Zhang J, et al. DNA Cleavage System of Nanosized Graphene Oxide Sheets and Copper Ions. ACS Nano 2010;4(12):7169–74.

130. Bianco A. Graphene: Safe or Toxic? The Two Faces of the Medal. Angew Chem Int Ed 2013;52(19):4986–97.

131. Orecchioni M, Ménard-Moyon C, Delogu LG, Bianco A. Graphene and the immune system: Challenges and potentiality. Adv Drug Deliv Rev 2016;105(Part B):163–75.

132. Lalwani G, D'Agati M, Khan AM, Sitharaman B. Toxicology of graphene-based nanomaterials. Adv Drug Deliv Rev 2016;105(Pt B):109–44.

133. Kumar S, Chatterjee K. Comprehensive Review on the Use of Graphene-Based Substrates for Regenerative Medicine and Biomedical Devices. ACS Appl Mater Interfaces 2016;8(40):26431–57.

134. Lee WC, Lim CHYX, Shi H, et al. Origin of Enhanced Stem Cell Growth and Differentiation on Graphene and Graphene Oxide. ACS Nano 2011;5(9):7334–41.

135. Zhang X, Yin J, Peng C, et al. Distribution and biocompatibility studies of graphene oxide in mice after intravenous administration. Carbon 2011;49(3):986–95.

136. Liu J-H, Yang S-T, Wang H, Chang Y, Cao A, Liu Y. Effect of size and dose on the biodistribution of graphene oxide in mice. Nanomed 2012;7(12):1801–12.

137. A. Jasim D, Ménard-Moyon C, Bégin D, Bianco A, Kostarelos K. Tissue distribution and urinary excretion of intravenously administered chemically functionalized graphene oxide sheets. Chem Sci 2015;6(7):3952–64.

138. Li B, Zhang X-Y, Yang J-Z, et al. Influence of polyethylene glycol coating on biodistribution and toxicity of nanoscale graphene oxide in mice after intravenous injection. Int J Nanomedicine 2014;9(1):4697–707.

139. Omid Akhavan, Elham Ghaderi, Ehsan Hashemi, Ebrahim Akbari. Dose-dependent effects of nanoscale graphene oxide on reproduction capability of mammals. carbon 2015;95:309–17.

140. Yang K, Gong H, Shi X, Wan J, Zhang Y, Liu Z. In vivo biodistribution and toxicology of functionalized nano-graphene oxide in mice after oral and intraperitoneal administration. Biomaterials 2013;34(11):2787–95.

141. Fu C, Liu T, Li L, Liu H, Liang Q, Meng X. Effects of graphene oxide on the development of offspring mice in lactation period. Biomaterials 2015;40:23–31.

142. Li B, Yang J, Huang Q, et al. Biodistribution and pulmonary toxicity of intratracheally instilled graphene oxide in mice. NPG Asia Mater 2013;5(4):e44.

143. Yan L, Wang Y, Xu X, et al. Can Graphene Oxide Cause Damage to Eyesight? Chem Res Toxicol 2012;25(6):1265–70.

144. Girish CM, Sasidharan A, Gowd GS, Nair S, Koyakutty M. Confocal Raman Imaging Study Showing Macrophage Mediated Biodegradation of Graphene In Vivo. Adv Healthc Mater 2013;2(11):1489–500.

CHAPTER 2: STUDY OF THE SURFACE CHEMISTRY OF GRAPHENE OXIDE

2.1 Introduction

GO is a promising nanomaterial in the biomedical field, but until today the surface chemistry is still unknown. The functional groups supposed to be present on GO are the hydroxyls, the epoxides, the carboxylic acids, the ketones and the lactones. But the type and quantity of these oxygenated groups on the surface of GO is variable. There are many factors influencing the surface composition, such as the oxidation procedure, the graphite used and the temperature (see parts 1.2 and 1.3). For these reasons we can find many different models in the literature trying to explain the composition of this material. Until today the most accepted model is the Lerf-Klinowski model in which there are hydroxyls and epoxides located on the basal plane and carboxylic acids localized at the edges. However, the precise atomic structure of graphene oxide remains still uncertain. Apart from the high variability of different GO samples, this is also due to a lack of sufficiently sensitive analytical techniques, to the complexity of this material related to its amorphous and berthollide character and to its high instability. As a matter of facts, the high instability of this material towards heating, X-ray and laser irradiation or current flow makes its characterization with the existing techniques, already complicated because of its complexity, even more difficult (see part 1.4.3).

Besides the surface composition, the biocompatibility and biodistribution of this material are of great importance in the biomedical field. Different studies have been reported in literature, but a high grade of purity and homogeneity of GO material is difficult to achieve. Therefore, the results obtained from the different studies are often contrasting.

2.2 Objectives of this chapter

With this study we would like to determine, in support of the classical characterization methods (*e.g.*, FT-IR, TGA, XPS), the surface composition and reactivity of GO using selective chemical reactions for each functional group supposed to be present in the structure. Moreover, we would like to compare different GO samples to investigate the relation between the synthesis procedure and the surface composition. For this purpose we purchased two differently synthesized GO samples: one from Grupo Antolin and the other from Nanoinnova Technologies. The GO from Grupo Antolin has been obtained by cutting and exfoliation of carbon fibers, while the one of Nanoinnova Technologies was obtained through the Hummers' oxidation procedure.

We performed the opening of the epoxides ring, the amidation and esterification on the carboxylic acid groups, the Wittig reaction on the ketone and the Williamson reaction and the esterification on the hydroxyl groups. We also included an improved SSNMR analysis of GO, in order to consolidate our data.

Furthermore, we exploited the opening of the epoxides for the biodistribution studies. To better understand the biodistribution of GO, we functionalized three highly water stable GO samples with different lateral sizes with a radionuclide chelating agent (*i.e.* a DOTA derivative). The purpose of this study was to investigate the relationship between the lateral size of the functionalized GO and the biodistribution and excretion profile of this material.

2.3 Results and discussion

2.3.1 Reactions performed on GO: Nanoinnova *versus* Antolin

To perform the study on surface composition, different aspects were carefully considered. Due to the high number of functional groups on the surface of GO, the selectivity of the reactions was taken into consideration. Highly selective reactions were chosen, and when not possible, potential side reactions were examined. Moreover, for all the reactions a control reaction was performed, to be sure that no side reactions and/or non covalent adsorption could happen. Control reactions are reactions performed in the

identical conditions of the reaction itself, but without a key reagent. These controls were also useful to establish if the reaction conditions affected the structure of GO. Indeed, besides the high number of different functional groups that can undergo side reactions, GO is highly sensitive to strong conditions that mainly cause the loss of the most labile oxygenated functions.

2.3.1.1 Epoxide *versus* carboxylic acid

To functionalize graphene oxide, amino-terminated chains were chosen because they can be easily further functionalized for other purposes. Moreover, the presence of a primary amine makes it possible to assess the amount of molecules introduced on GO using a colorimetric test, namely the Kaiser test.[1,2]

The opening of epoxides and the amidation reaction were performed in parallel. The amino-chain used for the amidation reaction can also react with the epoxide rings, thus this side reaction was considered. The amidation reaction (Scheme 2.1) was done by adding the di-*tert*-butyloxycarbonyl (Boc)-monoprotected 2,2'-(ethylenedioxy)bis(ethylamine) (**C1**) with *N*-hydroxybenzotriazole (HOBt) and EDC as coupling agents (see procedure **GO1** in Chapter 6).[3]

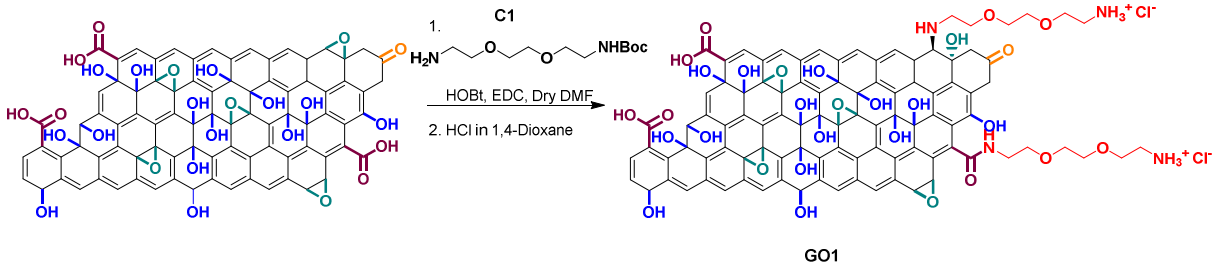

Scheme 2.1 Amidation reaction (the reaction has been drawn only on one functional group for sake of clarity).

The opening of the epoxides (Scheme 2.2) was performed in identical conditions, only without the coupling agents. Thus, only the Boc-monoprotected 2,2'-(ethylenedioxy)bis(ethylamine) (**C1**) was added in DMF at room temperature (see procedure **GO2** in Chapter 6).

A control reaction, **GO2_CONT**, was performed for both **GO1** and **GO2**. This control reaction was performed in the same conditions of **GO1** and **GO2,** without adding neither the coupling reagents nor **C1.** The purpose of this control reaction was to verify that the reaction conditions did not affect the structure of GO and that DMF did not adsorb on its surface.

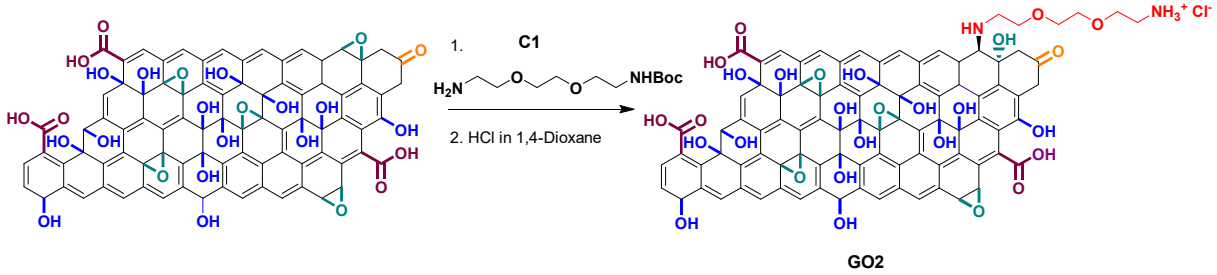

Scheme 2.2 Opening of epoxide (the reaction has been drawn only on one functional group for sake of clarity).

If we have a look to the Kaiser test results obtained after Boc deprotection (see **BD** procedure in Chapter 6), it is possible to notice that the loading was similar for both reactions, namely the opening of the epoxides and the amidation reaction (Table 2.1). If we consider that the opening of the epoxides happens as side reaction of the amidation, and that the loading of **GO2** was 262 µmol/g for Antolin (**Ant**) and 240 µmol/g for Nanoinnova (**NI**), then the carboxylic acid functionalization resulted negligible for **NI** and more

important for **Ant**. Indeed, by subtracting the value of **GO2** from that of **GO1**, we obtain 123 µmol/g for **Ant** and 35 µmol/g for **NI**. This result shows that the carboxylic acid is present only in a lower amount compared to the epoxides, and that there is a higher number of carboxylic acids on the surface of **GO-Ant** compared to **GO-NI**.

Table 2.1 Kaiser test data

	Antolin	**NanoInnova**
Opening of epoxides (GO2)	262 µmol/g	240 µmol/g
Amidation (GO1)	385 µmol/g	275 µmol/g
Esterification	98 µmol/g	41 µmol/g

To confirm this first result, the esterification reaction was performed on the carboxylic acids (Scheme 2.3). The reaction was done using the Steglich conditions (see procedure **GO3** in Chapter 6), with EDC and DMAP as coupling reagent to attach a Boc-protected 4-amino-1-butanol (**C2**). A control reaction was done, **GO3_CONT**, to verify if **C2** was adsorbed onto the GO surface. **GO3_CONT** was performed in the same conditions of **GO3**, without adding the coupling reagents.

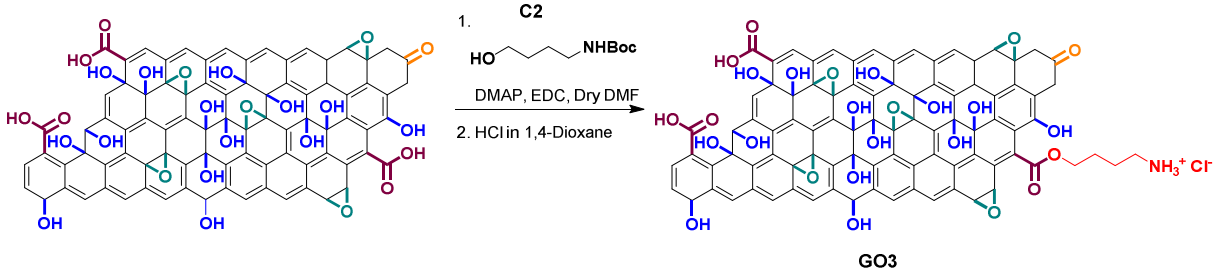

Scheme 2.3 Esterification reaction (the reaction has been drawn only on one functional group for sake of clarity).

The value obtained by Kaiser test after Boc deprotection (see **BD** procedure in Chapter 6) confirmed the results calculated by comparing the amidation reaction with the epoxide opening, with a loading of 98 µmol/g for the **GO3-Ant** and 41 µmol/g for **GO3-NI**.

From these results, we can conclude that there is a high number of epoxides on both GO samples, and only a low amount of carboxylic acids. Again, the results of the esterification show a slightly higher number of carboxylic acids for **GO-Ant**.

The overall outcome of the reactions was confirmed also by XPS analysis. In the survey spectra it is possible to identify the signal of the nitrogen present in the molecule covalently bound (Figure 2.1). For the amidation reaction 3% and 2.3% of nitrogen were identified for **GO1-Ant** and **GO1-NI**, respectively. For the opening of the epoxides, instead, 1.9% and 3% of nitrogen were found for **GO2-Ant** and **GO2-NI**, respectively. In the XPS spectra of the **GO2_CONT** reaction we can see that the reaction conditions did not strongly affect the structure of GO. Moreover, there is no residual DMF in the sample because no nitrogen was detected in the XPS spectra of **GO2_CONT**.

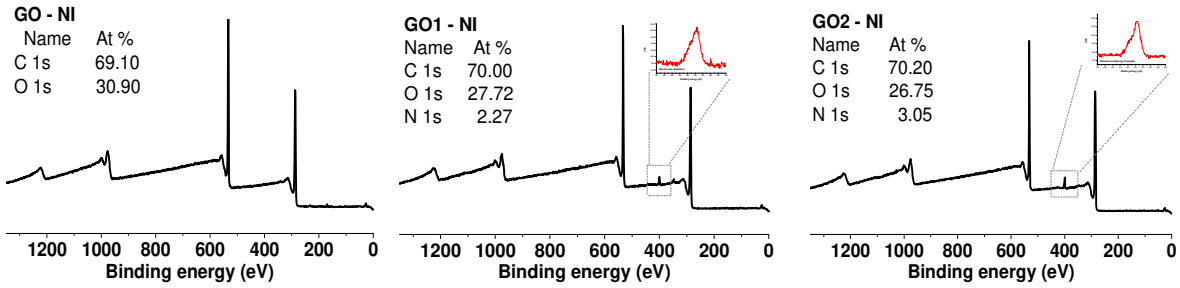

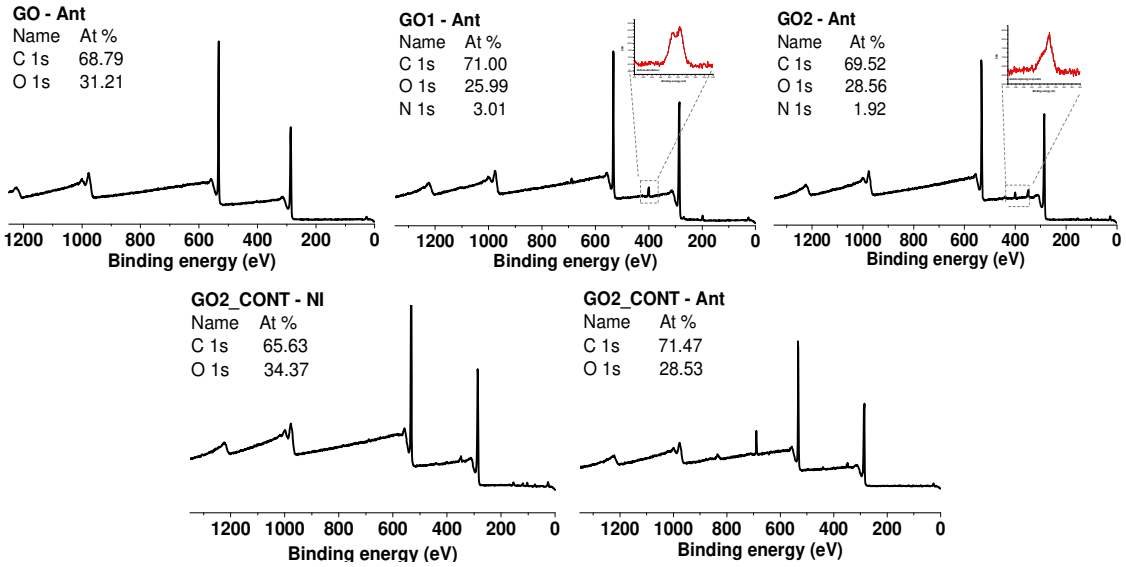

Figure 2.1 XPS survey spectra of **GO1**, **GO2** and **GO2_CONT** on Antolin and NanoInnova.

In the high resolution spectra of the C (1s) peak (Figure 2.2) five peaks were identified, one for the carbon-carbon sp^2 and sp^3 bond, one for the carbon-nitrogen bond, one for the epoxide and hydroxyl bond, one for the ketone and carboxylic acid and one for the π-π* transition. Due to the fact that the C-N bond, placed around 286 eV, is in an area where other two peaks overlap, there is a high imprecision in the identification of this peak. Nevertheless we could identify this signal in the spectra of the functionalized samples.

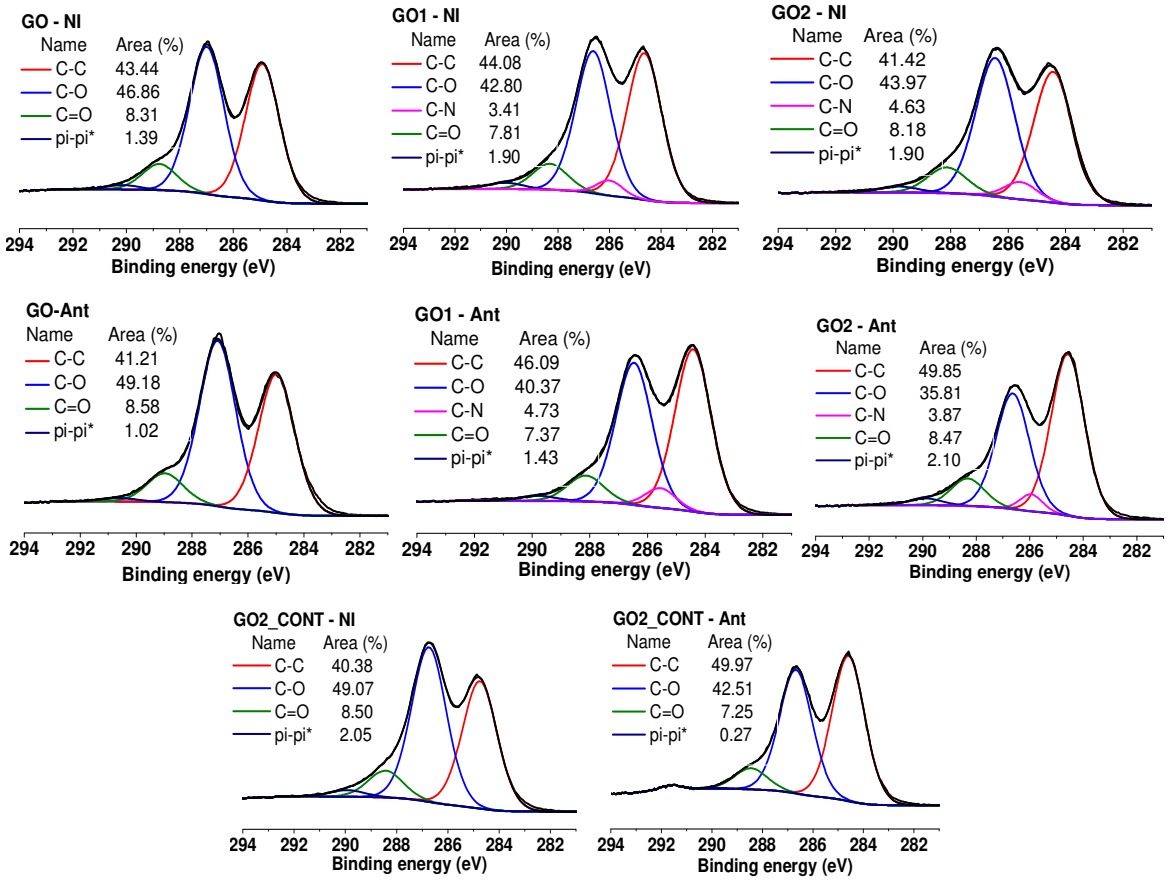

Figure 2.2 XPS carbon (1s) high resolution spectra of **GO1**, **GO2** and **GO2_CONT** on NanoInnova and Antolin.

For the esterification reaction, 1.6% and 1.5% of nitrogen were detected in the survey spectra of **GO3-Ant** and **GO3-NI**, respectively (Figure 2.3). These results confirm a lower amount of carboxylic acids on the surface of GO compared to the epoxides. Also in this case the absence of nitrogen in **GO3_CONT** confirms that both alcohol derivative **C2** and residual DMF did not adsorb onto GO. In the carbon high resolution spectra of **GO3-Ant** and **GO3-NI,** the C-N bond could be identified in low amount, in line with the results already obtained.

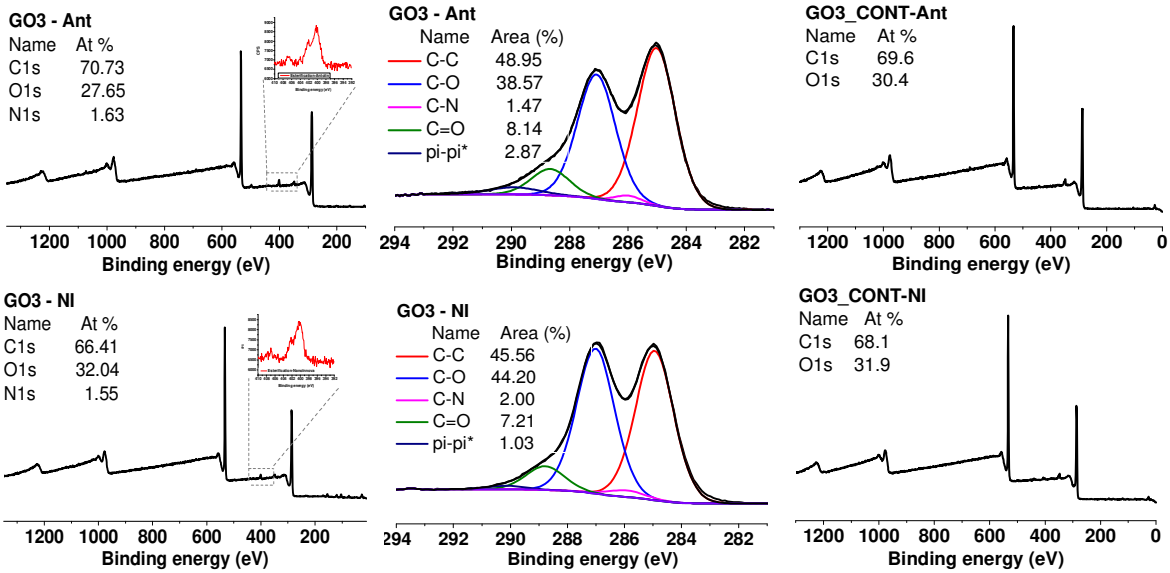

Figure 2.3 XPS survey and carbon (1s) high resolution spectra of **GO3-Ant** and **GO3-NI**.

FT-IR spectroscopy was then used to characterize the samples. By observing the spectra (Figure 2.4) it is possible to see an elevated number of signals. This is due to the complexity of the structure of GO and to the high number of functional groups present. In addition, the water adsorbed onto the surface of GO covers most of the region around 3000 cm^{-1}. For all these reasons, the FT-IR spectra are difficult to interpret.

It is rather complicated to follow the opening of the epoxides, because the band that could be assigned to the C-O-C vibration band of the epoxide (at ~1225 cm^{-1}) is small and covered by other bands. Nevertheless, the appearance of the bands at ~2918 and 2850 cm^{-1} of the methylene groups of **C1** can be detected in the spectra of **GO1** and **GO2**, more intense in the case of Antolin compared to NanoInnova, confirming the introduction of this molecule in both reactions. Moreover, the band at ~1720 cm^{-1}, usually assigned to the ketones and quinones, and visible in the starting material, disappears after functionalization in both **GO1** and **GO2**. This proves the labile character of these groups.

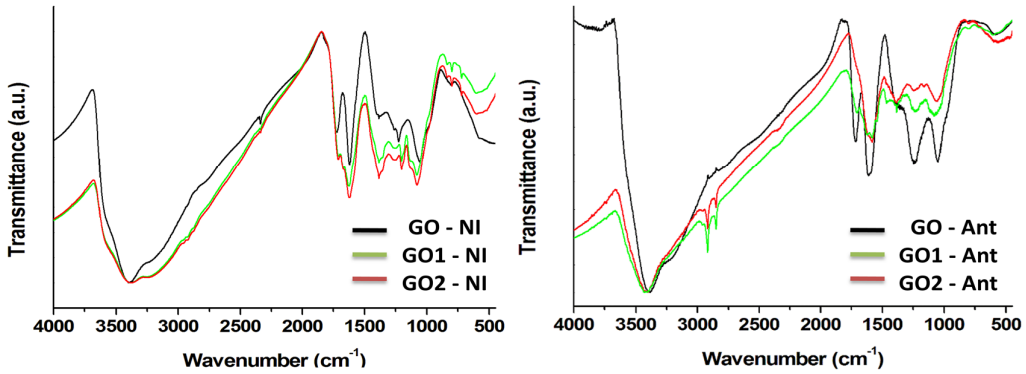

Figure 2.4 FT-IR spectra of GO, **GO1** and **GO2** for NanoInnova and Antolin.

Through TEM it is possible to confirm that the morphological characteristics of GO were preserved after derivatization (Figure 2.5). Similarly, by Raman spectroscopy, we can see that the amount of defects did not change after functionalization (Figure 2.6).

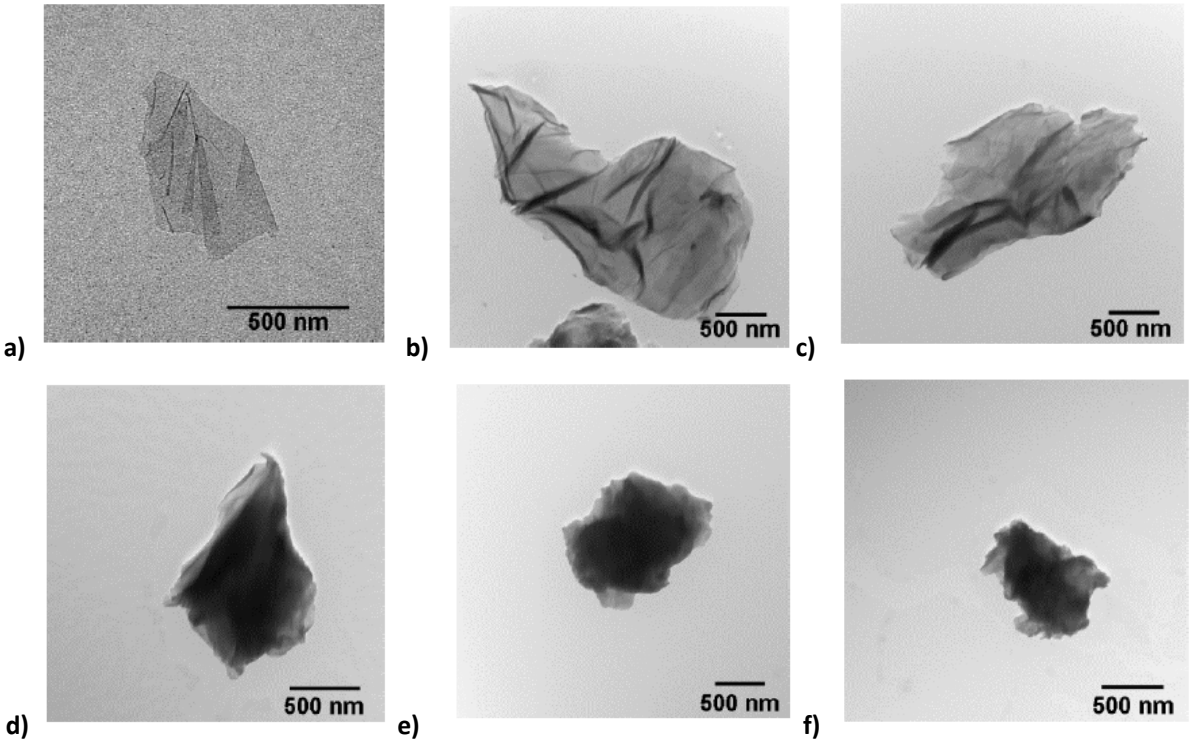

Figure 2.5 TEM images of GO-NI (a), **GO1-NI** (b), **GO2-NI** (c), GO-Ant (d), **GO1-Ant** (e), **GO2-Ant** (f).

As mentioned in the introduction (part 1.4.3), Raman spectroscopy is usually used to establish the degree of disorder by calculating the intensity ratio between the D band (~1350 cm^{-1}) and the G band (~1600 cm^{-1}). For GO this ratio is already high and there is no clear change after functionalization, meaning that the new defects have not been introduced, nor has GO been reduced.

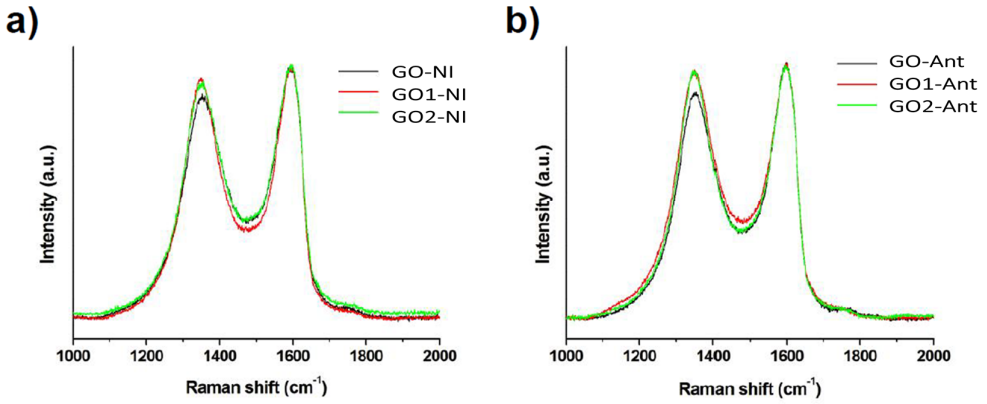

Figure 2.6 Raman spectra of GO, **GO1**, **GO2** for NanoInnova (a) and Antolin (b). The spectra were normalized to the G band intensity.

The thermal profile was assessed by TGA under nitrogen atmosphere (Figure 2.7). TGA is often used to establish the level of functionalization on carbon nanomaterials. In the case of GO this is rather difficult because of its thermal instability. In the thermogram of GO there are three steps of degradation. The first below 100°C is attributed to the loss of adsorbed water and some labile oxygen containing functions. Around 200°C there is the main weight loss, which is ascribed to the decomposition of other labile oxygen functionalities. The weight loss above 250°C can be assigned, instead, to the loss of the more stable oxygenated functional groups. Control reactions are of fundamental importance to interpret the TGA data, because of the instability of GO. Indeed, by comparing the starting GO with **GO2_CONT**, it is possible to notice a higher thermal stability of the **GO2_CONT** due to the loss of some labile oxygenated species, even though the conditions used for the reaction were mild (*i.e.* at room temperature).

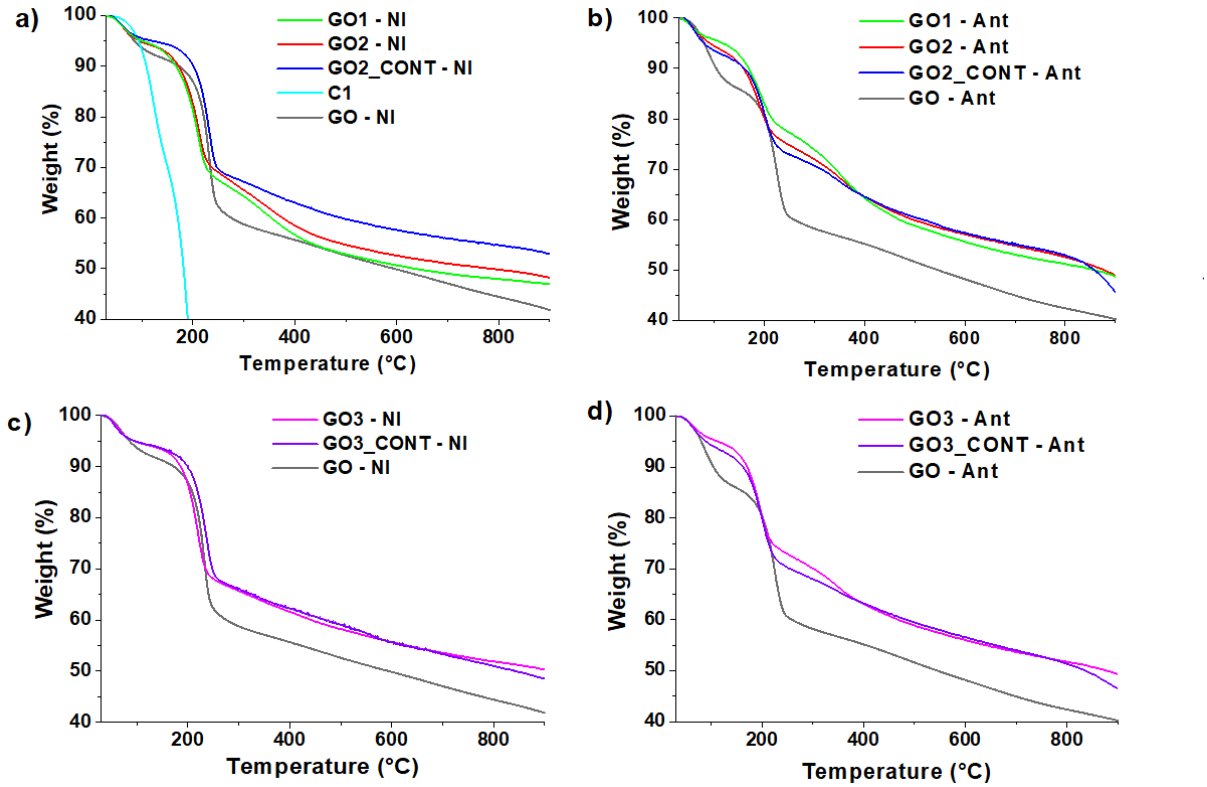

Figure 2.7 TGA of **a)** and **b) C1**, **GO**, **GO1**, **GO2**, **GO2_CONT; c)** and **d) GO3**, **GO3_CONT** for NanoInnova and Antolin.

There is no significant difference between the functionalized samples and the controls below 200°C (degradation temperature of **C1**); this suggests that the molecules have been grafted in a covalent way. (Figure 2.7). For **GO-NI** the introduction of **C1** is confirmed also by the higher weight loss of deprotected **GO1-NI** and **GO2-NI** compared to **GO2_CONT-NI**. The thermogravimetric curves of deprotected **GO1-NI** and **GO2-NI** are quite similar. Again, this indicates that the amount of **C1** introduced through amidation reaction was very low.

For **GO-Ant**, the interpretation of the TGA data is less clear (Figure 2.7 right). Indeed, the weight loss difference between deprotected **GO1-Ant**, **GO2-Ant** and **GO2_CONT-Ant** is not really significant. As previously mentioned, due to the thermal instability of GO, the interpretation can be quite difficult. This is also the case of **GO3**. Indeed, there is almost no difference between **GO3** and **GO3_CONT** for NanoInnova and also for Antolin. This is ascribed to both, the low molecular weight of the molecule and the really low amount of functionalization. Thus, it seems that TGA is not an appropriate technique to establish the level of functionalization for GO samples in case molecules of low molecular weight are used because of the thermal instability of GO.

2.3.1.2 Carboxylic acid *versus* opening of the epoxides: use of long PEG chains

To further prove the covalent grafting *via* opening of the epoxides through TGA, this reaction was repeated using a polyethylene glycol (PEG) chain with a molecular weight of ~1000 (Scheme 2.4). The reaction was performed in the same conditions of **GO2** by adding to **GO-NI** a mono-aminated long PEG chain, namely the aminopolyethylene glycol monomethyl ether (see procedure **GO4** in Chapter 6).[3]

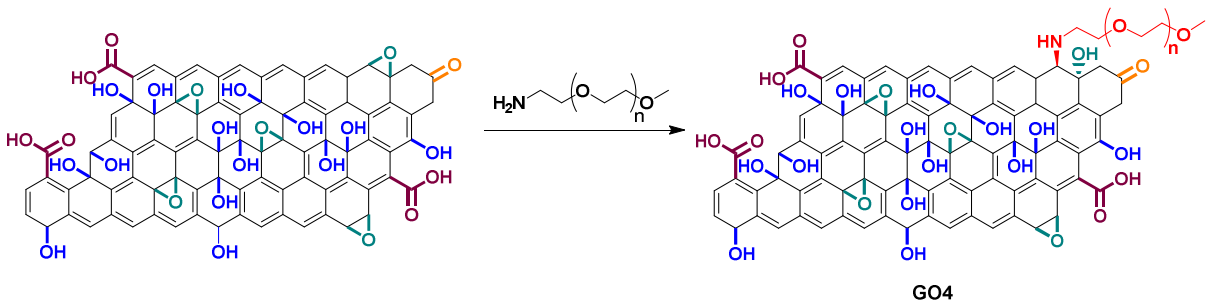

Scheme 2.4 Opening of epoxide **GO4** (the reaction has been drawn only on one functional group for sake of clarity).

PEG chains have the propensity to adsorb on GO, for this reason a control reaction was done (Scheme 2.5).[4] The control was accomplished using similar conditions to **GO4**, only adding poly(ethylene glycol) dimethyl ether (MW~1000) at the place of aminopolyethylene glycol monomethyl ether (see procedure **GO5** in Chapter 6).[3]

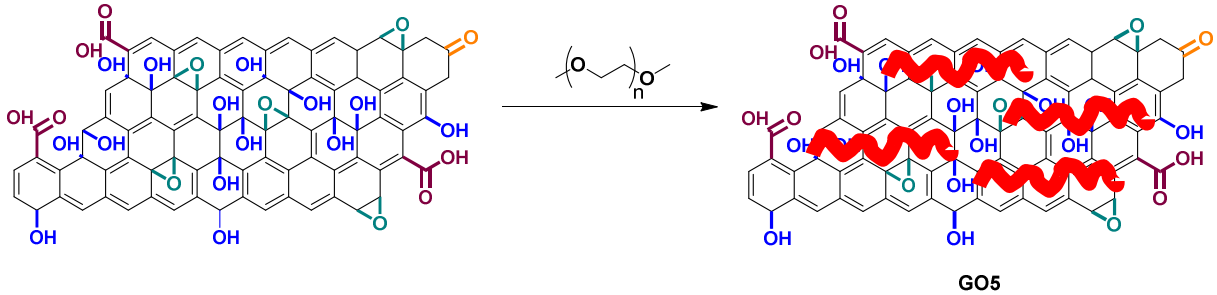

Scheme 2.5 Adsorption control **GO5** (red serpentines represent long PEG chains adsorbed on the surface of GO).

Both **GO4-NI** and **GO5-NI** were characterized by TGA under an inert atmosphere, and the thermal curves were compared to **GO2_CONT-NI** (Figure 2.8)**. GO5-NI** displays a similar weight loss compared to **GO2_CONT-NI**, proving that, with the reaction and purification conditions used, this PEG chain did not adsorb onto **GO-NI**. The thermal profile of **GO4-NI** is instead different. There is a lower weight loss below 100°C compared to **GO-NI** and **GO2_CONT-NI**, probably due to a lower amount of adsorbed water caused by the presence of PEG molecules onto GO. In addition, there is an important weight loss around 250-400°C that can be assigned to the removal of the covalently introduced PEG derivative.

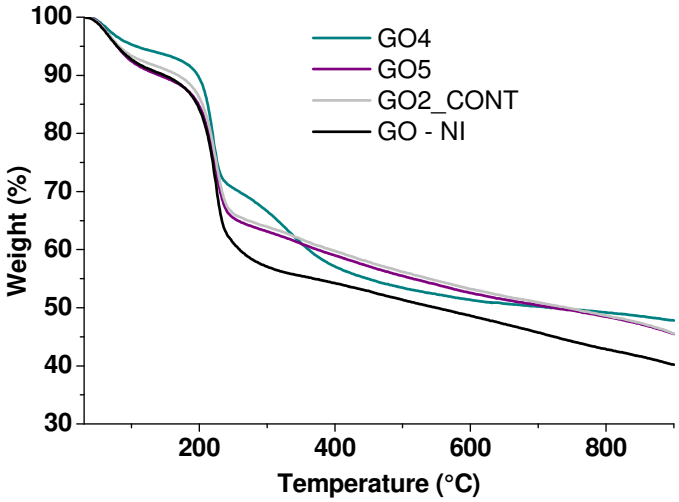

Figure 2.8 TGA for **GO4**, **GO5**, **GO2_CONT**, and GO on NanoInnova.

This results confirmed that the epoxide functional groups are present on GO and are opened by an amino-chain and that TGA can be a useful technique to characterize GO derivatized with high molecular weight molecules.

2.3.1.3 Carboxylic acid *versus* opening of the epoxides: a SS NMR study

As already mentioned in the introduction (part 1.4.3), SS MAS NMR is an interesting characterization technique used to establish the types of functional groups present on GO. In collaboration with Jésus Raya of the University of Strasbourg, we investigated the structure of both GO samples, NanoInnova and Antolin, using this spectroscopic technique to obtain additional information and try to elucidate the chemical structure of GO.[3] We performed also an advanced SSNMR 2D ^{1}H-^{13}C correlation experiment, namely a ^{1}H-^{13}C Frequency-Switched Lee Goldburg HETeronuclear CORrelation (FSLG-HETCOR) at high magnetic field and spinning speed.[5] Figure 2.9 clearly shows how very high fields (17.6 T) in 2D HETCOR experiments with FSLG irradiation during the evolution time gives an unattained resolution for proton in the solid state for this kind of materials. As a matter of fact, thanks to the combination of the high field, the 30 kHz MAS spinning speed and the careful set FSLG proton-proton decoupling, a 0.05 ppm resolution was reached.

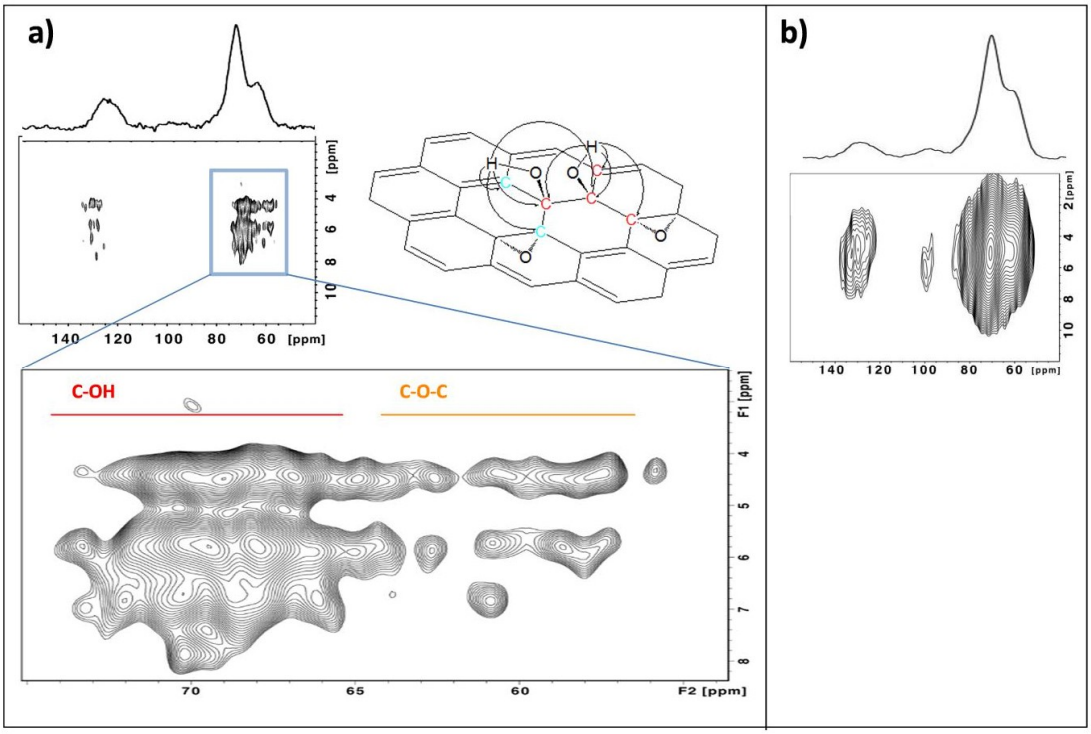

Figure 2.9 a) ^{13}C NMR and ^{1}H-^{13}C correlation spectra of **GO-NI** with magnification on the C-O region and a tentative chemical structure of GO; b) ^{13}C NMR and ^{1}H-^{13}C correlation spectra of **GO-Ant**.

To sort out most of the carbon atoms (that are unprotonated), an optimal Cross-Polarization (CP) contact time of 2 ms was applied. Under these conditions weak proton dipolar coupled rare spins, like carbonyls, give also rise to rather well detectable cross-peaks.

The FSLG-HETCOR spectrum (Figure 2.9) is a clear reflection of the complexity of the chemical environment of the carbon and hydrogen atoms present onto GO, for both NanoInnova and Antolin. Between 55 and 75 ppm, region of the aliphatic carbons, it is possible to detect around 25 cross-peaks that are associated with the spatial proximity and close contact between protons and carbons in C-OH and C-O-C groups. Between 125 and 135 ppm, region of the aromatic carbons, it is possible to count 13 cross peaks. They are generated by the spatial contact between the protons, most probably on the hydroxyl functional groups and the aromatic carbon double bonds. In both regions a certain number of peaks are also due to the presence of adsorbed water molecules, making a thorough description of the chemical structure difficult. In the upper right corner of figure 2.9, there is a possible chemical structure that could explain the proximity between the sp^2 and sp^3 carbons and the protons of the hydroxyl groups. This structure is based on the chemical shifts of the protons that cross-correlate with carbons on the same graphene sheet. The protons of the OH groups that are between 4.5 and 7.5 ppm can generate cross-peaks with the carbon in the aliphatic (55-70 ppm) and aromatic regions (125-135 ppm). Interlayer spatial interactions are also possible.

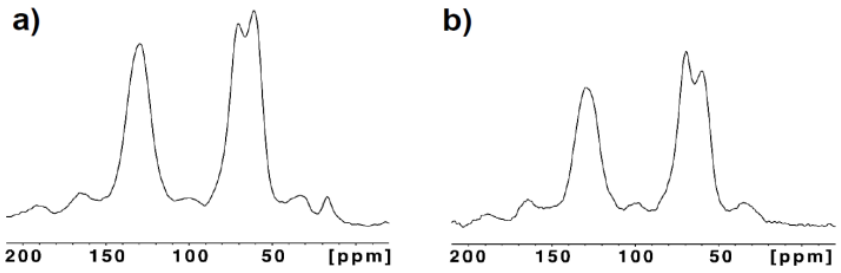

δ (ppm)	%
16.5	3.8
58.9	29.7
69.7	30.5
102.2	2.4
129.3	30.2
189.6	3.5

δ (ppm)	%
59.1	15.3
69.8	34.1
97.6	5.3
128.3	42.9
186.8	2.5

Figure 2.10 Quantitative ^{13}C SS MAS NMR of NanoInnova (a) and Antolin GO (b) and respective percentages of the different peaks (the chemical shift assigned to C=O is reported in red).

In figure 2.10 the quantitative ^{13}C SS MAS NMR are reported. In good agreement with the data reported in the literature, the peaks at 60.9 ppm and 70.8 ppm can be assigned to the epoxide and hydroxyl groups, respectively.[6–8] The peak located at 129.4 ppm is attributed instead to C=C double bonds, while the weak broad peak around 90-100 ppm could be assigned to lactols.[9,10] Carbonyl groups are instead localized around 160-190 ppm.[10] The difficulty to clearly identify a peak in this region confirms the absence or the very low amount of carboxylic acids.[9]

By integrating, after fitting, all the peaks in the quantitative ^{13}C spectra, it was possible to calculate the percentage of all peaks (Figure 2.10 bottom). The percentage of carbonyl groups (*e.g.*, carboxylic acids and ketones) was very low, 3.5% for **GO-NI** and 2.5% for **GO-Ant**. Thus, the MAS NMR experiments confirmed that the presence of the carboxylic acid group is negligible.

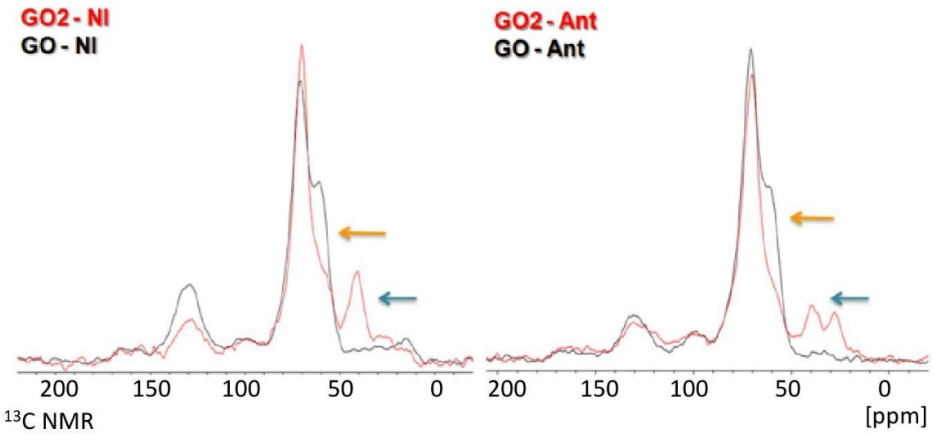

Figure 2.11 Qualitative ^{13}C SS MAS NMR of opening of epoxides and starting materials for NanoInnova (left) and Antolin (right). Yellow arrows point on the decrease of the epoxide groups, blue arrows on the comparison of the methylene and methyls groups of **C1**.

A qualitative ^{13}C SS MAS NMR spectra of **GO2** was taken for both NanoInnova and Antolin, and compared to the qualitative spectra of the respective starting material. An important decrease in the signal of the epoxide (~60 ppm) can be observed for both materials, meaning that the epoxide ring was opened by the amine derivative **C1**. Moreover, new signals appeared at ~30 and 40 ppm, that can be attributed to the methylene groups in alpha position to the nitrogen atoms and the methyls of the Boc group of **C1**.

This new peaks can be detected also in the FSLG-HETCOR spectra of **GO2-NI** and **GO2-Ant** (Figure 2.12).

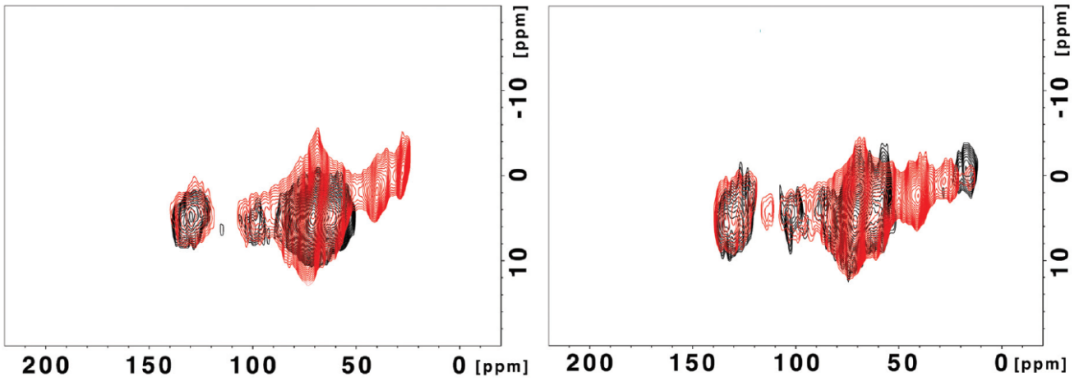

Figure 2.12 ^{1}H-^{13}C correlation spectra of Antolin on the left and NanoInnova on the right. In black the starting material and in red the functionalized **GO2**.

The MAS NMR experiments demonstrate that the reaction between GO and an amino-derivative occurs mainly *via* ring opening of the epoxide groups and not through amidation. Moreover, besides the low amount of carboxylic acids, they also prove the presence of the epoxide and hydroxyl groups in both samples, in an amount of 29.7% and 30.5% for **GO-NI**, and of 34% and 15% for **GO-Ant**, respectively.

2.3.1.4 Reactivity of the hydroxyl groups

To study the reactivity of the hydroxyl groups on the surface of GO, two reactions were performed, namely the Williamson and the esterification reaction.

The Williamson reaction (Scheme 2.6) was performed by adding a Boc-protected 4-iodo-butylamine (**C4**) with potassium carbonate as a base (see procedure **GO6** in Chapter 6). The basic conditions permit the deprotonation of the hydroxyl groups, which can undergo a substitution reaction with the iodo-compound. We chose K_2CO_3 and not stronger bases to avoid side reactions. Hypothesizing that the hydroxyl functions are phenolic, a base with lower pKa should be enough to perform the reaction.

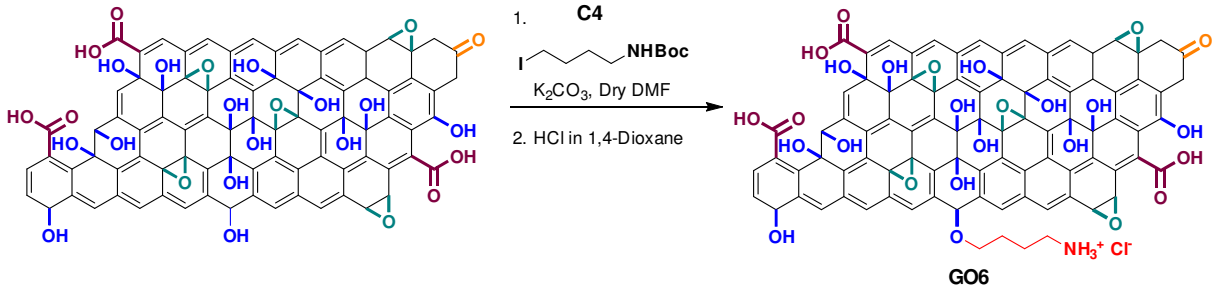

Scheme 2.6 Williamson reaction (the reaction has been drawn only on one functional group for sake of clarity).

The reaction was first performed at 80°C (**GO6-80-NI**), but at this temperature GO is partially reduced, as it can be observed in the thermogravimetric curves (Figure 2.13 right). Indeed the C/O ratio calculated by XPS augments from 2.2 of the starting material to 3.5 after derivatization (Table 2.2).

Thus, an optimization study of the reaction conditions was carried out on NanoInnova GO. The reaction was performed at 60°C, 40°C and at room temperature. Following the literature, the reaction at room temperature was performed also with Cs_2CO_3, which has been reported to promote the *O*-alkylation of phenols.[11]

Table 2.2 Optimization conditions for the Williamson reaction with Kaiser test and XPS data.

Name	Temperature	Base	Kaiser test (µmol/g)	C/O (XPS)	%N (XPS)
GO-NI	**-**	-	-	2.2	-
GO6-80-NI	**80°C**	K_2CO_3	69	3.5	1.77
GO6-60-NI	**60°C**	K_2CO_3	92	2.6	1.02
GO6-40-NI	**40°C**	K_2CO_3	123	2.8	0.87
GO6-RT-NI	**RT**	K_2CO_3	**132**	3.0	0.65
GO6-RT2-NI	RT	**Cs_2CO_3**	106	2.7	0.68

If we look at the Kaiser test values after deprotection (see **BD** procedure in Chapter 6), we can observe that the loading increases by decreasing the temperature (Table 2.2). The highest loading was obtained by performing the reaction at room temperature with potassium carbonate (**GO6-RT-NI**). If we compare the Kaiser test data with the nitrogen percentage calculated from the XPS survey spectra, it is possible to see an inverted tendency. Indeed, the percentage value of nitrogen decreases by decreasing the temperature. This could be explained by the fact that there is a loss of CO and CO_2 functions from GO at increased temperature (over 50°C), thus besides the introduction of nitrogen at high temperature there is also the elimination of carbon and oxygen.[12]

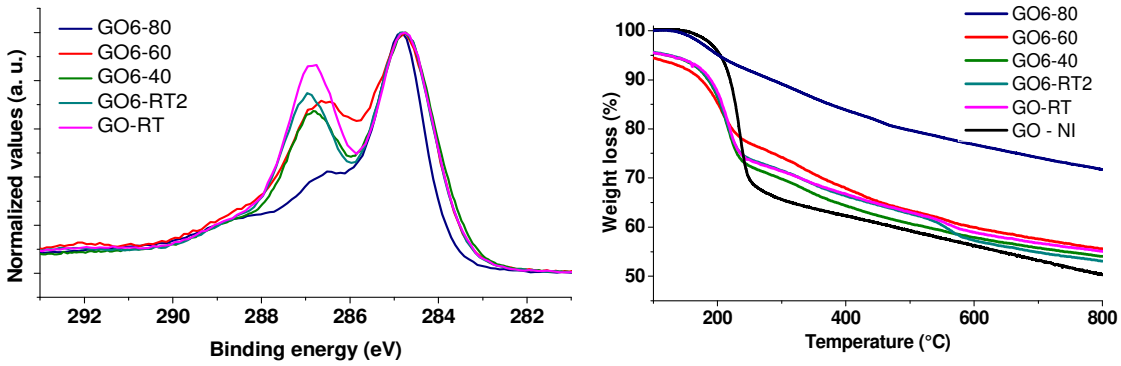

Figure 2.13 (Left) C (1s) high resolution XPS spectra of the optimization study; (Right) TGA of the reactions for the optimization study.

In addition, the reduction of GO under heating was confirmed by TGA and by the XPS carbon high resolution spectra (Figure 2.13). In the latter there is a temperature-dependant change of intensity of the peak in the C-O region. Meanwhile, in the former, **GO6-80-NI** and **GO6-60-NI** show a higher thermal stability, consistent with reduction.

Even though cesium was demonstrated to have a high sorption capacity onto GO, no residual cesium was detected in **GO6-RT2-NI** by XPS.[13] However, on GO, the use of cesium carbonate did not show improvements in the loading compared to the use of potassium carbonate. Thus, **GO6-RT-NI** was used for the subsequent studies. From here on, **GO6-RT-NI** will be named **GO6-NI**.

Once the optimal conditions were chosen, two control reactions were performed. **GO6_CONT1-NI** was done to test if the base could affect the structure of GO. **GO6_CONT2-NI** was instead done without using the base to verify that **C4** does not adsorb onto the surface of GO. Both controls displayed a higher thermal stability compared to the starting material, due to the loss of some labile oxygenated functions, that occurs even at room temperature, as already observed in the control reaction of the opening of epoxides. Moreover, they showed a similar thermal profile, thus the GO structure was not affected by the basic conditions. However, TGA was not conclusive to confirm neither the positive outcome of **GO6-NI** nor the potential adsorption, because of the low molecular weight of **C4** (Figure 2.14 left).

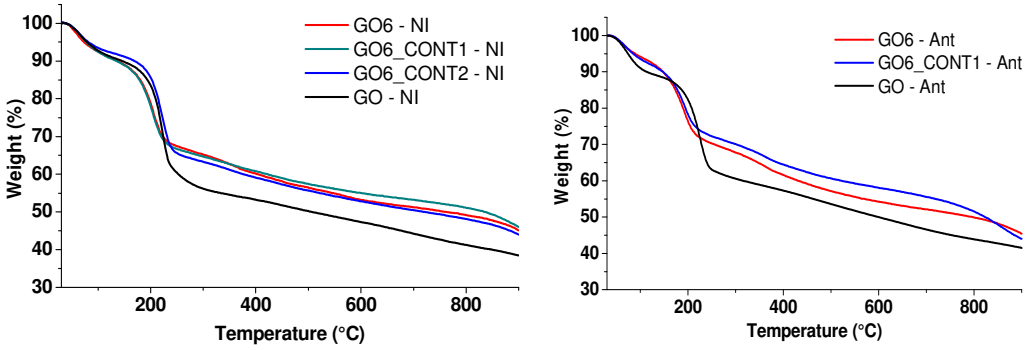

Figure 2.14 TGA of GO, **GO6** and **GO_CONT** of NanoInnova and Antolin.

The Williamson reaction was performed also on the Antolin GO (**GO6-Ant**), with **GO6_CONT1-Ant** as a control. In the case of **GO6-Ant**, its thermal profile showed a higher weight loss compared to the control, confirming the positive outcome of this reaction (Figure 2.14 right). The difference between **GO6-NI** and **GO6-Ant** in TGA could be explained by the higher loading for **GO6-Ant**. Indeed, the loading established by the Kaiser test after Boc deprotection (see **BD** procedure in Chapter 6) (Table 2.3) was 190 µmol/g for **GO6-Ant** compared to 132 µmol/g of **GO6-NI**.

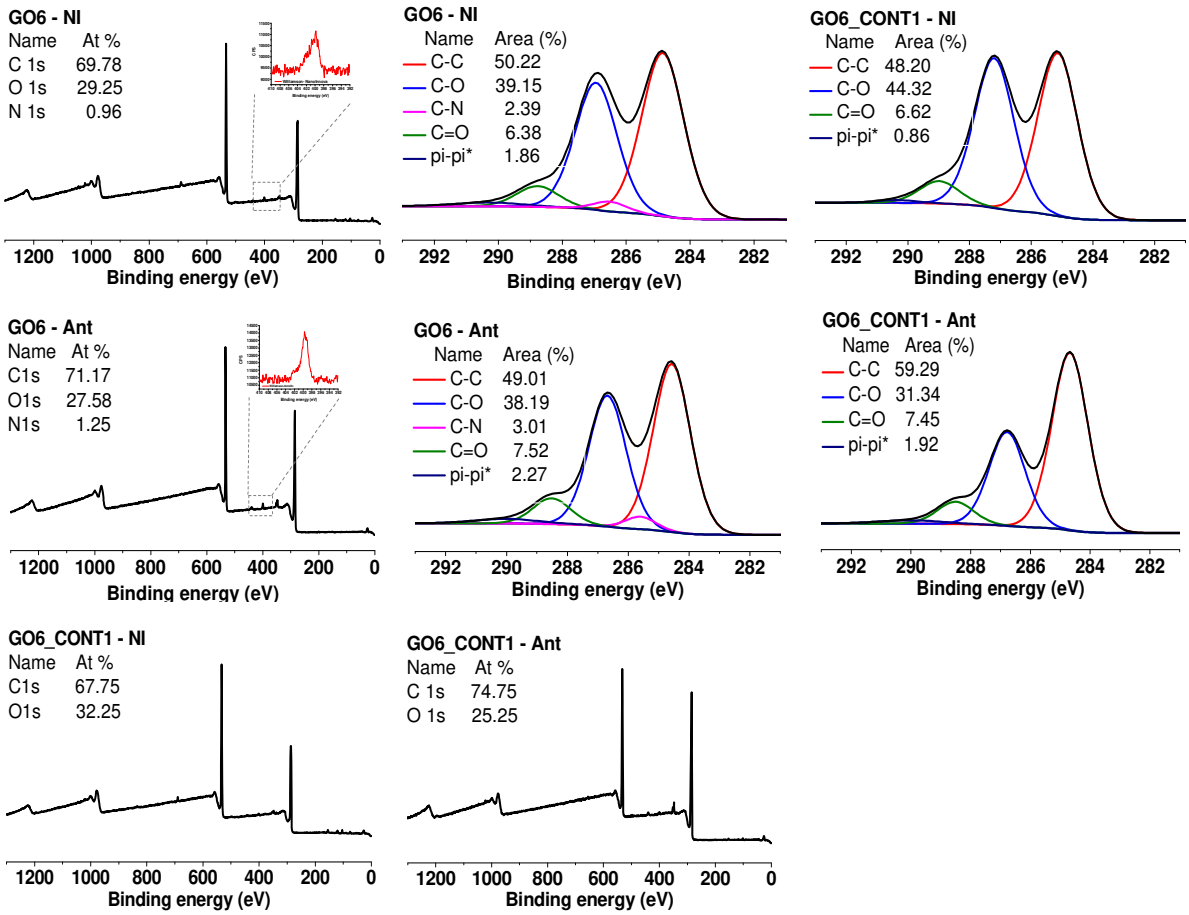

Figure 2.15 XPS survey and C (1s) spectra for the Williamson reaction of NanoInnova and Antolin.

In the XPS survey spectra a percentage of 0.96 and 1.25 of nitrogen was detected for **GO6-NI** and **GO6-Ant** respectively, in line with the results already obtained (Figure 2.15). Moreover, the C-N bond was identified in the carbon high resolution spectra, confirming the introduction of **C2** on GO *via* the Williamson reaction.

Table 2.3 Kaiser test data for the Williamson and the esterification reaction.

	NanoInnova	Antolin
Williamson	143 µmol/g	190 µmol/g
Esterification	165 µmol/g	136 µmol/g

Overall, the characterization of **GO6** by TGA, the Kaiser test and XPS indicates a higher number of hydroxyls on GO-Ant compared to GO-NI.

As already mentioned before, besides the Williamson reaction, an esterification reaction was also carried out on the hydroxyl groups. The esterification reaction (Scheme 2.7) was performed by adding Boc-protected aminocaproic acid (**C5**) with, as coupling reagents, EDC and DMAP (see procedure **GO7** in Chapter 6). Furthermore, a control reaction was performed without adding the coupling reagents to check if **C5** has a tendency to adsorb onto GO (**GO7_CONT**).

By Kaiser test a loading of 165 µmol/g and 136 µmol/g was calculated for **GO7-NI** and **GO7-Ant**, respectively, after Boc deprotection (see **BD** procedure in Chapter 6), confirming the positive outcome of this reaction (Table 2.3).

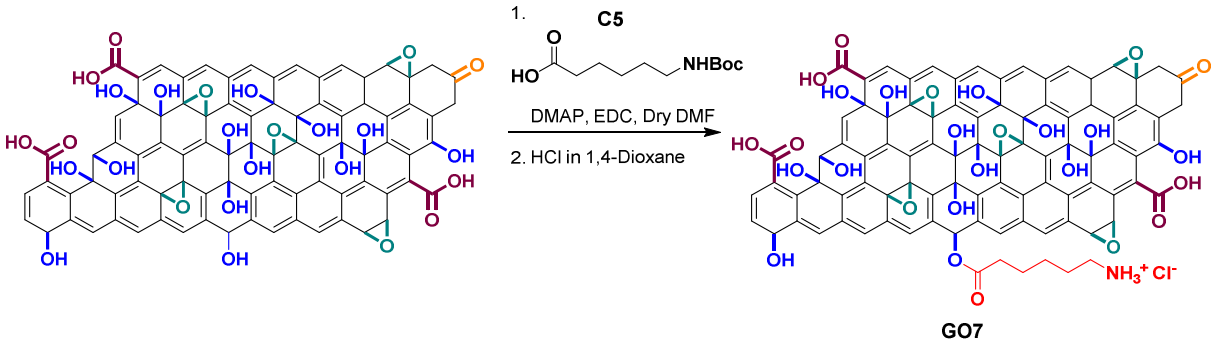

Scheme 2.7 Esterification reaction (the reaction has been drawn only on one functional group for sake of clarity).

In the TGA, as already observed before, the control reaction shows a higher thermal stability compared to the starting material, most probably due to the elimination of some labile functional groups from GO, even at room temperature. The thermogravimetric curves of both **GO7-NI** and **GO7-Ant** are similar to their control reactions, probably due to the low molecular weight of **C5**. **GO7-Ant** shows a slightly higher weight loss (between 200-400°C) compared to **GO7_CONT-Ant,** that could be due to the loss of **C5** (Figure 2.16 right). Instead, **GO7-NI** displays a different lineshape compared to its control in the same temperature interval, that could be assigned to **C5** (Figure 2.16 left). However, the total weight loss of **GO7-NI** is lower compared to **GO7_CONT-NI** in the same temperature range, suggesting a lower functionalization for **GO7-NI** compared to **GO7-Ant**. This is in agreement with the results obtained with **GO6-NI** versus **GO6-Ant**, confirming a higher number of hydroxyls for **GO-Ant**. Moreover, also in quantitative SS MAS NMR a slightly higher percentage of hydroxyls on **GO-Ant** was calculated, ~34% versus ~30% of **GO-NI** (Figure 2.10).

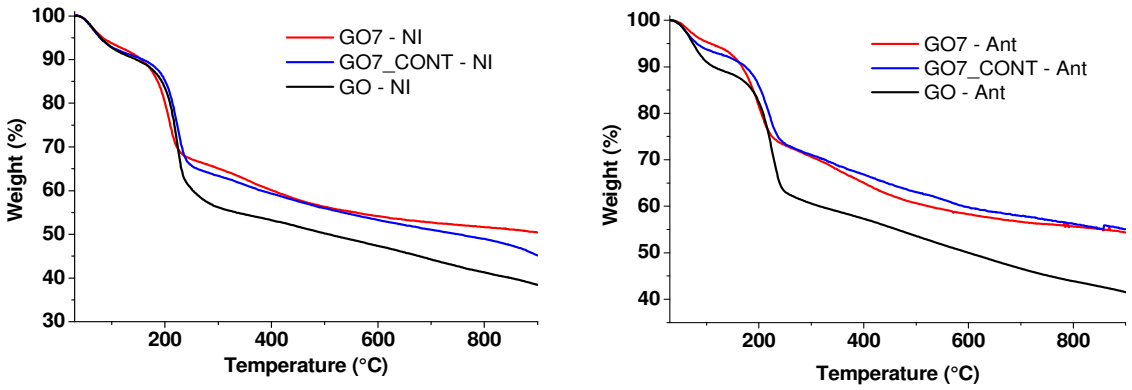

Figure 2.16 TGA of **GO7**, controls and starting material on NanoInnova and Antolin.

Similar results were obtained by establishing the atomic composition of **GO7** *via* XPS analysis. Indeed, the amount of nitrogen found by XPS was 2% for **GO7-NI**, while it was 2.4% for **GO7-Ant** (Figure 2.17). No nitrogen was detected instead in **GO7_CONT** for both NanoInnova and Antolin, confirming the covalent introduction of **C5**. In addition, in the carbon high resolution spectra it is possible to identify the signal of the C-N bond around 286 eV for both **GO7-NI** and **GO7-Ant**.

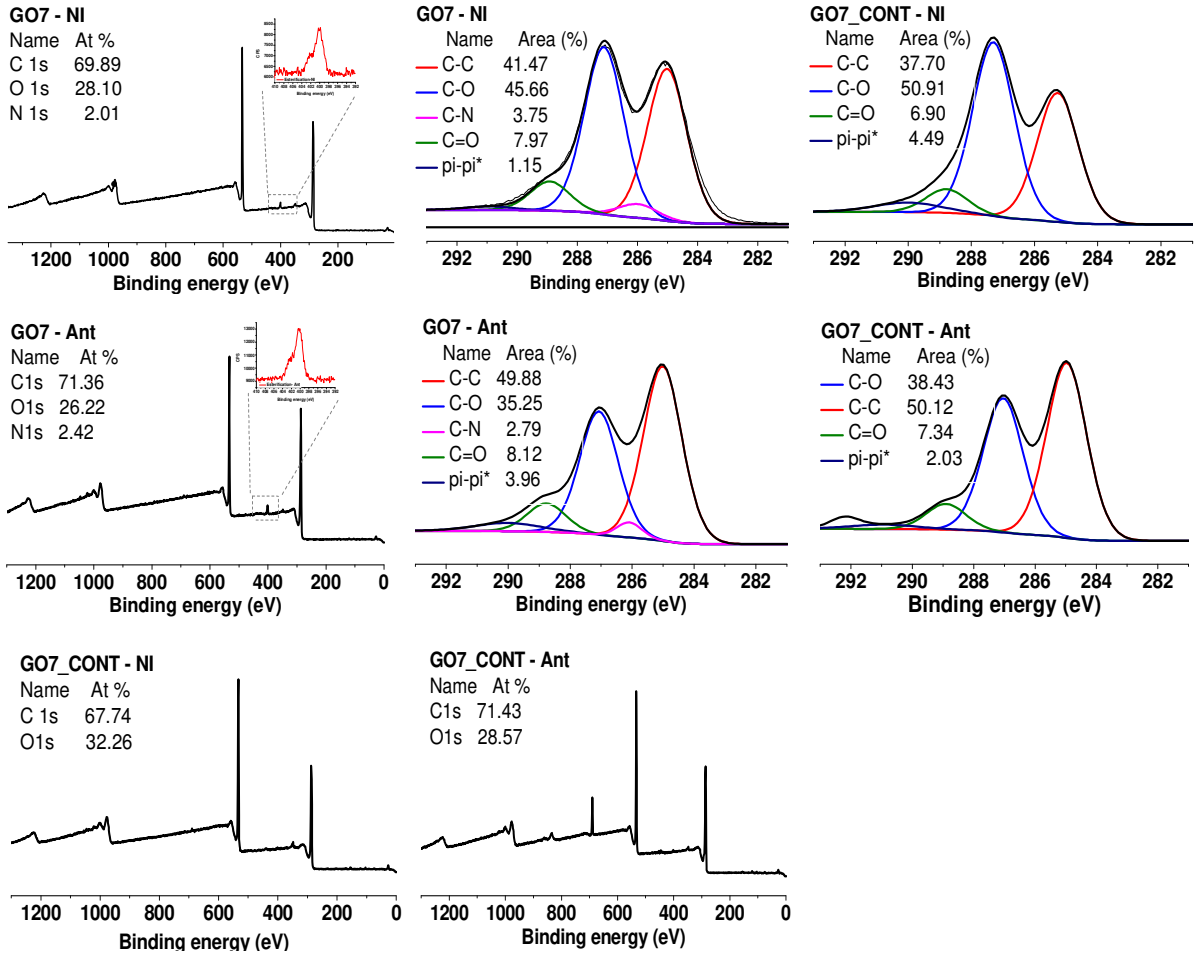

Figure 2.17 XPS survey and high resolution C (1s) spectra of **GO7** and **GO7_CONT** on NanoInnova and Antolin.

FT-IR spectroscopy was performed to identify the ester bands in **GO7-NI** and **GO7_CONT-NI** (Figure 2.18). But, due to the complexity of GO, no significant changes were detected on **GO7-NI** compared to the control reaction in the ester region (1735-1750 cm^{-1} for C=O bond and 1000-1300 cm^{-1} for the C-O bond). The only significant new peaks that appear in **GO7-NI** are the one at ~2918 and ~2850 cm^{-1} of the alkyl C-H stretch of **C5**. For this reason, FT-IR spectroscopy characterization was not performed on **GO7-Ant**.

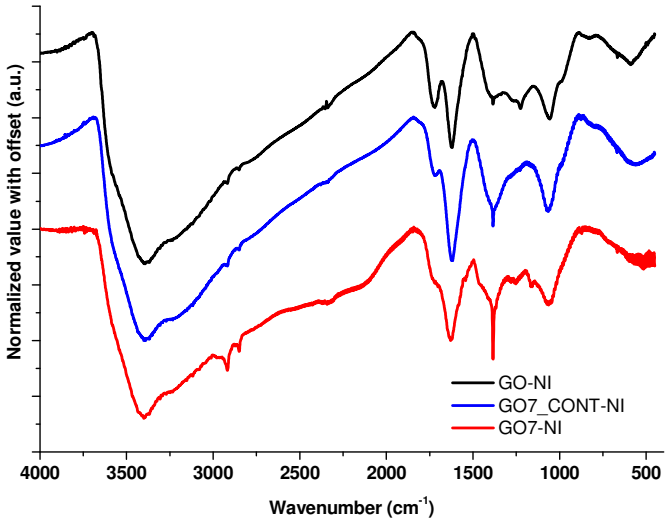

Figure 2.18 FT-IR spectra of GO, **GO7** and control on NanoInnova.

A qualitative ^{13}C SS MAS NMR was taken for both **GO7-NI** and **GO7-Ant** to confirm the introduction of **C5** *via* esterification. In the following spectra (Figure 2.19) we can observe two signals at around 25 and 40 ppm that can be assigned to **C5**, while around 160 ppm it is possible to identify for **GO7-Ant** a peak with lower intensity that can be assigned to the ester function (Figure 2.19 left).[10] For **GO7-NI** instead this peak is not visible without fitting of the data (Figure 2.19 right). This difference between the two spectra is probably due to the level of functionalization, confirming a higher functionalization with **C5** for **GO7-Ant** compared to **GO7-NI**, in agreement with XPS and TGA results. Thus, using this technique, it is possible to confirm the covalent introduction of **C5** through esterification if introduced above a certain amount.

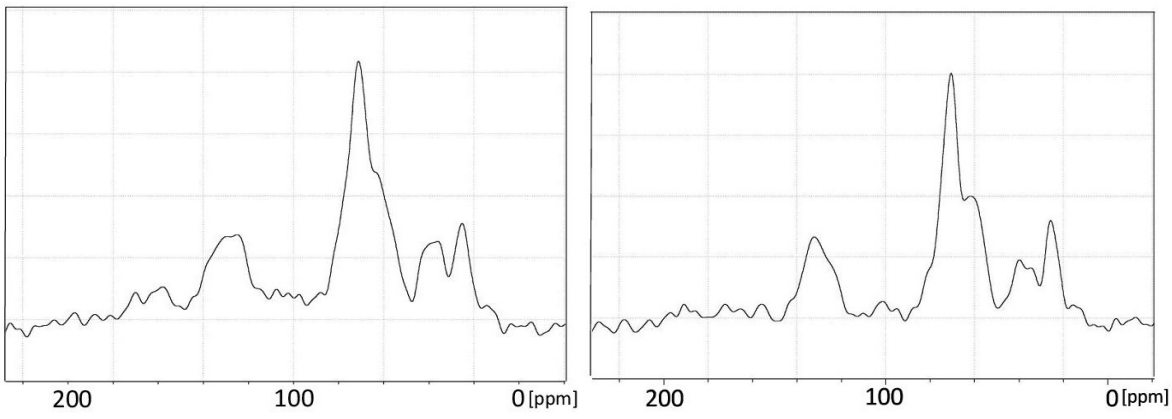

Figure 2.19 Qualitative ^{13}C SS MAS NMR spectrum of **GO7-Ant** (left) and **GO7-NI** (right).

Therefore, the presence of the hydroxyl groups was confirmed in both Antolin and NanoInnova GO by SS MAS NMR. These groups are reactive towards functionalization *via* the Williamson and esterification reactions, with an average level of functionalization of the hydroxyl groups of 154 µmol/g for GO-NI and of

163 µmol/g for GO-Ant. In addition, Antolin GO showed a slightly higher amount of this group using both SS MAS NMR analysis and surface investigation through chemical reactions.

2.3.1.5 Investigating the presence and reactivity of the ketone

To investigate the presence of ketones onto GO, the Wittig reaction was tested (Scheme 2.8). This reaction was performed in dry conditions with (4-amino-butyl)-triphenyl-phosphonium iodide (**C6**) and Potassium bis(trimethylsilyl)amide (KHMDS) as a base (see procedure **GO8** in Chapter 6). KHMDS was employed because of its sterical hindrance, to avoid undesired side reactions between the base and other oxygenated groups present on the surface of GO. A control reaction was performed without **C6** to verify that the base did not provoke changes in the structure of GO (**GO8_CONT**).

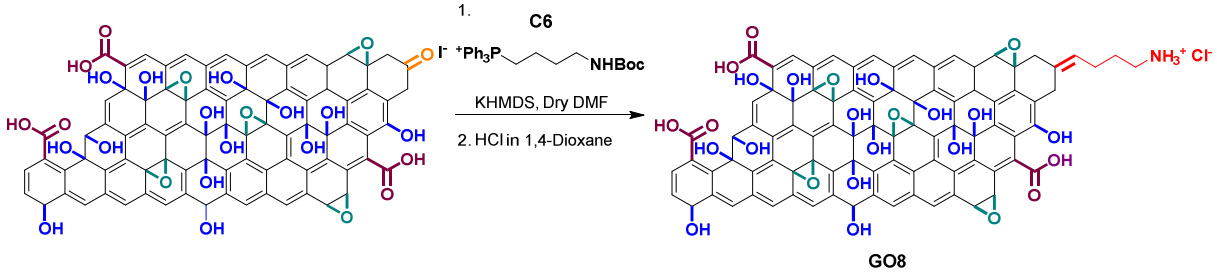

Scheme 2.8 Wittig reaction (the reaction has been drawn only on one functional group for sake of clarity).

The values calculated by the Kaiser test after Boc deprotection (see **BD** procedure in Chapter 6) were 22 µmol/g for **GO8-NI** and 26 µmol/g for **GO8-Ant** (Table 2.4), showing that the ketones are present in very low amount on the surface of both starting materials, or that the ketones present are not reactive enough towards the Wittig reaction.

Table 2.4 Kaiser test data for **GO8** on NanoInnova and Antolin.

	NanoInnova	Antolin
Wittig reaction	22 µmol/g	26 µmol/g

By XPS a really low amount of nitrogen was detected, around 0.5% for both **GO8** samples (Figure 2.20). Moreover, no C-N bond was identified in the carbon high resolution spectra.

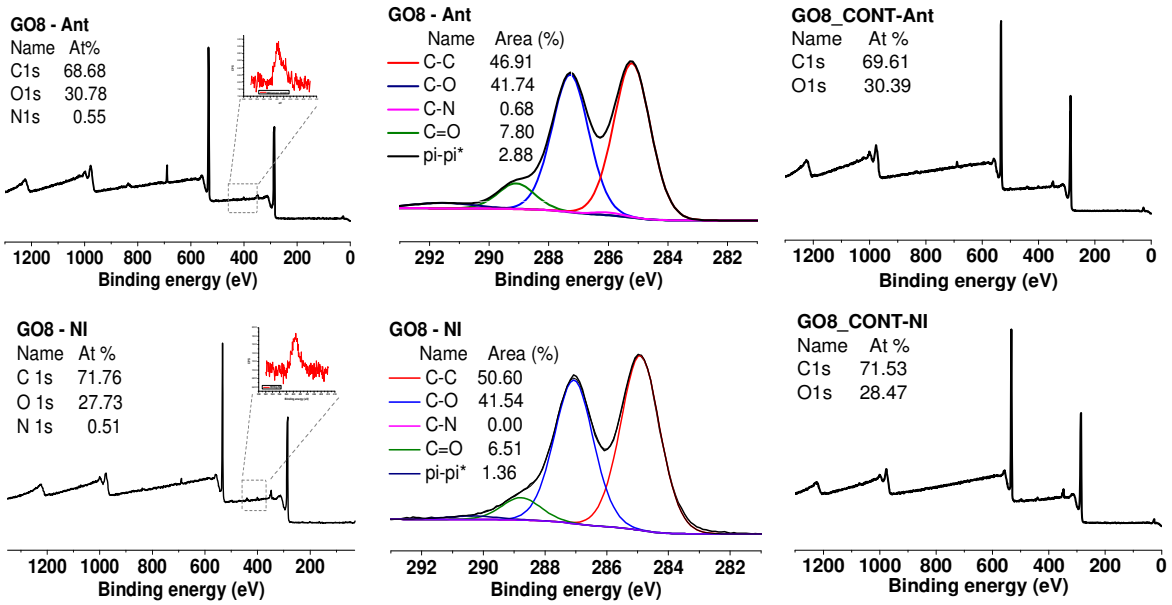

Figure 2.20 XPS survey and high resolution C (1s) for **GO8** on Antolin and NanoInnova.

The TGA shows for both graphs in figure 2.21 a similar thermal curve between **GO8** and **GO8_CONT**. However, the curve of GO-NI shows a more important weight loss for **GO8-NI** compared to its control. As already discussed before, TGA is not the appropriate characterization techniques for functionalization of GO with low molecular weight molecules. Thus, this little weight loss difference could be attributed to both, the adsorption of **C6** on the sample and the variability of GO samples.

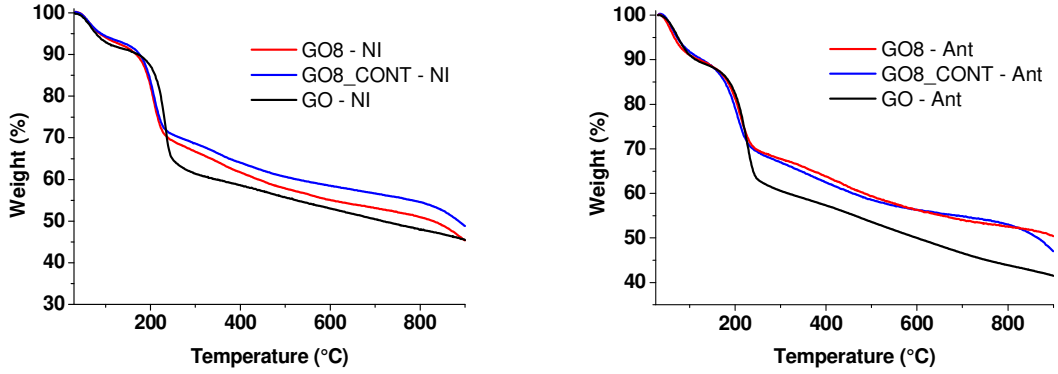

Figure. 2.21 TGA of **GO8**, control, and starting materials.

GO8-NI was characterized also through FT-IR spectroscopy and compared to **GO8_CONT-NI** (Figure 2.22). Between the two spectra no significant differences can be observed, confirming a negative outcome of the reaction.

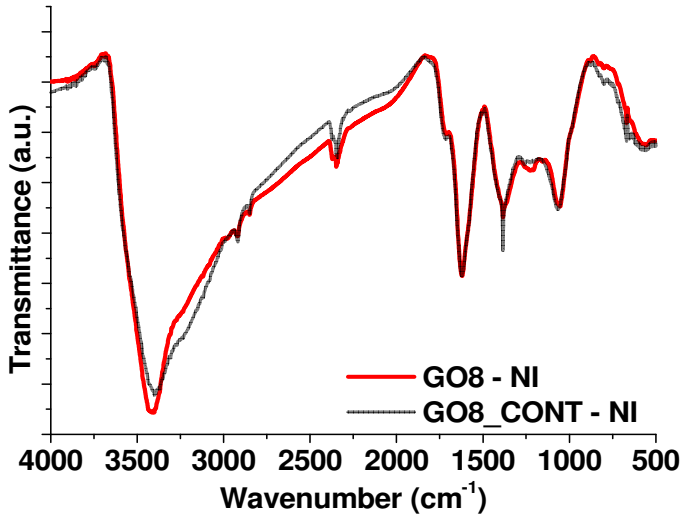

Figure 2.22 FT-IR for **GO8** and control on NanoInnova.

2.3.4 Exploiting the opening of epoxide for a biodistribution study

To study the biodistribution of GO in organs and tissues after administration into mice, three GO with different lateral sizes were derivatized *via* the opening of the epoxides with a commercially available NH_2-PEG_4-DOTA derivative (see procedure **GO9** in Chapter 6). DOTA are good chelating agents, facilitating their use for radiolabelling and *in vivo* imaging.

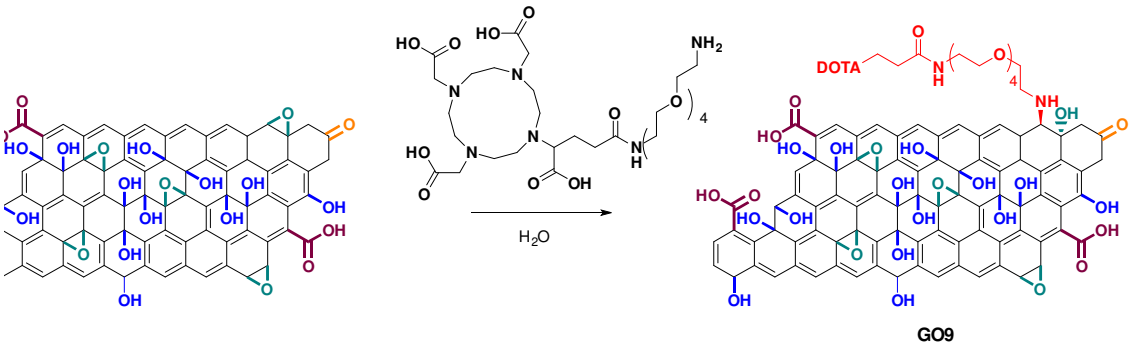

Scheme 2.9 Opening of the epoxides with long chain DOTA molecule (the reaction has been drawn only on one functional group for sake of clarity).

The GO samples used for this study were provided by Prof. Kostas Kostarelos (University of Manchester, UK) (**GO-K**), and his group performed also the radiolabeling and the biodistribution studies of the radiolabeled samples. Three **GO-K** with different lateral sizes were used, a large GO (l-GO) of 30 µm-10 µm, a small GO (s-GO) of 1 µm-100 nm, and an ultra-small GO (us-GO) of less than 50 nm.

GO-K was synthesized, as GO-NI, through the Hummers' oxidation method. Already before this project, we were working with GO-K in our laboratory. The previous batch we had from Manchester was not size sorted and it was analyzed, in collaboration with Jésus Raya of the University of Strasbourg, *via* SS MAS NMR analysis. As for GO-NI and GO-Ant, mainly hydroxyl and epoxide groups were identified on this first batch of GO-K (Figure 2.23). We expect similar surface composition results between the two batches, considering that the batch of GO-K we employed was obtained following the same procedure used for the previous one.

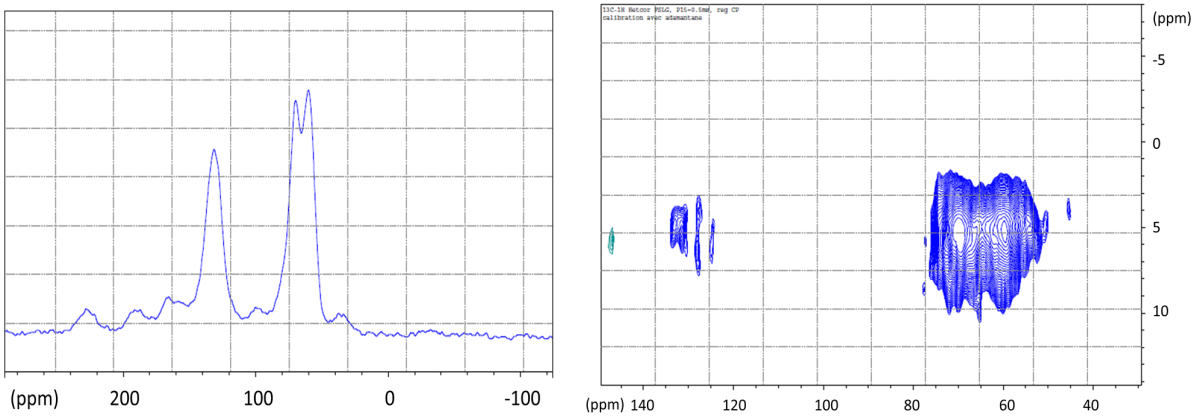

Figure 2.23 Quantitative ^{13}C SS MAS NMR spectrum of GO-K on the left and ^{1}H-^{13}C correlation on the right.

For **GO-K** only a very low quantity of carbonyls (2.9 % for the peak at 189 ppm) was also found after deconvolution of the quantitative ^{13}C SS MAS NMR spectrum (Table 2.5).

Table 2.5 Percentages of the peak fitting of the quantitative ^{13}C SS NMR.

Peak	59.4 ppm	69.75 ppm	96.40 ppm	131.66 ppm	189.08 ppm
%	19.60	33.99	4.93	38.54	2.93

GO9 was synthesized in milliQ water, without any solvent treatment nor sample drying, to avoid any kind of change (*i.e.* reduction or aggregation) in the structure of GO or risk of toxicity in mice due to residual

organic solvents. After functionalization, **GO9** was characterized by TGA, the xylenol orange (XO) test and XPS.[14,15]

As usual, TGA showed inconclusive results (Figure 2.24). This is also due to the fact that, in this case, no control reactions were performed because of a limited amount of starting materials. Only one aspect can be noticed in the different TGA spectra: the fact that all DOTA functionalized samples show a main weight loss at lower temperature (around 200°C) compared to the starting GO. This could be an indication of covalent functionalization.

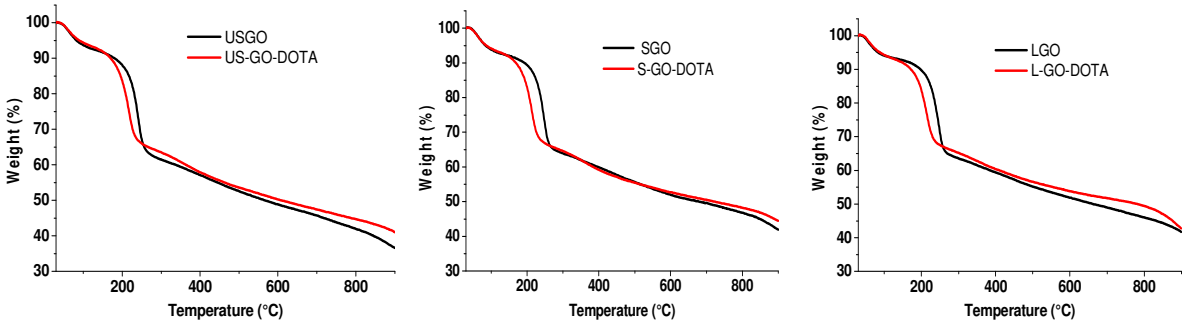

Figure 2.24 TGA of starting material and DOTA functionalized derivatives.

The XO test allows to calculate the amount of free gadolinium in solution. DOTA derivatives chelate gadolinium. Thus, a solution with a known concentration of gadolinium was added to **GO9**. After centrifugation, to separate **GO9** from the solution containing free gadolinium, the amount of gadolinium left in solution was assessed by UV-Vis spectroscopy using xylenol orange. Hence, this colorimetric test is an indirect method to establish the quantity of DOTA in the functionalized GO samples. This test was also performed on the starting material as a control to determine if GO had the tendency to chelate gadolinium non-specifically. Unluckily, this test was not conclusive due to the partly adsorption of gadolinium onto the surface of GO (Table 2.6). This high sorption capacity of GO has been already documented before in the literature.[13] But, we could notice that DOTA-functionalized GO samples showed a slightly higher value compared to pristine GO, which could suggest a positive outcome of the reactions.

Table 2.6 XO colorimetric test results of starting material and DOTA functionalized derivatives.

Gd chelation colorimetric test		
585 µmol/g of chelated Gd on l-GO-DOTA	**625** µmol/g of chelated Gd on s-GO-DOTA	**625** µmol/g of chelated Gd on us-GO-DOTA
565 µmol/g of Gd adsorption on pristine l-GO	**582** µmol/g of Gd adsorption on pristine s-GO	**582** µmol/g of Gd adsorption on pristine us-GO

Instead, the analysis of the XPS spectra (Figure 2.25, 2.26 and 2.27) allows to observe that the functionalization of GO with the DOTA derivative was successful. First, there is an introduction of nitrogen detected in the functionalized GO survey spectra compared to the starting materials. The amount is around 1.1-1.4% (Figure 2.26). Moreover, in the nitrogen high resolution spectra, it is possible to clearly identify the amine/amide and the ammonium peaks (Figure 2.25). Both amines and amides are present in the DOTA molecule introduced.

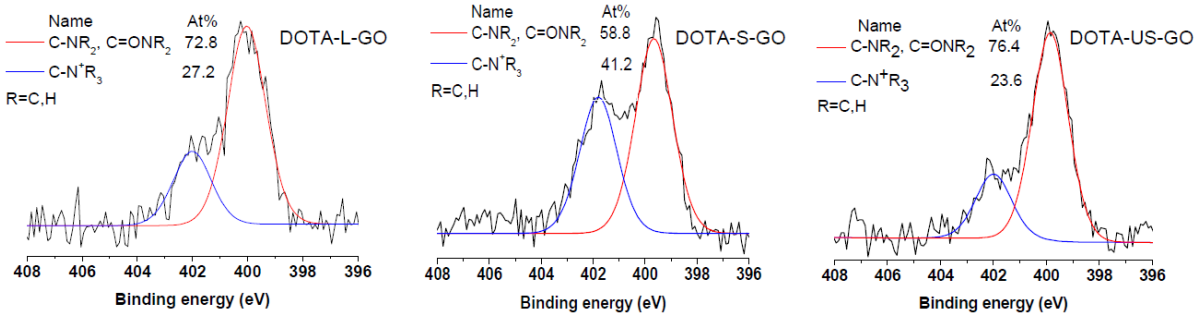

Figure 2.25 XPS high resolution N (1s) spectra of DOTA functionalized derivatives.

On the other hand, the interpretation of the carbon high resolution spectra is more complex (Figure 2.26). The ratio between the carbon-carbon bond region and the carbon-oxygen bond region changes. But this is often the case after any kind of treatment of GO, due to the loss of some labile oxygenated functional groups.

For this sample a more thorough deconvolution was done, to effectively confirm the introduction of DOTA molecules. Thus, in the C (1s) spectrum an asymmetric peak for C=C sp^2 was identified, and symmetric peaks for C-C sp^3, C-OH/C-N, C-O-C, C=O, C(O)OH and π-π* interactions (see chapter 6 for more information).

Survey	L-GO	S-GO	US-GO	DOTA-L-GO	DOTA-S-GO	DOTA-US-GO
Element	At %					
C 1s	68.6	68.5	69.8	71.4	69.6	68.9
O 1s	31.4	31.5	30.2	27.5	29.0	29.7
N 1s	-	-	-	1.1	1.4	1.4

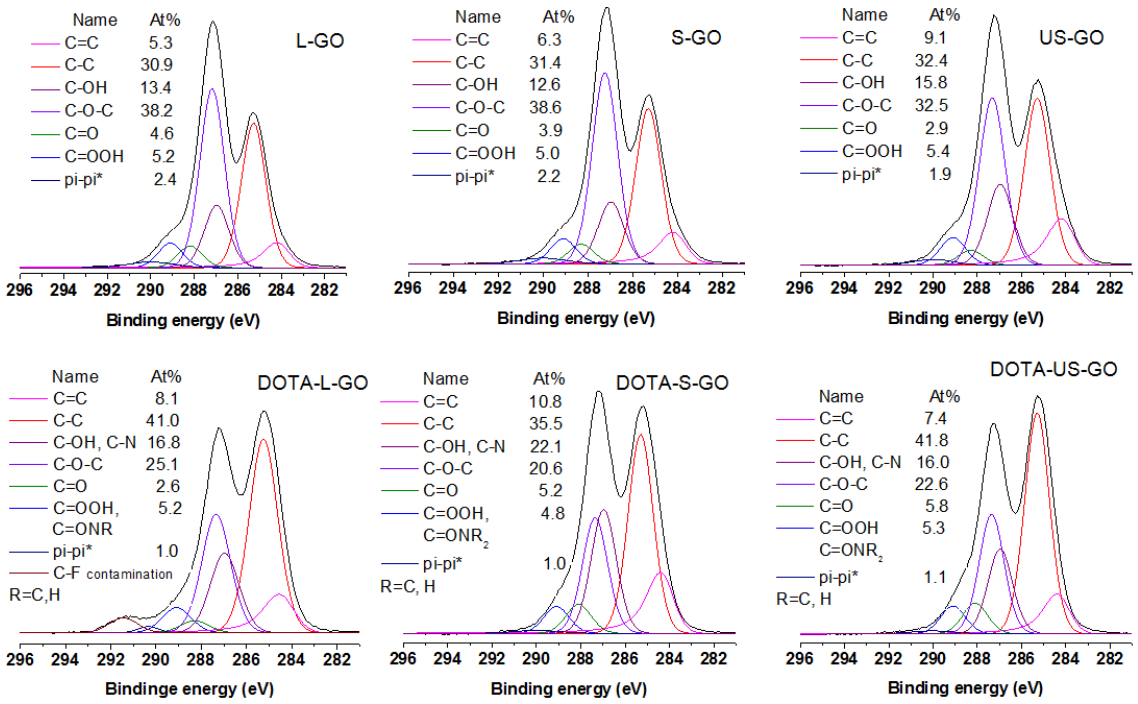

Figure 2.26 XPS surveys in the table on the top, and high resolution C (1s) spectra of starting materials and DOTA-functionalized derivatives.

Thus, what is possible to observe is the ratio between the C-O-C and the C-OH/C-N peak. There is an increase in the C-OH/C-N peak compared to the C-O-C peak. This happened because of the opening of the epoxides generating C-OH groups and the introduction of amino groups. However, the C-O-C peak does not disappear because there was a concomitant introduction of ether groups.

In the oxygen high resolution spectra instead, there is a clear increase in the percentage of the carbonyl peak (Figure 2.27). This is due to the introduction of carboxylic acids and amides of the DOTA molecule.

Thus, by XPS it was possible to confirm the introduction of DOTA derivatives on the surface of GO.

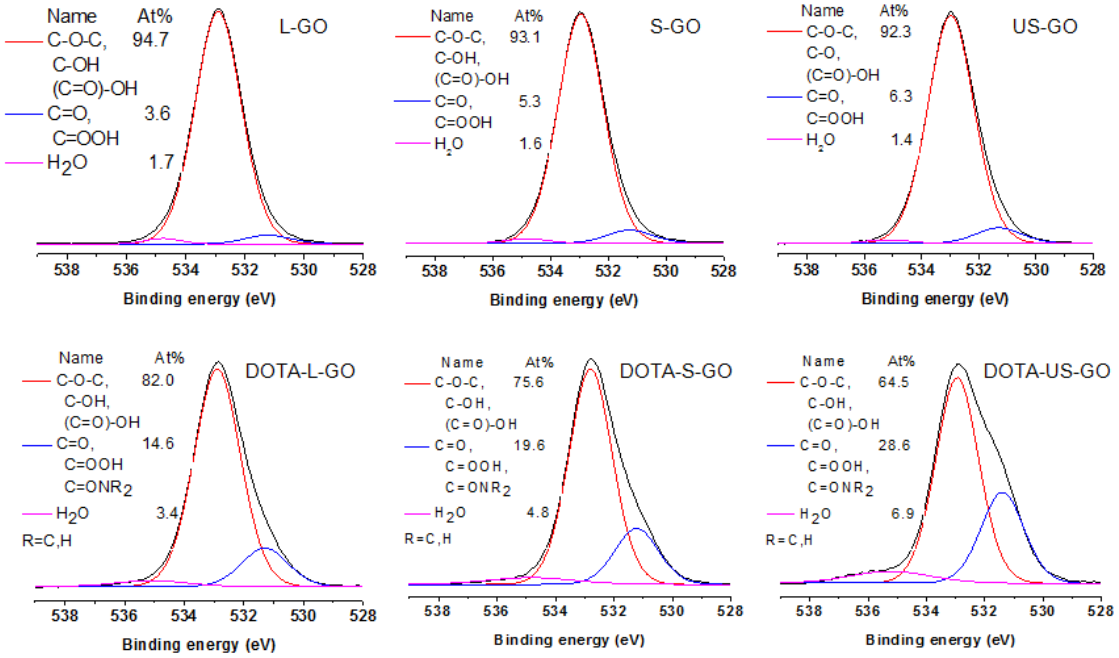

Figure 2.27 XPS high resolution O (1s) spectra of starting materials and DOTA-functionalized derivatives.

2.3.4.1 Biodistribution study of DOTA-GO

Once the functionalization of GO has been proven, these samples were shipped back to Manchester where further characterization and biodistribution studies were performed.

First the efficiency, purity and stability of radiolabeling of GO-DOTA with the radionuclide indium[111] [(^{111}In)GO-DOTA] was verified.

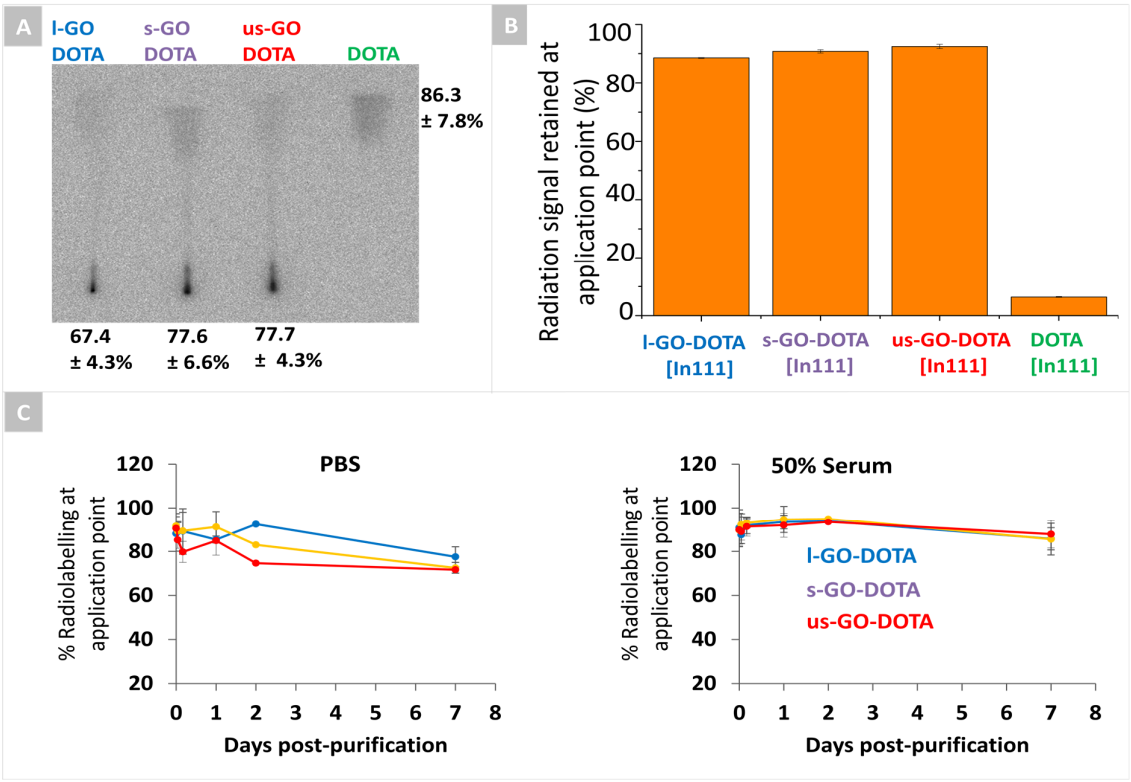

Figure 2.28 Radiolabeling efficiency and stability. A) Efficiency of radiolabeling of the three types of GO (l-GO-DOTA, s-GO-DOTA and us-GO-DOTA) compared to control DOTA. B) Radiolabeling purity of the three samples after centrifugation. C) Stability of radiolabeling in PBS and 50% serum up to 7 days.

The efficiency of radiolabeling of the three types of GO (l-GO-DOTA, s-GO-DOTA and us-GO-DOTA) was compared to control (^{111}In)DOTA as shown in Figure 2.28A. The radiolabeling efficiency of the three samples was ~70% at the application point. The samples were centrifuged to remove unbound (^{111}In)DOTA. The purity after centrifugation was ~90% (Figure 2.28B). The three samples were stable and their radiolabeling purity retained in 50% serum, while they had insignificant variability in PBS at 37°C up to 1 week as shown in Figure 2.28C, right and left respectively.

Afterwards, the pharmacokinetics and tissue distribution after intravenous administration into mice were studied. The biodistribution and excretion of (^{111}In)GO-DOTA are shown in Figure 2.29 and 2.30.

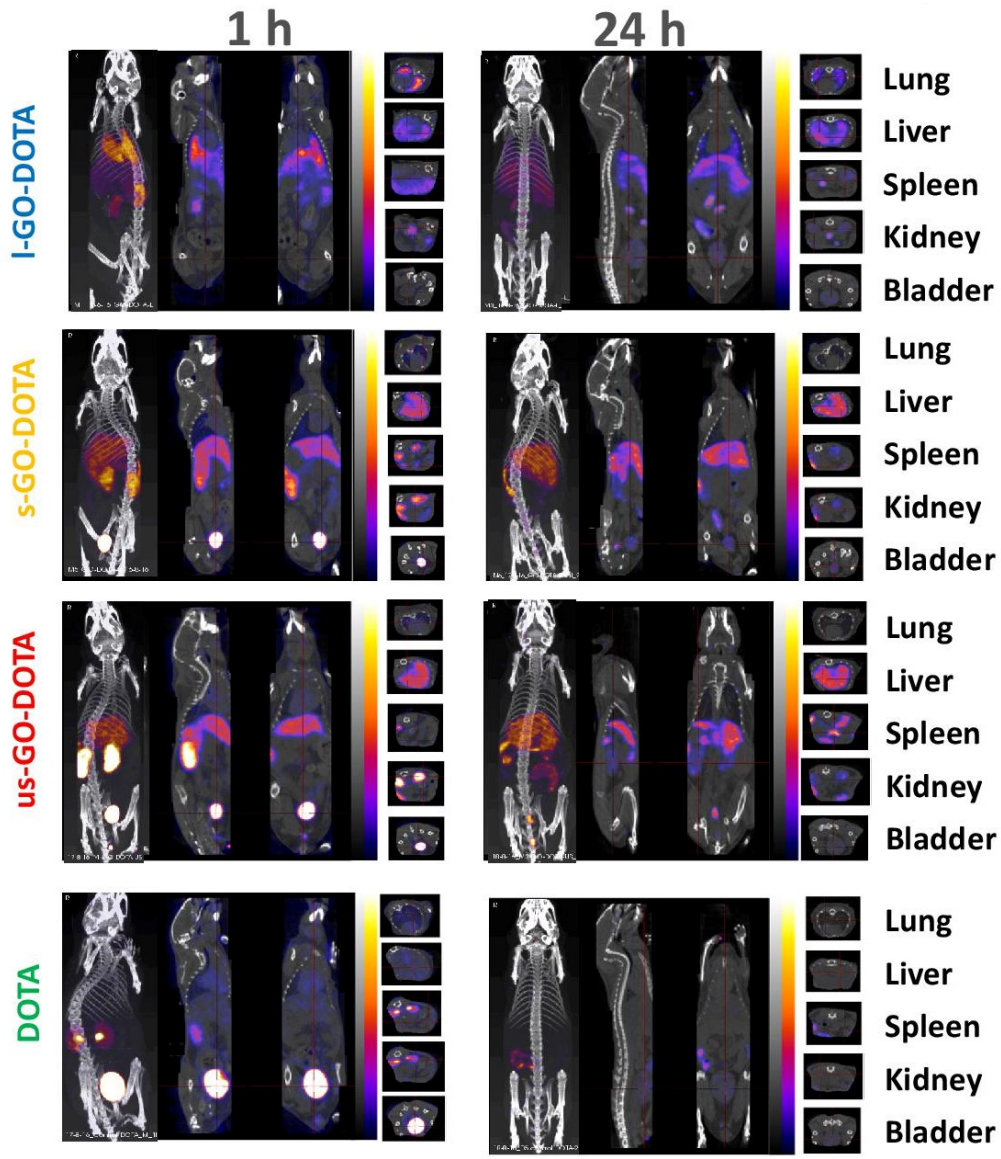

Figure 2.29 Biodistribution of the three types of GO (l-GO-DOTA, s-GO-DOTA and us-GO-DOTA) compared to control DOTA at 1 h and 24 h.

All three materials were removed from blood very rapidly (Figure 2.30A) and there is a clear relation between the lateral size of graphene sheets and the tissue distribution (Figure 2.29). The large material (l-GO-DOTA) accumulated in the lungs early after injection, while the small material (s-GO-DOTA) accumulated in the liver and spleen. All three materials were excreted into the urine at early time points. However, the us-GO-DOTA was excreted to the largest extent among the three samples (Figure 2.30B). l-GO-DOTA was also urinary excreted, which indicated that the larger lateral dimension does not seem to affect its renal elimination. Some faecal excretion was seen as compared to previous studies, perhaps as a result of the short PEG moieties attached to the GO-DOTA (Figure 2.30C).[16] The control sample (DOTA) was totally excreted after 1 h.

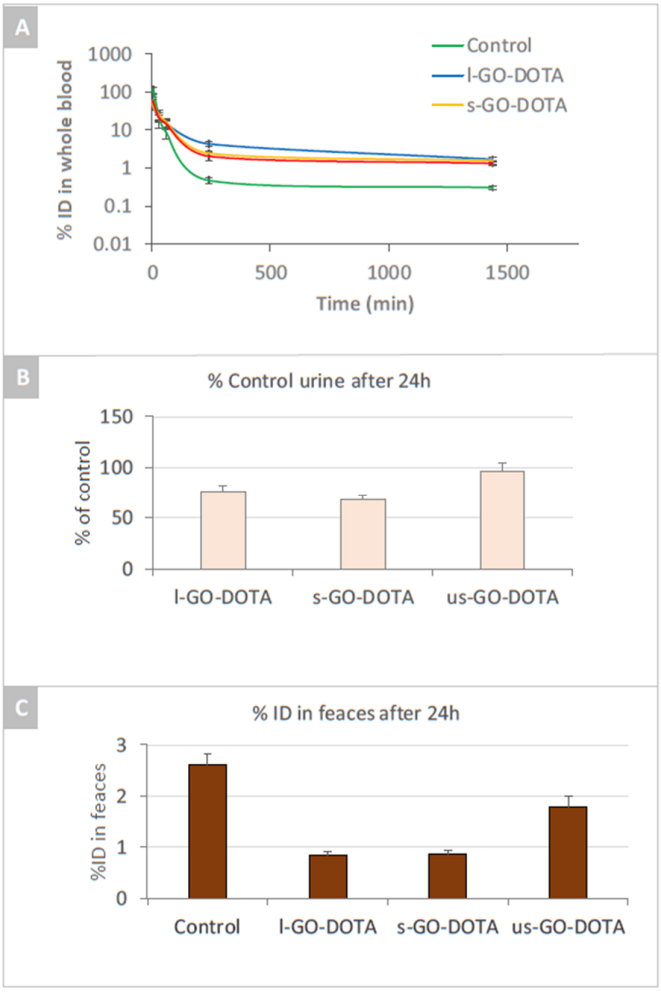

Figure 2.30 Blood and excretion profile. A) Blood profile of the three types of GO (l-GO-DOTA, s-GO-DOTA and us-GO-DOTA) compared to control DOTA. B) Urinary excretion profile and C) faecal excretion of the three materials compared to the control.

2.7 Conclusion

In conclusion for the surface composition study, a majority of epoxides and hydroxyl groups were found on the surface of both GO samples from Antolin and NanoInnova Technologies. This result was confirmed by SS MAS NMR analysis. These groups showed a good reactivity towards functionalization *via* the opening of epoxides, as well as the Williamson and esterification reactions on the hydroxyl groups. The Williamson reaction was performed at room temperature. Most strategies for the derivatization reactions on the hydroxyl groups reported so far are performed under heating. Only a low amount of carboxylic acids was detected on both samples, while the ketone seems to be present even in a lower amount, almost negligible. This could be as well due to the instability of this group on the surface of GO. Between the two differently synthesized GO samples, only minor differences were noticed in the amount of the functional groups. No difference, instead, was noticed in the type of functional groups present.

In most studies reported in the literature, the main strategies for the functionalization of GO is the amidation of the carboxylic groups of GO with amine derivatives.[17–20] However, as mentioned before, multiple reactions can happen at the same time. The epoxides, for example, are highly reactive towards nucleophilic attack reactions, thus it can undergo epoxy ring opening under the conditions used to perform the amidation.[21–32] Unfortunately, many articles in the literature mention the amidation reaction as only

reaction happening on GO in these conditions. With this study, we demonstrated that the main reaction happening, instead, is the opening of epoxides.

In the biodistribution study a relation between organ distribution and lateral size was observed. However, all three materials showed a rapid and high excretion in both urines and faeces (to a much lower extent).

2.8 Bibliography

1. Kaiser E, Colescott RL, Bossinger CD, Cook PI. Color test for detection of free terminal amino groups in the solid-phase synthesis of peptides. Anal Biochem 1970;34(2):595–8.

2. Ménard-Moyon C, Fabbro C, Prato M, Bianco A. One-Pot Triple Functionalization of Carbon Nanotubes. Chem – Eur J 2011;17(11):3222–3227.

3. Vacchi IA, Spinato C, Raya J, Bianco A, Ménard-Moyon C. Chemical reactivity of graphene oxide towards amines elucidated by solid-state NMR. Nanoscale 2016;8(28):13714–21.

4. Barroso-Bujans F, Fernandez-Alonso F, Pomposo JA, Cerveny S, Alegría A, Colmenero J. Macromolecular Structure and Vibrational Dynamics of Confined Poly(ethylene oxide): From Subnanometer 2D-Intercalation into Graphite Oxide to Surface Adsorption onto Graphene Sheets. ACS Macro Lett 2012;1(5):550–4.

5. B.-J. Rossum, H. Förster, H.J.M. de Groot. High-Field and High-Speed CP-MAS13C NMR Heteronuclear Dipolar-Correlation Spectroscopy of Solids with Frequency-Switched Lee–Goldburg Homonuclear Decoupling. J Magn Reson 1997;124(2):516–9.

6. Lerf A, He H, Forster M, Klinowski J. Structure of Graphite Oxide Revisited. J Phys Chem B 1998;102(23):4477–82.

7. He H, Riedl T, Lerf A, Klinowski J. Solid-State NMR Studies of the Structure of Graphite Oxide. J Phys Chem 1996;100(51):19954–8.

8. Cai W, Piner RD, Stadermann FJ, et al. Synthesis and Solid-State NMR Structural Characterization of ^{13}C-Labeled Graphite Oxide. Science 2008;321(5897):1815–7.

9. Dimiev AM, Alemany LB, Tour JM. Graphene Oxide. Origin of Acidity, Its Instability in Water, and a New Dynamic Structural Model. ACS Nano 2013;7(1):576–88.

10. Gao W, Alemany LB, Ci L, Ajayan PM. New insights into the structure and reduction of graphite oxide. Nat Chem 2009;1(5):403–8.

11. Parrish JP, Sudaresan B, Jung KW. Improved Cs2Co3 Promoted O-Alkylation of Phenols. Synth Commun 1999;29(24):4423–31.

12. Eigler S, Dotzer C, Hirsch A, Enzelberger M, Müller P. Formation and Decomposition of CO2 Intercalated Graphene Oxide. Chem Mater 2012;24(7):1276–82.

13. Klímová K, Pumera M, Luxa J, et al. Graphene Oxide Sorption Capacity toward Elements over the Whole Periodic Table: A Comparative Study. J Phys Chem C 2016;120(42):24203–12.

14. Barge A, Cravotto G, Gianolio E, Fedeli F. How to determine free Gd and free ligand in solution of Gd chelates. A technical note. Contrast Media Mol Imaging 2006;1(5):184–8.

15. Kang S-W, Park C-M, Cho K-H, Han H-S. Studies on the Spectrophotometric Determination and Electrochemical Behavior of Heavy Lanthanide Ions in Nonaqueous System and Heavy Metal Chelate Complexes with Bidentate Legands : (Part Ⅰ) Flow Injection Spectrophotometric Determination of Heavy Lant. Bul Korean Chem Soc 1993;14(1):59–62.

16. A. Jasim D, Ménard-Moyon C, Bégin D, Bianco A, Kostarelos K. Tissue distribution and urinary excretion of intravenously administered chemically functionalized graphene oxide sheets. Chem Sci 2015;6(7):3952–64.

17. Wang J, Geng H-Z, Luo Z-J, et al. Preparation, characterization, and chemical-induced hydrophobicity of thermostable amine-modified graphene oxide. RSC Adv 2015;5(127):105393–9.

18. Qin H, Gong T, Cho Y, Lee C, Kim T. A conductive copolymer of graphene oxide/poly(1-(3-aminopropyl)pyrrole) and the adsorption of metal ions. Polym Chem 2014;5(15):4466–73.

19. Wu H, Shi H, Wang Y, et al. Hyaluronic acid conjugated graphene oxide for targeted drug delivery. Carbon 2014;69:379–89.

20. Bao H, Pan Y, Ping Y, et al. Chitosan-Functionalized Graphene Oxide as a Nanocarrier for Drug and Gene Delivery. Small 2011;7(11):1569–78.

21. Eigler S, Hu Y, Ishii Y, Hirsch A. Controlled functionalization of graphene oxide with sodium azide. Nanoscale 2013;5(24):12136–9.

22. Thomas HR, Marsden AJ, Walker M, Wilson NR, Rourke JP. Sulfur-Functionalized Graphene Oxide by Epoxide Ring-Opening. Angew Chem Int Ed 2014;53(29):7613–8.

23. Taniguchi T, Kurihara S, Tateishi H, et al. pH-driven, reversible epoxy ring opening/closing in graphene oxide. Carbon 2015;84:560–6.

24. Xue B, Zhu J, Liu N, Li Y. Facile functionalization of graphene oxide with ethylenediamine as a solid base catalyst for Knoevenagel condensation reaction. Catal Commun 2015;64:105–9.

25. Lee JU, Lee W, Yi JW, et al. Preparation of highly stacked graphene papers via site-selective functionalization of graphene oxide. J Mater Chem A 2013;1(41):12893–9.

26. Ryu SH, Shanmugharaj AM. Influence of long-chain alkylamine-modified graphene oxide on the crystallization, mechanical and electrical properties of isotactic polypropylene nanocomposites. Chem Eng J 2014;244:552–60.

27. Azizi N, Saidi MR. Highly Chemoselective Addition of Amines to Epoxides in Water. Org Lett 2005;7(17):3649–51.

28. Bonollo S, Lanari D, Vaccaro L. Ring-Opening of Epoxides in Water. Eur J Org Chem 2011;2011(14):2587–98.

29. Bourlinos AB, Gournis D, Petridis D, Szabó T, Szeri A, Dékány I. Graphite Oxide: Chemical Reduction to Graphite and Surface Modification with Primary Aliphatic Amines and Amino Acids. Langmuir 2003;19(15):6050–5.

30. Yang H, Shan C, Li F, Han D, Zhang Q, Niu L. Covalent functionalization of polydisperse chemically-converted graphene sheets with amine-terminated ionic liquid. Chem Commun 2009;0(26):3880–2.

31. Wang S, Chia P-J, Chua L-L, et al. Band-like Transport in Surface-Functionalized Highly Solution-Processable Graphene Nanosheets. Adv Mater 2008;20(18):3440–6.

32. Mei Q, Zhang K, Guan G, Liu B, Wang S, Zhang Z. Highly efficient photoluminescent graphene oxide with tunable surface properties. Chem Commun 2010;46(39):7319–21.

CHAPTER 3 : DOUBLE FUNCTIONALIZATION OF GRAPHENE OXIDE

3.1 Introduction

Graphene oxide family materials are highly interesting in the biomedical field because of the surface functionalizability, amphiphilicity, and excellent aqueous processability (*i.e.* GO) and electric and thermal conductivity when they are in their reduced form (*i.e.* rGO).[1,2] The wide surface area and the chemical structure of GO enable several chemical modifications and make it an excellent platform for multifunctionalization. Multifunctionalization can be covalent or non-covalent or a mixture of the two. This strategy allows to combine several molecules, thus several properties, obtaining a multifunctional material. Until now, only few covalent multifunctionalization strategies for GO exist, and mainly exploit the same functional groups on the surface of GO. Wang *et al.* developed a multi-functionalized GO complex by modifying GO after carboxylation with PEI and attaching a PEG chain on PEI and subsequently folic acid on PEG.[3] On this GO complex the authors loaded non-covalently a plasmid-based Stat3 siRNA (small interfering RNA) *via* electrostatic adsorption, thus obtaining a system with an excellent ability to silence *in vitro* Stat3 expression on hepatocellular carcinoma. Stat3 is a signal transducer and activator of transcription 3 and is often regarded as an oncogene. Indeed, a high expression of Stat3 has been found in different cancers.[3] Rezaei *et al.* developed instead a one-pot multifunctionalization procedure for nanographene oxide, using a Ugi four component assembly process.[4] This is a one-step multifunctionalization using oxo-compounds, an amine, cyclohexylisocyanide on the surface of GO, after having increased the amount of carboxylic acids (scheme 3.1).

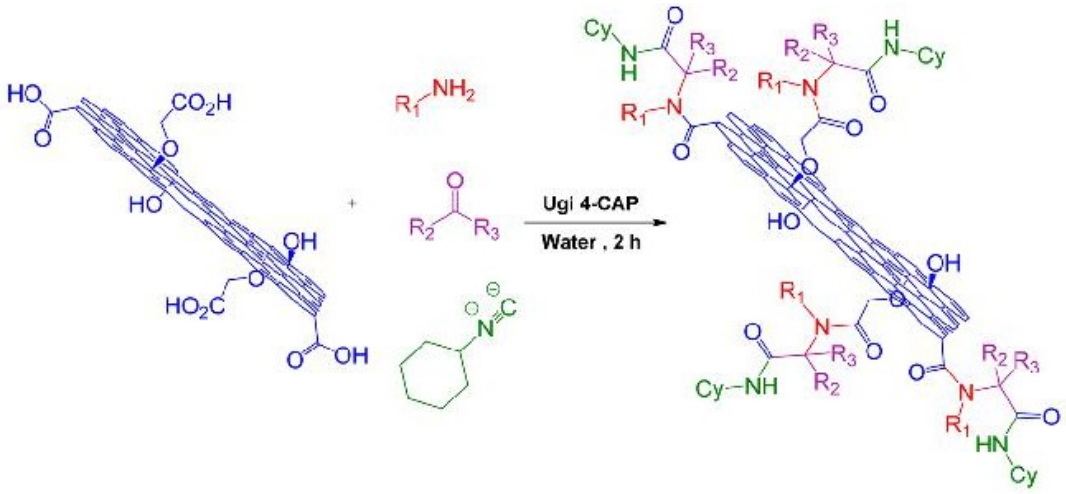

Scheme 3.1 Schematic representation of Ugi four component assembly process on carboxylated-GO surface to generate a multifunctionalized GO. Figure taken from reference 4.

The authors used this protocol to graft an enzyme, the *Bacillus thermocatenulatus lipase*, and a contrast marker. In both examples listed above only one type of functional group on the surface of GO has been used, namely the carboxylic acid group. Just one research group developed a multifunctionalization process targeting two functional groups already present on the surface of GO.[5] Recently, Mei *et al.* synthesized an azide and an alkyne double functionalized GO. The azide acted as nucleophile to open the epoxides, meanwhile the alkyne, present on an alcohol chain, was introduced using the Steglich esterification on the carboxylic acid groups. On this azide/alkyne GO the authors further introduced angiopep-2 and a N_3-PEG_{3500}-N_3 chain, *via* a double Cu(I)-catalyzed Huisgen 1,3-dipolar cycloaddition reaction, to prove the efficacy of this system for drug delivery applications. No other similar examples are reported in the literature.

3.2 Objectives of this chapter

Our objectives were to develop a covalent multifunctionalization strategy targeting two functional groups already present on the surface of GO. We opted for mild conditions to affect the structure of this material as less as possible. Indeed, strong conditions often cause partial reduction of GO, drastically decreasing its water dispersibility. As established with the previous experiments (see Chapter 2), the main functional groups present on the surface of GO are the epoxides and the hydroxyls. For this reason, we decided to target these two groups. We chose to combine the reactions investigated in the previous chapter that showed an elevated functionalization amount. Thus, we combined the opening of epoxides with the Williamson or the esterification reactions on the hydroxyl groups.

Moreover, to improve the dispersibility of GO in physiological conditions we decided to study the polymerization of glycidol on GO. Because of the partial tendency of GO to reaggregate, the stability of this material is sometimes not satisfying enough, in particular for biomedical applications. This can be the case also after functionalization, as functionalization often changes the surface charge of GO, potentially affecting its water dispersibility. In addition, GO, besides having a good dispersibility in water, also needs to be stable in physiological medium. For this reason, it is really important to study and improve the dispersibility of GO for biological applications. We decided to investigate the polymerization of glycidol because this polymer was already proven to be highly biocompatible and water dispersible by the group of Komatsu.[6,7] Moreover, Mu *et al.* recently demonstrated that polyglycidol increases the biocompatibility of GO and that the PG-GO conjugate shows low toxicity *in vitro* and *in vivo*, and good blood compatibility with negligible effects on the hemolysis and blood coagulation.[8]

Once obtained the PG-GO conjugate, the purpose was to develop a multifunctionalization strategy on this system, to obtain a multifunctional highly water stable and biocompatible GO conjugate.

3.3 Result and discussion

For the multifunctionalization study a control reaction was performed for every reaction, to verify the structural changes of GO caused by the multiple processing. The risk of potential side reactions was also considered. Indeed, because of the multiple functionalization, side reactions can easily occur. All the multifunctionalization trials performed directly on GO were done on the GO from NanoInnova Technologies. The multifunctionalization performed on PG-GO was instead done using a GO obtained from Professor Yuta Nishina (University of Okayama, Japan).

Different experiments were done to find the working protocol for the multifunctionalization. Moreover, prior to multifunctionalization, orthogonal protecting groups were studied to control further derivatization on double functionalized GO.

3.3.1 Finding orthogonal protecting groups for graphene oxide

We started to study potential orthogonal protecting groups to mainly use amino terminated chains. We opted for amino-terminated chains for two reasons: to establish the functionalization amount through the Kaiser test, and ii) because this group can be easily further functionalized for biological applications.

After a careful literature research for appropriate amino-protecting groups, we decided to combine a photocleavable protecting group with the Boc.[9–14] Finding the right protecting group and deprotecting conditions without affecting the surface of GO is quite difficult. In fact, all reducing and drastic conditions to remove them should be avoided. Photocleavable groups are an attractive alternative. As photocleavable protecting group we initially opted for a nitro-derivative, namely the 6-nitroverantroyloxycarbonyl group (NVOC).

4,5-Dimethoxy-2-nitrobenzyl chloroformate (NVOC-Cl) was added to 2,2'-(ethylenedioxy)bis(ethylamine) to synthesize **C7**(R=H) (scheme 3.2) (see procedure **C7** in Chapter 6).

Because of the high amount of impurities in the product of the photocleavage of **C7**(R=H), we decided to use the Boc-protected derivative **C7**(R=Boc) to find the best deprotection conditions.

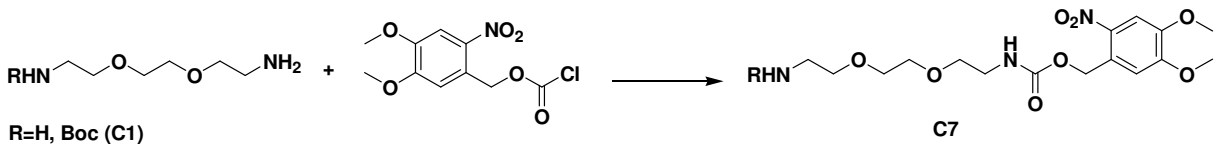

Scheme 3.2 NVOC protection reaction of an amino derivative.

The photocleavage of NVOC occurs at the irradiation wavelength of 365 nm. Thus, we used a 100 W lamp at this wavelength in different reaction conditions to fulfil the photocleavage of **C7**(R=Boc) (scheme 3.3).

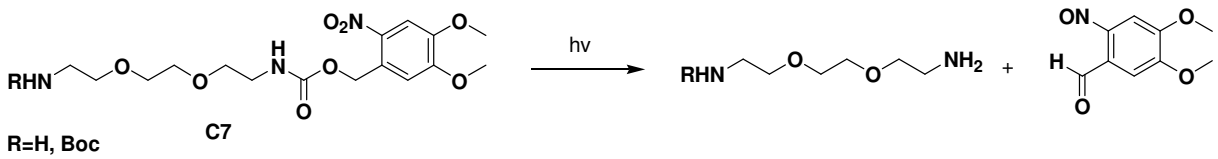

Scheme 3.3 Photocleavage reaction of **C7**.

The photocleavage mechanism of NVOC is based on the photochemically-induced photoisomerization of *o*-nitrobenzyl alcohol derivatives into *o*-nitrosobenzaldehyde (scheme 3.4).[11]

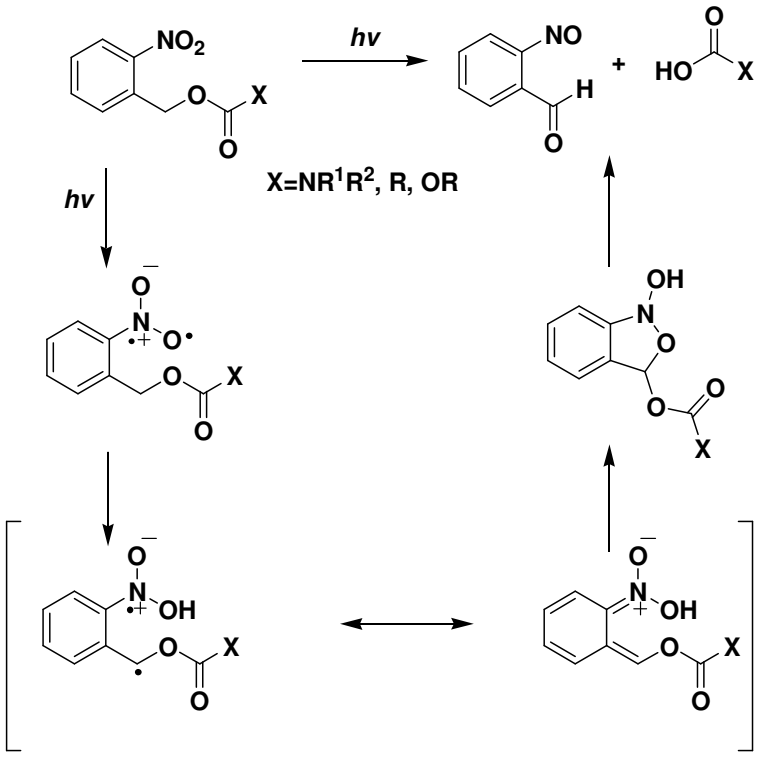

Scheme 3.4 Nitrobenzyl photocleavage mechanism taken from reference 11.

The photocleavage reaction was followed by TLC, HPLC, LC-MS and NMR analysis. I tested different solvents, times, concentrations, nitrobenzyl derivatives, temperatures, irradiation intensities and I also added a radical scavenger to the reaction mixture. I tried different reaction conditions because of the high

number of side products obtained. Nevertheless, despite all these trials, we obtained side products in the product mixture, but I did succeed in limiting their amount.

A critical issue with this deprotection reaction, that is unavoidable, is the formation of imine side products. Indeed, the aldehyde group in the photoproduct can react with the formed amine.[13] The formation of imine side products could be suppressed by adding to the reaction mixture a carbonyl scavenger, such as semicarbazide hydrochloride.[11,12] But semicarbazide can react also with GO, thus it was not the best solution for our study. Therefore, I tried to perform the reaction in relatively low polar solvent systems, such as THF, where the imine by-product formation has lower probability to occur.[13] Still, even using a low polar solvent system, we could detect a high number of side products after irradiation.

Since the occurrence of imine side products can also be blocked using an alkyl or aryl substitution at the benzylic position of the nitrobenzyl derivative we decided to change the NVOC group to another nitrobenzyl derivative. Indeed, the presence of a substituent in the benzylic position leads to the formation of less reactive ketones compared to aldehydes.[13]

A new photocleavable protecting group was synthesized by adding di(*N*-succimidyl)carbonate to 1-(2-nitrophenyl)ethanol (see procedure **C8** in Chapter 6). **C8** was then added to **C1** to obtain the nitrobenzyl protected product **C9** (see procedure **C9** in Chapter 6).

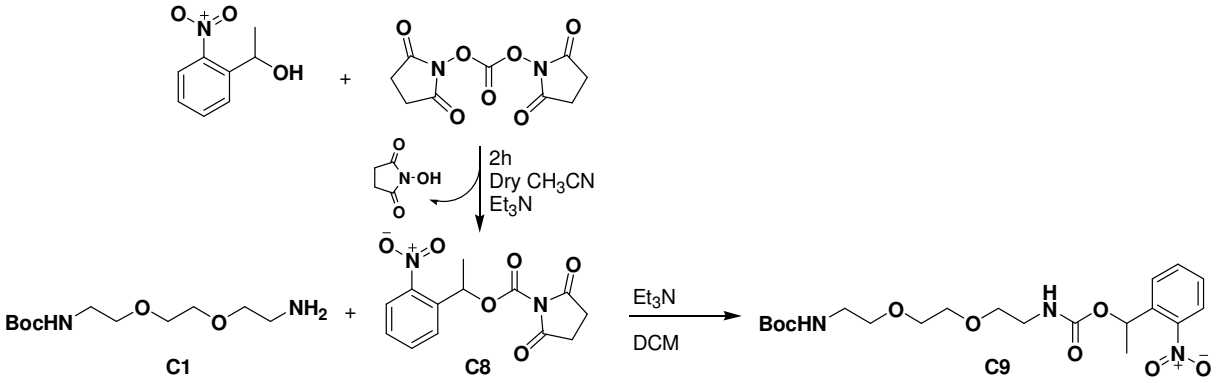

Scheme 3.5 Reaction mechanism to synthesize **C9**.

The photocleavage mechanism is the same as shown in scheme 3.4, with the difference that a ketone nitroso compound is obtained as product of the cleavage (Scheme 3.6).

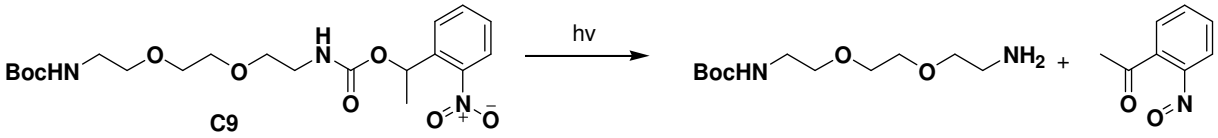

Scheme 3.6 Photocleavage of **C9**.

Even by changing to the nitrobenzyl protecting group, we kept having side products after photodeprotection.

Beside the imines formed, the high number of side products is also due to the fact that the products released after UV-induced photodeprotection can undergo multiple photoreactions including photorearrangements.[15] The uncaging rate and stability of the 2-nitrosophenyl derivative formed is strongly influenced by the type of substituent group at the α-position of 2-nitrobenzyl ester.[15] The number of photoinduced side reactions depends also on the irradiation intensity. Thus, the irradiation intensity was optimized.[16,17] Since the irradiance decreases with the square of the distance, I simply performed the photocleavage at different distances from the lamp. The best distance was 16 cm from the lamp. Moreover, due to the heating caused by the irradiation, the photocleavage was performed in an ice bath to

avoid the reduction of GO. Different solvents were tested: MeOH, MeOH/water mixture, dry THF, DCM and $CHCl_3$. Chloroform was found to be the most suitable one for photocleavage.[17]

The most reactive side products are the radical species. The photolysis of nitrobenzyl-caged compounds forms radical and anion radical species as intermediates.[14] Because of the elevated reactivity of radicals, these species could undergo uncontrollable reactions with the surface of GO.

To verify the presence of radical side products we repeated the best conditions with the addition of a radical scavenger, triisopropyl silane. No differences could be noticed in the final product mixture, suggesting a negligible number of radical products that could react with GO.

All the conditions that has been tried to optimize the photocleavage of the nitrobenzyl derivative are listed in table 3.1. The details of the final photocleavage protocol are reported in Chapter 6 (**C9-PD**).

Table 3.1 Different photocleavage conditions tried (TIS=triisopropylsilane)

Molecule	Solvent	Conc. (mM)	Lamp distance (cm)	Radical scavenger	Reaction time	Temperature
C7 (R=H)	MeOH	16	-	-	7h	RT
C7 (R=H)	MeOH/H_2O	14.3	-	-	10h	Ice bath
C7 (R=Boc)	Dry THF	20	5	-	1h+1h	30' cooling down time between irradiation
C9	Dry THF	16	5	-	2h	Ice bath
C9	Dry THF	10	5	-	4h	Ice bath
C9	Dry THF	7.8	5	-	5h	Ice bath
C9	DCM	7.8	5	-	3h	Ice bath
C9	$CHCl_3$	8.9	25-27 cm	-	3h	Ice bath
C9	$CHCl_3$	8.9	15	-	3h	Ice bath
C9	$CHCl_3$	8.9	15	-	4h30'	Ice bath
C9	$CHCl_3$	8.9	15	-	6h	Ice bath
C14	$CHCl_3$	8.9	15	-	7h	Ice bath
C14	$CHCl_3$	8.9	15	-	4h30'	Ice bath
C9	$CHCl_3$	8.9	15	0.02% TIS	4h30'	Ice bath
C14	$CHCl_3$	8.9	15	0.02% TIS	4h30'	Ice bath

Once we found the best conditions for the photocleavage of the nitrobenzyl protected chain, I prepared **C10** for the opening of epoxides on GO (Scheme 3.7) (see procedure **C10** in Chapter 6).

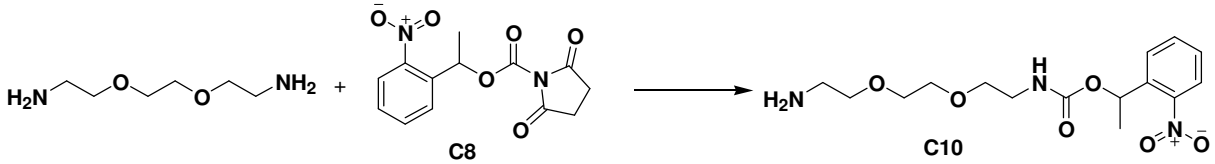

Scheme 3.7 Synthesis of **C10**.

As shown in scheme 3.8, **C10** was then mixed with GO, following the opening of epoxide procedure, obtaining **GO10** (see procedure **GO10** in Chapter 6).

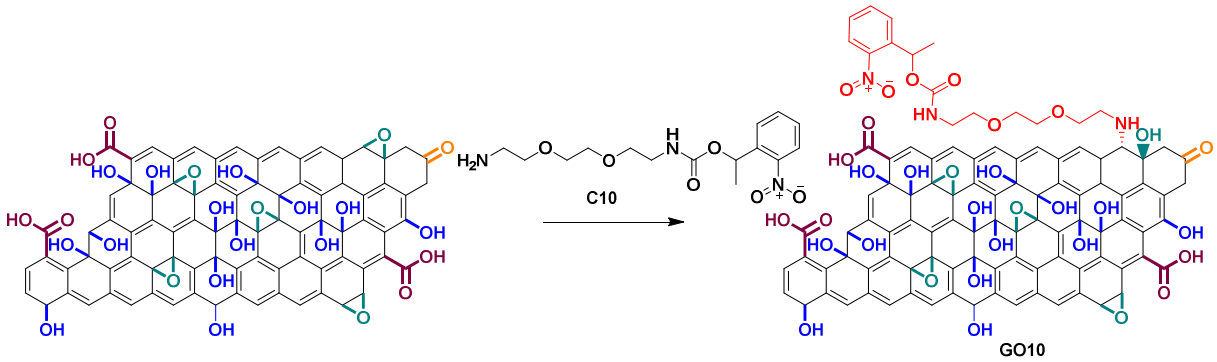

Scheme 3.8 Scheme of the opening of epoxides on GO with **C10** (The reaction is shown only on one functional group for clarity reasons).

After introduction of **C10** onto GO, the photocleavage was tested on **GO10** (scheme 3.9), by irradiation of the sample (365 nm, 100 W) to obtain **GO11** (Chapter 6). Afterwards, the two samples were analyzed by TGA and XPS.

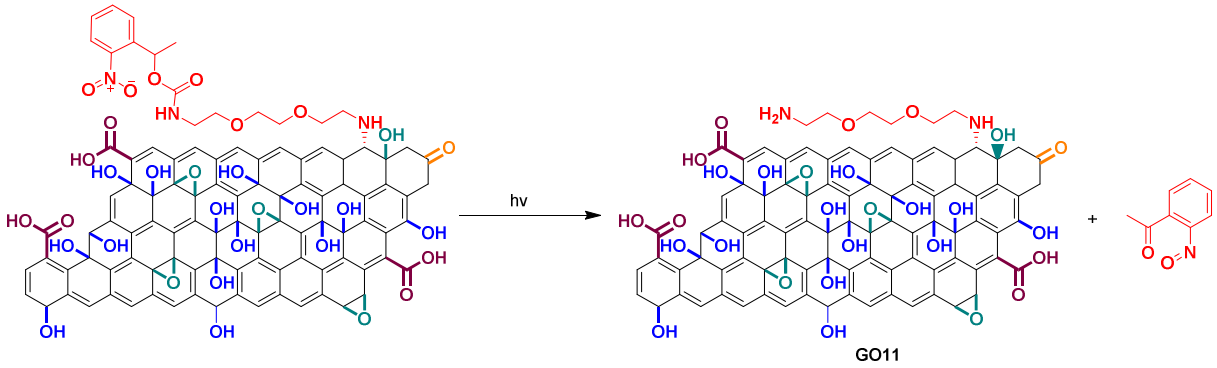

Figure 3.9 Scheme of the photocleavage of **GO10** (The reaction is shown only on one functional group for clarity reasons).

The thermogravimetric curve of **GO10** shows a similar weight loss to its control reaction **GO2_CONT**, as already observed before in Chapter 2, because of the low molecular weight of the molecule introduced (Figure 3.1). If we observe the shape of the curves, a slight difference can be noted between 250-400°C, that could be assigned to the loss of **C10**. This supports the positive result of the reaction. **GO11**, instead, shows a more important weight loss at low temperatures (below 200°C), probably due to some adsorbed products generated during the photocleavage reaction. Meanwhile, above 250 °C **GO11** shows a higher thermal stability compared to **GO10** that can be assigned to the loss of the photocleavable protecting group. Still, irradiation does not show to significantly affect the surface composition of GO.

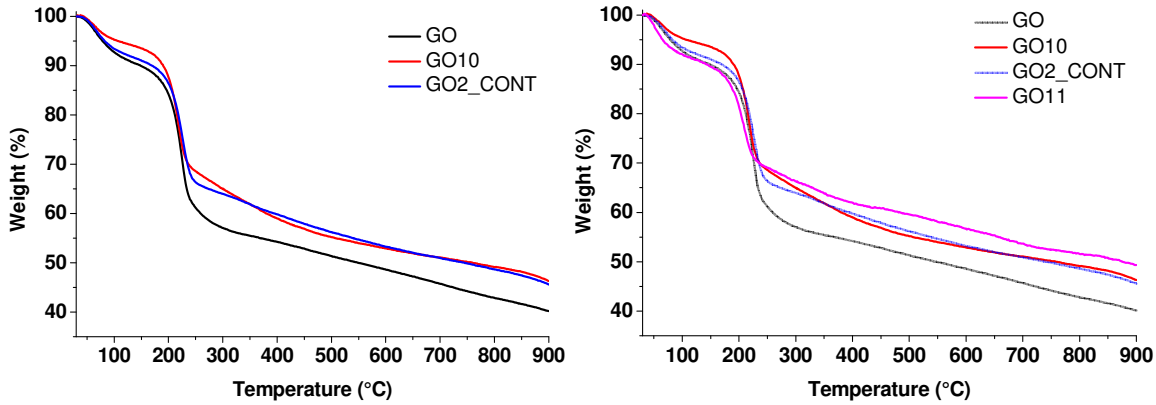

Figure 3.1 TGA of **GO10**, **GO2_CONT** and **GO**.

XPS analysis allowed to measure 2.07% of nitrogen introduced in **GO10** (Figure 3.2). Moreover, in the nitrogen high resolution spectrum, the characteristic peak of the nitro group could be clearly identified at 405.7(±0.2) eV. After deprotection the content of nitrogen detected decreased to 1.72%, due to the loss of the nitrobenzyl protecting group. Beside the decrease of the nitrogen content, the photocleavage was also confirmed by a change in the shape of the nitrogen high resolution spectra. The characteristic peak for the nitro group of the photocleavable protecting group (at 405.7±0.2 eV) disappeared in the spectrum of **GO11**. Oxygen high resolution spectra afforded interesting information too. There is an increase in the carbonyl content and the appearance of the signal of the nitro group in the spectrum of **GO10,** due to the introduction of **C10**. This latter signal has however an elevated margin of error because of its proximity to the C-O signal. **GO11,** instead, seems not to show anymore this nitro peak. The carbon high resolution spectra are instead of more difficult interpretation. A decrease in the intensity of the epoxide peak indicated the positive result of the reaction leading to **GO10**. This signal does not totally disappear because there is also the introduction of ether groups. Meanwhile, no major changes could be observed in **GO11** compared to **GO10**. This is due to the high amount of signals present for GO, that makes the detection of small changes very difficult. However, an important conclusion from the carbon high resolution spectra of **GO10** and **GO11** is that UV irradiation at 365 nm with a lamp of 100 W at 16 cm distance, did not significantly affect the structure of GO.

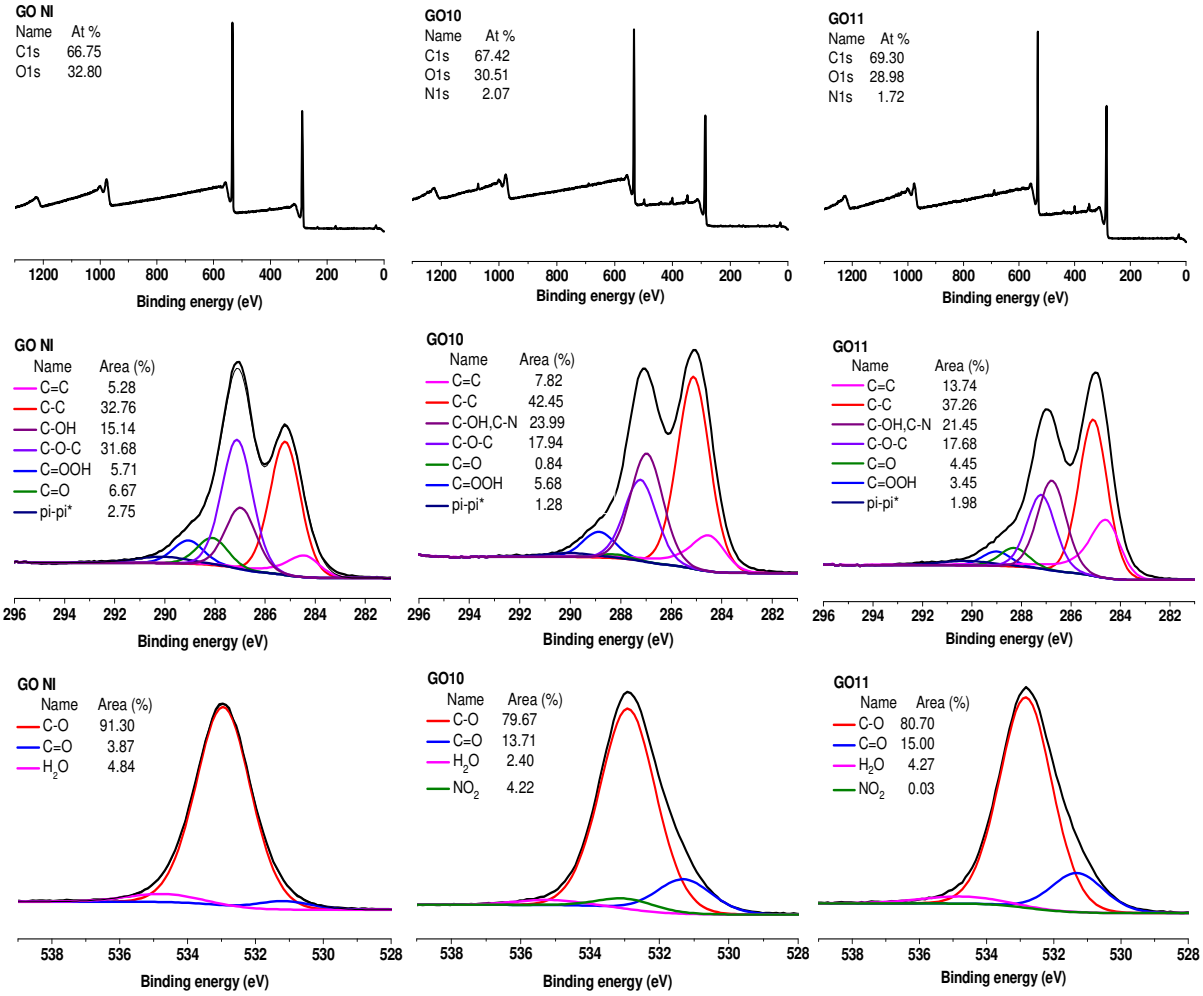

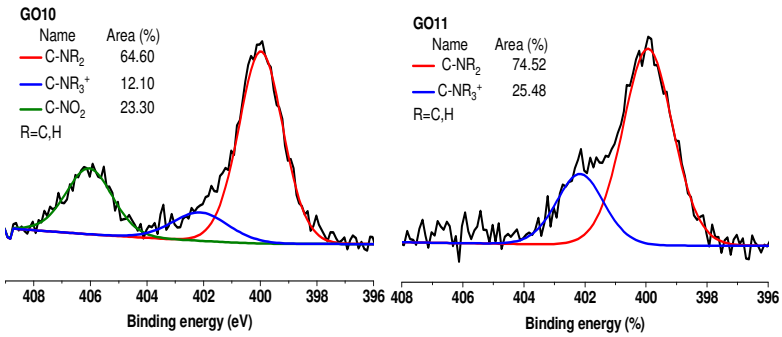

Figure 3.2 XPS survey spectra and C1s, N1s and O1s high resolution spectra of **GO NI**, **GO10** and **GO11**.

The Kaiser test was performed on **GO10** and **GO11**, showing a loading of molecule of 166 µmol/g confirming both the positive result of the opening of epoxide and of the photocleavage.

Table 3.1 Kaiser test value for **GO10** and **GO11**.

	Kaiser test
GO11	166 µmol/g

To verify that no adsorption phenomena nor secondary reactions happened between GO and the product mixture obtained after photocleavage, a control reaction was performed (see **GO11_CONT** protocol in Chapter 6). For this control first **C14** (a Boc and nitrobenzyl protected ethylenediamine) underwent photocleavage, and then the product mixture obtained after irradiation was added to GO. After two hours of stirring the supernatant of the reaction was analyzed by HPLC and compared to the HPLC spectrum taken before the addition of GO. Only negligible variation could be detected, confirming the negligible interactions between GO and the side products of photocleavage.

3.3.2 Combining the opening of epoxides with the Williamson reaction

3.3.2.1 Multifunctionalization with short chains

For the first multifunctionalization approach, the opening of the epoxides was performed followed by the Williamson reaction on the hydroxyl groups. We decided to perform the reactions in this sequence because the number of hydroxyl groups is increased after the opening of epoxide reaction, thus more hydroxyls can be derivatized through the Williamson reaction. The same reaction conditions established in Chapter 2 (see paragraph 2.3.1.1 and 2.3.1.3) were used. The optimization of the photocleavage conditions and this multifunctionalization reaction were performed in parallel, the reason why at the beginning only Boc was used as protecting group for both reactions.

The opening of the epoxides was performed by adding **C1** on GO, obtaining **GO12** (see procedure **GO12** in Chapter 6). After the workup, part of **GO12** was used to perform the subsequent reaction. It was mixed with **C4** and potassium carbonate as a base to obtain **GO13** (see procedure **GO13** in Chapter 6) (Scheme 3.10).

The control reactions were done in the same conditions, only without adding **C1** and **C4** for **GO12_CONT** and **GO13_CONT**, respectively. **GO13_CONT** was performed on part of **GO12_CONT**, while **GO13** was performed on **GO12**.

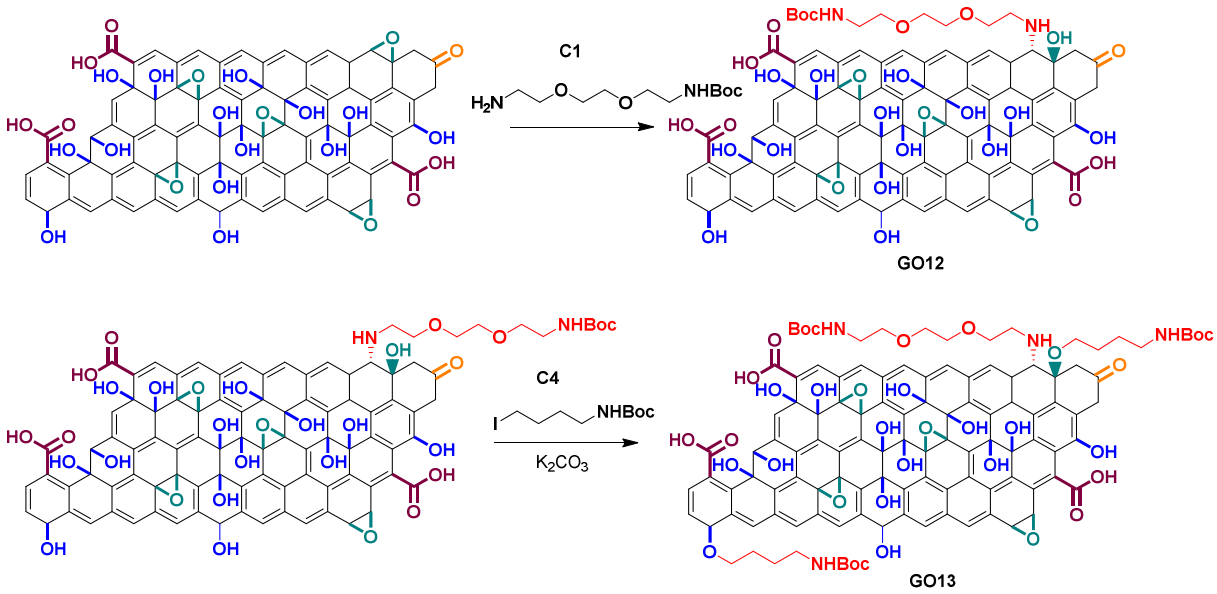

Scheme 3.10 Scheme of the multifunctionalization reactions performed by combining the opening of the epoxides with the Williamson reaction (The reactions are shown only on one functional group for clarity reasons).

The Kaiser test values were calculated for the two samples after Boc deprotection (see **BD** procedure in Chapter 6). The opening of the epoxides showed a loading of 145 µmol/g, the total loading of both reactions, instead, was 175 µmol/g. The outcome for the Williamson reaction is the difference between the two loadings, and was approximately 30 µmol/g. Thus, the combination of these two reactions in the sequence chosen was successful. If we consider that each reaction, if performed alone, gives a Kaiser test loading above 100 µmol/g, then the outcome of the Williamson reaction performed after the opening of epoxides was positive but lower than the one of the same reaction performed on pristine GO.

Table 3.2 Kaiser test values for **GO12** and **GO13**.

Kaiser test	
GO12	145 µmol/g
GO13	175 µmol/g
GO12_CONT	9 µmol/g
GO13_CONT	12 µmol/g

The thermogravimetric analysis was then performed on these samples and on their controls (Figure 3.3). The thermogravimetric curves of the functionalized samples, **GO12** and **GO13**, show a different weight loss compared to their controls in the range of 250-400°C that could be assigned to the covalently introduced molecules. Moreover, **GO13** displays a slightly higher weight loss compared to **GO12**, suggesting that both reaction happened on the surface of GO.

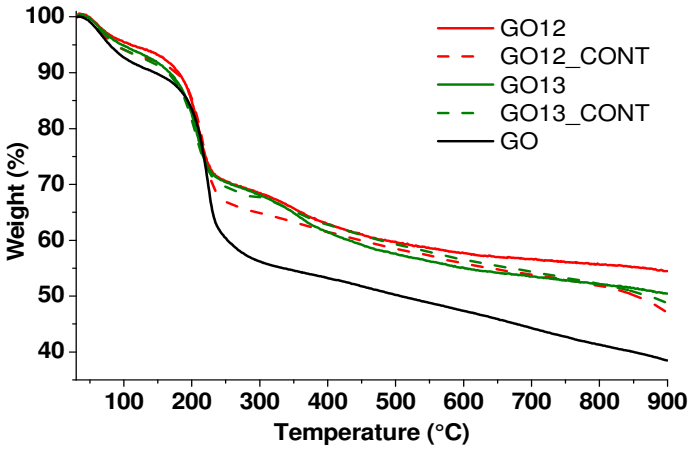

Figure 3.3 TGA curves of GO**, GO12**, **GO13**, **GO12_CONT** and **GO13_CONT**.

I measured then an introduction of 1.45% and 1.70% of nitrogen by XPS analysis for **GO12** and **GO13**, respectively (Figure 3.4). As for the Kaiser test, there is a significant difference, even if not high, in nitrogen percentage between the two steps of the multifunctionalization, confirming that both reaction happened. No nitrogen could be identified in **GO12_CONT**, meanwhile in **GO13_CONT** 0.72% was identified. This could suggest a partial adsorption of DMF on the surface of GO, confirmed by the binding energy of the peak identified in the nitrogen high resolution spectrum and by the augmentation of the carbonyl peak in the oxygen high resolution spectrum of **GO13_CONT** compared to **GO12_CONT**. No increase of the carbonyl peak could be observed for **GO13**, suggesting that this surface adsorption is limited to the control reaction. In the oxygen high resolution spectrum of **GO12** an augmentation of the carbonyl peak could be identified due to the Boc protecting group present in **C1** molecules. Meanwhile, only little difference was observed in the oxygen high resolution spectrum of **GO13** if compared with that of **GO12**, suggesting both no adsorption of DMF and low introduction of **C4**. The carbon high resolution spectrum of **GO12** shows a lower number of epoxides compared to the control reaction **GO12_CONT**, in line with the fact that we opened the epoxide groups. No differences were seen in the carbon high resolution spectrum of **GO13**. But, this could also be due to the proximity of the C-OH and C-O-C signal that cause a non-negligible margin of error in the interpretation of these two peaks. To limit this error, the peaks were kept at a fixed binding energy. No important differences were detected also between **GO12_CONT** and **GO13_CONT**, proving that the reaction conditions did not affect the surface of GO.

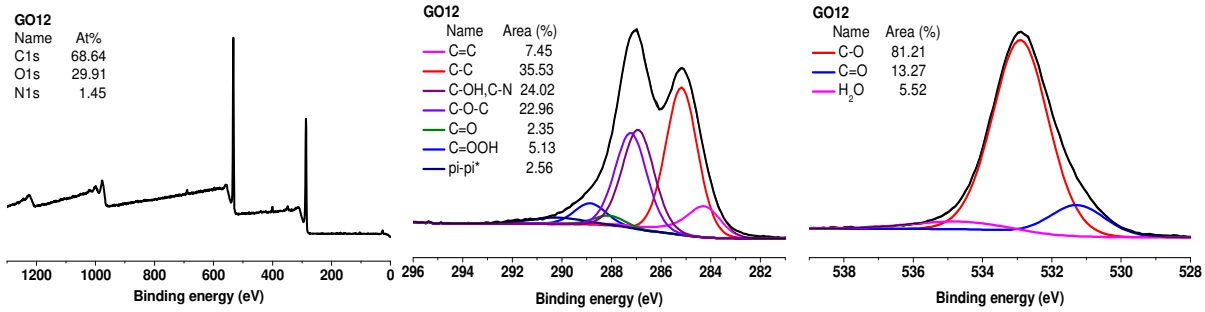

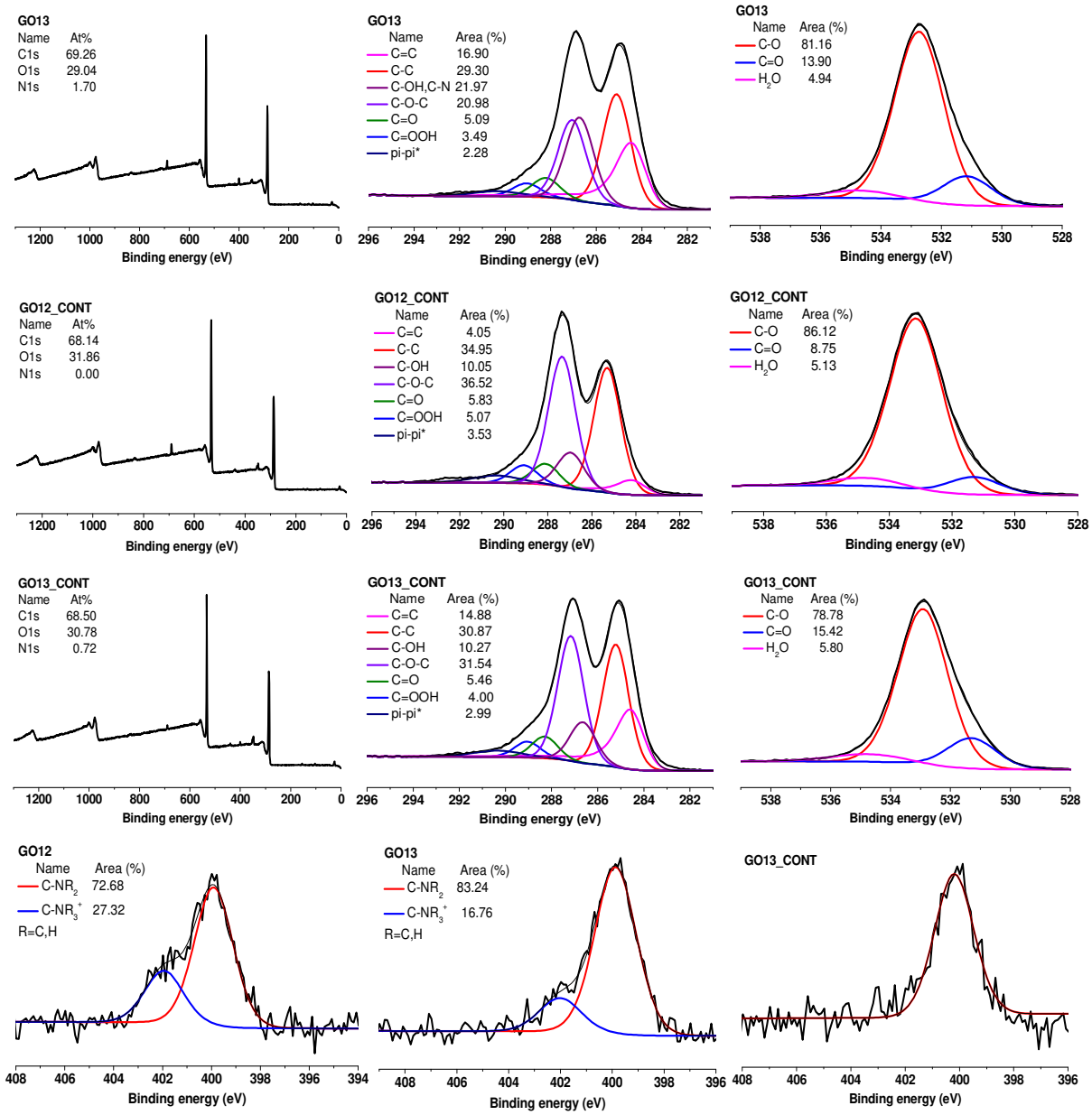

Figure 3.4 XPS survey and C1s and O1s high resolution spectra of **GO12**, **GO13**, **GO12_CONT** and **GO13_CONT**; and N1s high resolution spectra of **GO12**, **GO13** and **GO13_CONT.**

In the nitrogen high resolution spectra of **GO12** and **GO13**, two peaks were identified: one corresponding to the amino and amide peak (399.4±0.8 eV and 399.7±0.3 eV, respectively) and one for the ammonium peak (401.6±0.6 eV), typical signals for **C1** or **C4**.[18] Thus, *via* XPS analysis it was possible to confirm the good result of the first reaction, the opening of epoxides, and a positive result of the second reaction, **GO13**, even if the loading of **C4** is low. Again, by XPS, the presence of **C4** could not be confirmed without any doubt.

In conclusion, it was possible to confirm the positive result of the first step of the multifunctionalization strategy; instead, the second one gave less satisfying results. Looking at the results obtained, it seems that some phenomena prevented reaching a high loading for the second reaction leading to **GO13**. A possible explanation could be the loss of hydroxyl groups from the surface of GO during the processing of this material. To understand better what happened, we decided to repeat this multifunctionalization with

longer ethylene oxide chains, to have more evident weight changes between the different steps in the characterization by TGA.

3.3.2.2 Multifunctionalization with long chains

Due to the difficulty to confirm the second step of the multifunctionalization to form **GO13**, we chose to repeat this protocol with heavy PEG chains that would be easily detectable by TGA. To make the XPS detection even easier an azide derivative was then chosen for the Williamson reaction, because it can be immediately detected in the nitrogen high resolution spectrum. In addition, this group has an elevated potential because it can be further functionalized through Cu(I)-catalyzed Huisgen 1,3-dipolar cycloaddition reaction. The opening of epoxides and the Williamson reactions with long chains were first tried independently to test their efficacy. For the opening of epoxides, a commercially available NH_2-PEG_{23}-NHBoc chain (MW=1173 g/mol) was added to the reaction mixture to obtain **GO14** (scheme 3.11) (see protocol **GO14** in Chapter 6).

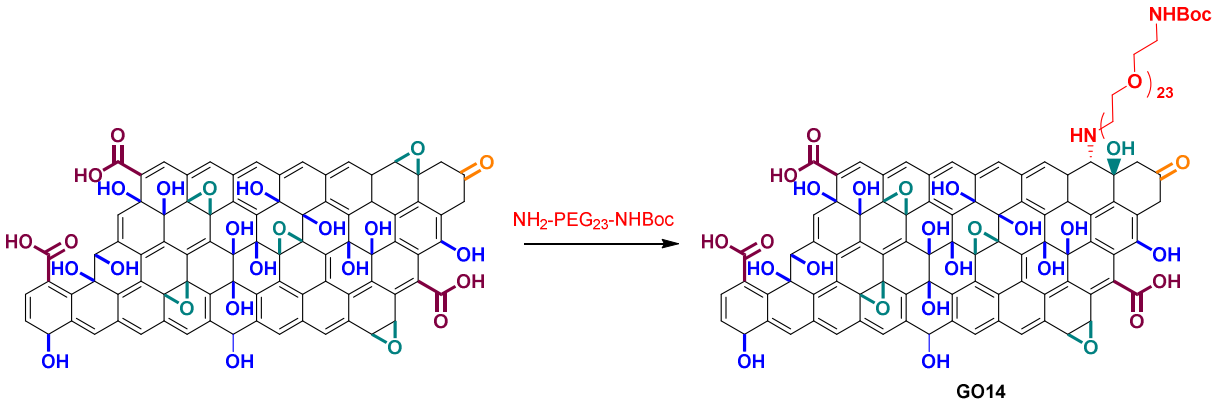

Scheme 3.11 Scheme of the opening of the epoxides with a long PEG chain (The reaction is shown only on one functional group for clarity reasons).

For the Williamson reaction, first **C11** was synthesized, and then this molecule was added to the reaction mixture to obtain **GO15** (see procedure **GO15** in Chapter 6). A tosyl-derivative (MW=1739 g/mol) was chosen for the Williamson reaction, instead of the iodo-derivative because the reaction yield to synthesize the latter is low and the cost of the long PEG chain is high.

As control reactions **GO2_CONT** and **GO6_CONT1**, were planned. These reactions were performed in the same conditions of the reactions only without NH_2-PEG_{36}-NHBoc and **C11,** respectively.

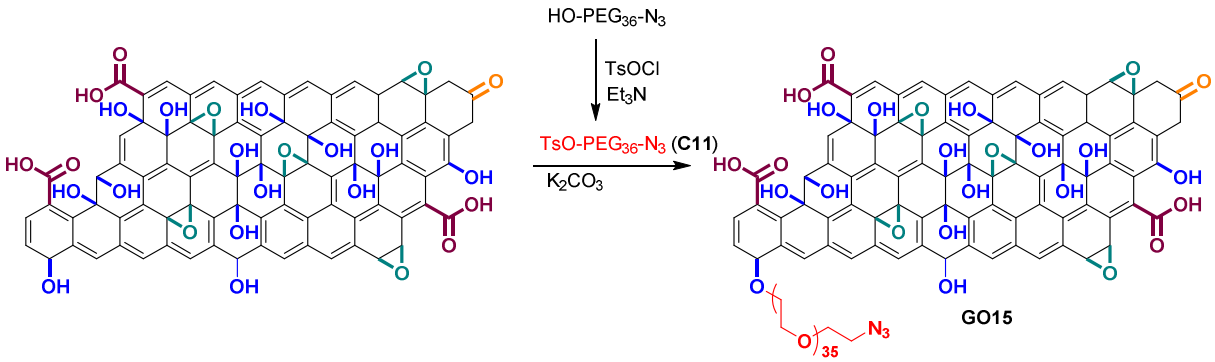

Scheme 3.12 Scheme of the Williamson reaction with a long PEG chain (The reaction is shown only on one functional group for clarity reasons).

The Kaiser test value was calculated after Boc deprotection of **GO14** (see **BD** procedure in Chapter 6), and the result was 16 µmol/g, indicating a negative result of the opening of the epoxides with the long PEG chain (Table 3.3).

Table 3.3 Kaiser test value for **GO14**.

Kaiser test	
GO14	16 µmol/g

To verify this result, a ^{13}C SS MAS NMR analysis was performed (Figure 3.5). By looking at the spectra and the relative peak percentages it was possible to observe a partial decrease in the intensity of the epoxide peak from 30.5% to 14.5% (see paragraph 2.3.1.3 for the spectrum of the starting material), that could suggest the insertion of the PEG chain. However, the peaks of the PEG chain are supposed to appear mainly around 70 ppm, where already the hydroxyl peak of GO is located.[19,20] Thus, it is finally not possible to draw conclusions from the ^{13}C SS MAS NMR. The spectra do not show significant changes, compared to the starting material (see paragraph 2.3.1.3), suggesting a low or negligible introduction of PEG on **GO14**.

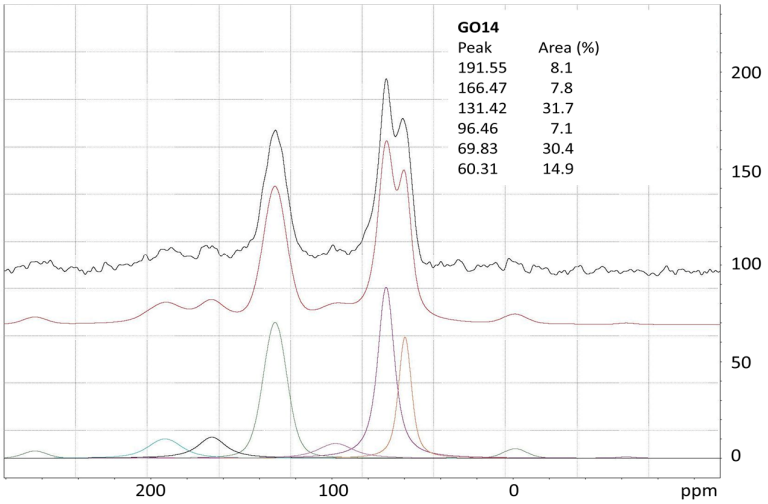

Figure 3.5 ^{13}C SS MAS NMR spectrum of **GO14** with the fitted one below and the single component of deconvolution and relative peaks percentages.

The thermogravimetric curves were taken for both **GO14** and **GO15** (Figure 3.6). **GO14** showed a higher weight loss compared to its control **GO2_CONT**, that could suggest a positive functionalization. Only little differences were identified instead in the shape of the two curves. Thus, it is possible that **GO2-CONT** underwent some modification, such as loss of oxygenated species, whereas **GO14** was not exposed. This would be in line with the SS MAS NMR spectrum and the Kaiser test results. **GO15,** instead, showed a similar thermal stability compared to its control reaction **GO6_CONT1**, with a little difference in the shape of the curve around 250-350 °C. It is not a weight loss difference that we would expect for a high molecular weight PEG. This suggests a low loading of **C11** through the Williamson reaction.

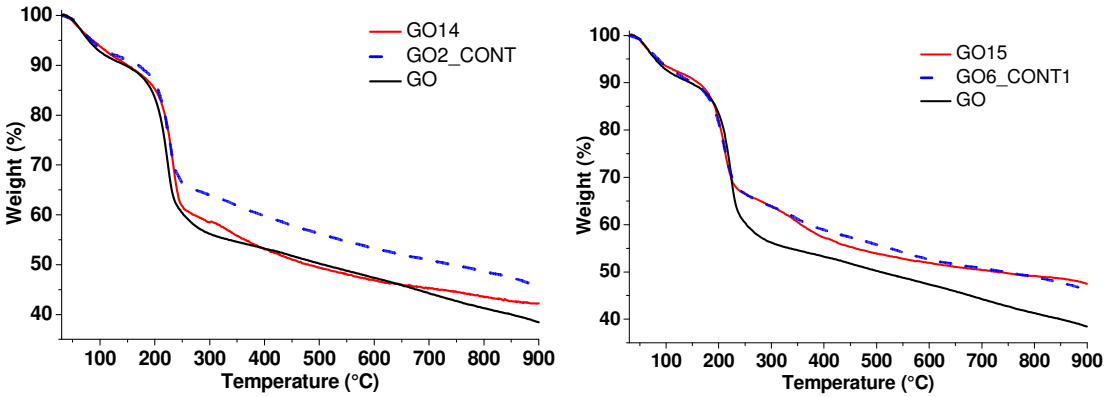

Figure 3.6 TGA curves of GO, **GO14**, **GO15**, **GO2_CONT** and **GO6_CONT1**.

The XPS data, in agreement with the previous characterizations, proved only a small introduction of nitrogen in both **GO14** (0.5%) and **GO15** (0.7 %) (Figure 3.7). These low percentages could be explained by the fact that we introduced a much higher number of carbon and oxygen atoms compared to nitrogen, but it is still not a proof of a positive outcome of the reactions. The carbon high resolution spectrum of **GO14** displayed an important content of C-O-C that could either suggest the negative result of the reaction, or could be due to the numerous ether functions of the few PEG molecules inserted on the surface of GO. For the carbon high resolution spectrum of **GO15** no clear conclusions could be also taken. Indeed, it does not show significant changes that could confirm the occurrence of the reaction. The same remark applies also to the oxygen high resolution spectra of both reactions. This is likely due to the fact that the PEG chains have mainly C-O functions that are already present in an important amount on the surface of GO.

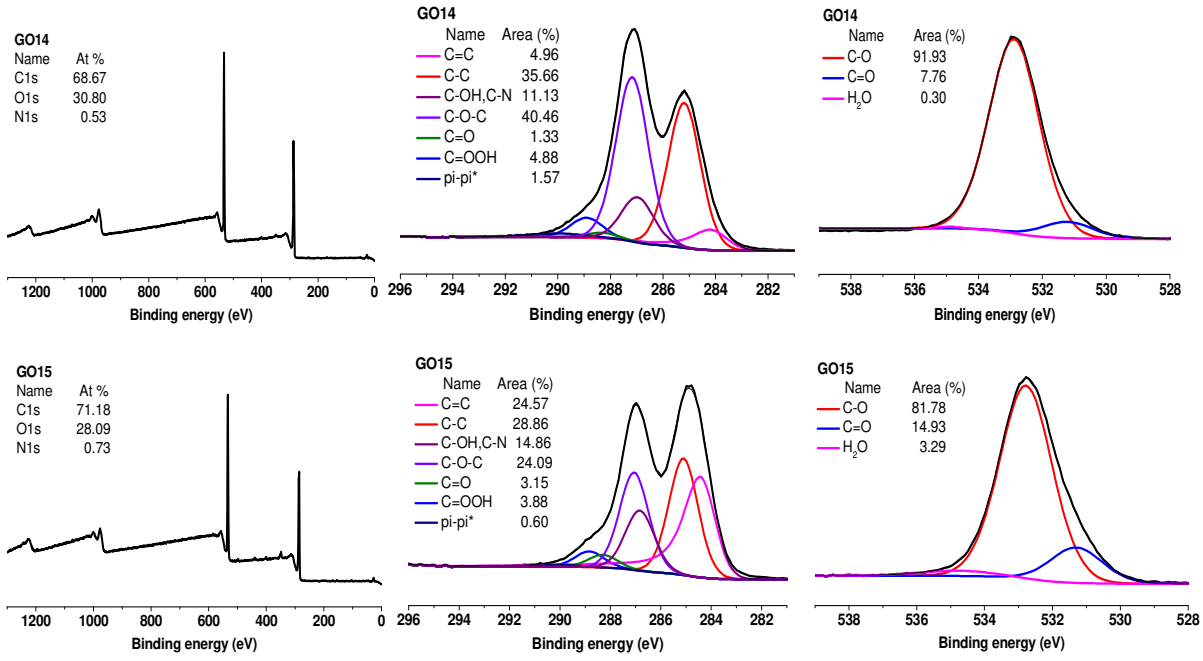

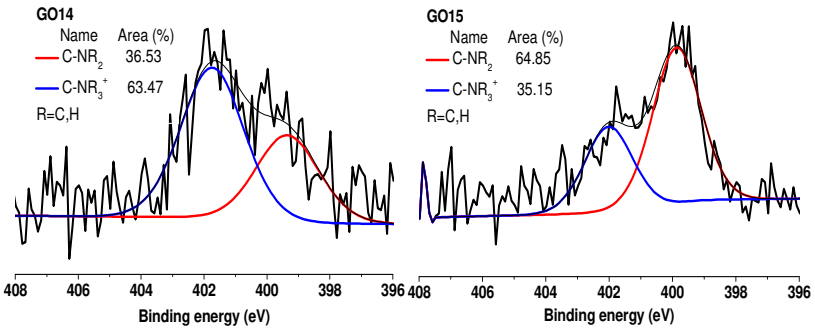

Figure 3.7 XPS survey spectra and C1s, O1s and N1s high resolution spectra of **GO14** and **GO15**.

In the nitrogen high resolution spectrum of **GO15** two characteristic peaks would be expected at 405.4 eV (N=N=N) and 401.8 eV (N=N=N) for the azido group. Only one peak above 400 eV is instead present, suggesting the negative result of the reaction to obtain **GO15**.[21] Thus, by analysing the XPS spectra, no conclusion could be taken for **GO14**, but it seems that the outcome of **GO15** is negative.

The interpretation of the data obtained from the characterization of **GO14** and **GO15** appeared to be more difficult than expected. The overall characterization of both reactions suggests a low or negligible loading of the PEG molecule. It could be due to a structural reason, because of the length of the PEG chain. This factor could bring to a limited accessibility of the amine to the epoxides on the surface of GO.

Considering the results obtained, we abandoned the idea of using long chains and further trials were repeated with short chains.

3.3.2.3 One-pot multifunctionalization

Due to the results obtained in the previous section, it has not been possible to improve the multifunctionalization reactions performed by combining in sequence the opening of the epoxides and the Williamson reaction, and to understand why the second functionalization reaction (Williamson) gave such a low loading. A possible explanation would be the removal of the labile hydroxyl groups from the surface of GO.[22] Indeed, a lower loading for the Williamson and the esterification reaction, if performed after basic treatment of GO in NaOH to open the epoxide groups, has been already observed before (data not shown).If we look at the ^{13}C SS NMR spectrum of NaOH treated GO at 0°C (Figure 3.8), it is possible to observe an overall diminution of the oxygenated functions.

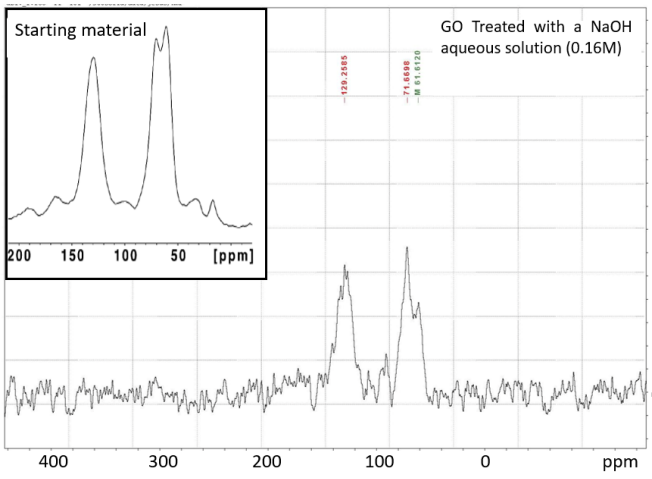

Figure 3.8 ^{13}C SS MAS NMR spectrum of NaOH (0.16 M) treated GO.

By calculating the percentages of the peaks in this semi-quantitative spectrum, 27.5% was detected for C-OH (compared to 30% for the starting material) and 22% for C-O-C (compared to 31% for the starting material). Thus, there is a partial opening of the epoxides by NaOH, confirmed by a decrease in the percentage of the epoxide groups compared to the starting material (see paragraph 2.3.1.3), but also a significant loss of hydroxyl groups. Indeed, the percentage of the hydroxyl groups diminishes instead of increasing. This could suggest an instability of the hydroxyl groups on the surface of GO. Reduction of GO treated in NaOH has been already observed before in the literature, but not if the reaction was performed at low temperatures.[23] A partial reduction was observed in our case, most probably due to an instability of the hydroxyl groups on GO if present in elevated amount.

To verify this hypothesis, we decided to perform the multifunctionalization in one-pot conditions, to limit as much as possible the reaction time and treatments in which elimination of OH groups could happen. Thus, the opening of the epoxides was performed by adding **C10** to GO, and after 24 h of stirring, **C4** with the base were subsequently added to the mixture, thus obtaining **GO16** (Scheme 3.13). **C4** was used in excess compared to the amino-chain, because part of it could undergo side reactions with free **C10** (see procedure **GO16** in Chapter 6). Orthogonal protecting groups were used to allow the control of the derivatization of each of the amine and to enable the calculation of the loading of both chains separately by Kaiser test. A control reaction was done in parallel, leading to **GO16_CONT**, in the same conditions of the one-pot reaction without adding **C10** and **C4**.

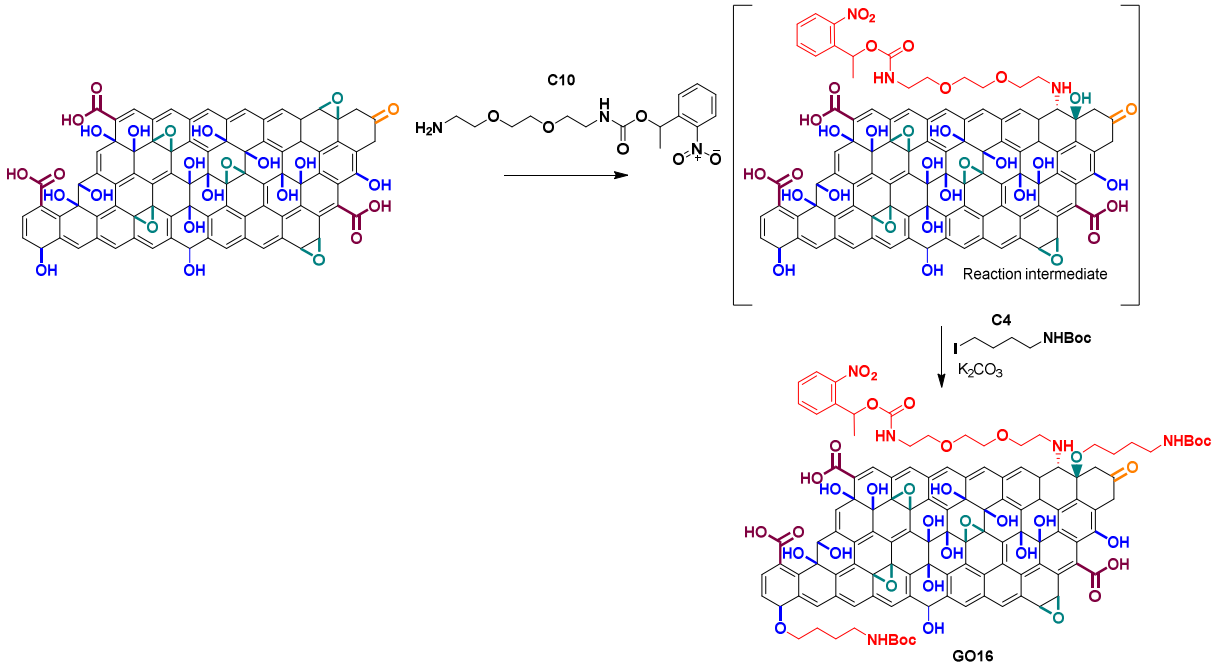

Scheme 3.13 Scheme of one-pot reaction (The reactions are shown only on one functional group for clarity reasons).

Once the reaction was performed, the product was first irradiated at 365 nm in the conditions optimized before to cleave the nitrobenzyl protecting group (see **PD** procedure in Chapter 6) obtaining **GO16(PD)**, and then it was Boc deprotected (see **BD** procedure in Chapter 6) to get **GO16(PD-BD)**.

Table 3.4 Kaiser test value for **GO16** one pot reaction.

Kaiser test	
GO16(PD)	189 µmol/g
GO16(PD-BD)	185 µmol/g

The Kaiser test result for **GO16(PD)** and **GO16(PD-BD)** did not show differences. The reaction in one-pot conditions did not improve the loading of the second reaction, the Williamson reaction. The one-pot reaction was also examined by TGA (Figure 3.9). Since no workup was performed between the two reactions, the TGA was done directly on the final product **GO16**. **GO16** displays a slightly higher weight loss compared to **GO16_CONT**. Moreover, the shape of the curves is different in the range of 200-400 nm, potentially due to the loss of covalently introduced molecules. Thus, TGA confirms the positive functionalization of **GO16**, but it is not possible to establish by TGA, if it is due to the insertion of **C10** or **C4** or both. By analyzing the thermal curve of **GO16(PD)**, it is instead possible to notice that its thermal stability is similar to **GO16**, proving that irradiation did not significantly affect the structure of GO. Meanwhile, at temperatures below 200°C, **GO16(PD)** shows a more important weight loss, probably due to some adsorbed species from the photocleavage on the surface of **GO16(PD)**.

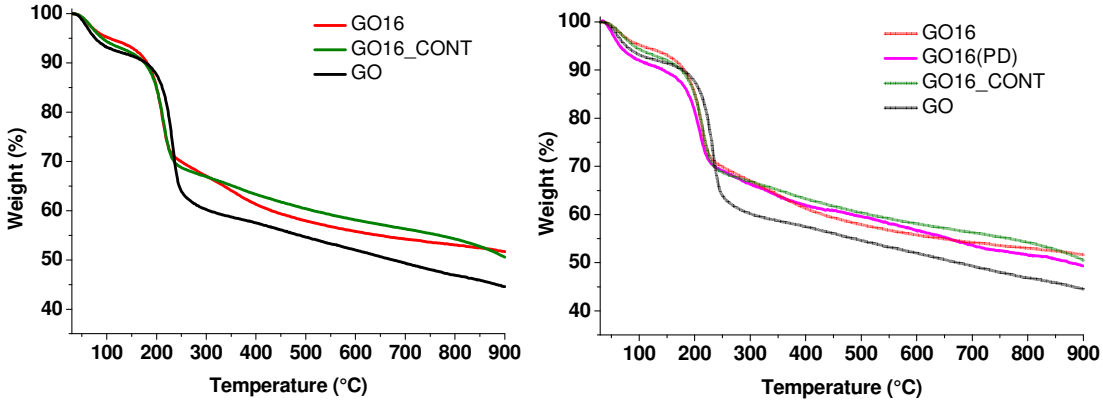

Figure 3.9 TGA curves of GO, **GO16**, **GO16(PD)** and **GO16_CONT**.

XPS spectra were taken for **GO16** and **GO16_CONT** (Figure 3.10). A quantity of 2% of nitrogen was identified in the survey of **GO16**, indicating that functionalization happened. In the nitrogen high resolution spectrum of **GO16**, the nitro group signal at 405.7±0.2 eV was clearly identified confirming the presence of **C10**, the peak instead around 400 eV belongs to both **C10** and **C4**, thus the presence of **C4** could not be completely confirmed.[18] In the oxygen high resolution spectrum the peak of the nitro group could be detected confirming again the presence of **C10**, while no clear information confirming the presence of **C4** could be found. Comparing the carbon high resolution spectrum of **GO16** to that of **GO16_CONT**, there is an important decrease of the C-O-C peak compared to the C-OH, indicating the opening of the epoxides. However, due to the proximity of these two peaks, a certain degree of error should be considered.

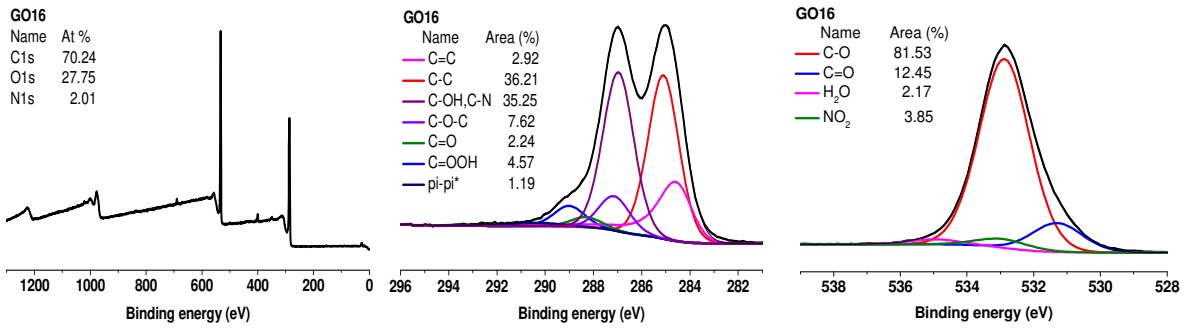

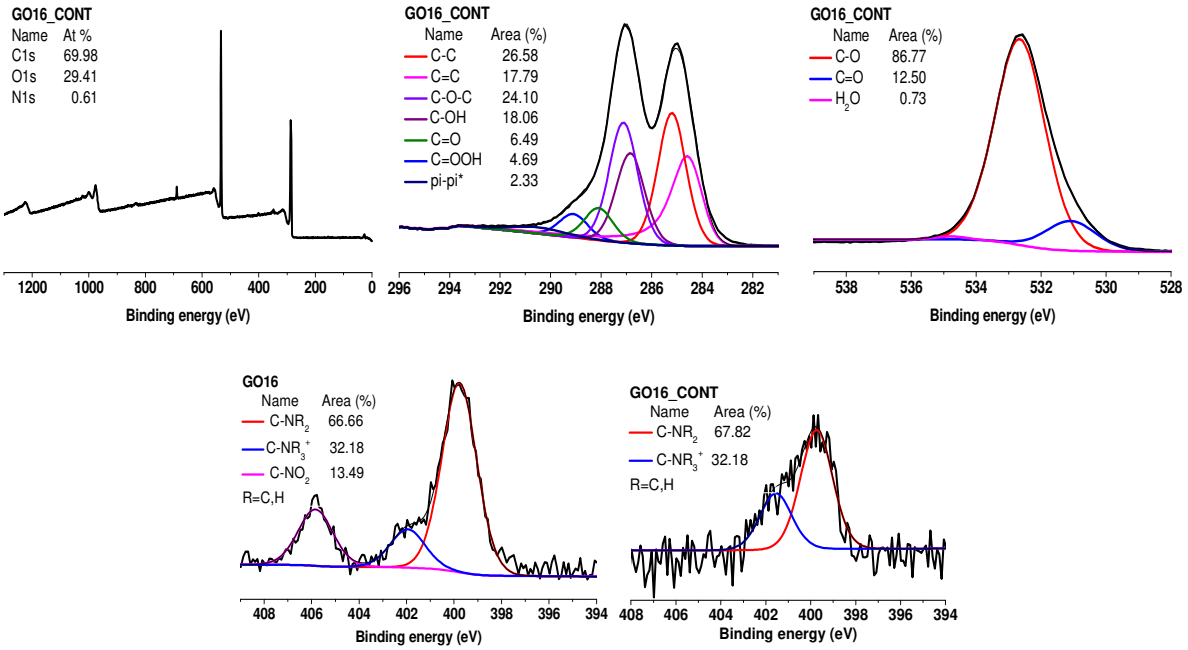

Figure 3.10 XPS survey spectra and C1s, O1s and N1s high resolution spectra of **GO16** and **GO16_CONT**.

Nitrogen was detected in the control reaction, **GO16_CONT**, probably due to the adsorption of DMF. This was also confirmed by the binding energy value of the peak found in the nitrogen high resolution spectrum, and by an increased intensity of the signal of the carbonyl groups in the oxygen high resolution spectrum of **GO16_CONT**.

Thus, via one-pot multifunctionalization it was possible to confirm the positive outcome of the opening of epoxides but not of the Williamson reaction. Thus, we hypothesize that the loss of hydroxyl groups happens during the first step even without any work up or there is another reason that causes a low loading for the second reaction of the double functionalization.

3.3.2.4 Opening of epoxides and Williamson reaction: Inverse approach

Considering the results obtained in the previous experiments, we decided to try another strategy. The impossibility to solve the problem by performing a one-pot reaction suggested us that the hydroxyl groups seem to be released almost immediately from the surface of GO, once the epoxides are open. Thus, we tried to invert the two reactions, by performing first the Williamson reaction and afterwards the opening of the epoxides. To accomplish this multifunctionalization reaction, **C4** was first added to GO in basic condition, to get **GO17**. After the workup, **C1** was added to **GO17** to open the epoxides obtaining **GO18** (Scheme 3.14) (see procedure **GO17** and **GO18** in Chapter 6). A control reaction was done for both reactions, **GO18_CONT** and **GO19_CONT**, without adding **C4** and **C1**.

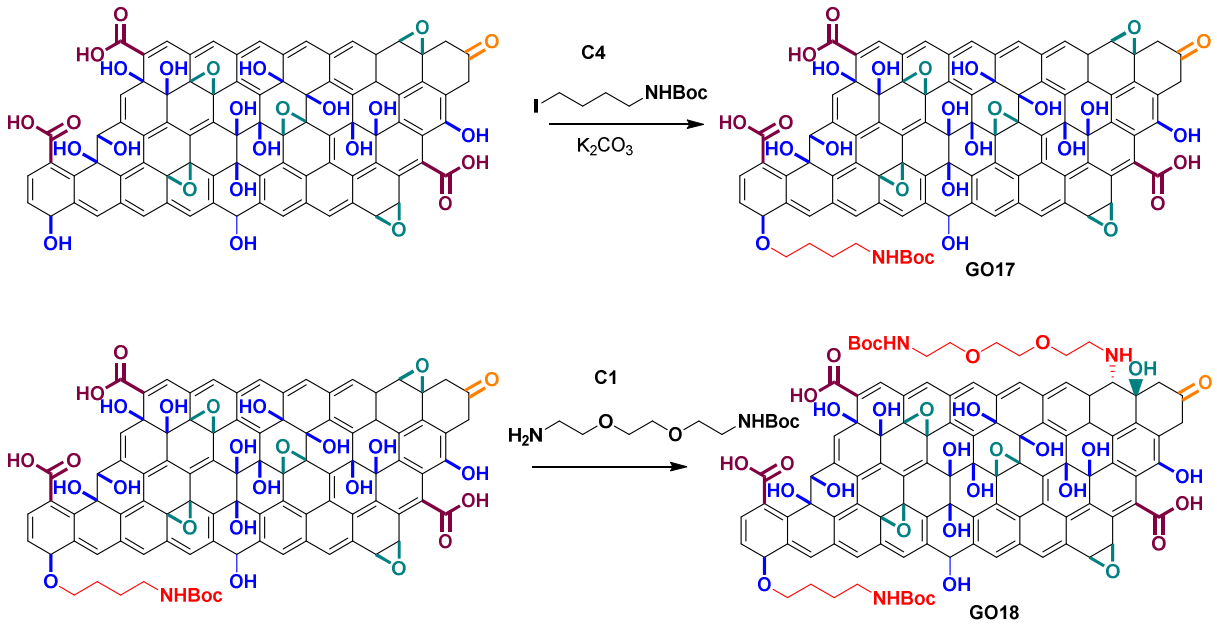

Scheme 3.14 Scheme of the multifunctionalization of GO performed by combining the Williamson reaction with the opening of epoxides (The reactions are shown only on one functional group for clarity reasons).

The loading was calculated using the Kaiser test after Boc deprotection (see **BD** procedure in Chapter 6). **GO17** and **GO18** showed a loading of 106 µmol/g and 145 µmol/g, respectively. Surprisingly, the difference of loading between the two reactions, that gives the loading of the second reaction, was 40 µmol/g, similar to the one between **GO12** and **GO13** (145 µmol/g and 175 µmol/g). Thus, by inverting the reactions we increased the loading of only 10 µmol/g. This suggests that, besides the instability of the hydroxyl group, there must be other phenomena, such as sterical hindrance, that do not allow reaching a higher loading.

Table 3.5 Kaiser test values of **GO17** and **GO18**.

Kaiser test	
GO17	106 µmol/g
GO18	145 µmol/g

The thermogravimetric curves of the two reactions **GO17** and **GO18** do not show significant differences between them and their controls **GO17_CONT** and **GO18_CONT** (Figure 3.11). The curve shape of **GO18** shows a slight difference between 250 and 350°C that could be assigned to the covalently introduced molecules. The fact that it is possible to identify it more easily for **GO18** compared to **GO17** could be due to a little higher number of molecules present on **GO18**. Still, the fact that low molecular weight molecules were used makes the interpretation of the TGA data even more complicated.

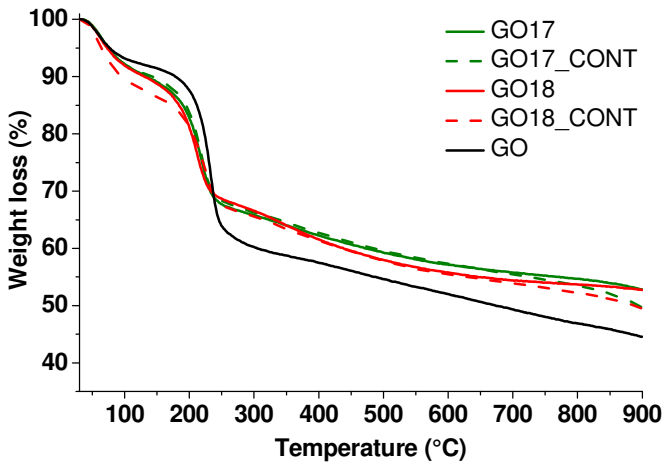

Figure 3.11 TGA curves of GO, **GO17**, **GO18**, **GO17_CONT** and **GO18_CONT**.

The XPS analysis was then performed on these samples (Figure 3.12). For **GO17** and **GO18** 0.96% and 1.57% of nitrogen were measured, respectively. In this case, compared to **GO12** and **GO13,** the difference of nitrogen introduced between the two reactions is more important. For **GO17** compared to **GO17_CONT**, the carbon and oxygen high resolution spectra show a slightly decreased amount of the hydroxyl groups and an increased amount of the carbonyls due to the introduction of **C4**. These results confirm the positive outcome for **GO17**. If we compare the carbon high resolution spectra of **GO17** and **GO18,** there is a decrease of the C-O-C peak indicating the opening of the epoxides and the covalent introduction of **C1**. In the oxygen high resolution spectrum, instead, there is no difference in the carbonyl peak intensity between **GO17** and **GO18**. This could be due to the low amount of **C1** introduced. In the nitrogen high resolution spectra, the respective signals of both **C1** and **C4** could be identified in both **GO17** and **GO18**. Since they show the same peak, no conclusion can be taken from these spectra. Again, a low adsorption of DMF could be observed for both control reactions.

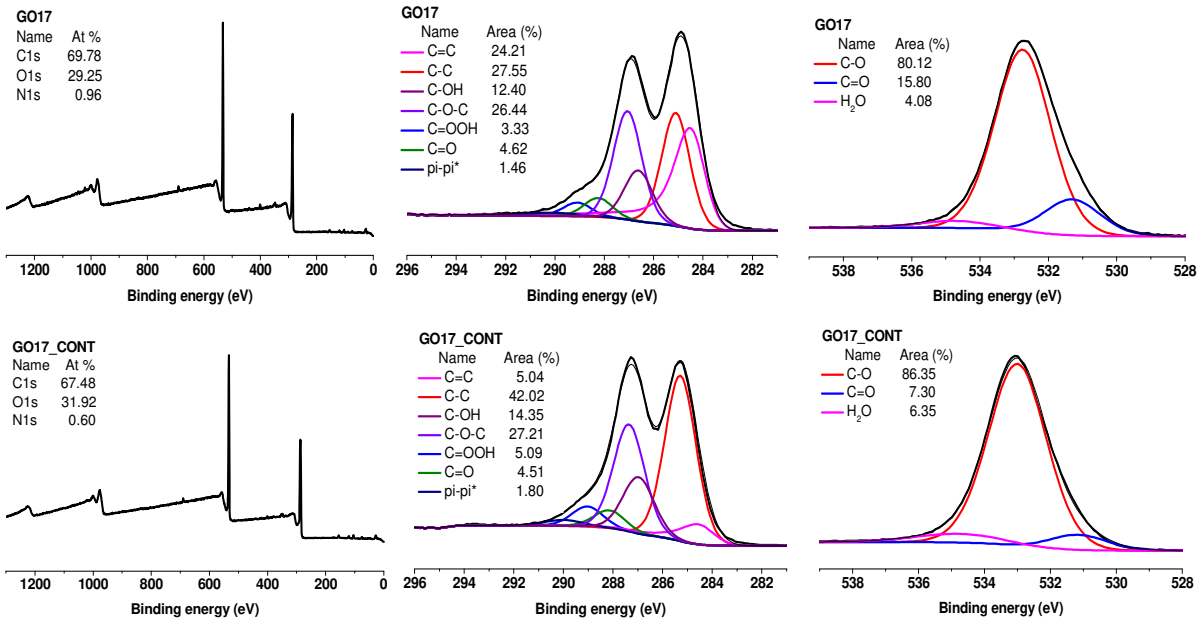

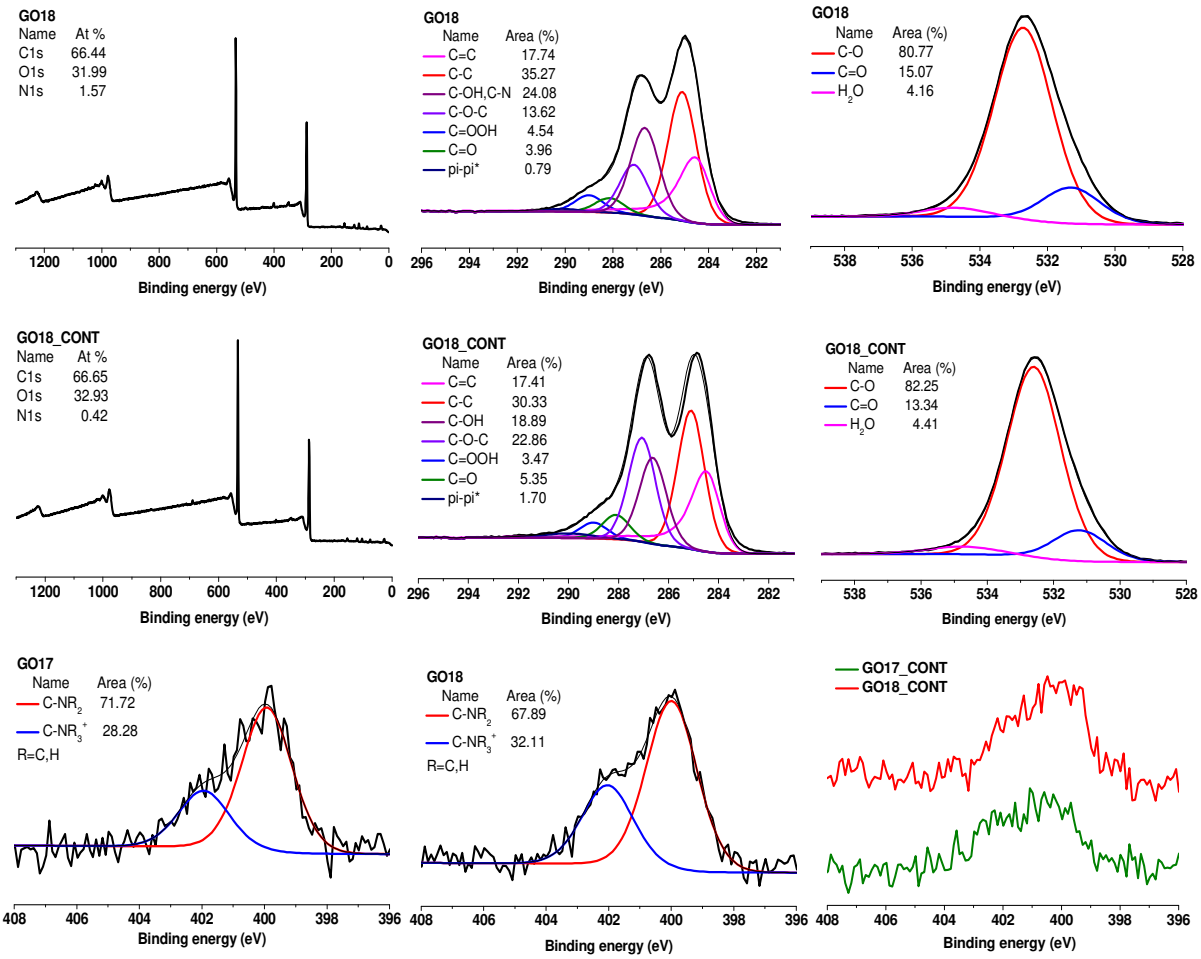

Figure 3.12 XPS spectra and C1s, O1s and N1s high resolution spectra of **GO17**, **GO18**, **GO17_CONT** and **GO18_CONT.**

In conclusion, we had a slightly increased loading for the second reaction compared to the previous multifunctionalization trial. This suggest that besides the instability of the hydroxyl groups there are other phenomena that limit a higher loading of the second reaction, such as sterical hindrance. Another factor that could influence the loading of the second reaction is the dispersibility of the sample. Indeed, GO-NI shows a variable dispersibility in its pristine form, and this dispersibility is often decreased after functionalization. This could also influence the result of the second reaction.

3.3.3 Combining the opening of epoxides with the esterification reaction

Once established that the loss of the hydroxyls could not be the only phenomenon happening on GO, another multifunctionalization experiment was done to understand better the problem. This time the opening of the epoxides was performed followed by the esterification reaction on the hydroxyl groups. To obtain **GO19**, **C1** was added to the reaction mixture with GO (see procedure **GO19** in Chapter 6). After the workup, **GO19** was mixed with **C5** and the coupling agents to get **GO20** (see procedure **GO20** in Chapter 6) (scheme 3.15). The control reactions were also performed. **GO19_CONT** was done without the addition of **C1**. Instead, **GO20_CONT** was done on **GO19_CONT** without the coupling reagents.

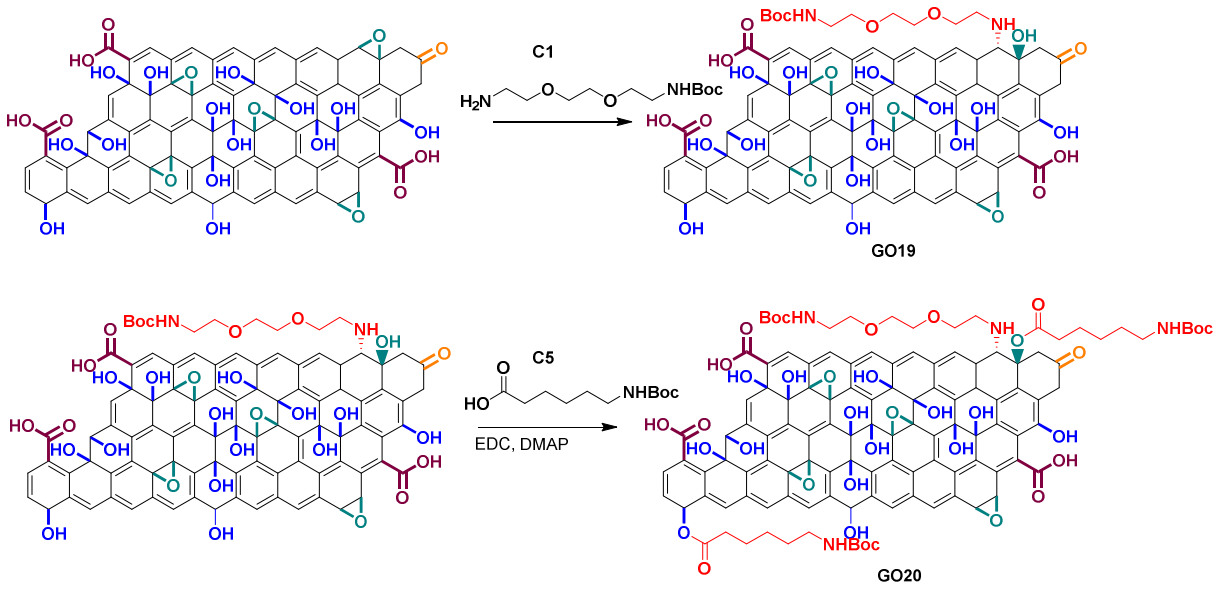

Scheme 3.15 Scheme of the multifunctionalization of GO performed by combining the opening of the epoxides with esterification reaction (Each reaction is shown only on one functional group for clarity reasons).

The loadings were calculated using the Kaiser test after Boc deprotection of **GO19** and **GO20** (see **BD** procedure in Chapter 6), and they were 179 and 231 µmol/g, respectively (Table 3.6). This time the difference of loading between the two reactions is more important than for the previous trials (52 µmol/g of loading for the esterification reaction), suggesting a better result of both reactions. Nevertheless, the second reaction gave a lower loading compared to the esterification reaction performed alone (165 µmol/g). It is possible that some phenomena hinder a higher loading for the second step.

Table 3.6 Kaiser test values for **GO19**, **GO20** and **GO20_CONT**.

Kaiser test	
GO19	179 µmol/g
GO20	231 µmol/g
GO20_CONT	6 µmol/g

In the literature, an island localization of the oxygen bearing functional groups on the surface of GO has been reported.[24] It is possible that, due to this close localization of the functional groups, the second reaction cannot reach higher loadings because of the sterical hindrance caused by the molecules inserted during the first reaction. The Kaiser test value was calculated also for **GO20_CONT**, after Boc deprotection treatment, to verify potential surface adsorption of **C5**. The outcome was negative confirming the absence of **C5** non-covalently adsorbed on the samples.

By TGA it is possible to observe that both **GO19** and **GO20** show a different form of the curves between 200-400°C, if compared to their controls, **GO19_CONT** and **GO20_CONT** (Figure 3.13). This can be assigned to the loss of the covalent molecules and confirms the positive outcome of both reactions. Indeed, **GO20** displays a slightly higher weight loss in this region compared to **GO19**, confirming that the esterification occurred.

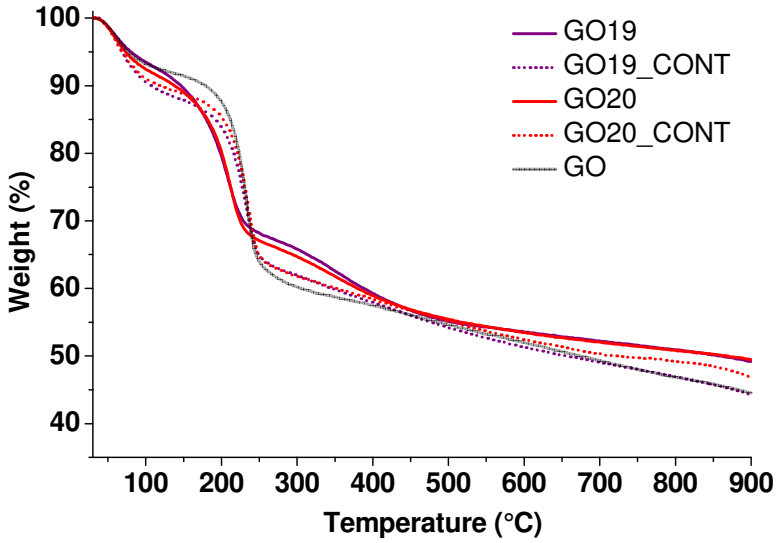

Figure 3.13 TGA of GO, **GO19**, **GO20**, **GO19_CONT** and **GO20_CONT**.

These reactions were analyzed also by XPS (Figure 3.14), and an introduction of 1.96 and 2.47% of nitrogen was detected for **GO19** and **GO20**, respectively. These results confirm again that both reactions occurred on the surface of GO. In the carbon high resolution spectrum of **GO19** it was possible to identify a decrease in the intensity of the epoxide peak compared to its control, **GO19_CONT**, confirming the introduction of **C1**. In the spectrum of **GO20** there is instead an important decrease in the intensity of the hydroxyl peak due to the insertion of **C5**. The intensity of the C-O-C peak is still important due to the presence of the ether bonds of **C1**. However, we should consider the margin of error due to the proximity of the C-OH and C-O-C group. The ratio between the carbon and the oxygen region in the carbon high resolution spectrum changes with a decrease of the C-O area (288-286 eV), because of the conversion of the hydroxyl groups into esters (290-288 eV, O-C=O region) and the introduction of a mostly aliphatic chain (**C5**). This is also confirmed by a slight increase of the COOH/COOR peak in the same spectrum of **GO20**, due to the insertion of **C5**. Similar results could be observed in the oxygen high resolution spectra. Indeed, there is an increase in the percentage of the carbonyl peak between **GO19** and **GO19_CONT**, due to the urethane group of the Boc moiety of **C1**. This amount increases between **GO19** and **GO20** due to the introduction of the ester functions and the Boc group of **C5**. The nitrogen high resolution spectrum displays the typical peaks of **C1** and **C5**, confirming the general positive outcome of the functionalization.

For these experiments I have recorded the C KLL Auger spectra for all samples. The analysis of these peaks gives an idea of the quantity of C sp^3 and C sp^2 atoms present.[25–29] This estimation is obtained by calculating the distance between the maximum and the minimum of the first derivative of the C KLL spectra. As it is possible to observe, there is no important difference in distance for the different reactions. The only sample that displays closer maximum and minimum is **GO20**, indicating a slightly more important content of C sp^3 atoms. This could be related to the C sp^3 atoms introduced with **C1** and **C5**.

A low amount of adsorbed DMF could be observed for the control reactions analyzed by XPS.

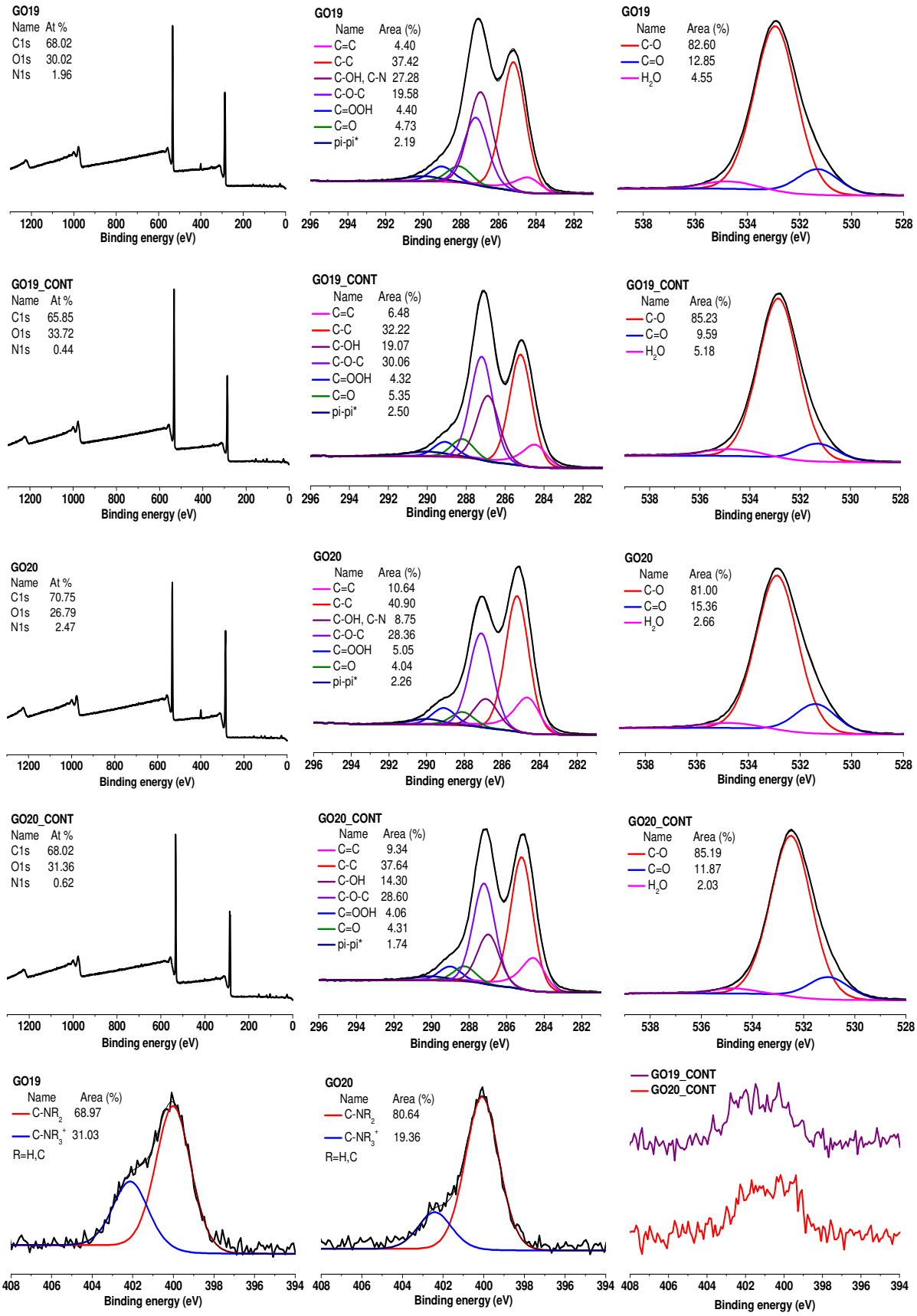
GO19
Name At %
C1s 68.02
O1s 30.02
N1s 1.96
Binding energy (eV)
GO19
Name Area (%)
C=C 4.40
C-C 37.42
C-OH, C-N 27.28
C-O-C 19.58
C=OOH 4.40
C=O 4.73
pi-pi* 2.19
Binding energy (eV)
GO19
Name Area (%)
C-O 82.60
C=O 12.85
H2O 4.55
Binding energy (eV)
GO19_CONT
Name At %
C1s 65.85
O1s 33.72
N1s 0.44
Binding energy (eV)
GO19_CONT
Name Area (%)
C=C 6.48
C-C 32.22
C-OH 19.07
C-O-C 30.06
C=OOH 4.32
C=O 5.35
pi-pi* 2.50
Binding energy (eV)
GO19_CONT
Name Area (%)
C-O 85.23
C=O 9.59
H2O 5.18
Binding energy (eV)
GO20
Name At %
C1s 70.75
O1s 26.79
N1s 2.47
Binding energy (eV)
GO20
Name Area (%)
C=C 10.64
C-C 40.90
C-OH, C-N 8.75
C-O-C 28.36
C=OOH 5.05
C=O 4.04
pi-pi* 2.26
Binding energy (eV)
GO20
Name Area (%)
C-O 81.00
C=O 15.36
H2O 2.66
Binding energy (eV)
GO20_CONT
Name At %
C1s 68.02
O1s 31.36
N1s 0.62
Binding energy (eV)
GO20_CONT
Name Area (%)
C=C 9.34
C-C 37.64
C-OH 14.30
C-O-C 28.60
C=OOH 4.06
C=O 4.31
pi-pi* 1.74
Binding energy (eV)
GO20_CONT
Name Area (%)
C-O 85.19
C=O 11.87
H2O 2.03
Binding energy (eV)
GO19
Name Area (%)
C-NR2 68.97
C-NR3+ 31.03
R=H,C
Binding energy (eV)
GO20
Name Area (%)
C-NR2 80.64
C-NR3+ 19.36
R=H,C
Binding energy (eV)
GO19_CONT
GO20_CONT
Binding energy (eV)

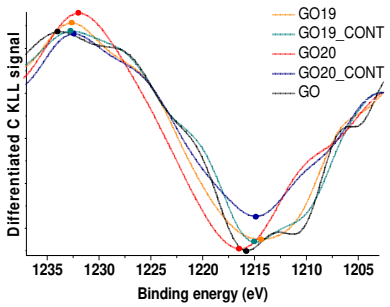

Figure 3.14 XPS survey spectra and C1s, O1s, N1s and first derivative C KLL high resolution spectra of **GO19**, **GO20**, **GO19_CONT** and **GO20_CONT**.

GO20 was examined by quantitative ^{13}C SS MAS NMR, and it was possible to notice the appearance of the peaks of **C1** and **C5**, at 40 ppm for the aliphatic chain and 27 ppm for the Boc protecting group. However, no more conclusions can be drawn from this spectrum. Indeed, if there is a signal of the ester around 170 ppm, it is of low intensity and cannot be seen without deconvolution of the spectrum. Indeed, ester peaks are of difficult identification in SS NMR spectra if present in low amount. The peak at 70 ppm instead is common for hydroxyl and ether groups. This could explain why it is quite intense after hydroxyl derivatization, as a matter of facts, **C1** inserted in the first step of the multifunctionalization present two ether groups.

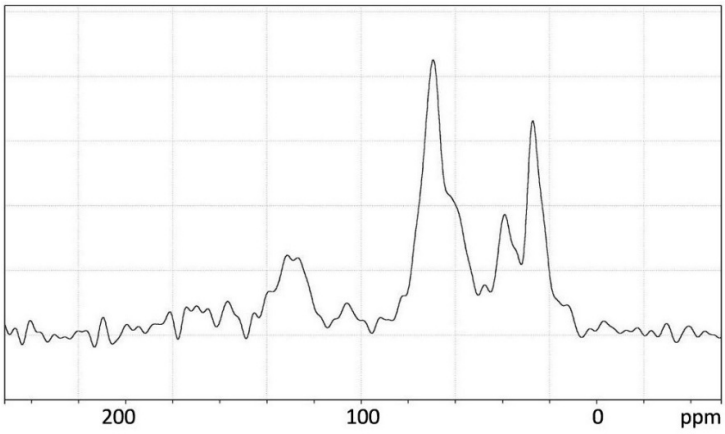

Figure 3.15 Qualitative ^{13}C SS MAS NMR of **GO20.**

By XPS, TGA, Kaiser test and SS NMR it was possible to confirm a positive outcome of both reactions, leading to a double functionalized GO. However, it should be taken into consideration that the loading of the second reaction does not correspond to the total amount of the functional group (*i.e.* the hydroxyl groups) supposed to be present on the surface of GO. The only reasonable explanation for this result consists in the combination of two phenomena: 1) the partial instability of the hydroxyl groups on the surface of GO and 2) the island localization of the functional groups that, due to the molecules introduced, causes a sterical hindrance for the second reaction of the multifunctionalization.

3.3.4 Multifunctionalization of a higher water stable graphene oxide derivative

Since the multifunctionalization on the functional groups already present on the surface of GO did not give the results we were hoping for, we decided to try another approach. In addition, we decided first to increase the dispersibility of GO in water and then to develop a multifunctionalization strategy. Indeed, often the dispersibility of GO decreases after functionalization due to a change in the surface charge of GO. Thus, we decided to attach on the surface of GO a highly water dispersible polymer, polyglycidol. We were

not the only one developing this derivative. Indeed, shortly after the end of the optimization study of PG derivatization of GO, Mu S. *et al.* proved the capacity to improve the biocompatibility of GO by adding polyglycidol on its surface, with the purpose to use this conjugate as a drug carrier.[8] Opposite to us, they performed the reaction in harsher condition with the addition of KH to deprotonate GO before adding glycidol. By stirring the mixture at 80°C for 16 h they obtained a yield of 52%.

3.3.4.1 *In situ* polymerization of glycidol on graphene oxide: an optimization study

This project was done in collaboration with the laboratory of Professor Naoki Komatsu (Kyoto University, Japan, during a three month stay at his laboratory. Prof. Komatsu has pioneered the polymerization of glycidol on the surface of different types of nanomaterials.[7,30] Thus, I took inspiration from their protocol and adapted it for GO. Indeed, in their procedure the polymerization of glycidol is usually performed at 140°C for 20 h. It is a temperature at which GO would be reduced. Thus, we decided to lower the temperature and increase the reaction times. The polymerization of glycidol on the surface of GO has already been performed at 80°C for 48 h, to obtain a PG-GO composite for gas separation applications.[31] Since GO undergoes significant modifications also if treated at 80°C, we tested the polymerization at different temperatures to find the best conditions to obtain a highly stable and not too reduced GO.
I tried the *in situ* polymerization of glycidol for 48 h at 140°C, 80°C and at room temperature (Scheme 3.16). The reaction has been performed at 140 °C only as reference for comparison, indeed, from the previous research projects of Prof. Komatsu's group we know that it is possible to reach 37% polymer loading on nanodiamonds (calculated by TGA) if glycidol is polymerized at 140°C. Thus, we wanted to see how much the loading of the polymer would be by lowering the temperature. Moreover, to improve the loading of the polymerization performed at room temperature we added NaOH or Et_3N.[32] In the literature two possibilities are reported to raise the rates of the polymerization of glycidol at room temperature. It is possible to use a base or a Lewis acid as catalyst.[32–39] A possible issue about the Lewis acid is that it can adsorb on the surface of GO or can even reduce it.[40,41] Thus, we opted for the base to perform the room temperature polymerization of glycidol.

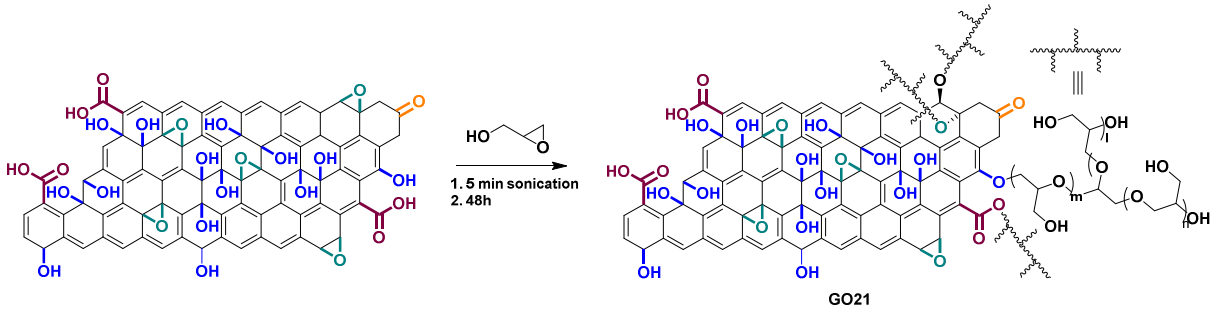

Scheme 3.16 Scheme of the glycidol polymerization (The reaction is shown only once on each functional group involved in the polymerization for clarity reasons).

The reaction was performed at 140°C (**GO21-a**), at 80°C (**GO21-b**), at room temperature (RT) without catalyst (**GO21-c**), at RT with NaOH (**GO21-d**), at RT with Et_3N (**GO21-e**) and at RT with a higher quantity of Et_3N (**GO21-f**). Control reactions were done for **GO21-a** and **GO21-b**, (namely **GO21-a_CONT** and **GO21-b_CONT**, respectively) to establish potential thermal reduction. The control reactions were performed in the same conditions using glycerol at the place of glycidol. The different samples were analyzed by FT-IR, and for all it was possible to identify the bands of the polymer (Figure 3.15).

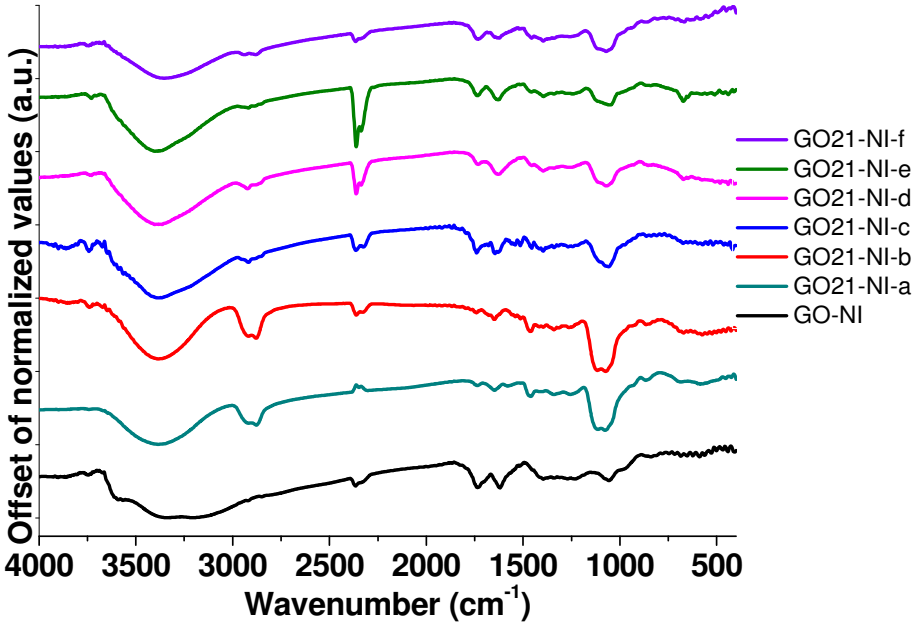

Figure 3.15 FT-IR spectra of **GO21** obtained from the reactions performed in different conditions.

In the FT-IR spectra, we can observe the peaks of the methylene groups around 2800 and 2900 cm^{-1} and of the ether bond around 1080 cm^{-1}.[8,42] It is also possible to observe a difference in the intensity of the peaks of the polymer compared to the bands attributed to GO in the different samples, indicating a diverse loading of the polymer. Thus, the best loadings appear to be for the reaction performed by heating at 80°C and 140°C.

The thermogravimetric curves were taken for all the samples under air and under nitrogen atmosphere (Figure 3.16). The degradation of the polymer happens around 350 °C, for both, under air and under nitrogen.[30] Under air it is possible to see also the weight loss due to the carbonization of GO between 400-600 °C. When this study was performed, in the laboratory of Professor Komatsu in Japan, only the analysis under air was available. Theoretically the samples run under air and under nitrogen should show a similar shape of the curves, beside the last section above 450 °C regarding the degradation of GO. This is not the case for the reactions performed under heating, where little differences can be observed between the two TGA graphs (Figure 3.16 a and c). This is probably due to a huge loading of polymer for **GO21-NI-a** and **GO21-NI-b**. Thus, as it appears by looking at these two graphs, the loading of polymer for **GO21-NI-a** and **GO21-NI-b** is around 89-95% and 87-93%, respectively. For the reactions performed at room temperature this difference is not present. What we can observe is that the lowest loading was achieved by performing the reaction at room temperature without catalyst, with a value of 20% (**GO21-NI-c**). With the addition of NaOH or Et_3N the loading increased to 30% (**GO21-NI-d** and **GO21-NI-e**). The same volume of NaOH (7.2 mmol) and Et_3N was used in **GO21-NI-d** and **GO21-NI-e,** as described in the article of Sandler and Berg.[32] Considering the similar outcome obtained using 7.2 and 2.2 mmol, respectively, we decided to verify if the addition of 7.2 mmol of Et_3N would increase the polymerization of PG. As we can observe **GO21-NI-f** shows a loading increased only to 35%.

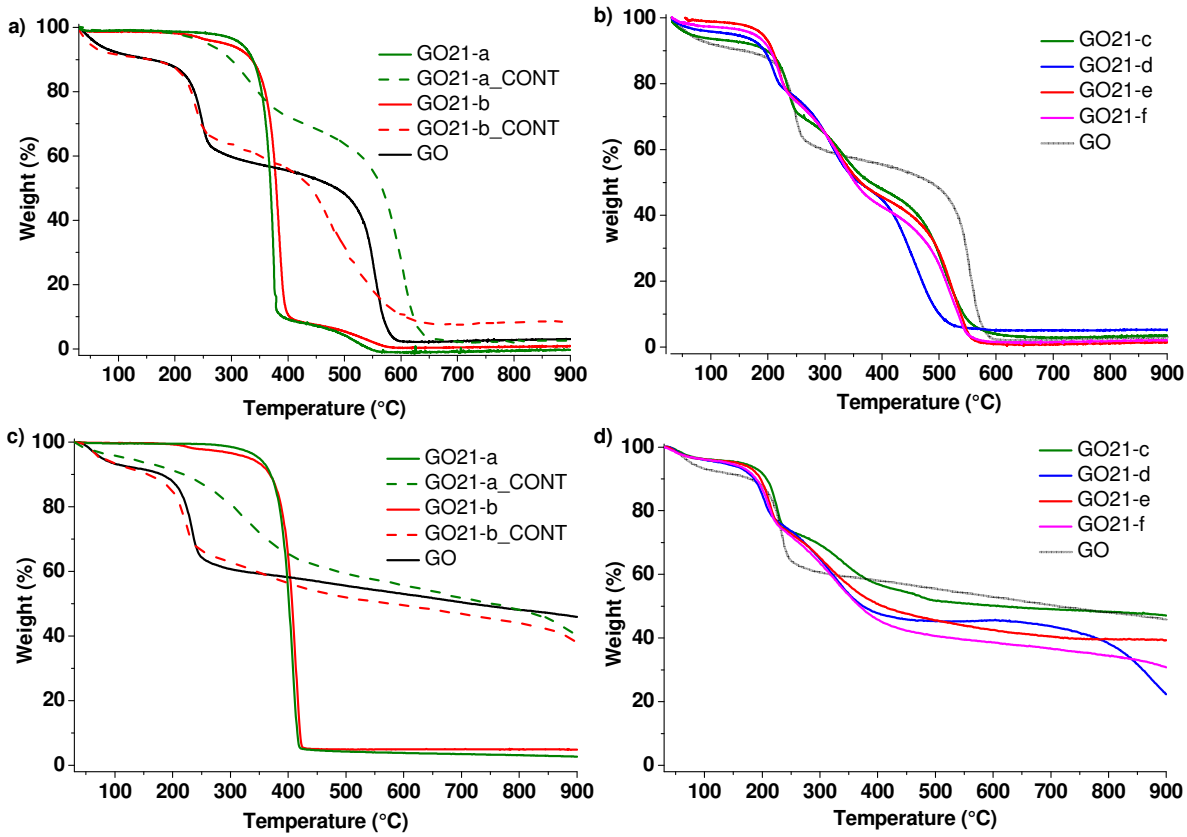

Figure 3.16 TGA curves of **GO21** (performed in the different conditions) taken under air for **a** and **b**; and under nitrogen for **c** and **d**.

The use of a catalyst did not allow to reach the same loadings of polymer compared to the reactions performed under heating.

According to TGA, a reduction of GO could be observed in the case of **GO21-NI-a_CONT** (control performed at 140°C). This seems not to be the case for **GO21-NI-b_CONT** (Control performed at 80°C). We were expecting thermal reduction of GO already at 80°C, but there was no reduction in observable amount for **GO21-NI-b**, by looking at his control.

The different samples were analyzed also by XPS. Considering that with the addition of polyglycidol we introduce carbon and oxygen in a 3:2 ratio no remarkable changes are expected in the C/O ratio (Table 3.7). Thus, the more PG we introduce on the surface of GO the more we expect the C/O ratio turn to 1.5, and this is also the case. Meanwhile, if we compare **GO-NI** with **GO21-NI-b_CONT** it is possible to notice, similarly to TGA, that the treatment at 80°C did not strongly affect the surface of GO. The C/O value of **GO21-NI-a** is justified by the important introduction of polymer that makes it difficult to observe the thermal reduction of GO treated at 140°C. If compared with **GO21-NI-b** the C/O ratio is slightly higher, likely consistent with reduction of GO. In **GO21-NI-d**, **GO21-NI-e** and **GO21-NI-f**, some residual sodium and nitrogen were detected, likely due to NaOH and Et_3N trapped into the polymer. More interestingly, the D parameter was calculated for these samples. The D parameter can be calculated from the first derivative of the C KLL Auger peak, and gives an idea of the C sp^2 amount in the total carbon content, as mentioned before.[43] If we look at the percentages in Table 3.7, it is possible to see how these values turn to 0% due to the high amount of polymer for **GO21-NI-a** and **GO21-NI-b**. Meanwhile **GO21-NI-c** presents still 25% of C sp^2, value that diminishes with the addition of a catalyst (**GO21-NI-d**, **GO21-NI-e** and **GO21-NI-f**) due to the increased addition of polymer.

Table 3.7 XPS C/O ratio, N1s and Na 1s percentages and D parameter for **GO21** obtained from the reactions performed in different conditions.

Name	C/O	N 1s (%)	Na 1s (%)	D parameter-C sp^2 (%)
GO-NI	2.2			47
GO21-NI-a	1.8	-	-	0
GO21-NI-b	1.7	-	-	0
GO21-NI-b_CONT	2.2	-	-	30
GO21-NI-c	2.2	-	-	25
GO21-NI-d	1.9	-	0.5	12
GO21-NI-e	2.1	0.64	-	28
GO21-NI-f	2.0	0.79	-	22

The interpretation of the carbon and oxygen high resolution spectra is instead more delicate (Figure 3.17). Indeed, the spectra change significantly with the formation of the polymer, mainly for the carbon spectra. For **GO21-NI-a** and **GO21-NI-b** there is one major peak, the one of the C-O bond of the polyglycidol. On the other hand, for **GO21-NI-c** it is possible to see the changes in the spectrum if compared to the starting GO-NI, due to the presence of the aliphatic C-O bond in the sample. Another feature that can be observed is the absence of major changes for **GO21-NI-b_CONT** compared to the starting material, a further prove of negligible reduction for **GO21-NI-b**. The difference between **GO21-NI-b_CONT** and GO-NI could be due to a low amount of glycerol that reacted with GO or that adsorbed on the surface. An interesting characteristic is the shift in the C-O signal towards the C-C peak. This can be explained by the fact that the signal for the aliphatic ether bond appears at more positive binding energies compared to the aromatic one, as it is the case for the aliphatic ethers compared to the aromatic ethers in the oxygen spectra.[18,44,45] A similar pattern can be also observed for the sample treated at room temperature with NaOH and Et_3N. For the latter a decrease in the C-C peak compared to the C-O peak can be observed because of an increased amount of polymer present.

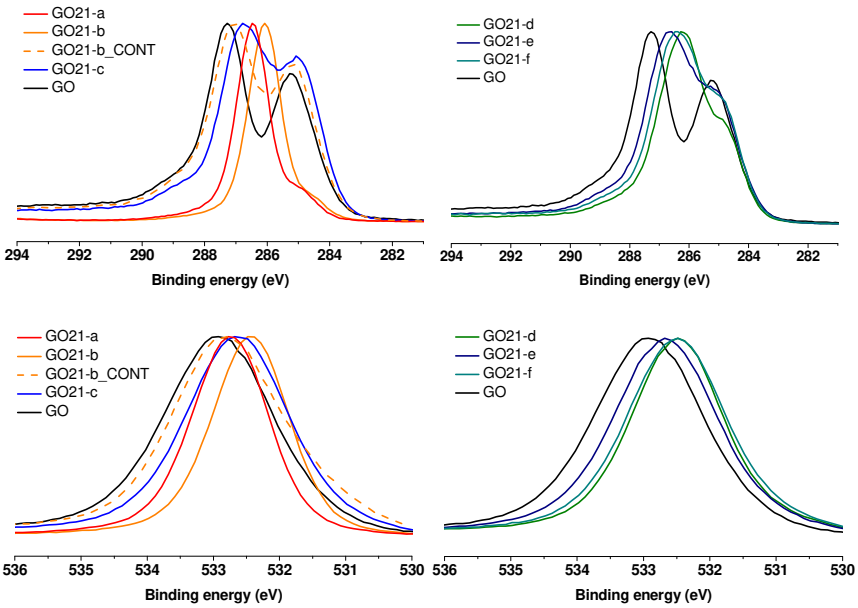

Figure 3.17 Normalized XPS C1s and O1s high resolution spectra of **GO21** obtained from the reactions performed in different conditions.

In the oxygen high resolution spectra, the shift of the maximum of the peak can be also observed in the spectra of the different samples of functionalized GO compared to the starting GO. Indeed, as already mentioned before, the aliphatic ether and the hydroxyl groups appear at more positive binding energies

compared to aromatic ones. Because of a gradual increase of the polymer present, the maximum of the peak shifts progressively from 533 eV to 532 eV.

To study the morphology of the conjugates after PG polymerization, SEM and TEM images were taken for the different samples, using a STEM apparatus. (Figure 3.18 and 3.19).

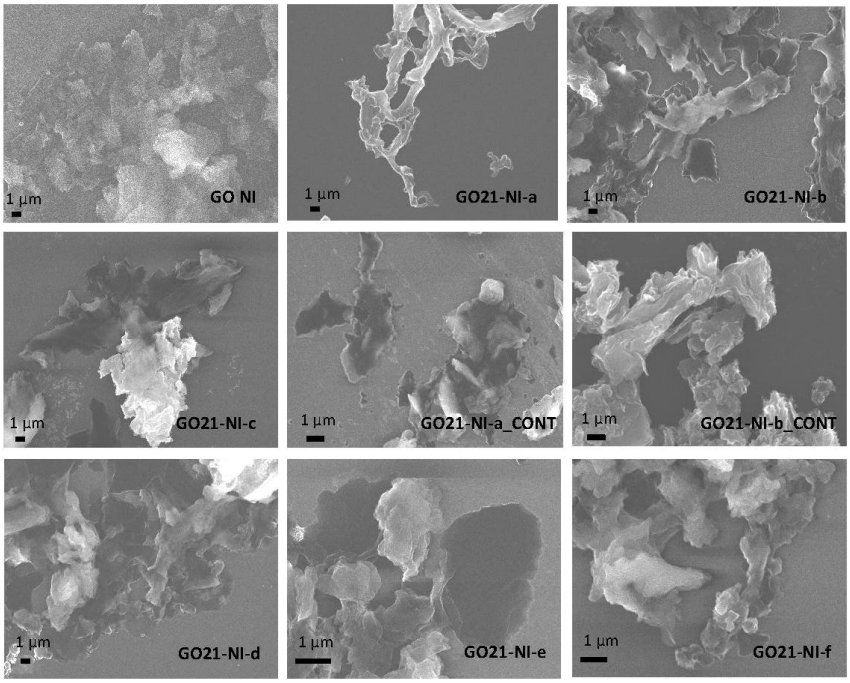

Figure 3.18 SEM images of **GO NI, GO21-NI-a**, **GO21-NI-b**, **GO21-NI-c**, **GO21-NI-d**, **GO21-NI-e**, **GO21-NI-f**, of **GO21-NI-a_CONT** and **GO21-NI-b_CONT**.

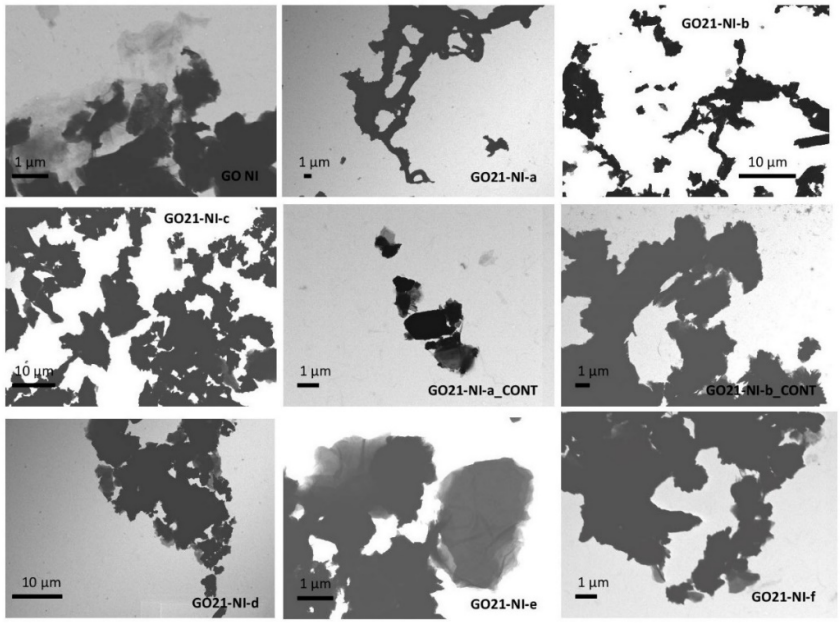

Figure 3.19 TEM images of **GO NI, GO21-NI-a**, **GO21-NI-b**, **GO21-NI-c**, **GO21-NI-d**, **GO21-NI-e**, **GO21-NI-f**, of **GO21-NI-a_CONT** and **GO21-NI-b_CONT**.

For both TEM and SEM, no significant changes can be noticed for the different samples. The only one showing a changed morphology is **GO21-NI-a**, probably due to the reduction of GO combined with the high polymer amount. No similar changes were observed in the corresponding control sample.

Afterwards, to assess the improvement of the dispersibility of GO, the stability of the different samples in water was analyzed (Figure 3.20). GO-NI starting material is not water stable for long time; consequently, it starts to precipitate already after 15 minutes. Because of the presence of the polymer, there is an important increase in water dispersibility and stability of the different functionalized samples. This stability increases proportionally to the amount of PG introduced onto the surface of GO. Thus, the samples that showed the highest stability are **GO21-NI-a** and **GO21-NI-b**. A change in the color between these two samples can be observed too, which is typical of the reduction of GO. Indeed, **GO21-NI-a** shows a more blackish color, typical of reduced GO, compared to **GO21-NI-b** that still shows the brownish color of GO. **GO21-NI-b** was still precipitating after one week. Since we wanted a highly stable PG-GO derivative for further multifunctionalization, we decided to perform the polymerization on another GO obtained from the laboratory of Professor Yuta Nishina (Okayama University, Japan) (GO-Jp). In his laboratory, they produce a highly water stable GO.

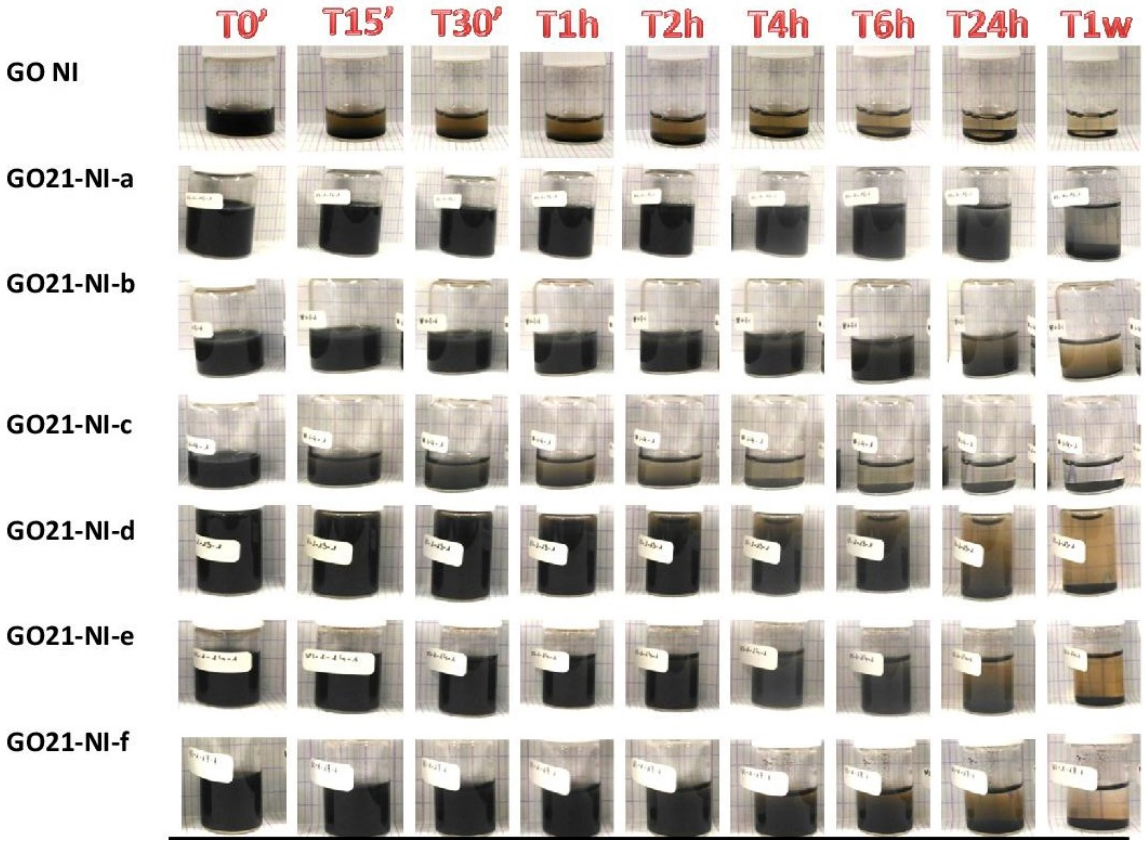

Figure 3.20 Water stability study for **GO21** obtained from the reactions performed in different conditions.

I started analyzing this GO by quantitative ^{13}C solid state MAS NMR spectrum (Figure 3.21). Compared to the previous samples in this GO the peaks of the ketones and carboxylic acids can be clearly detected at 192 and 164 ppm, proving a higher content of these groups.[24,46,47]

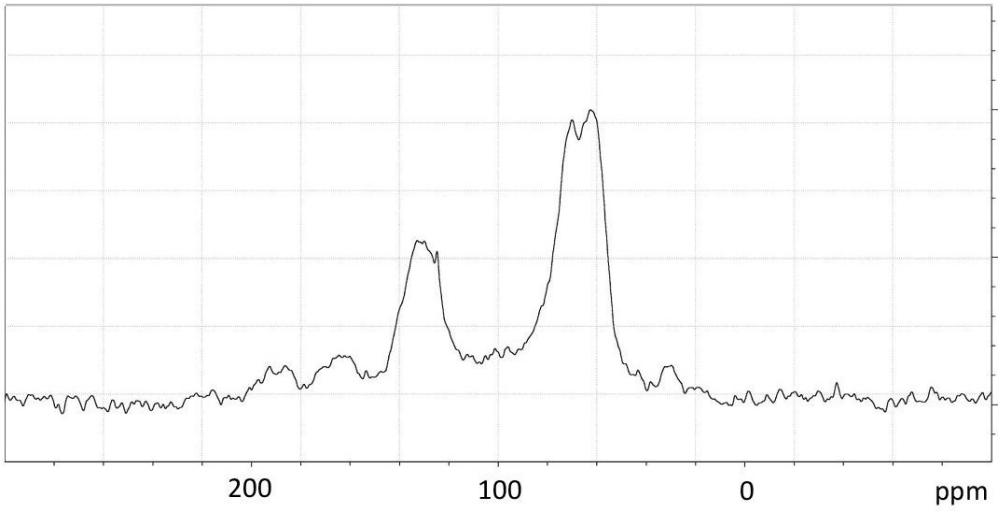

Figure 3.21 Quantitative ^{13}C SS MAS NMR spectrum of GO-Jp.

For this GO-Jp only the best reaction conditions were tried, **GO21-Jp-b** and **GO21-Jp-f**. As for GO-NI, different intensities were detected in the FT-IR spectra related to the different PG loadings (Figure 3.22, left). By both FT-IR and TGA (Figure 3.22, right), the formation of the polymer in **GO21-Jp-b** and **GO21-Jp-f** was confirmed. In TGA a loading of 85 and 60% was estimated for **GO21-Jp-b** and **GO21-Jp-f**, respectively. This time the reaction performed at RT with Et_3N, showed higher loadings, probably due to the higher number of oxygenated groups on GO, the grafting points of the polymer.

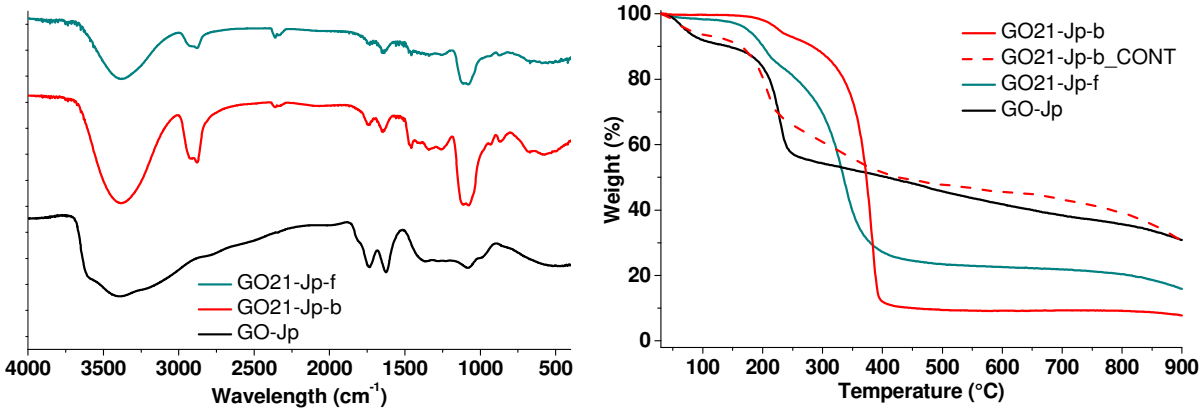

Figure 3.22 (Left) FT-IR of **GO21** on GO-Jp and (Right) TGA (in nitrogen atmosphere) of **GO21** on GO-Jp.

As for GO-NI, also for GO-Jp the PG polymerization slightly decreased the C/O ratio towards 1.5 because carbon and oxygen atoms are introduced in a 3:2 ratio (Table 3.8). This time the D parameter shows a C sp^2 amount between 0-3% for both samples because of the elevated amount of polymer introduced in both **GO21-Jp-b** and **GO21-Jp-f**. Contrary to **GO21-NI-f**, no Et_3N contamination was found for **GO21-Jp-f**.

Table 3.8 XPS C/O ratio, N1s percentage, and D parameter for **GO21** obtained from the reactions performed in different conditions.

Name	C/O	N 1s (%)	D parameter-sp^2 (%)
GO-Jp	2.0	-	30%
GO21-Jp-b	1.8	-	0%
GO21-Jp-b_CONT	1.8	-	23%
GO21-Jp-f	1.8	-	3%

A pattern similar to **GO21-NI** can be observed also in the XPS carbon and oxygen high resolution spectra of **GO21-Jp**, due to the introduction of the polymer (Figure 3.23). Again, no significant changes could be seen for **GO21-Jp-b_CONT**, indicating a negligible effect of the temperature on GO for **GO21-Jp-b**. Moreover, the carbon high resolution spectrum of **GO21-Jp-f** shows a more intense C-O region versus the C-C once compared to **GO21-NI-f,** consistent with the higher polymerization ratio of **GO21-Jp-f** also observed by TGA.

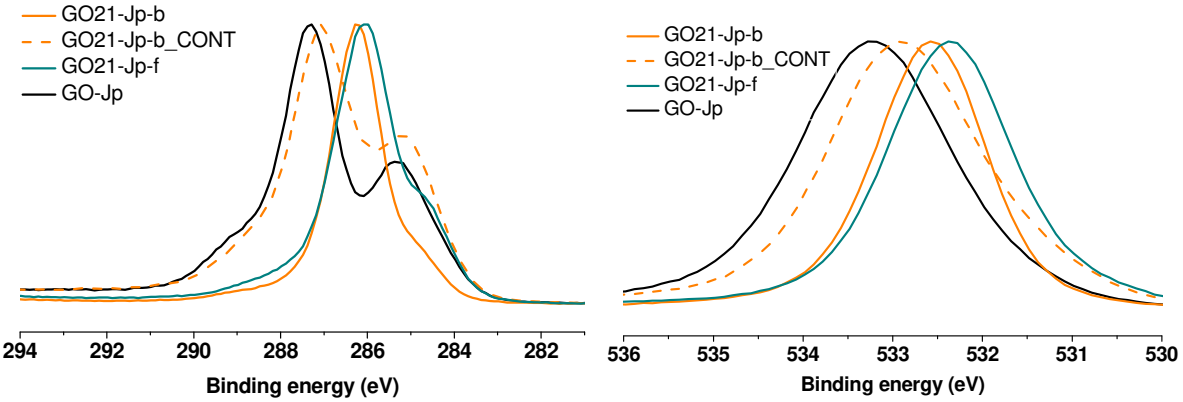

Figure 3.23 XPS C1s and O1s high resolution spectra of **GO21** performed on GO-Jp in two conditions.

GO-Jp did not show any precipitation after one week. **GO21-Jp-b** and **GO21-Jp-f** resulted also highly stable in water (Figure 3.25).

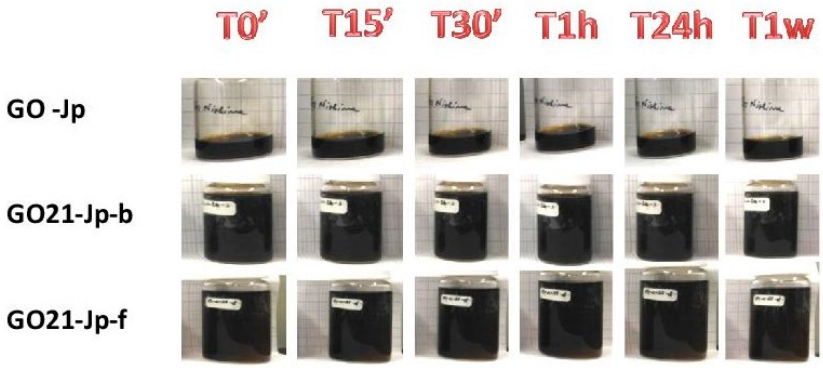

Figure 3.25 Water stability evaluation of **GO21-Jp.**

DLS measurements were performed for all samples. An increase in size could be observed, strongly dependent to the degree of polymerization. For the **GO21-NI** samples, often more than one family size distribution was observed, due to a less homogeneous starting material with a higher aggregation tendency. GO-Jp instead is more dispersible and has also a lower lateral size compared to GO-NI, as it can be observed by DLS. Due to the absent aggregation of GO-Jp a single-family dimension can be observed also after the polymerization process.

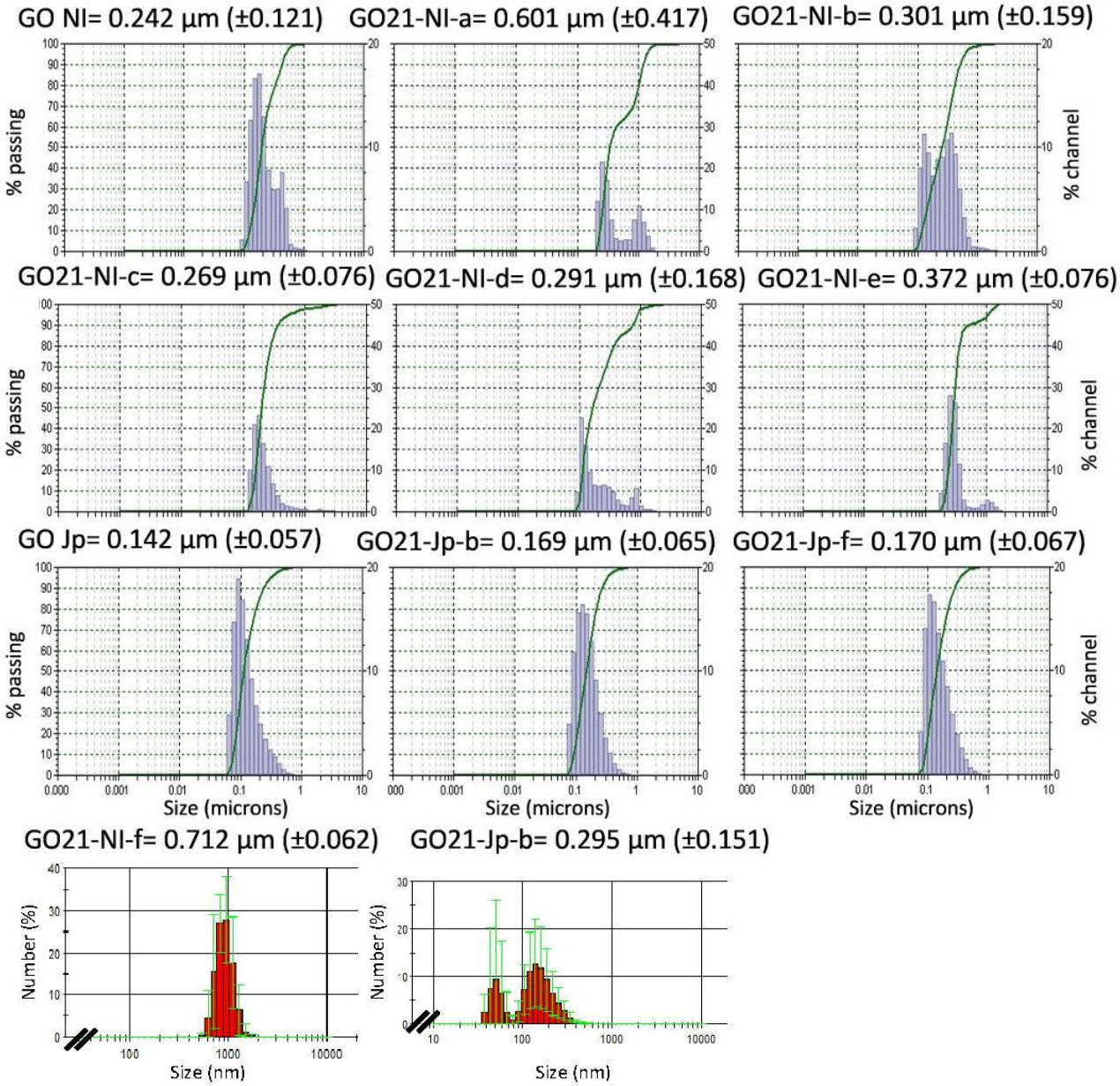

Figure 3.26 DLS data of **GO21** obtained from the reactions performed in different conditions on GO-NI and GO-Jp. (**GO21-NI-f** was taken on another DLS apparatus, thus, **GO21-Jp-b** was taken to compare the two instruments).

In conclusion, we obtained a highly stable PG-GO conjugate using GO-Jp. As we decided to use **GO21-Jp-b** for further multifunctionalization studies, we decided to analyze further this sample using ^{13}C SS MAS NMR (Figure 3.27).

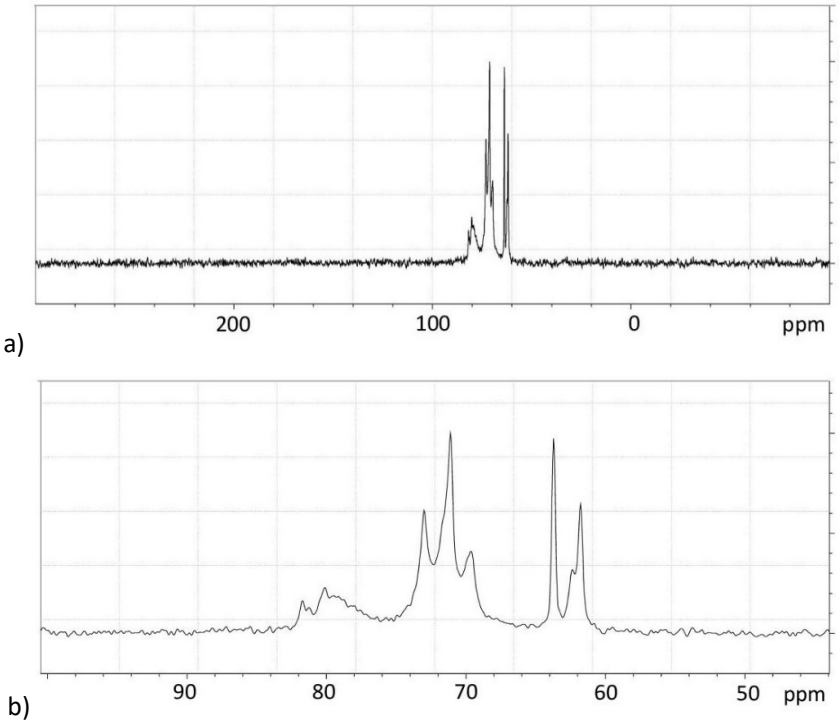

Figure 3.27 a) Quantitative ^{13}C SS MAS NMR spectrum of **GO21-Jp-b** and b) the respective magnified spectrum.

The ^{13}C SS MAS NMR spectrum shows a totally different pattern from GO. No signals of GO are present in the spectrum (Figure 3.27 a). The polymer loading is supposed to be very high (above 95%). It is possible to identify, instead, the characteristic peaks of polyglycidol even if the spectrum definition for **GO20-Jp-b** is low since similar conditions were used to take the spectrum of GO (Figure 3.27 b).[48–51] As we can notice, the polyglycidol polymer displays a rather complex spectrum, but the values found are in agreement with those in the literature.[48–51]

3.3.4.2 Multifunctionalization on graphene oxide-polyglycidol conjugate

Once we obtained the highly water stable PG-GO, we developed a strategy of multifunctionalization. PG-GO, contrary to non-functionalized GO, presents only one oxygenated functional group, the hydroxyl. Thus, we envisaged two options: 1) to activate only part of the hydroxyls to obtain azides and then to functionalize separately the hydroxyls and the azides, or 2) to transform the totality of the hydroxyls in azides and to perform twice a Cu(I)-catalyzed Huisgen 1,3-dipolar cycloaddition reaction, also called click reaction, on part of the azides with two different molecules. In Professor Komatsu's laboratory similar multifunctionalization protocols have been already established on polyglycidol.[52,53] We decided to use mild conditions to avoid the reduction of GO. Considering the difficulty to establish the amount of hydroxyl groups without an XPS or NMR apparatus available in Japan, I decided first to try the conversion of the hydroxyl groups into azido groups and then to establish the amount of conversion to decide the next step.
The hydroxyl groups were first activated to tosyl groups to obtain **GO22-Jp** (see procedure **GO22** in Chapter 6), and then NaN_3 was added to obtain the azido derivative, **GO23-Jp** (see procedure **GO23** in Chapter 6) (Scheme 3.17).[52,53] A control reaction was performed starting from **GO21-Jp-b_CONT** for these reactions, leading to **GO22-Jp_CONT** and **GO23-Jp CONT**, performed without adding tosyl chloride and sodium azide, respectively. Once **GO23-Jp** obtained, the amount of azide introduced was measured by XPS in Strasbourg. Then, as a proof of concept, a kidney-targeting peptide was anchored to the azide through click reaction.

The idea was to combine this peptide with a fluorophore on the surface of PG-GO to follow *in vivo* the biodistribution and prove the renal targeting capacity [$(KKEEE)_3K$] of the conjugate. The specific kidney-targeting capacity of the $(KKEEE)_3K$ peptide was recently demonstrated in the literature.[54] Moreover, its good tolerability and high plasma stability were also proved.[55] An alkyne derivatized $(KKEEE)_3K$ was prepared in our laboratory through peptide solid-phase synthesis and added to **GO23-Jp** to get **GO24-Jp** in the presence of copper sulfate and sodium ascorbate (see procedure **GO24** in Chapter 6). A control reaction was performed for **GO24-Jp**, **GO24-Jp_CONT**, to verify if the peptide can adsorb on the surface of **GO23-Jp**. This control reaction was performed by adding the peptide to **GO23-Jp** without sodium ascorbate and copper sulfate.

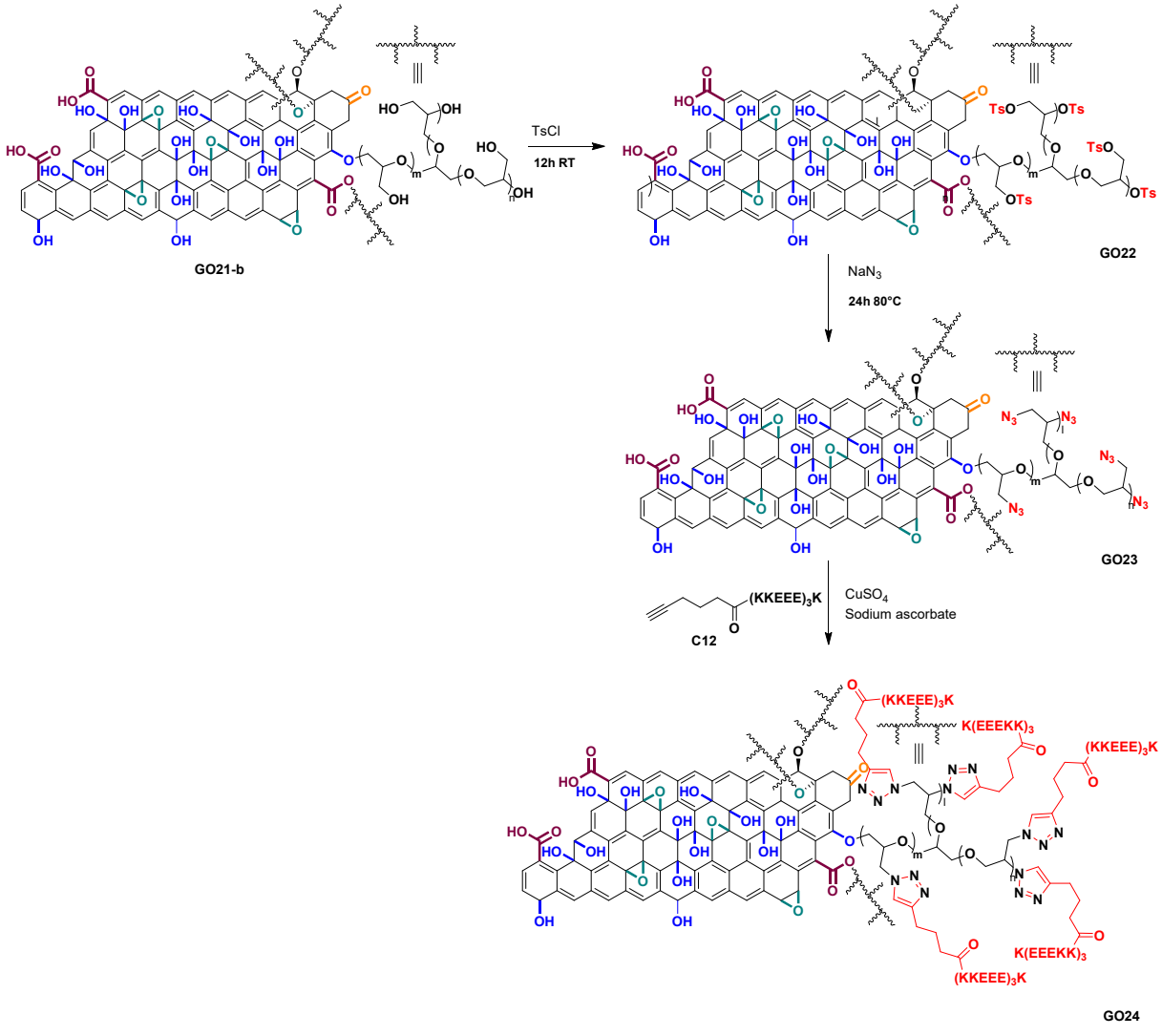

Scheme 3.17 Schematization of the derivatization reaction performed on **GO21-Jp-b** (The reactions **GO22**, **GO23** and **GO24** are shown only on one PG branch for clarity reasons).

FT-IR and TGA were recorded for **GO21-Jp**, **GO22-Jp** and **GO23-Jp** (Figure 3.28). The identification of the tosyl group in the FT-IR is difficult because the bands are located in an area where GO-PG shows numerous signals. The bands at 1597, 1350 and 1176 cm^{-1} can be attributed to C=C stretching of the benzene ring and to the asymmetric and symmetric stretching of S=O of the tosyl group in **GO22-Jp**.[52] Opposite, in **GO23-Jp** the band of the azide group can be clearly identified around 2100 cm^{-1}, proving the positive result of the

reaction. In the TGA no significant changes in the control reactions were observed. Thus, no major changes were caused on the structure of GO by the reaction conditions used. Meanwhile, **GO22-Jp** shows two slopes, a weight loss between 200 and 250 °C and one between 400 and 450°C, both related to the tosyl derivative, as already reported in the literature.[56] In **GO23-Jp**, due to the consumption of the tosyl group, the slope at 200-250°C disappears. Compared to **GO21-Jp-b**, the thermal decomposition of **GO23-Jp** started at lower temperatures, probably due to the presence of the azido group.

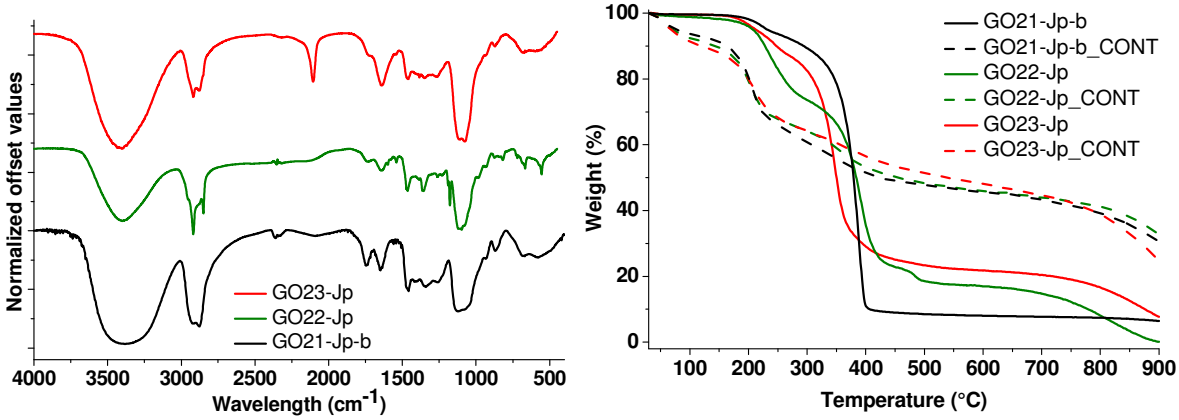

Figure 3.28 FT-IR spectra of **GO21-Jp-b**, **GO22-Jp**, **GO23-Jp** on the left and TGA of **GO21-Jp-b**, **GO22-Jp**, **GO23-Jp**, **GO21-Jp-b_CONT**, **GO22-Jp_CONT** and **GO23-Jp_CONT** performed in nitrogen atmosphere on the right.

More information was obtained, instead, from the XPS analysis (Figure 3.29). Indeed, in **GO22-Jp** 1.28% of sulfur was introduced with the tosyl group, meanwhile in **GO23-Jp** sulfur was no more detected and 2.95% of nitrogen was measured. Thus, there was a complete conversion of the tosyl group into azide, also confirmed by the fact that the percentage of nitrogen is almost three times that of sulfur.

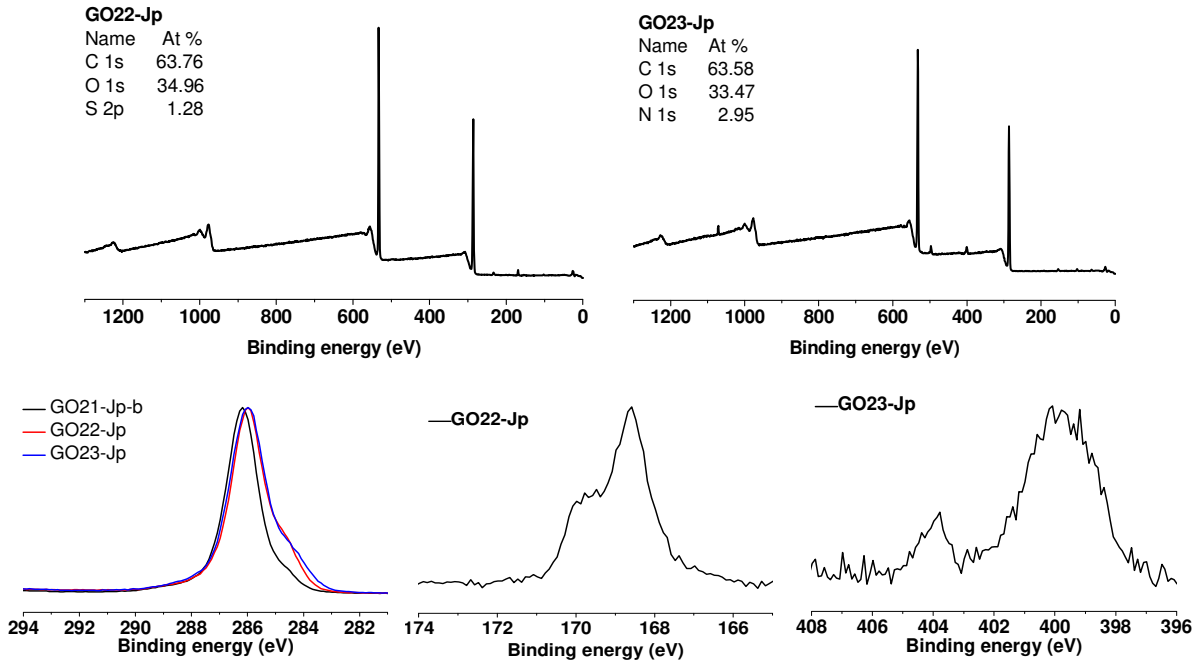

Figure 3.29 XPS survey spectra of **GO22-Jp** and **GO23-Jp**; C1s high resolution spectra of **GO21-Jp-b**, **GO22-Jp** and **GO23-Jp**, S2p high resolution spectra for **GO22-Jp** and N1s high resolution spectra for **GO23-Jp.**

In the C1s spectra a difference can be observed due to the introduction of the C-S or C-N bond for **GO22-Jp** and **GO23-Jp**, respectively. The sulfur high resolution spectra of **GO22-Jp** presents the peak of the tosyl group, as reported in literature, at 169.2 eV for S $2p_{3/2}$ and 170.1 eV for S $2p_{1/2}$.[57] The nitrogen high resolution spectra of **GO23-Jp**, instead, displays the typical two peaks of the azide group, at 400.8 eV and 404.5 eV. The peak at 400.8 eV can be assigned to the two outer nitrogen atoms and the one at 404.5 eV to the electron poor middle nitrogen atom.

After conjugation of the peptide *via* the click reaction in **GO24-Jp**, there is a main change in the nitrogen high resolution spectrum (Figure 3.30). Indeed, due to the formation of the 1,2,3-triazole the characteristic peak of the azido group at 404.5 eV disappears and the peak at 400.8 eV is shifted to 400.5 eV, characteristic signal of the triazole, as reported in literature.[58–60] The typical pattern of the azido group can be still observed instead in the nitrogen high resolution spectra of the control sample **GO24-Jp_CONT**, which indicates that the azide did not undergo degradation phenomena in the conditions used. In addition, in the survey spectra of **GO24-Jp,** compared to **GO24-Jp_CONT,** a higher content of carbon atoms can be detected due to the introduction of the peptide. Meanwhile, major changes can be observed in the carbon high resolution spectra of **GO24-Jp**. Indeed, the peak in the region of the C-C bonds becomes more intense compared to the one in the C-O region, due to the presence of the peptide.

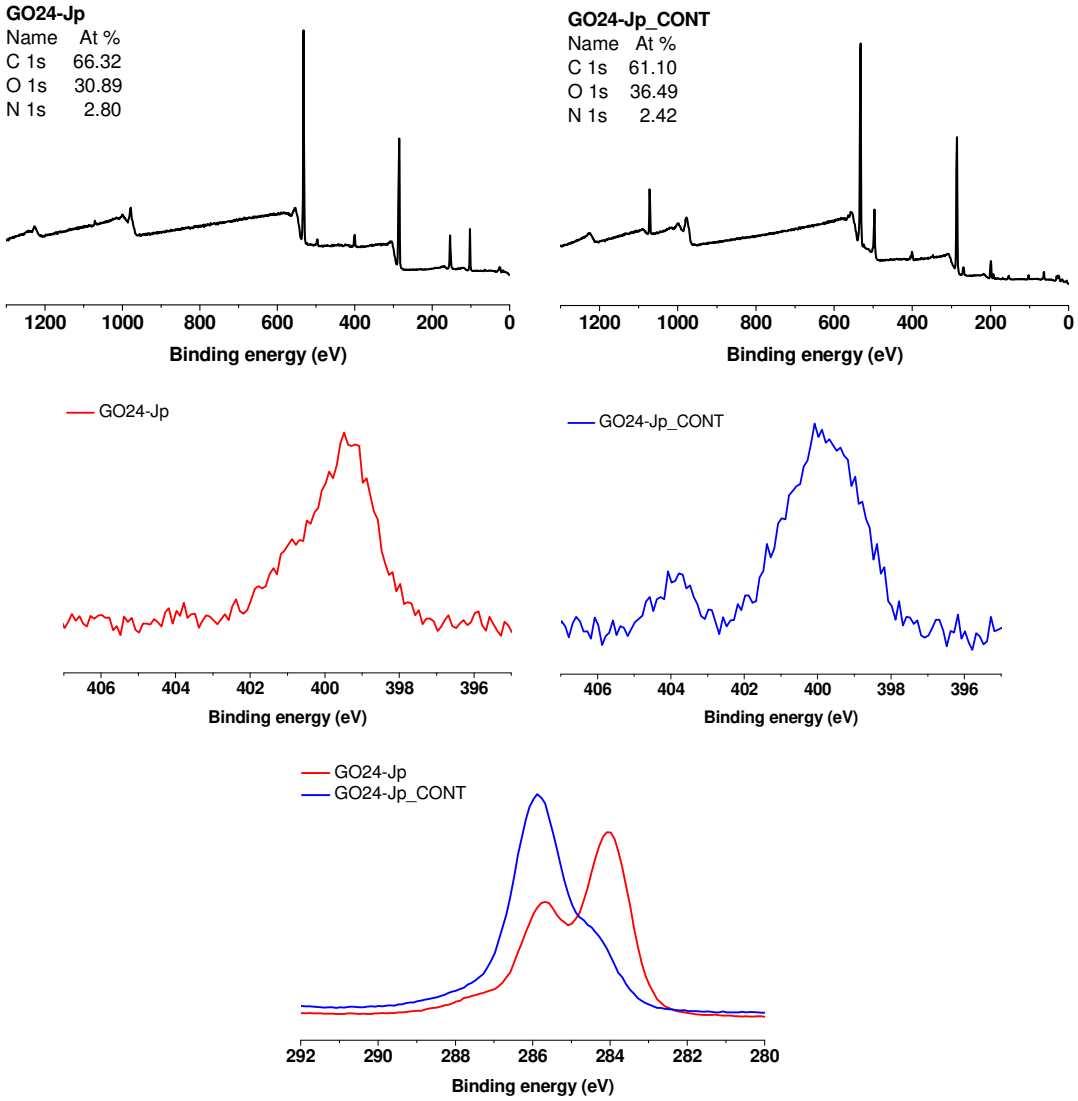

Figure.3.30 XPS survey, N1s and C1s spectra of **GO24-Jp** and **GO24-Jp_CONT**.

GO24-Jp and **GO24-Jp_CONT** were also analyzed through FT-IR and compared to **GO23-Jp** (Figure 3.32). A decrease in the intensity of the signal of the azide is visible for **GO24-Jp** compared to **GO24-Jp_CONT** and **GO23-Jp**, due to transformation in triazole. Moreover, some of the characteristic peaks of the peptide appear only in **GO24-Jp** at 1653 and 1534 cm^{-1}, confirming the introduction of the kidney targeting peptide *via* the click reaction. The absence of these peaks in the control reaction, **GO24-Jp_CONT** proves the absence of adsorption of the peptide on the surface of the GO conjugate.

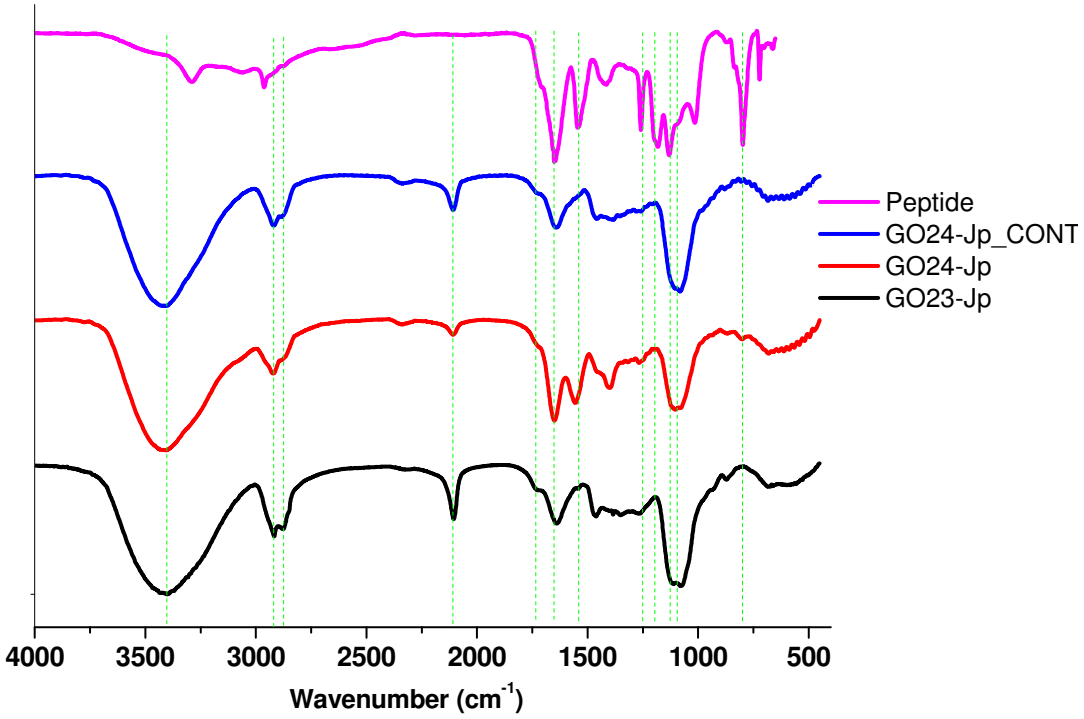

Figure 3.32 FT-IR spectra of **GO23-Jp**, **GO24-Jp**, **GO24-Jp_CONT** and the peptide alone.

Taken together, these data show the efficiency of our strategy to synthesize the PG-GO-peptide conjugate. But, due to a lack of time I could not start to investigate the addition of a fluorophore to this system.

3.4 Conclusion

In conclusion, I tried different multifunctionalization protocols on the oxygenated functional groups present on the surface of GO and the best procedure appeared to be the combination of the opening of epoxides with the esterification reaction on the hydroxyl groups. The loading resulted not to give the expected outcomes, most probably due to the sterical hindrance caused by the island localization of the functional groups on the surface of GO.

At the same time, I explored another approach of multifunctionalization by conjugating polyglycidol on GO to increase water dispersibility and biocompatibility of GO. On this PG-GO conjugate, a peptide was attached to target specifically the kidneys. This conjugate will be further functionalized with a fluorophore to allow *in vitro* imaging and *in vivo* biodistribution studies.

3.5 Bibliography

1. Urbas K, Aleksandrzak M, Jedrzejczak M, et al. Chemical and magnetic functionalization of graphene oxide as a route to enhance its biocompatibility. Nanoscale Res Lett 2014;9(1):656.

2. Dan Wang, Weihua Hu, Yonghua Xiong, Yang Xu, Chang Ming Li. Multifunctionalized reduced graphene oxide-doped polypyrrole/pyrrolepropylic acid nanocomposite impedimetric immunosensor to ultra-sensitively detect small molecular aflatoxin B1. Biosens Bioelectron 2015;63:185–9.

3. Wang C, Wang X, Lu T, et al. Multi-functionalized graphene oxide complex as a plasmid delivery system for targeting hepatocellular carcinoma therapy. RSC Adv 2016;6(27):22461–8.

4. Rezaei A, Akhavan O, Hashemi E, Shamsara M. Ugi Four-Component Assembly Process: An Efficient Approach for One-Pot Multifunctionalization of Nanographene Oxide in Water and Its Application in Lipase Immobilization. Chem Mater 2016;28(9):3004–16.

5. Mei K-C, Rubio N, Costa PM, et al. Synthesis of double-clickable functionalised graphene oxide for biological applications. Chem Commun 2015;51(81):14981–4.

6. Zhao L, Takimoto T, Ito M, Kitagawa N, Kimura T, Komatsu N. Chromatographic Separation of Highly Soluble Diamond Nanoparticles Prepared by Polyglycerol Grafting. Angew Chem Int Ed 2011;50(6):1388–92.

7. Zhao L, Chano T, Morikawa S, et al. Hyperbranched Polyglycerol-Grafted Superparamagnetic Iron Oxide Nanoparticles: Synthesis, Characterization, Functionalization, Size Separation, Magnetic Properties, and Biological Applications. Adv Funct Mater 2012;22(24):5107–17.

8. Shansong Mu, Guowei Li, Yuanyuan Liang, Ting Wu, Dong Ma. Hyperbranched polyglycerol-modified graphene oxide as an efficient drug carrier with good biocompatibility. Mater Sci Eng C 2017;78:639–46.

9. Isidro-Llobet A, Álvarez M, Albericio F. Amino Acid-Protecting Groups. Chem Rev 2009;109(6):2455–504.

10. Levin E, Mavila S, Eivgi O, Tzur E, Lemcoff NG. Regioselective chromatic orthogonality with light-activated metathesis catalysts. Angew Chem Int Ed Engl 2015;54(42):12384–8.

11. Bochet CG. Photolabile protecting groups and linkers. J Chem Soc, Perkin Trans 1 2002;0(2):125–42.

12. Kessler M, Glatthar R, Giese B, Bochet CG. Sequentially Photocleavable Protecting Groups in Solid-Phase Synthesis. Org Lett 2003;5(8):1179–81.

13. Richard S. Givens, Peter G. Conrad, II, Abraham L. Yousef, Jong-III Lee. Photoremovable Protecting Groups. In: CRC Handbook of Organic Photochemistry and Photobiology. William Horspool, Francesco Lenci; 2003. p. 2904 pages.

14. Corrie JET, Furuta T, Givens R, Yousef AL, Goeldner M. Photoremovable Protecting Groups Used for the Caging of Biomolecules [Internet]. In: Goeldner urice, Givens RS, editors. Dynamic Studies in Biology. Wiley-VCH Verlag GmbH & Co. KGaA; 2005. p. 1–94.Available from: http://onlinelibrary.wiley.com/doi/10.1002/3527605592.ch1/summary

15. Kasuga NC, Saito Y, Okamura N, et al. Influences of alpha-substituent in 4,5-dimethoxy-2-nitrobenzyl-protected esters on both photocleavage rate and subsequent photoreaction of the generated 2-nitrosophenyl ketones: A novel photorearrangement of 2-nitrosophenyl ketones. J Photochem Photobiol Chem 2016;321:41–7.

16. Tsung-Che Chang, Avijit K. Adak, Ting-Wei Lin, et al. A photo-cleavable biotin affinity tag for the facile release of a photo-crosslinked carbohydrate-binding protein. Bioorg Med Chem 2016;24(6):1216–24.

17. Andrew M. Piggott, Peter Karuso. Synthesis of a new hydrophilic o-nitrobenzyl photocleavable linker suitable for use in chemical proteomics. Tetrahedron Lett 2005;46(47):8241–4.

18. M. C. Biesinger. X-ray Photoelectron Spectroscopy (XPS) database [Internet]. X-Ray Photoelectron Spectrosc. XPS Ref. Pages. Available from: http://www.xpsfitting.com/

19. Wulff M, Aldén M, Tegenfeldt J. Solid-State NMR Investigation of Indomethacin−Cyclodextrin Complexes in PEG 6000 Carrier. Bioconjug Chem 2002;13(2):240–8.

20. Voorhees KJ, Stevenson DN, Sun Y, Maciel GE. A solid state 13C nuclear magnetic resonance investigation of the thermal degradation of a poly(ethylene glycol) and poly(vinyl alcohol) binder in an alumina ceramic. J Mater Sci 1997;32(8):2115–20.

21. Gouget-Laemmel AC, Yang J, Lodhi MA, et al. Functionalization of Azide-Terminated Silicon Surfaces with Glycans Using Click Chemistry: XPS and FTIR Study. J Phys Chem C 2013;117(1):368–75.

22. Gao X, Jang J, Nagase S. Hydrazine and Thermal Reduction of Graphene Oxide: Reaction Mechanisms, Product Structures, and Reaction Design. J Phys Chem C 2010;114(2):832–42.

23. Eigler S, Grimm S, Hof F, Hirsch A. Graphene oxide: a stable carbon framework for functionalization. J Mater Chem A 2013;1(38):11559–62.

24. Hunt A, Dikin DA, Kurmaev EZ, et al. Epoxide Speciation and Functional Group Distribution in Graphene Oxide Paper-Like Materials. Adv Funct Mater 2012;22(18):3950–7.

25. Al-Azizi AA, Eryilmaz O, Erdemir A, Kim SH. Surface Structure of Hydrogenated Diamond-like Carbon: Origin of Run-In Behavior Prior to Superlubricious Interfacial Shear. Langmuir 2015;31(5):1711–21.

26. Kaciulis S, Mezzi A, Calvani P, Trucchi DM. Electron spectroscopy of the main allotropes of carbon. Surf Interface Anal 2014;46(10–11):966–9.

27. Lascovich JC, Scaglione S. Comparison among XAES, PELS and XPS techniques for evaluation of Sp2 percentage in a-C:H. Appl Surf Sci 1994;78(1):17–23.

28. Barlow AJ, Scott O, Sano N, Cumpson PJ. Multivariate Auger Feature Imaging (MAFI) – a new approach towards chemical state identification of novel carbons in XPS imaging. Surf Interface Anal 2015;47(2):173–5.

29. Lascovich JC, Giorgi R, Scaglione S. Evaluation of the sp2/sp3 ratio in amorphous carbon structure by XPS and XAES. Appl Surf Sci 1991;47(1):17–21.

30. Zhao L, Nakae Y, Qin H, et al. Polyglycerol-functionalized nanodiamond as a platform for gene delivery: Derivatization, characterization, and hybridization with DNA. Beilstein J Org Chem 2014;10:707–13.

31. Wu Y, Jia P, Xu L, et al. Tuning the Surface Properties of Graphene Oxide by Surface-Initiated Polymerization of Epoxides: An Efficient Method for Enhancing Gas Separation. ACS Appl Mater Interfaces 2017;9(5):4998–5005.

32. Sandler SR, Berg FR. Room temperature polymerization of glycidol. J Polym Sci [A1] 1966;4(5):1253–9.

33. Wilms D, Stiriba S-E, Frey H. Hyperbranched Polyglycerols: From the Controlled Synthesis of Biocompatible Polyether Polyols to Multipurpose Applications. Acc Chem Res 2010;43(1):129–41.

34. Dworak A, Walach W, Trzebicka B. Cationic polymerization of glycidol. Polymer structure and polymerization mechanism. Macromol Chem Phys 1995;196(6):1963–70.

35. He B, Zhou L. Efficient tailoring of the surface of upconversion nanoparticles via surface-initiated cationic ring-opening polymerization. RSC Adv 2015;5(118):97764–72.

36. Ul-Haq MI, Shenoi RA, Brooks DE, Kizhakkedathu JN. Solvent-assisted anionic ring opening polymerization of glycidol: Toward medium and high molecular weight hyperbranched polyglycerols. J Polym Sci Part Polym Chem 2013;51(12):2614–21.

37. Spears BR, Waksal J, McQuade C, Lanier L, Harth E. Controlled branching of polyglycidol and formation of protein-glycidol bioconjugates via a graft-from approach with "PEG-like" arms. Chem Commun Camb Engl 2013;49(24):2394–6.

38. Spears BR, Marin MA, Montenegro-Burke JR, Evans BC, McLean J, Harth E. Aqueous Epoxide Ring-Opening Polymerization (AEROP): Green Synthesis of Polyglycidol with Ultralow Branching. Macromolecules 2016;49(6):2022–7.

39. Asenjo-Sanz I, Santos JI, Bittner AM, Pomposo JA, Barroso-Bujans F. Zwitterionic ring-opening polymerization for the facile, efficient and versatile grafting of functional polyethers onto graphene sheets. Eur Polym J 2015;73:413–22.

40. Klímová K, Pumera M, Luxa J, et al. Graphene Oxide Sorption Capacity toward Elements over the Whole Periodic Table: A Comparative Study. J Phys Chem C 2016;120(42):24203–12.

41. Xie Y-L, Yuan J, Ye H-L, Song P, Hu S-Q. Facile ultrasonic synthesis of graphene/SnO2 nanocomposite and its application to the simultaneous electrochemical determination of dopamine, ascorbic acid, and uric acid. J Electroanal Chem 2015;749:26–30.

42. Rezaeifar Z, Es'haghi Z, Rounaghi GH, Chamsaz M. Hyperbranched polyglycerol/graphene oxide nanocomposite reinforced hollow fiber solid/liquid phase microextraction for measurement of ibuprofen and naproxen in hair and waste water samples. J Chromatogr B 2016;1029:81–7.

43. XPS Interpretation of Carbon [Internet]. [cited 2017 Jul 26];Available from: http://xpssimplified.com/elements/carbon.php

44. M. C. Biesinger. X-ray Photoelectron Spectroscopy (XPS) database [Internet]. X-Ray Photoelectron Spectrosc. XPS Ref. Pages. Available from: http://www.xpsfitting.com/search/label/Oxygen

45. Ganguly A, Sharma S, Papakonstantinou P, Hamilton J. Probing the Thermal Deoxygenation of Graphene Oxide Using High-Resolution In Situ X-ray-Based Spectroscopies. J Phys Chem C 2011;115(34):17009–19.

46. Thomas HR, Day SP, Woodruff WE, et al. Deoxygenation of Graphene Oxide: Reduction or Cleaning? Chem Mater 2013;25(18):3580–8.

47. MacIntosh AR, Harris KJ, Goward GR. Structure and Dynamics in Functionalized Graphene Oxides through Solid-State NMR. Chem Mater 2016;28(1):360–7.

48. Mohammadifar E, Bodaghi A, Dadkhahtehrani A, Nemati Kharat A, Adeli M, Haag R. Green Synthesis of Hyperbranched Polyglycerol at Room Temperature. ACS Macro Lett 2017;6(1):35–40.

49. Timothy Royappa A, Vogt ML, Sharma V. Composition and long-term stability of polyglycidol prepared by cationic ring-opening polymerization. J Appl Polym Sci 2004;91(2):1344–51.

50. Panja P, Das P, Mandal K, Jana NR. Hyperbranched Polyglycerol Grafting on the Surface of Silica-Coated Nanoparticles for High Colloidal Stability and Low Nonspecific Interaction. ACS Sustain Chem Eng 2017;5(6):4879–89.

51. Sunder A, Hanselmann R, Frey H, Mülhaupt R. Controlled Synthesis of Hyperbranched Polyglycerols by Ring-Opening Multibranching Polymerization. Macromolecules 1999;32(13):4240–6.

52. Zhao L, Xu Y-H, Akasaka T, et al. Polyglycerol-coated nanodiamond as a macrophage-evading platform for selective drug delivery in cancer cells. Biomaterials 2014;35(20):5393–406.

53. Zhao L, Xu Y-H, Qin H, et al. Platinum on Nanodiamond: A Promising Prodrug Conjugated with Stealth Polyglycerol, Targeting Peptide and Acid-Responsive Antitumor Drug. Adv Funct Mater 2014;24(34):5348–57.

54. Janzer M, Larbig G, Kübelbeck A, Wischnjow A, Haberkorn U, Mier W. Drug Conjugation Affects Pharmacokinetics and Specificity of Kidney-Targeted Peptide Carriers. Bioconjug Chem 2016;27(10):2441–9.

55. Wischnjow A, Sarko D, Janzer M, et al. Renal Targeting: Peptide-Based Drug Delivery to Proximal Tubule Cells. Bioconjug Chem 2016;27(4):1050–7.

56. Awada H, Daneault C. Chemical Modification of Poly(Vinyl Alcohol) in Water. Appl Sci 2015;5(4):840–50.

57. Diop A, Awada H, Zerrouki R, Daneault C, Montplaisir D. Tosylation and Characterization of Lignin in Water. Ind Eng Chem Res 2014;53(43):16771–6.

58. Finšgar M. EQCM and XPS analysis of 1,2,4-triazole and 3-amino-1,2,4-triazole as copper corrosion inhibitors in chloride solution. Corros Sci 2013;77:350–9.

59. Ciampi S, Böcking T, Kilian KA, James M, Harper JB, Gooding JJ. Functionalization of Acetylene-Terminated Monolayers on Si(100) Surfaces: A Click Chemistry Approach. Langmuir 2007;23(18):9320–9.

60. Brosnan SM, Brown AH, Ashby VS. It Is the Outside That Counts: Chemical and Physical Control of Dynamic Surfaces. J Am Chem Soc 2013;135(8):3067–72.

CHAPTER 4: HOW TO IMPROVE XPS ANALYSIS AND DATA INTERPRETATION TO STUDY GRAPHENE OXIDE AND OTHER NANOMATERIALS

4.1 Introduction

XPS is a non-destructive surface analysis technique. With this method it is possible to measure the atomic composition and the chemical state of the constituents on a surface (3-10 nm thickness).[1] The information on the chemical state can be easily extracted since the binding energies between atoms are sensitive to the chemical environment of the same atoms. The chemical environments that deshield the atom of interest will cause increased binding energies on the core electrons. Vice versa decreased binding energies will be observed for the core electrons of atoms that withdraw electrons from their neighbouring atoms.[2]

This spectroscopy technique is often used to analyse nanomaterials. Establishing the atomic composition is convenient to find contaminants and presence of trace elements, or to quantify the introduction of certain functional groups. For graphene derivatives, XPS has been widely applied to determine the amount and type of oxygenated species still present after chemical processes (*i.e.* reduction).[3–7] Indeed, from the chemical shift of the elements, it is possible to understand the type of chemical bonds that are present in the sample.[2]

Due to the complexity of GO, this technique is valuable to understand better the surface chemistry of this material. XPS analysis can prove the presence of contaminants on the surface of GO left from the synthesis process and the type and amount of the functional groups present. In addition, by combining the data obtained with different characterization techniques, the risk of misinterpretation and loss of information due to potential modification of the material during the analysis decreases. Indeed, as mentioned in the Introduction (Paragraph 1.4.3), GO is sensitive to heating, irradiation and other conditions used for characterization. XPS, for example, can cause X-ray degradation of GO, mainly due to local heating. Similar degradations can be observed for GO also in Raman and AFM measurements as well. To limit this phenomenon and avoid misinterpretations, it is important to shorten the analysis time and use also other characterization techniques.

For GO, considering that carbon is the main element present, the attention is focused on the interpretation of the C1s high resolution spectrum. In the literature, a lot of different interpretations of the carbon high resolution spectra of GO can be found. Indeed, the data interpretation is a sensitive matter due to the complexity of the material. Still, there are too many differences, most probably due to the partially insulating character of GO that causes a charge accumulation and consequently a shift of the peaks, and to the difficulty to have XPS peak standards (XPS analysis of similar simpler molecules taken on the same instrument to have the exact values for each functional group) for this material.

Dubin *et al.* used XPS analysis to confirm the reduction of GO.[5] They deconvoluted the spectra in C-C, C-O, C=O, COOH peaks (Figure 4.1). The interpretation of the spectra of GO and reduced GO seems plausible. However, it appears that there is a charge shift to higher binding energies for the spectrum of GO. GO usually shows as main peaks the C-C/C=C and the C-O peak. In this article, instead, the C-O and C=O appears to be the main peaks. There are two possibilities: either the composition of GO is different than usual, or the sample underwent a charging effect during XPS analysis, shift that brought to a wrong interpretation of the data. Indeed, GO opposite to graphene, due to its partial insulating character, which is related to its oxidation degree, can undergo this type of charging phenomena.

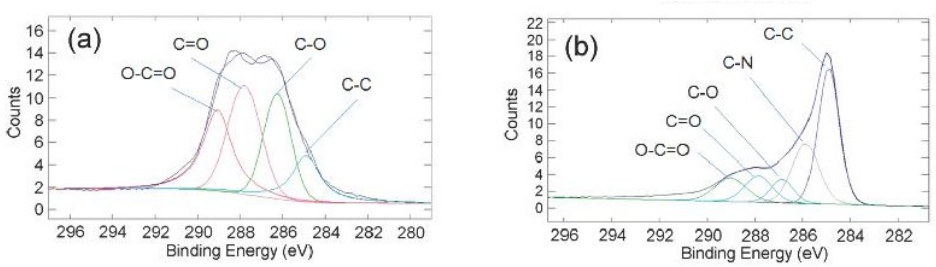

Figure 4.1 XPS carbon high resolution spectra of a) GO and b) rGO. Figures adapted from reference 5.

In another study performed by Ganguly *et al.*, XPS analysis was used to test the thermal deoxygenation of GO. The carbon high resolution spectra has been corrected to the C1s reference line at 284.5±0.2 eV prior to deconvolution, to correct this charging phenomenon.[3] Afterwards, the spectra have been deconvoluted in C=C, C-OH, C-O-C, C=O, COOH (Figure 4.2). This is a plausible interpretation. However, GO is composed of both C sp^2 and C sp^3, detected at 284.5 eV and 285.2 eV, respectively, in an unknow ratio between them. Thus, is it correct to do a charge correction to the C1s at 284.5 eV if we do not know what is the major carbon component present? Or is this choice a too high approximation if afterwards we divide the spectra in peaks that are separated between each other by about 1 eV?

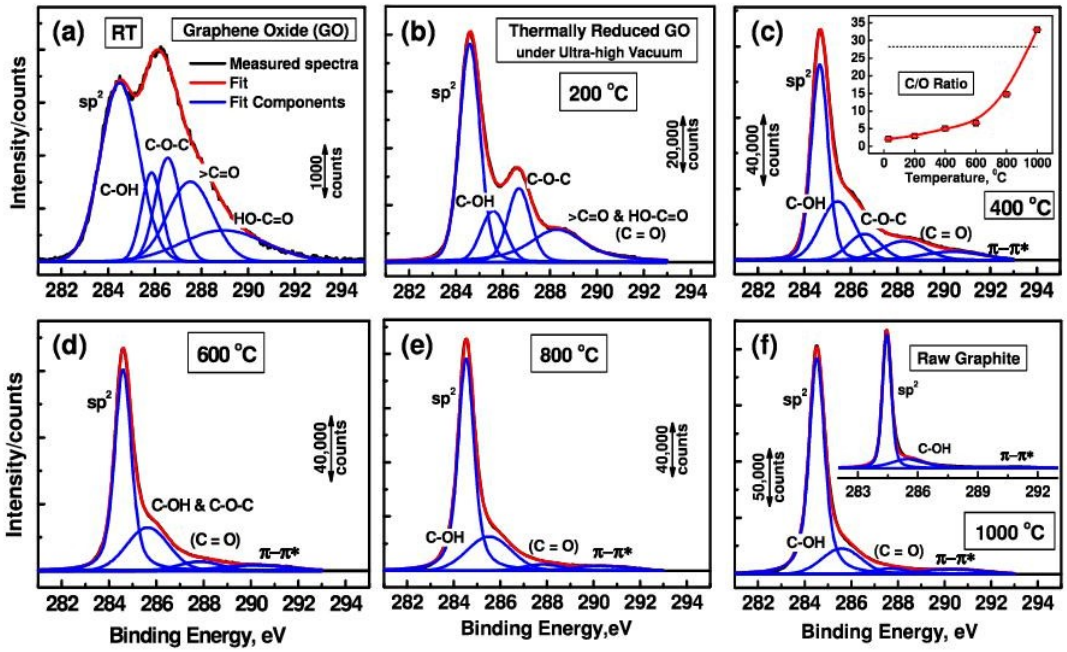

Figure 4.2 XPS carbon high resolution spectra of a) GO b) GO treated at 200°C c) GO treated at 400°C d) GO treated at 600°C e) GO treated at 800°C and f) GO treated at 1000°C. Figure adapted from reference 3.

All these interpretation issues brought to an elevated number of values assigned to the chemical species present in GO. If we compare the binding energies assigned to the different functional groups of GO, we can find important discrepancies. Indeed, if we analyse the carbon high resolution spectra deconvolution of two articles, one of Kumar *et al.* and the other of Kadam *et al.*, there are clear differences in the peak assignment.[8,9] In the spectrum interpretation of Kumar *et al.*, C=C, C-C, C-OH, C-O-C, C=O, COOH are located at 284.4, 284.8, 286.0, 286.7, 287.9 and 288.9 eV, respectively (Figure 4.3 a). In the interpretation of the spectrum of Kadam *et al.* instead, these same peaks are located at 284.0, 284.5, 285.5, 286.5, 287.5 and

288.4 eV (Figure 4.3 b). Many other similar examples exist in the literature. Only to mention other two contributions, Stobinski *et al.* assigned the C=C, C-C, C-OH, C-O-C, C=O, COOH at 284.5, 285.2, 286.4, 287.1, 288.0 and 289.2 eV, respectively, meanwhile Yang *et al.* assigned C-C/C-H, C-OH, C=O and COOH at 284.5-285.0, 286.0-286.5, 287.0-287.5 and 288.5-289 eV(Figure 4.3 c,d).[7,10] Due to the proximity of the binding energies of the peaks present in the GO carbon spectra, these little differences are significant and can lead to an important misinterpretation of the data.

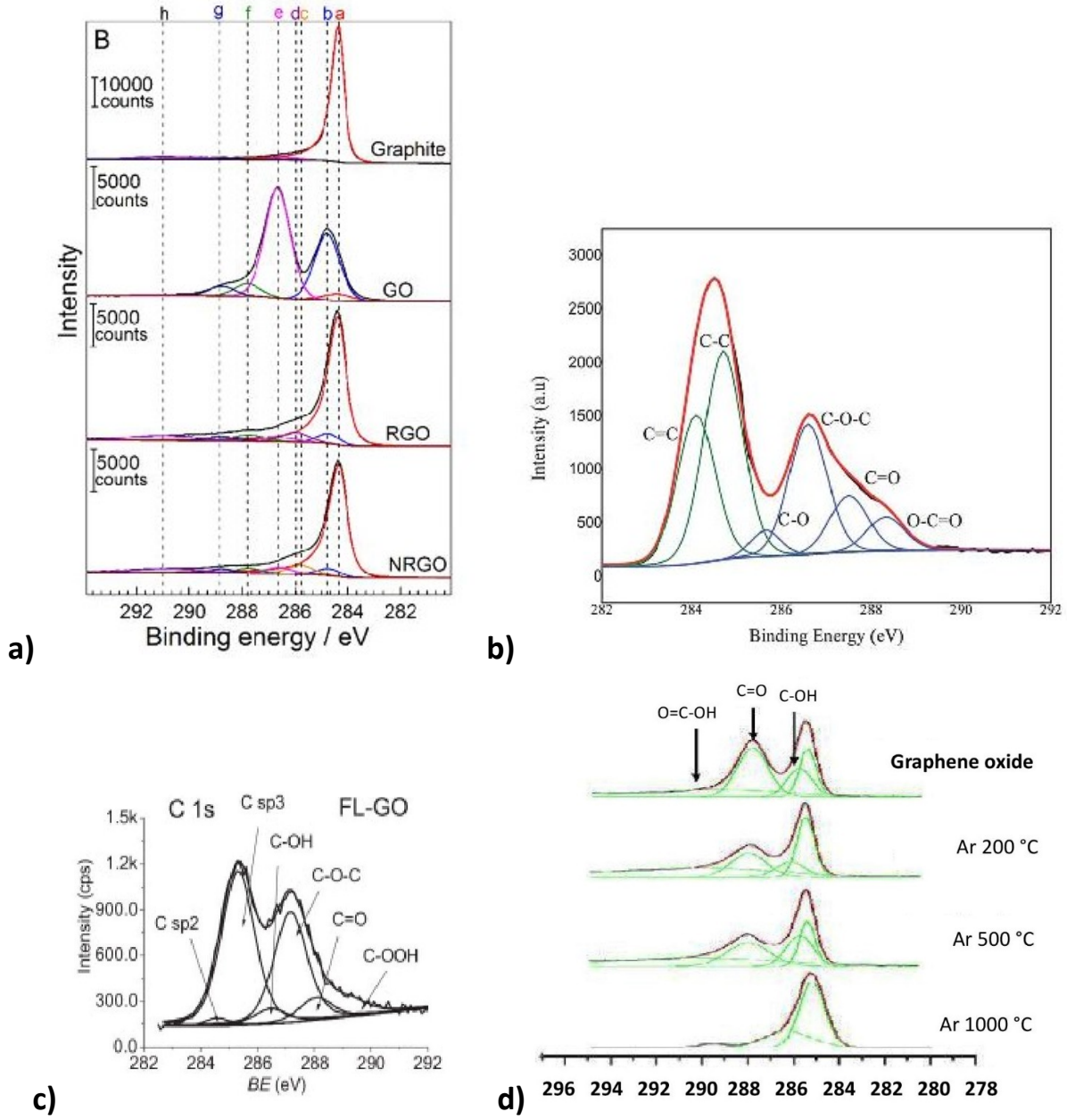

Figure 4.3 XPS carbon high resolution spectra of a) Kumar *et al.* showing: graphite, GO, rGO and N-doped rGO (a: C sp^2; b: C sp^3; c: C–N; d: C–OH; e: C–O–C; f: C=O; g: C(O)O; h: π → π* groups), b) Kadam *et al.* showing GO, c) Stobinski *et al.* showing few-layer GO and d) Yang *et al.* showing GO treated at different temperatures. Figures adapted from references 7, 8, 9 and 10.

At this point two questions arise:

- What is the best XPS data interpretation to limit erroneous conclusions?
- What is the range of error that we should accept?

4.2 Objectives of this chapter

In the main research topics of my project there has been an extensive need of high-resolution characterization techniques to understand the chemistry of GO and the changes it underwent following its surface functionalization. Because of the long times needed to obtain a solid state MAS NMR analysis and the quantity of samples required (~ 20 mg), XPS analysis was used as main technique for its fast and high resolution measurement. As soon as I started to use it, I faced these two main issues: i) charge shift, and ii) peak assignments. Thus, my objective was to improve XPS analysis of GO samples and limit shift phenomena in order to be able to exploit at maximum the information that can be taken from this spectroscopic technique.

4.3 Results and discussion

I have applied XPS analysis mainly to GO, but I have also analyzed other nanomaterials, including boron nitrite, molybdenum sulfide, carbon nanotubes and graphene.[11–15] Besides GO, all the other nanomaterials analyzed have a good conductivity, thus they do not generate charging problems during XPS analysis. GO, instead, due to the mixed composition of conductive and insulating patches, shows differential charging that makes a precise analysis difficult.

4.3.1 Carbon nanomaterials

Different strategies were tested to improve XPS analysis of GO. First, the instrument settings were improved to verify if it was possible to obtain a better definition of the spectra. Afterwards, several substrates were investigated to see if it was possible to limit the charging effects. Finally, reference elements were studied to see if it was possible to use them to correct the shifts in the spectra caused by charging.

4.3.1.1 Instrument settings: Adjusting energy pass and binding energy step size

To improve the XPS analysis for GO, I first started to change the XPS parameters used during the analysis. There are two main parameters to consider improving the resolution of the spectra: 1) the energy pass (Ep), and 2) the binding energy step size (Es). The Es is the number of points taken in the binding energy interval analyzed (Figure 4.4 a). By decreasing the Es, the information is collected at smaller intervals. The Ep is the potential difference between both hemispheres of the analyser.[16] When the Ep is increased, more electrons pass through the analyser, obtaining signals with higher intensity but lower resolution. By using lower Ep, we obtain higher resolutions in the spectra. As a matter of facts, by decreasing the energy pass, the number of photoelectrons collected is reduced and the signal/noise ratio is increased. Therefore, by decreasing the Ep, the full width at half maximum (FWHM) of the peaks decreases, and it is easier to separate different peaks. But the intensity of the signal decreases as well (Figure 4.4 b). Usually an Ep between 10 and 25 eV is suggested for high resolution spectra, and for nanomaterials, including GO, an Ep of 10-15 eV is preferred.[17]

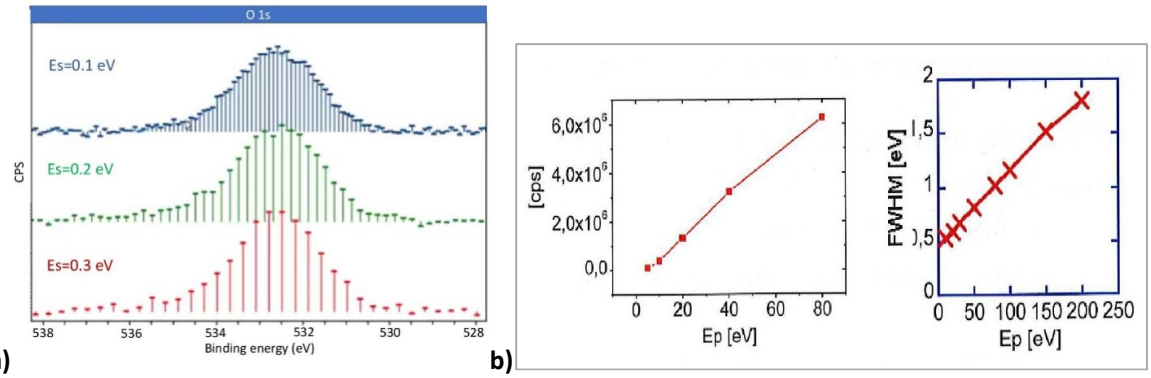

Figure 4.4a) XPS O1s high resolution spectra taken with different Es; b) Graphs showing the behaviour of FWHM and signal intensity by changing the Ep. Figures adapted from references 17,18.

In my analyses, I first tried to modify the Es. The Es suggested for the XPS apparatus I used, a ThermoFisher K-alpha, is 0.1 eV that can be decreased to 0.05 eV in case spectra of better quality are needed. I tested both Es values (Figure 4.5 a) and I could notice that there was no significant difference in the spectra and in their deconvolution. Thus, considering that a spectrum with a Es of 0.05 eV takes twice the time of the spectrum taken at Es of 0.1 eV, time in which the sample could also undergo degradation, I opted to keep the Es at 0.1 eV.

Afterwards, I tested different Ep values. For a ThermoFisher K-alpha an Ep=50 eV is suggested for high resolution spectra by the apparatus supplier. Considering that for nanomaterials an Ep=10 eV is generally recommended, I investigated the possibility to decrease this parameter. A Ep of 10, 20, 30, 40, 50 eV was tried on GO, keeping the time of the analysis constant (Figure 4.5 b).

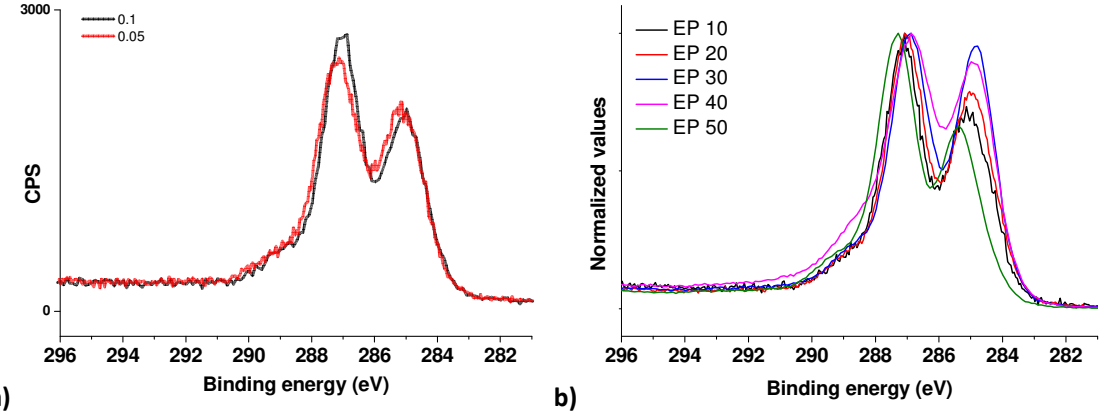

Figure 4.5 XPS carbon (1s) high resolution spectra of GO taken a) with different Es; b) with different Ep (normalized spectra).

For the trials with different Ep values, the same GO batch was employed. The analysis was repeated three times for each Ep on different positions (only one analysis is shown), and for each trial at the Ep chosen a different sample deposition was analyzed. Thus, we should consider the variability of the starting material, of the thickness of the deposition and the variability due to charging of the material. Unfortunately, no improvements in the resolution quality of the spectra could be observed for ThermoFisher K-alpha apparatus by changing the Ep. Indeed, by looking at the carbon high resolution spectra, in Figure 4.5b, no changes in the resolution could be observed. The analysis taken with an Ep=10 appears to be noisier since less electrons were collected, but the quality of the signal should be improved. Longer times could be employed for lower Ep, but longer times increase the risk of degradation of GO. Moreover, longer times

would, probably, only decrease the noise. The spectra were not charge shift corrected, thus, as it appears, the analysis performed with an Ep=50 displayed a more important charge shift compared to the others. Other differences that could be detected are in the ratio between the C-O area and the C-C one. No conclusion from these differences can be taken before having repeated the analysis, due to the high variability in GO samples. As it appears, the broadening caused by the apparatus at the Ep applied is less important than the broadening introduced by the characteristics of the material (material composition and homogeneity and thickness of the deposition).
In Figure 4.6 the same carbon high resolution spectra as for Figure 4.5b are reported, without normalization of the data.

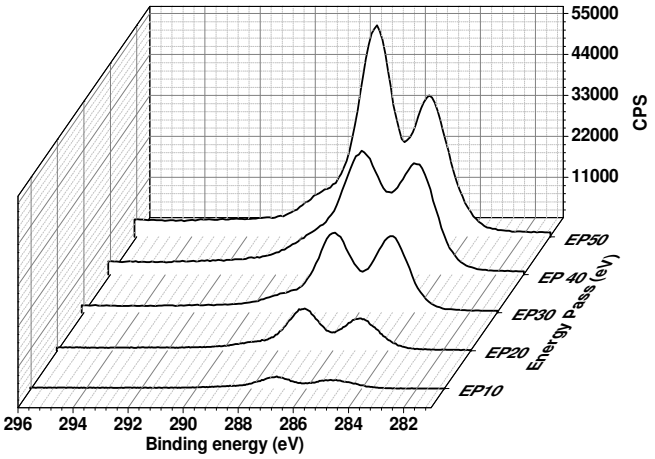

Figure 4.6 XPS carbon (1s) high resolution spectra of GO taken with different Ep values.

As it is possible to observe there is a significant decrease in the intensity of the signal in the spectra by decreasing the Ep. Thus, considering that by decreasing Ep we lose signal intensity without obtaining a better resolution we decided to use an Ep=50 eV.

In conclusion, no significant improvement for the analysis of GO was obtained on a ThermoFisher K-alpha by changing the analysis settings. Thus, to obtain a good intensity of signals, we decided to perform the XPS analysis with an Es=0.1 eV and an Ep=50 eV.

4.3.1.2 Substrate matters: insulating *versus* conductive

In XPS, the electrical charging of insulating samples is a main concern. The electrical conductivity of GO depends on the degree of oxidation. Thus, GO can be semi-conductive as well as insulating. Insulating samples pose a unique challenge for XPS analysis. Due to the loss of photoelectrons during the photoemission process, a positive charge will build up on the samples. This effect produces a shift of the peaks in the spectrum to higher binding energies. Commonly, a low energy electron flood gun is used to replace the emitted electrons.[2] An overcompensation is often encountered too, leading to an excess of negative charging.[19] In post-processing, the peaks can then be shifted back using an internal standard.
The charging effect of the insulators depends on different factors: i) on the experimental conditions (irradiation conditions, flood gun settings and surrounding conditions during analysis), and ii) the characteristics of the sample (sample composition and preparation).[20,21] The lack in homogeneity of GO also contributes to the difficulty to obtain a well repeatable spectrum.[17] This inhomogeneity has already been noticed before for other carbon nanomaterials. Moreover, GO, due to its mixed semi-conductive and

insulating character, can show differential charging.[2] In differential charging there are two contributions: 1) a vertical differential charging, and 2) an horizontal (also called lateral) differential charging. The first one broadens the peak uniformly; meanwhile, the second one usually produces a shoulder. The lateral differential charging can result from the fact that the area viewed by the analyser is larger than the irradiated area, or also because of the inhomogeneities in the sample composition, generating in both cases a peak shift and broadening.[22] The vertical differential charging instead results from the electrons flowing from the ground to the analyzed surface. This charging depends also on the thickness of the deposition and it disappears when the sample is insulated from the spectrometer.[22] These effects result in changes in the peak positions, and an erroneous assignments of the chemical states may result. Two factors can help to avoid or limit this differential charging. The first one is the sample preparation: the flatter is the sample, the lower charging differences are expected in the different spectra of the same sample. The second factor is the choice of the substrate. It has been reported that the electrical insulation of the entire sample from the specimen holder would avoid this vertical differential charging effect.[2] This insulation would make the entire sample to behave as non-conductive. Thus, I tried to do both: to improve the sample preparation and to test different substrates. As substrates, I chose a silicon wafer with a SiO_2 coating of about 10 nm, indium foil with 99.99% purity, carbon tape and copper tape. These are all commonly used substrates for XPS.

This study has been done at the same time of the previous studies reported in chapter 2 and 3. Thus, there has been a double intent, to improve the XPS analysis for GO samples and obtain the XPS data of the samples I was working with in the other projects. For the sake of clarity the less modified samples were chosen for comparison: starting materials and control samples.

GO has been drop casted on the silicon wafer or pressed onto indium foil with a FT-IR KBr tablet pressing system to improve the sample preparation, and compared to the analysis taken on the sample as powder.

In Figure 4.7 it is possible to compare the analysis of GO taken as a powder or drop-casted on a silicon wafer.

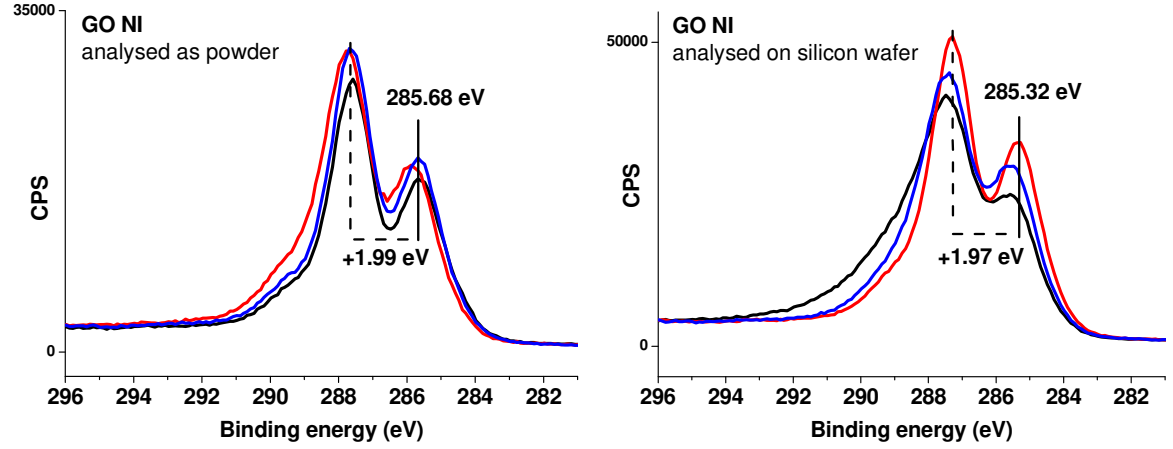

Figure 4.7 XPS C1s high resolution spectra of **GO NI** analyzed as a powder on the left and drop casted on a silicon wafer on the right. Every analysis was repeated on three different positions on the same samples. These three analyses are shown in black, red and blue, respectively. The maximum of the peak of the carbon region is reported in the spectra, with the respective distance from the peak maximum in the carbon oxygen bond region.

The change of preparation method did not show important differences in the repeatability of the spectra. Indeed, both gave a good analysis depending on the flatness of the sample. For the powder, it depended on how the sample was pressed prior to analysis. Meanwhile, for the drop-casted sample it was related to the

dispersibility of the sample in the solvent used. If the sample was aggregating while drying on the support, a less flat deposition was obtained. Thus, to improve the flatness of the sample, I tried to press it on an indium foil. The sample has been analyzed on In foil directly in contact with the support, or on In foil deposited on a silicon wafer (Figure 4.8). Indium foil is a conductive substrate and it was compared with indium foil on silicon wafer to have a sample electrically insulated from the support. The main difference in peak intensity between **GO-Jp** and **GO17_CONT**, as mentioned in the previous chapters, is due to the loss of some labile oxygenated function from the surface of GO in the case of **GO17_CONT** that happens even in mild conditions.

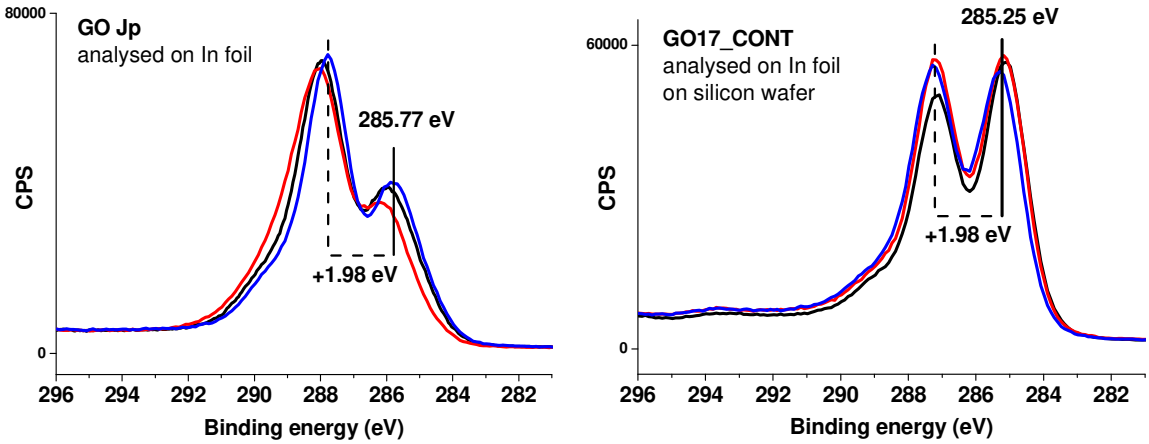

Figure 4.8 XPS C1s high resolution spectra of **GO Jp** and **GO17_CONT** pressed onto an In foil and Indium foil on silicon wafer, respectively. Every analysis has been repeated on three different positions on the same samples. These three analyses are shown in black, red and blue, respectively. The maximum of the peak of the carbon region is reported in the spectra, with the respective distance from the peak maximum in the carbon oxygen bond region.

In both cases, there has been a little improvement in the quality of the spectra. But, still, differences in charging and repeatability of the analysis has been noticed (only the best spectra were chosen for all the figures). Thus, the sample flatness is not the only factor to take into consideration. Between the two substrates only little improvement can be observed in the charge shift of the spectra (285.8 eV *versus* 285.3 eV from the C sp^2 and sp^3 at 284.5-285.2 eV).

As mentioned before, I decided to deposit the sample also on a tape. Tapes are a suggested support for carbon nanomaterials. We chose two types of tapes, a classic carbon tape and a copper tape (Figure 4.9). The carbon tape was attached on a silicon wafer, meanwhile the copper tape was directly put in contact with the support. Thus, the first one is an insulating substrate, meanwhile the second is a conductive one. The samples were manually pressed on the tape.

The samples analyzed on a tape, for both carbon and copper tape, showed a better repeatability of the analysis. Nevertheless, little differences could be still noticed. This could be probably attributed to the inhomogeneity in the composition of GO (for both) and the thickness of the deposition (for GO-Jp, because of the conductive substrate) that causes also differences in charging. Interestingly, for carbon tape and In foil deposited on silicon wafer, less differences in charge shift can be observed in the spectra of the same sample (Figure 4.8b and 4.9a). This is probably due to the insulating character of the silicon wafer that causes less interactions between the GO sample and the XPS support. This would confirm what was stated before: that insulating substrates would make the sample behave as non-conductive, limiting vertical differential charging phenomena.

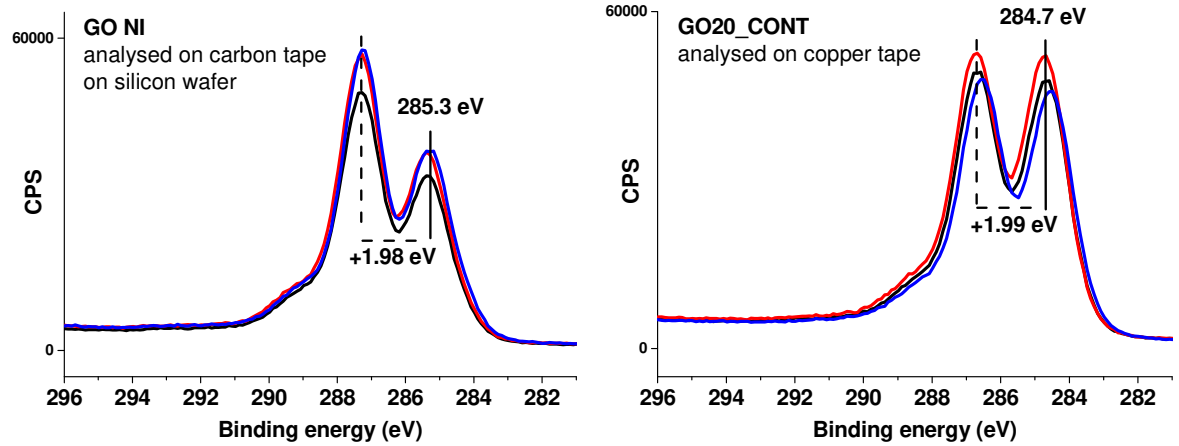

Figure 4.9 XPS C1s high resolution spectra of **GO NI** analyzed on a carbon tape deposited on a silicon wafer and **GO20_CONT** analyzed on a copper tape. Every analysis has been repeated on three different positions on the same samples. These three analyses are shown in black, red and blue, respectively. The maximum of the peak of the carbon region is reported in the spectra, with the respective distance from the peak maximum in the carbon oxygen bond region.

By changing the sample preparation and the type of substrate, I tried to both improve the repeatability of the analysis and the overall charge shift of the samples. If we compare all the spectra, by looking at the peak value of the carbon-carbon bond area, an important charge shift can be observed for all the specimens (from the C sp^2 and sp^3 values at 284.5 and 285.2 eV, respectively). All the spectra shown above were taken in the same conditions (also the flood gun settings were kept constant). The fact that this shift is different for all spectra excludes the possibility of a systematic machine error. Considering that only pristine GO and control samples were considered for comparison, no major differences in the peak position are expected because of sample composition. This is also confirmed by the constant distance between the two main peaks in the spectra (around 1.98 eV), which indicates that the contribution between the C sp^2 and C sp^3 is similar and differences between the samples were not the cause of this charge shift. All spectra show a different charge shift mainly to higher binding energies. This shift has not been significantly improved by changing the substrate. The only spectrum that shows a less important shift is **GO20_CONT** measured on a copper tape. Thus, this substrate seems to be the most appropriate to avoid both charge shift and repeatability issues.

The choice of the silicon wafer and In foil was also considered because it allows to have an internal reference to use for peak shift correction. Carbon and copper tapes, instead, show in the spectra a major carbon peak (because of the glue on the surface and the adventitious carbon). Thus, there are two negative aspects to consider for tapes: 1) the absence of an internal reference, and 2) the impossibility to verify if there is a contribution of the substrate in the spectrum of the sample. Instead, by using silicon wafers and In foil, if the elements of the substrate can be identified in the survey spectra, it can be immediately indicated an insufficient sample deposition on the substrate. Moreover, another difference was noticed between the analysis of the sample in form of a powder or deposited on a substrate. Indeed, a higher content of impurities was detected in the sample deposited on a substrate. Thus, extreme care should be taken by preparing the samples and pressing them on the substrate to avoid contamination.

In conclusion, all substrates show positive and negative aspects. The tape seems the most appropriate substrate to limit charge shift and differential charging. Indium foil and silicon wafer instead can also be used as peak shift reference for charge correction (if the high resolution spectra of the respective elements are taken). Moreover, insulating substrates showed to limit vertical differential

charging of the samples. However, in all the cases there is still an important peak shift that should be corrected.

4.3.1.3 Charge correction to a reference material

The first attempt for charge correction was done by measuring the signal of gold during the XPS analysis. For gold, the spectrum of Au 4f was recorded. For this spectrum, a spin orbit splitting is expected. Thus, two peaks can be observed with an area ratio of 3:4. Au $4f_{7/2}$ peak is expected at 83.95 eV.[2] Analysis of gold on silicon wafer was performed as reference when the spectra of GO NI deposited on silicon wafer were investigated. These two samples were analyzed on different silicon substrates, one after the other during the same analysis. As we can observe in Figure 4.10 there is a different charge shift, one to higher and one to lower binding energies. As it appears they undergo different charging effects when analyzed with the support of an electron flood gun for charge compensation.

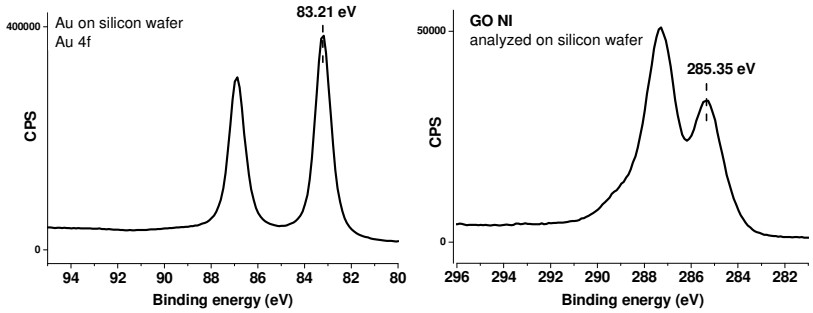

Figure 4.10 XPS high resolution spectra of Au4f for a gold sample and C1s for **GO NI**.

To obtain a better reference that shows the same charging effect of the sample, the substrate onto which the sample was deposited, was analyzed. As for gold, also In 3d shows spin orbit splitting. Thus, two peaks can be observed in the spectra with an area ratio of 2:3 (Figure 4.11 left). As we can observe in the spectra of In 3d (Figure 4.11 a,b) there is a main contribution of In_2O_3 on the surface of the In foil, confirmed by the In:O ratio in the survey. Thus, we considered as reference the peak of In $3d_{5/2}$ for In_2O_3 that is expected at a binding energy of 444.8 eV.[2] For the sample deposited on silicon wafer the spectra of Si 2p was recorded. Si 2p shows closely spaced spin orbit components (Δ=0.63 eV) with an area ratio of 1:2. The peak of Si $2p_{3/2}$ is expected at a binding energy of 99.4 eV.[2]

If we observe Figure 4.11, taking the signal of the substrate as reference for charge shift, correction seems a good option. Similar results were obtained for both In foil and silicon wafer (Figure 4.11 and 4.12).

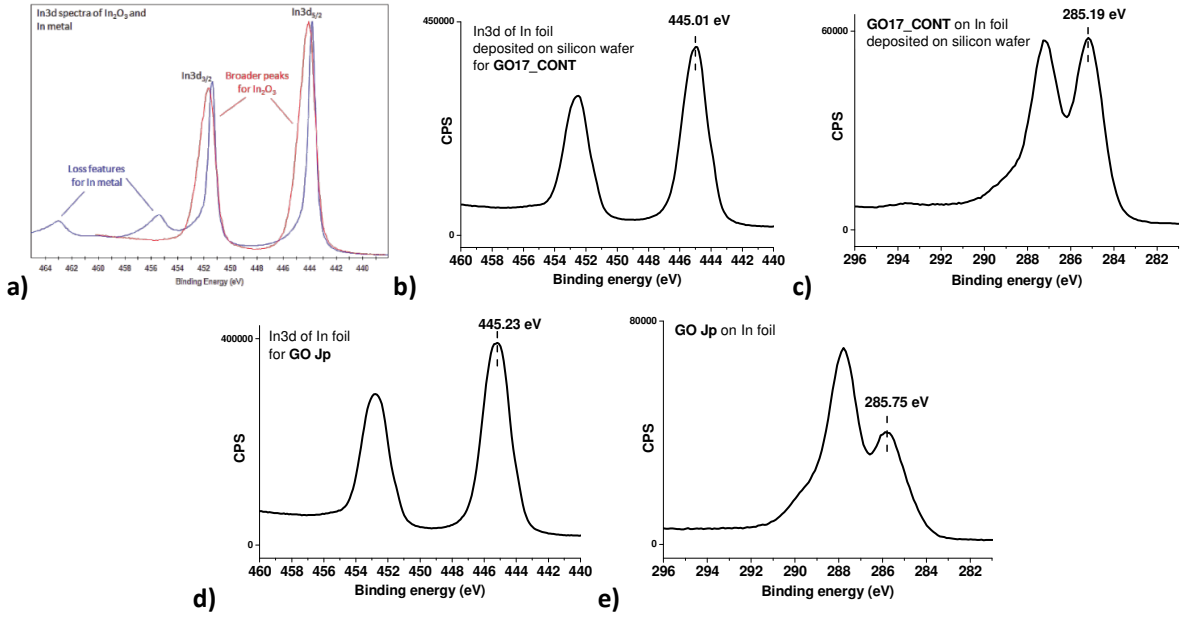

Figure 4.11 XPS high resolution spectra of In3d taken from reference 23 (a), and In foil (b,d) and C1s of **GO17_CONT** and **GO Jp** (c,e).

For **GO17_CONT** the correction would shift the spectra from 285.19 eV to 284.99 eV, meanwhile for **GO Jp** it would shift from 285.75 eV to 285.3 eV. If for **GO17_CONT** it seems a plausible correction, for **GO Jp** the final value appears not to be the appropriate yet.

Surprisingly, **GO11** analyzed on silicon wafer did not show a significant charge shift during this analysis, confirmed by the binding energy value of Si $2p_{3/2}$ (99.48 eV instead of 99.40 eV – Figure 4.12).

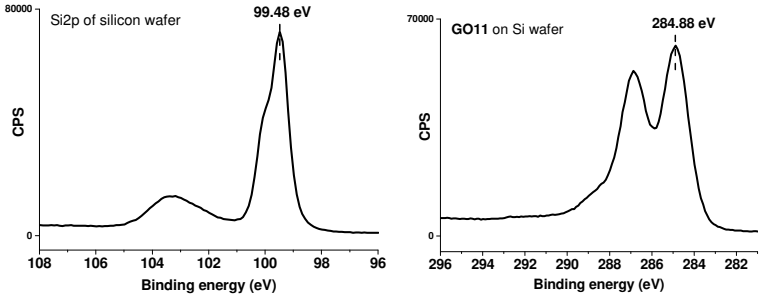

Figure 4.12 XPS high resolution spectra of Si2p taken from the substrate and C1s of **GO11**.

Another trial was performed to further improve the charge correction with the support of a reference element for GO. NaCl was mixed to GO before XPS analysis to have a reference mixed to the sample. This trial was done to obtain the perfect charge shift value for GO. Indeed, since NaCl was mixed to GO, the same charge shift was expected in the spectra. NaCl was chosen because its signals are not supposed to overlap with those of GO. GO and NaCl were mixed in powder form in a mortar and then pressed onto indium foil. The peak of Na 1s is expected at 1071.9 eV for NaCl.[2] Meanwhile Cl 2p has two spin orbit components, close to one another and Cl $2p_{3/2}$ is expected at 198.2 eV for NaCl.[2] If we look at Figure 4.13, we can observe that there are different charge shifts for the element analyzed. Moreover, it seems that some degradation phenomenon occurred if we look at the C1s high resolution spectra of **GO8_CONT** after mixing with NaCl, phenomenon that is still unclear.

Thus, with the information available until now, mixing NaCl to GO, to have a reference inside the sample, appears not to be a good option. The use, instead, of the substrate as reference seems preferable.

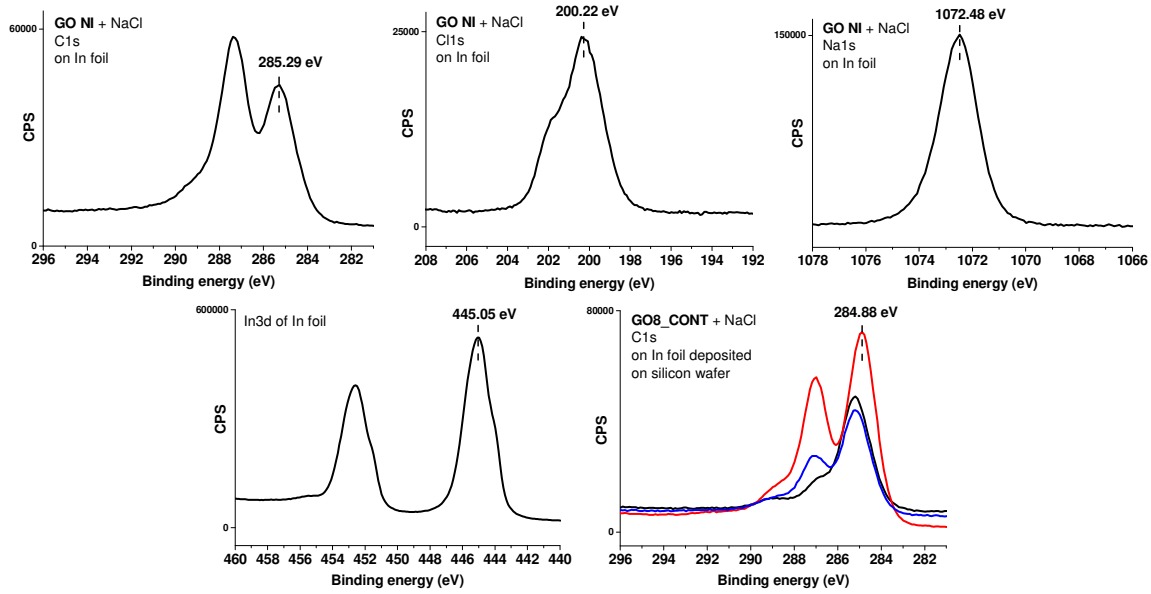

Figure 4.13 XPS C1s, Cl2p and Na1s high resolution spectra of **GO NI**, In3d high resolution spectrum of In substrate and C1s high resolution spectra of **GO8_CONT**.

4.3.1.4 Optimization of data analysis

To understand how to interpret the results obtained from the data analysis, I performed a thorough literature research. As one can notice from Figure 4.14, many different values are reported for the different functional groups of graphene oxide.[3,7–10,24–51] As mentioned in the Introduction of this chapter, this is most probably due to the charging issues of GO and to its chemical complexity. From this study, the average value for each functional group was kept in consideration for data analysis and compared to the values reported in XPS free databases (xpsfitting and xpssimplified). Unfortunately, it was not possible to take standards on the same XPS apparatus, which would be a preferable option. Indeed, it would be the most reliable choice to avoid machine differences (between the one used in this study and those used in the references of the literature) and variability due to the chemical environment of the functional groups. In our case, the standards we would choose would be similar molecules to GO; thus, partial aromatic molecules bearing only one functional group for each molecule, in the way to obtain the precise value for each functional group present on GO.

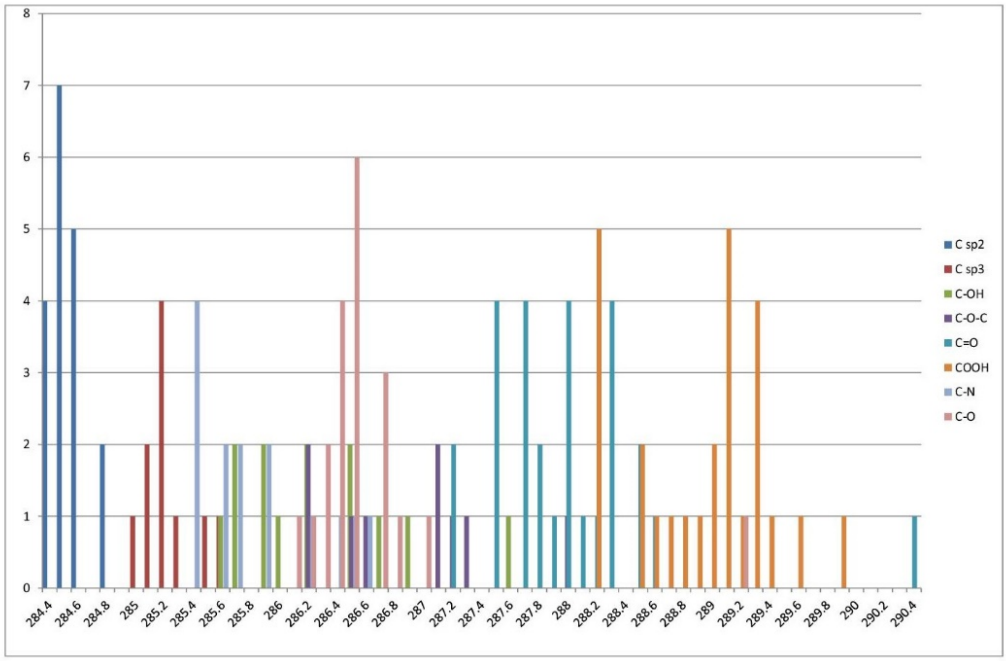

Figure 4.14 Binding energy values reported in the literature for the functional groups present on the surface of GO.[3,7–10,24–51] The values of each functional group are reported and also those for general C-O and C=O when hydroxyls, epoxides, ketones and carboxylic acids were not considered separately for fitting (the number of the articles in the y axis and the binding energy in the x axis).

Due to the inhomogeneity of carbon nanomaterials, the best would be to perform XPS imaging to increase the number of analysis taken to have statistically valid spectra. Limited by the elevated costs and time for XPS imaging, the analysis for each sample was repeated three times or more if the spectra obtained did not show a satisfactory result. By optimizing the sample preparation and substrate type, charge correction could still be ameliorated and the analysis could be partially improved. The carbon KLL Auger spectrum are often taken for diamond and graphitic materials to calculate the C sp^2 percentage of the sample in a semi-quantitative way.[52–56] Recently, this technique was also applied to GO.[57] The D parameter is not dependent from peak shift, thus, it could be used to ameliorate the charge shift correction in addition to charge correction using the substrate as reference.

In Figure 4.16, C KLL Auger spectrum of the **GO NI** is shown. The D parameter was calculated and the ratio obtained for the sample was 45 % of hybridized sp^2 carbon. This value was used to correct the charge shift of the carbon high resolution spectra and from this one all the other. Indeed, the C 1s high resolution spectrum was charge shift corrected to obtain a 45 % contribution of sp^2 carbon atoms. Hence, the maximum of the carbon-carbon bond area of the carbon high resolution spectrum was shifted from 285.6 eV to 284.8 eV. This charge shift was, afterwards, applied also to the other spectra. The deconvolution of the carbon and oxygen high resolution spectra was compared to cross check and verify the relevance of the data interpretation. In the fitting, the peak position and FWHM were constrained to increase the reliability of the analysis of the data (see Chapter 6 for details).

As it is possible to observe in Figure 4.16, this data interpretation method appears to be a good procedure to obtain reliably analyzed XPS data for GO samples.

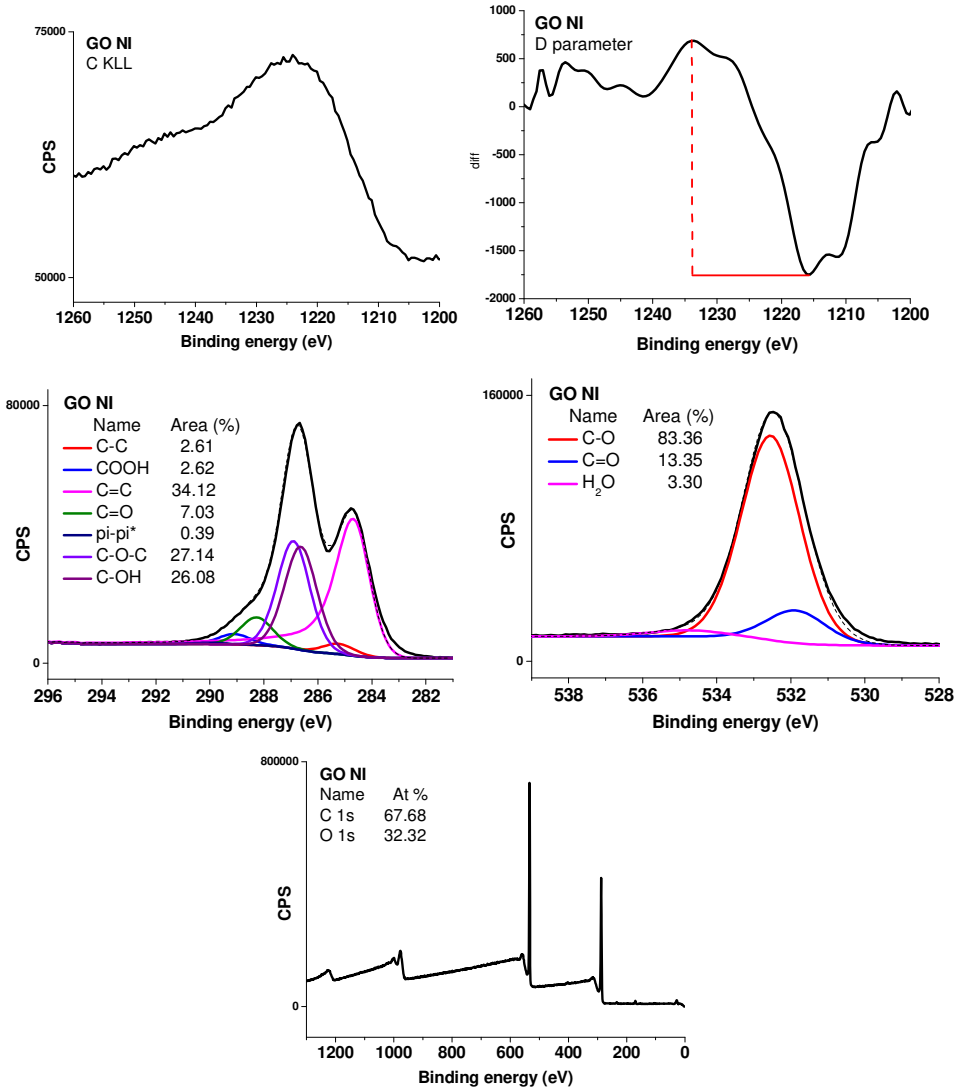

Figure 4.16 XPS survey and C1s, O1s, C KLL and first derivative C KLL high resolution spectra of **GO NI** pressed on In foil.

In conclusion, the XPS acquisition was improved considering different aspects, including the analysis conditions, the sample preparation and the spectrum comparison. We established that the important factors are:

- Careful preparation of the sample, making it flat;
- Choice of a proper substrate for XPS;
- Correct the charge shift by taking the C KLL spectra to know the sp^2/sp^3 ratio;
- To use peak and FWHM constrains for spectra deconvolution;
- To crosscheck the fitting of the different elements.

4.3.2 Other materials: Boron nitrite and molybdenum disulfide

I was also involved in the XPS analysis of molybdenum disulfide and boron nitrite in the frame of a biodegradation study. The biodegradability was investigated for future biomedical applications of these materials.

4.3.2.1 Boron nitrite

Hexagonal boron nitride (hBN) is an emerging 2D material, also known as white graphene that shows a strong oxidation resistance. The degradation of hBN treated with horseradish peroxidase (HRP), a plant enzyme, myeloperoxidase (MPO), a human enzyme from neutrophils, and UV-assisted photo-Fenton (P.F.) reaction was studied by our group.[15] In the frame of this study, the P.F. reaction was followed *via* XPS analysis. The P.F. reaction of hBN nanosheets was performed in the presence of $FeCl_3$ and H_2O_2 at pH 4 under UV irradiation at 365 nm for 100 h. This reaction generates hydroxyl radicals catalyzed by $FeCl_3$. By looking at the XPS survey spectra taken at 0, 40 and 100 h, a strong oxidation of BN was observed (Figure 4.17, left). Indeed, the percentages of boron and nitrogen decreased with a simultaneous increase in the percentage of oxygen (Table 4.1).

Table 4.1 XPS atomic percentages of hBN samples after 0, 40 and 100 h treatment *via* P.F. reaction.

	B1s	N1s	O1s
0 h	46.5 %	42.9 %	10.6 %
40 h	18.8 %	17.1 %	64.1 %
100 h	3.9 %	9.0 %	87.1 %

In the XPS high resolution spectra, instead, it is possible to observe an important decrease in the intensity of the signal of boron and a shift of nitrogen towards higher binding energies, which can be attributed to the formation of bonds with hydrogen during the oxidation process in presence H_2O_2.[58] In the oxygen high resolution spectra, instead, no significant changes can be detected, beside the increase in intensity. Moreover, due to the deposition of a small volume of sample on silicon wafer, the contribution of SiO_2 should be considered as well at 532.9 eV, that limits the interpretation of the oxygen spectra.

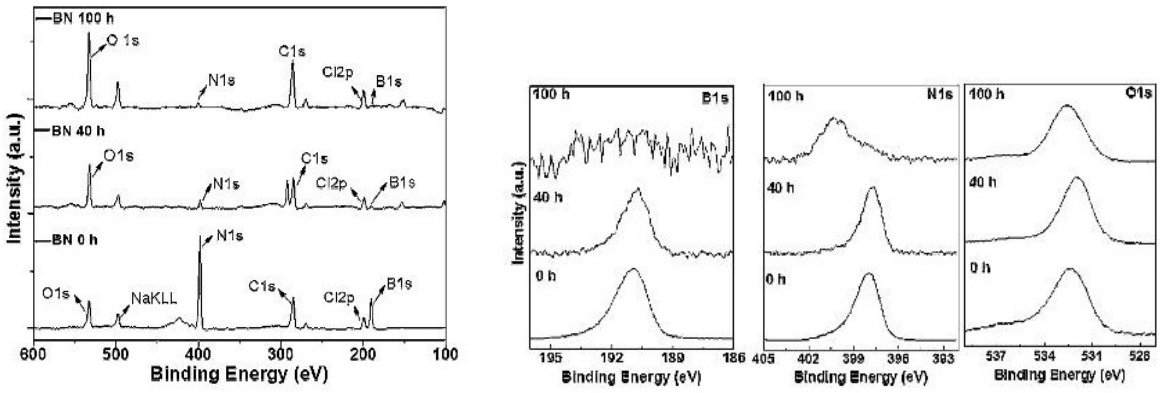

Figure 4.17 XPS spectra of hBN sheets. Left: survey spectra of hBN at 0, 40, and 100 h of P.F. reaction. Right: High resolution spectra of B1s, N1s and O1s of hBN at 0, 40, and 100 h, respectively. Figure adapted from reference 15.

Overall, the XPS analysis confirmed the degradation of BN during P.F. reaction.

4.3.2.2 Molybdenum disulfide

The biodegradability of exfoliated pristine and covalently functionalized MoS_2 (*f*-MoS_2) was investigated by our group.[14] Opposite to hBN, MoS_2 is unstable in ambient condition, it is subjected to environmental degradation over a period of several months.[59] The degradation of MoS_2 and *f*-MoS_2 was studied in presence of HRP in phosphate buffer, MPO in NaCl solution, both with addition of H_2O_2, and in presence of only H_2O_2. XPS analysis was performed to get more details about the oxidation degree of molybdenum

during the degradation process. XPS analysis was taken from the samples after treatment with HRP for 30 days, with MPO for 24 hours and H_2O_2 alone after 14 days for MoS_2 and 30 days for *f*-MoS_2.

Mo 3d is subjected to spin orbit splitting showing two peaks with 3/2 and 5/2 *j* values and an area ratio of 2:3 (Δ=3.15). S 2p, as also Mo 3d, shows spin orbit splitting as well. For S 2p there are two peaks with 1/2 and 3/2 *j* values in an area ratio of 1:2 (Δ=1.16 eV). If the two spin orbit components show two separate peaks for molybdenum, this is not the case of sulfur, because of the proximity of the two peaks. For sulfur an asymmetry can be noticed due to the contribution of S $2p_{1/2}$ and S $2p_{3/2}$.

Because of spin orbit splitting MoS_2 starting material is expected to show two peaks in the Mo 3d spectra, Mo $3d_{5/2}$ and Mo $3d_{3/2}$ at 229.1 eV and 232.3 eV, respectively.[60] After the degradation, instead, the appearance of Mo $3d_{5/2}$and Mo $3d_{3/2}$ at 232.2 eV and 235.4 eV, respectively, is expected, due to the oxidation of Mo^{IV} to Mo^{VI}.[60] In the starting material the Mo^{VI} peaks are absent.[14]

In Figure 4.18 for *f*-MoS_2 (B, D, and F) a partial degradation can be observed in the Mo 3d spectra, beside for the sample treated with MPO (D). Indeed, both species can be detected, Mo^{IV} of MoS_2 and Mo^{VI}. Pristine MoS_2, instead, showed a complete degradation in all conditions (Figure 4.18 A, C and E).

Apparently, *f*-MoS_2 shows a higher resistance to degradation compared to pristine MoS_2.

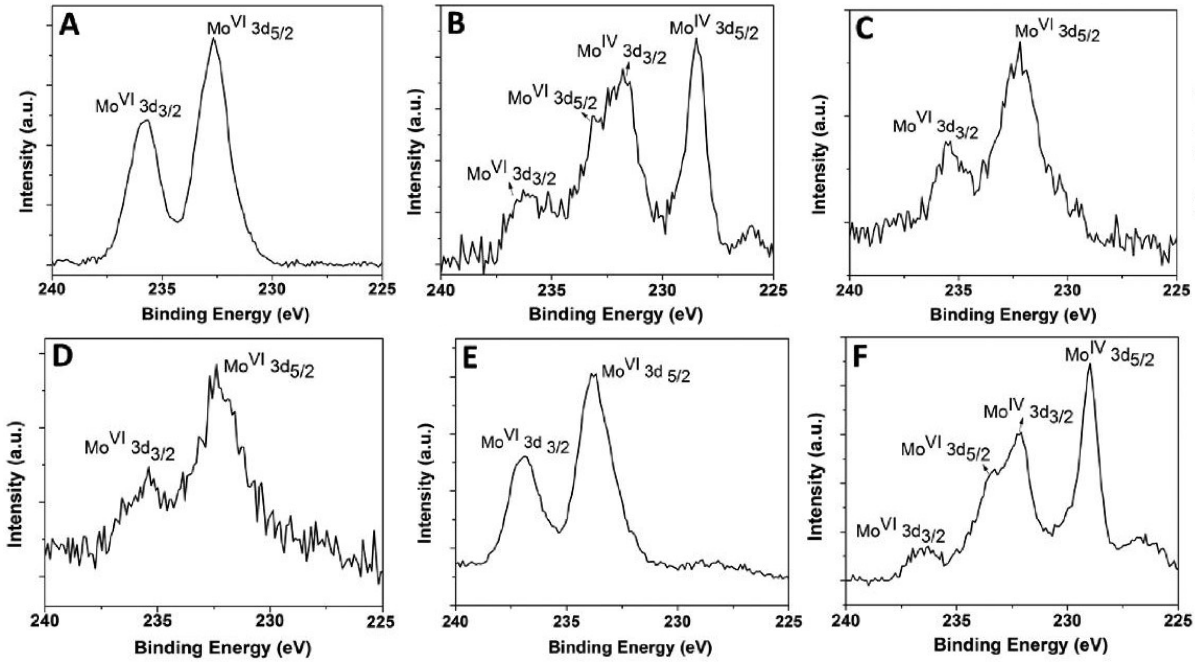

Figure 4.18 XPS Mo 3d high resolution spectra of MoS_2 and *f*-MoS_2 treated with: A,B) HRP+H_2O_2 (after 30 d); C,D) MPO+H_2O_2 (after 20h); and E,F) H_2O_2 alone (after 14 d for MoS_2 and 30 d for *f*-MoS_2). The differences in the signal intensities of the XPS spectra of the three conditions (HRP, MPO and H_2O_2) are due to the varied amounts of the final solutions recovered. In addition, the presence of salts and enzymes in the buffer used for the treatments contributes to the low signal intensities. Figure taken from reference 14.

In the spectra of sulfur, the oxidation of S^{2-} into SO_4^{2-} was confirmed. S^{2-} for MoS_2 is expected to show two peaks at 162.0 and 163.2 eV, for S $2p_{3/2}$ and S $2p_{1/2}$ respectively.[60] After oxidation, the peaks of SO_4^{2-} appear at 168.9(±0.6) eV for S $2p_{3/2}$ and 170.1(±0.6) eV for S $2p_{1/2}$ (constant distance of 1.2 eV between S $2p_{3/2}$ and S $2p_{1/2}$).[2] As in the case of Mo 3d spectra, also for sulfur partial degradation was observed for *f*-MoS_2. Indeed, the peaks of both species can be observed in the spectra of Figure 4.19 B and F. Again, exception is taken for *f*-MoS_2 treated with MPO. Total degradation is confirmed, instead, for pristine MoS_2, in line with what was observed in Mo 3d high resolution spectra.

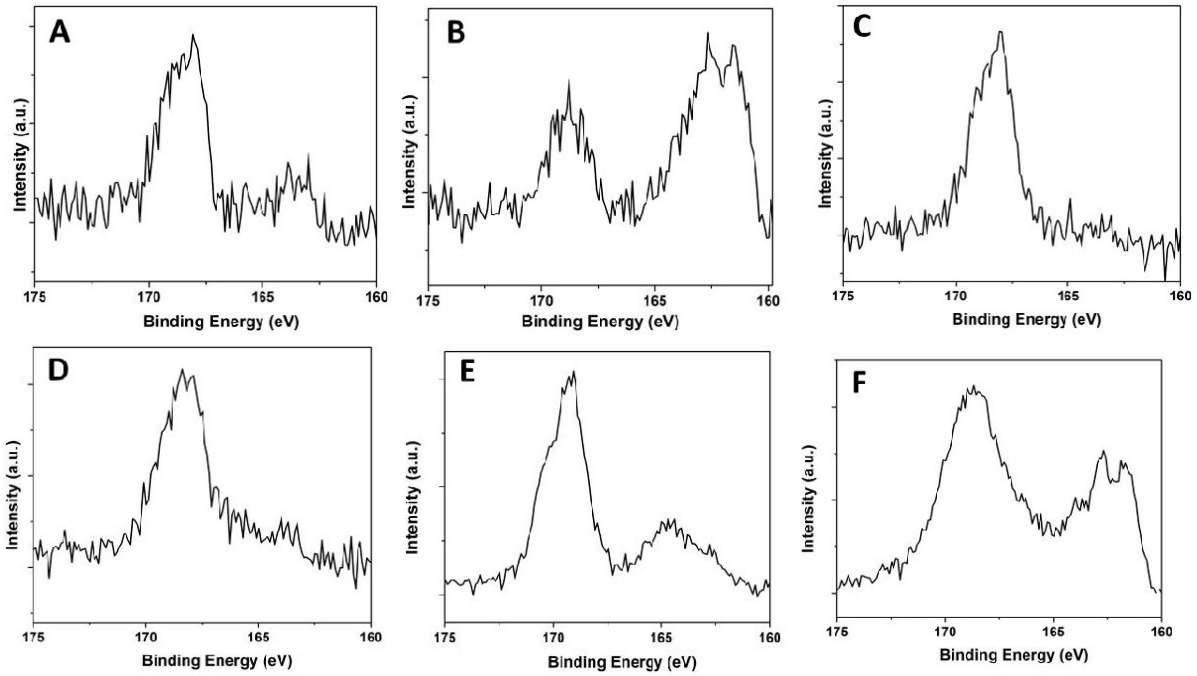

Figure 4.19 XPS S2p high resolution spectra of MoS_2 and *f*-MoS_2 treated with: A, B) HRP+H_2O_2 (after 30 d); C,D) MPO+H_2O_2 (after 20h); and E,F) H_2O_2 alone (after 14 d for MoS_2 and 30 d for *f*-MoS_2). Figure taken from reference 14.

In summary, the biodegradability of MoS_2 in biological conditions was demonstrated, using XPS as supporting tool to understand the transformation that happened.

4.4 Conclusion

In conclusion, we succeeded in the optimization of the XPS analysis conditions for GO samples to increase the reliability of the analysis and data interpretation for this material. Moreover, XPS was used also on other 2D nanomaterials mainly to follow their biodegradation. Both, hBN and MoS_2 resulted degradable, aspect that makes them suitable for biomedical applications.

4.5 Bibliography

1. Turner NH, Schreifels JA. Surface Analysis: X-ray Photoelectron Spectroscopy and Auger Electron Spectroscopy. Anal Chem 1994;66(12):163–85.

2. M. C. Biesinger. X-ray Photoelectron Spectroscopy (XPS) database [Internet]. X-Ray Photoelectron Spectrosc. XPS Ref. Pages. Available from: http://www.xpsfitting.com/

3. Ganguly A, Sharma S, Papakonstantinou P, Hamilton J. Probing the Thermal Deoxygenation of Graphene Oxide Using High-Resolution In Situ X-ray-Based Spectroscopies. J Phys Chem C 2011;115(34):17009–19.

4. Rella S, Giuri A, Corcione CE, et al. X-ray photoelectron spectroscopy of reduced graphene oxide prepared by a novel green method. Vacuum 2015;119:159–62.

5. Dubin S, Gilje S, Wang K, et al. A One-Step, Solvothermal Reduction Method for Producing Reduced Graphene Oxide Dispersions in Organic Solvents. ACS Nano 2010;4(7):3845–52.

6. Schwenzer B, Kaspar TC, Shin Y, Gotthold DW. Spectroscopic Study of Graphene Oxide Membranes Exposed to Ultraviolet Light. J Phys Chem C 2016;120(23):12559–67.

7. Yang D, Velamakanni A, Bozoklu G, et al. Chemical analysis of graphene oxide films after heat and chemical treatments by X-ray photoelectron and Micro-Raman spectroscopy. Carbon 2009;47(1):145–52.

8. Kumar K, Canaff C, Rousseau J, et al. Effect of the Oxide–Carbon Heterointerface on the Activity of Co3O4/NRGO Nanocomposites toward ORR and OER. J Phys Chem C 2016;120(15):7949–58.

9. Kadam MM, Lokare OR, Kireeti KVMK, Gaikar VG, Jha N. Impact of the degree of functionalization of graphene oxide on the electrochemical charge storage property and metal ion adsorption. RSC Adv 2014;4(107):62737–45.

10. Stobinski L, Lesiak B, Malolepszy A, et al. Graphene oxide and reduced graphene oxide studied by the XRD, TEM and electron spectroscopy methods. J Electron Spectrosc Relat Phenom 2014;195:145–54.

11. Vacchi IA, Spinato C, Raya J, Bianco A, Ménard-Moyon C. Chemical reactivity of graphene oxide towards amines elucidated by solid-state NMR. Nanoscale 2016;8(28):13714–21.

12. Miyako E, Pichon BP, Ménard-Moyon C, et al. Design, synthesis, characterization and properties of magnetic nanoparticle–nanocarbon hybrids. Carbon 2016;96:49–56.

13. Chau NDQ, Reina G, Raya J, et al. Elucidation of siRNA complexation efficiency by graphene oxide and reduced graphene oxide. Carbon 2017;122:643–52.

14. Kurapati R, Muzi L, de Garibay APR, et al. Enzymatic Biodegradability of Pristine and Functionalized Transition Metal Dichalcogenide MoS2 Nanosheets. Adv Funct Mater 2017;27(7): DOI10.1002/adfm.201605176.

15. Kurapati R, Backes C, Ménard-Moyon C, Coleman JN, Bianco A. White Graphene undergoes Peroxidase Degradation. Angew Chem Int Ed 2016;55(18):5506–11.

16. XPS,AES,UPS and ESCA, laSurface.com [Internet]. [cited 2017 Aug 5];Available from: http://www.lasurface.com/xps/erosion.php

17. Delphine Flahaut, Sven Tougaard, Neal Fairley, Mark Biesinger, Vincent Fernandez, John Walton. Ecole Thematique XPS Analysis- From measurements to scientific answers. Roscoff: 2016.

18. CasaXPS Casa Software. Peak Area, Counts per Second, Energy Step-Size and Quantification of XPS Spectra in CasaXPS [Internet]. [cited 2017 Aug 5]. Available from: https://www.youtube.com/watch?v=YuUA39vGEo4

19. Suzer S. Differential Charging in X-ray Photoelectron Spectroscopy: A Nuisance or a Useful Tool? Anal Chem 2003;75(24):7026–9.

20. Cazaux J. About the charge compensation of insulating samples in XPS. J Electron Spectrosc Relat Phenom 2000;113(1):15–33.

21. Tielsch BJ, Fulghum JE. Differential Charging in XPS. Part I: Demonstration of Lateral Charging in a Bulk Insulator Using Imaging XPS. Surf Interface Anal 1996;24(1):28–33.

22. Vereecke G, Rouxhet PG. Surface charging of insulating samples in x-ray photoelectron spectroscopy. Surf Interface Anal 1998;26(7):490–7.

23. Thermo Scientific XPS: Knowledge Base [Internet]. [cited 2017 Aug 9];Available from: http://xpssimplified.com/elements/indium.php

24. Reddy DA, Choi J, Lee S, Ma R, Kim TK. Green synthesis of AgI nanoparticle-functionalized reduced graphene oxide aerogels with enhanced catalytic performance and facile recycling. RSC Adv 2015;5(83):67394–404.

25. Ejigu Andinet, Edwards Matthew, Walsh Darren A. Synergistic Catalyst-Support Interactions in a Graphene-Mn3O4 Electrocatalyst for Vanadium Redox Flow Batteries. ACS Catal 2015;5(12):7122–30.

26. Chang X, Dong L, Yin Y, Sun S. A novel composite photocatalyst based on in situ growth of ultrathin tungsten oxide nanowires on graphene oxide sheets. RSC Adv 2013;3(35):15005–13.

27. Meng T-T, Zheng Z-B, Wang K-Z. Layer-by-Layer Assembly of Graphene Oxide and a Ru(II) Complex and Significant Photocurrent Generation Properties. Langmuir 2013;29(46):14314–20.

28. Tong W, Zhang Y, Zhang Q, et al. Achieving significantly enhanced dielectric performance of reduced graphene oxide/polymer composite by covalent modification of graphene oxide surface. Carbon 2015;94:590–8.

29. Hsiao M-C, Liao S-H, Yen M-Y, et al. Preparation of Covalently Functionalized Graphene Using Residual Oxygen-Containing Functional Groups. ACS Appl Mater Interfaces 2010;2(11):3092–9.

30. Navaee A, Salimi A. Efficient amine functionalization of graphene oxide through the Bucherer reaction: an extraordinary metal-free electrocatalyst for the oxygen reduction reaction. RSC Adv 2015;5(74):59874–80.

31. Schultz BJ, Dennis RV, Aldinger JP, et al. X-ray absorption spectroscopy studies of electronic structure recovery and nitrogen local structure upon thermal reduction of graphene oxide in an ammonia environment. RSC Adv 2013;4(2):634–44.

32. Kim S, Zhou S, Hu Y, et al. Room-temperature metastability of multilayer graphene oxide films. Nat Mater 2012;11(6):544–9.

33. Yue ZR, Jiang W, Wang L, Gardner SD, Pittman Jr. CU. Surface characterization of electrochemically oxidized carbon fibers. Carbon 1999;37(11):1785–96.

34. Panagiota Stathi, Dimitrios Gournis, Yannis Deligiannakis, Petra Rudolf. Stabilization of Phenolic Radicals on Graphene Oxide: An XPS and EPR Study. Langmuir 2015;31(38):10508–16.

35. Haubner K, Murawski J, Olk P, et al. The Route to Functional Graphene Oxide. ChemPhysChem 2010;11(10):2131–9.

36. Lei Y, Tang Z, Liao R, Guo B. Hydrolysable tannin as environmentally friendly reducer and stabilizer for graphene oxide. Green Chem 2011;13(7):1655–8.

37. Xue Y, Liu Y, Lu F, Qu J, Chen H, Dai L. Functionalization of Graphene Oxide with Polyhedral Oligomeric Silsesquioxane (POSS) for Multifunctional Applications. J Phys Chem Lett 2012;3(12):1607–12.

38. Chua CK, Pumera M. Renewal of sp2 bonds in graphene oxides via dehydrobromination. J Mater Chem 2012;22(43):23227–31.

39. Zhang L, Ji L, Glans P-A, Zhang Y, Zhu J, Guo J. Electronic structure and chemical bonding of a graphene oxide-sulfur nanocomposite for use in superior performance lithium-sulfur cells. Phys Chem Chem Phys PCCP 2012;14(39):13670–5.

40. Mu L, Gao Y, Hu X. L-cysteine: a biocompatible, breathable and beneficial coating for graphene oxide. Biomaterials 2015;52:301–11.

41. Spyrou K, Calvaresi M, Diamanti EK, et al. Graphite Oxide and Aromatic Amines: Size Matters. Adv Funct Mater 2015;25(2):263–9.

42. Dave K, Park KH, Dhayal M. Two-step process for programmable removal of oxygen functionalities of graphene oxide: functional, structural and electrical characteristics. RSC Adv 2015;5(116):95657–65.

43. Ruben Sánchez-Hidalgo DL-D. Graphene Oxide Thin Films: Influence of Chemical Structure and Deposition Methodology. Langmuir 2015;31:2697−2705.

44. Baer DR, Engelhard MH. XPS analysis of nanostructured materials and biological surfaces. J Electron Spectrosc Relat Phenom 2010;178:415–32.

45. Lee M, Yang S, Kim K, Kim S, Lee H. Comparison of the Catalytic Oxidation Reaction on Graphene Oxide and Reduced Graphene Oxide. J Phys Chem C 2014;118(2):1142–7.

46. Li Y, Alain-Rizzo V, Galmiche L, et al. Functionalization of Graphene Oxide by Tetrazine Derivatives: A Versatile Approach toward Covalent Bridges between Graphene Sheets. Chem Mater 2015;27(12):4298–310.

47. Petit C, Seredych M, Bandosz TJ. Revisiting the chemistry of graphite oxides and its effect on ammonia adsorption. J Mater Chem 2009;19(48):9176–85.

48. Stathi P, Gournis D, Deligiannakis Y, Rudolf P. Stabilization of Phenolic Radicals on Graphene Oxide: An XPS and EPR Study. Langmuir 2015;31(38):10508–16.

49. Yang M, Jiang T-J, Wang Y, et al. Enhanced electrochemical sensing arsenic(III) with excellent anti-interference using amino-functionalized graphene oxide decorated gold microelectrode: XPS and XANES evidence. Sens Actuators B Chem 2017;245:230–7.

50. Chen L, Xu Z, Li J, et al. Modifying graphite oxide nanostructures in various media by high-energy irradiation. RSC Adv 2013;4(2):1025–31.

51. Das SK, Dickinson C, Lafir F, Brougham DF, Marsili E. Synthesis, characterization and catalytic activity of gold nanoparticles biosynthesized with Rhizopus oryzae protein extract. Green Chem 2012;14(5):1322–34.

52. Al-Azizi AA, Eryilmaz O, Erdemir A, Kim SH. Surface Structure of Hydrogenated Diamond-like Carbon: Origin of Run-In Behavior Prior to Superlubricious Interfacial Shear. Langmuir 2015;31(5):1711–21.

53. Kaciulis S, Mezzi A, Calvani P, Trucchi DM. Electron spectroscopy of the main allotropes of carbon. Surf Interface Anal 2014;46(10–11):966–9.

54. Lascovich JC, Scaglione S. Comparison among XAES, PELS and XPS techniques for evaluation of Sp2 percentage in a-C:H. Appl Surf Sci 1994;78(1):17–23.

55. Barlow AJ, Scott O, Sano N, Cumpson PJ. Multivariate Auger Feature Imaging (MAFI) – a new approach towards chemical state identification of novel carbons in XPS imaging. Surf Interface Anal 2015;47(2):173–5.

56. Lascovich JC, Giorgi R, Scaglione S. Evaluation of the sp2/sp3 ratio in amorphous carbon structure by XPS and XAES. Appl Surf Sci 1991;47(1):17–21.

57. Barlow AJ, Popescu S, Artyushkova K, et al. Chemically specific identification of carbon in XPS imaging using Multivariate Auger Feature Imaging (MAFI). Carbon 2016;107:190–7.

58. Zhi CY, Bando Y, Terao T, Tang CC, Kuwahara H, Golberg D. Chemically Activated Boron Nitride Nanotubes. Chem – Asian J 2009;4(10):1536–40.

59. Gao J, Li B, Tan J, Chow P, Lu T-M, Koratkar N. Aging of Transition Metal Dichalcogenide Monolayers. ACS Nano 2016;10(2):2628–35.

60. Ganta D, Sinha S, Haasch RT. 2-D Material Molybdenum Disulfide Analyzed by XPS. Surf Sci Spectra 2014;21(1):19–27.

CHAPTER 5: CONCLUSION AND PERSPECTIVES

5.1 CONCLUSIONS

With this study, I got an overall comprehension of GO, from its surface composition, to its reactivity towards mono and multifunctionalization and to its biodistribution in mice. Moreover, I improved the characterization and water dispersibility of GO.

I started by studying the surface composition and reactivity towards functionalization of the oxygenated groups supposed to be present on the surface of GO. Thus, the amidation and esterification reactions were performed on the carboxylic acids, the opening of epoxide rings, as well as the esterification and Williamson reactions on the hydroxyl groups and finally the Wittig reaction on the ketones. The main groups that appeared to be present on the surface of GO and prone to functionalization are the hydroxyl groups and the epoxide rings. Only a negligible amount of carboxylic acids was detected on the surface of GO. This result has been confirmed by solid state MAS NMR analysis.

The reactivity of differently synthesized GO samples commercially available was investigated. One type of GO was obtained through the Hummers oxidation process (GO NI) and another type of GO was generated *via* cutting and exfoliation of carbon nanofibers (GO Ant). These two differently synthesized GO showed the same type of functional groups with only little variability in their amount. I also had the opportunity to work with two other GO samples, both obtained *via* the Hummers' method (GO-K and GO-Jp). On their surface mainly hydroxyls and epoxide rings were detected. Only on GO-Jp a higher content of carboxylic acids was measured by solid state MAS NMR. Although other GO samples obtained with different synthesis processes should be tested, with the information collected within this study, we can already state that the surface of GO is generally composed mainly of epoxides and hydroxyls independently of the synthesis process and conditions.

Among the reactions developed on GO, the opening of epoxides was exploited to attach a radionuclide chelating agent to complex In [111] for an *in vivo* biodistribution study. In the frame of this study, size sorted GO was used: large GO, small GO and ultra-small GO. GO showed a size-dependent biodistribution and all samples were excreted *via* mainly urines but also faeces.

We exploited the reactions investigated for the surface composition study to develop a multifunctionalization strategy. Multifunctionalization is highly promising to obtain a multifunctional material. Different strategies were examined mainly by functionalizing the hydroxyl and epoxide groups. Orthogonal protecting groups were found to be able to control independently the two chains. The combination of an acid sensitive (Boc) and a photocleavable group, *ortho*-nitrobenzyl derivative, appeared to be the best to avoid alteration of the surface composition of GO due to the deprotection conditions. The best multifunctionalization strategy seemed to be the combination of the opening of epoxides with a diamino-derivative with the esterification on the hydroxyl groups. Interestingly, during multifunctionalization, we discovered that it was not possible to graft molecules above a certain amount, limit that could be explained by the island localization of the oxygen-containing functional groups on the surface of GO. Thus, due to sterical hindrance of the first molecule introduced, the second one cannot be grafted efficiently to the surface of GO above a certain amount. Moreover, we noticed that often the dispersibility of GO samples is decreased after functionalization. This is a real issue in the production of GO conjugates for biomedical applications. Thus, we investigated an alternative multifunctionalization strategy. First, the dispersibility of GO was increased with a highly water dispersible and biocompatible polymer, the polyglycidol. The polymerization was tested in different conditions to find the best polymerization conditions without thermally affecting the surface of GO that would result in the reduction of GO. High loadings of polyglycidol on GO were obtained (up to 95%). Subsequently, functionalization was performed on the hydroxyl groups of this polymer. The multifunctionalization strategy envisaged to partially convert the hydroxyl in azides and to perform a click reaction on the azide group and an esterification on the

hydroxyls left on the surface of the polymer. I efficiently conjugated a kidney targeting peptide *via* click reaction. However, due to a lack of time I did not manage to perform the second step of the multifunctionalization in order to conjugate a fluorophore for imaging purposes.

Finally, the characterization of GO samples has been improved. Indeed, characterization of GO with high resolution techniques is important due to the complexity of this material. Solid state MAS NMR and XPS were thoroughly exploited. The solid state MAS NMR analysis of several GO samples were performed in collaboration with Jesus Raya of the University of Strasbourg. Quantitative ^{13}C MAS NMR and ^{1}H-^{13}C FSLG-HETCOR were recorded. For XPS analysis, a thorough study was performed to optimize the analysis conditions and improve the data interpretation for GO samples. Indeed, due to partial insulating and partial semi-conductive character, this material undergoes complex charging effects. The sample preparation and choice of substrate were ameliorated. Moreover, I found that the best way to treat XPS data is to use constrains for peak position and FWHM, to compare the deconvolution of the spectra of the different elements present in the sample, and to exploit the C KLL Auger peak to calculate the C sp^2 and sp^3 ratio and to exploit it to apply the charge shift correction to the spectra.

XPS analysis was also employed to follow biodegradation experiments of hBN and MoS_2, emerging 2D materials in the biomedical field. Both proved to be biodegradable.

In conclusion, I focused on key aspects for GO, in particular the surface composition, reactivity, biodistibution and characterization. These are all important aspects to be able to further exploit this material for a plethora of applications in different fields, and especially, in our case, in nanomedicine.

5.2 PERSPECTIVES

For the surface composition study, an investigation of the localization of the functional groups on the surface of GO can be envisaged. This investigation would help to understand better the characteristics and reactivity of this material. In addition, other reactions could be tested on GO, reactions that could be afterwards exploited to design new multifunctionalization strategies (such as the formation of stable cyclic acetals on the carbonyl group, the Appel reaction on the hydroxyl groups).

The next objective for the multifunctionalization study will be to obtain a double functionalized GO conjugate for targeting purposes. Indeed, *via* multifunctionalization an imaging molecule in addition to the targeting peptide could be grafted. Because of its excellent aqueous processability, amphiphilicity, surface functionalizability and fluorescence quenching ability, GO is a promising material for biomedical applications. The knowledge assimilated with this study will help to develop covalently multifunctionalized GO materials and to design new strategies for multifunctionalization.

CHAPTER 6: EXPERIMENTAL SECTION

6.1 Materials

6.1.2 Graphene oxide: source and synthesis method

For the surface chemistry study, GO samples were provided by Grupo Antolin (Spain) and NanoInnova Technologies (Spain) (batch2: GO.M.60-8; batch3: NIT.GO.Z.10.4; batch4: NIT.GO.R.10.1; batch 5: NIT.GO.M.10.200). NanoInnova graphene oxide is prepared by the Hummers' method. GO from Antolin is derived from carbon nanofibers that consist of ribbons of about five stacked graphene layers rolled up along the fiber axis and developing a continuous spiral. These rolled carbon nanofibers are cut and exfoliated into GO. The thickness of the NanoInnova GO layers reaches 20 nm, indicating the presence of aggregated GO sheets. Differently, GO obtained from Antolin contains monolayer sheets of ~1 nm thickness, along with many irregular particles with a thickness from 3 to 10 nm.

For the biodistribution study, the GO was obtained from the research group of Prof. Kostas Kostarelos (University of Manchester, UK). Three batches were used. The large-GO has a lateral size distribution of 30 μm-10 μm, the small-GO of 1 μm-100 nm and the ultrasmall-GO <50 nm.

For the dispersibility and multifunctionalization study, besides the GO NanoInnova, a GO from Prof. Yuta Nishina (Okayama University, Japan) was used. This GO has an average lateral size of 1 μm.

6.1.3 Chemicals and Solvents

Chemicals were purchased from Sigma-Aldrich, Acros, Alfa Aesar Laboratories, and used as received without any further purification. DOTA derivatives were purchased from CheMatech (Macrocycle design technologies), meanwhile NH_2-PEG_{23}-NHBoc and N_3-PEG_{36}-OH from Quanta BioDesign. All solvents used for synthesis were analytical grade. When anhydrous conditions were required, high quality commercial dry solvents were used. Water was purified using a Millipore filter system MilliQ® equipped with a Biopak® filter for pyrogen-free, DNase-free and RNare-free ultrapure water (Lot. F7HA16783; code 0310).

6.1.4 Characterization Methods and Instrumentation

Thin Layer Chromatography (TLC) - TLC was conducted on pre-coated aluminium plates with 0.25 mm *Macherey-Nagel* silica gel with fluorescent indicator UV254.

Column Chromatography - Chromatographic purifications were carried out with silica gel (Merck Kieselgel 60, 40-60 μm, 230-400 mesh ASTM).

Nuclear Magnetic Resonance - ^{1}H-NMR and ^{13}C-NMR spectra were recorded in deuterated solvents using Bruker Avance I – 300 MHz and Bruker Avance III – 400 MHz. Chemical shifts are reported in ppm using the residual signal of deuterated solvent as reference. The resonance multiplicity is described as *s* (singlet), *d* (doublet), *t* (triplet), *q* (quartet), *qt* (quintuplet), *m* (multiplet), *bs* (broad singlet), *bd* (broad doublet), *bt* (broad triplet). Coupling constants (*J*) are given in Hz.

Infrared Spectroscopy - IR spectra were recorded on a Perkin Spectrum One ATR-FT-IR spectrometer or IR Prestige-21 SHIMADZU (for PG-GO) using KBr pellets.

ESI Mass Spectrometry - Mass spectra were recorded on a Thermo Fisher Finnigan LCQ Advantage Max Instrument.

UV-Vis-NIR Spectroscopy - UV-Vis-NIR spectra were recorded using a Varian Cary 5000 spectrophotometer, using 1 cm path quartz glass cuvettes.

Transmission Electron Microscopy - TEM analysis was performed on a Hitachi H600 or on a Hitachi H7500 microscope with an accelerating voltage of 75 kV or 80 kV, respectively. The samples were dispersed in water/MeOH (1:1) at a concentration of 0.05 mg·mL^{-1} and the suspensions were sonicated for 15 min. Ten

microliters of the suspensions were drop-casted onto a carbon-coated copper grid (Formvar/Carbon 300 Mesh, Cu from Delta Microscopies) and left for evaporation under ambient conditions.

Scanning Transmission Electron Microscopy - For PG-polymerized samples a JOEL JSM-7500F field emission scanning electron microscope at 25 kV accelerating voltage for TEM model has been used. Samples were drop-casted onto carbon-coated copper grids.

Thermogravimetric Analysis – TGA was performed using TGA1 (Mettler Toledo) apparatus from 30°C to 900°C with a ramp of 10°C min^{-1} under N_2 using a flow rate of 50 mL min^{-1} and platinum pans. For TGA under air a Q-50 analyzer (TA instruments) was used, with a heating rate of 20°C min^{-1} and a flow rate of 60 mL min^{-1} and platinum pans.

Quantitative Kaiser Test **-** Three solutions were prepared separately:

- 10 g of phenol dissolved in 20 ml of ethanol (solution I)
- 2 ml of KCN 1 mM (aqueous solution) dissolved in 98 ml of pyridine (solution II)
- 1.0 g of ninhydrin dissolved in 20 ml of ethanol (solution III)

An amount of approximately 200 µg of GO conjugates was carefully weighted and then the following solutions were carefully added into the test tube: 75 µl of solution I, 100 µl of solution II and 75 µl of solution III. As blank solution, the three solutions were mixed in a test tube without GO. The test tube was sonicated in a water bath for 5 minutes, heated at 110°C for 5 minutes and then cooled rapidly in an ice bath to stop the reaction. 2.75 ml of 60% ethanol were added and the suspension was mixed. A UV-Vis cuvette was filled with the blank solution to collect the baseline. The absorbance of each sample was measured at 570 nm. The calculation of the amine loading was made using the Equation V.1.

The result was expressed as micromole of amino group per gram of material. The test was performed at least three times for each sample.

$$\mu mol/g = \frac{[Abs_{sample} - Abs_{blank}] \cdot dilution\ (mL) \cdot 10^6}{Molar\ extinction\ coefficient \cdot sample\ weight(mg)}$$

Equation 6.1: GO loading calculation. Dilution is equal to 5 ml and molar extinction coefficient to 15000 $M^{-1} \cdot cm^{-1}$.[1]

X-Ray Photoelectron Spectroscopy **-** XPS was performed on a Thermo Scientific K-Alpha X-ray photoelectron spectrometer with a basic chamber pressure of 10^{-8}-10^{-9} bar and an Al anode as the X-ray source (1486 eV). The samples were analyzed as powder or deposited on a support *via* drop-casting on a silicon wafer coated with SiO_2 (200 nm±5% of SiO_2, Tedpella 21620-6) or pressed onto indium foil (0.127 mm, 99.99%, from Alfa Aesar) or presses onto scotch tape (3M™ EMI Copper Foil Shielding Tape 1182; or 3M Scotch® carbon tape). Spot size of 400 µm was used. The survey spectra are average of 10 scans with a pass energy of 200.00 eV and a step size of 1 eV. The high resolution spectra are an average of 10 scans with a pass energy of 50 eV and a step size of 0.1 eV. The pass energy of 50.00 eV corresponds to Ag $3d_{5/2}$ line FWHM of 1.3 eV. A pass energy of 50.00 eV for the high resolution spectra was applied because lower pass energies has shown no improvement in FWHM for graphene materials on Thermo Scientific K-ALPHA. An ion gun was turned on during analysis. For each sample, the analysis was repeated three times. Because of the difficulty to take standards for carbon nanomaterial, database and articles were used as peak reference value.[2] Thirty five articles on GO and XPS characterization were examined; a selection of four articles is found in references.[3–6] For data analysis casaXPS (2.3.18) software was used. A shirley background subtraction and charge correction were applied if needed (to the C-C peak at 285.2-285.3 eV). When applied, potential error due to this charge correction was considered. Reference elements were also studied for charge correction. A line-shape 70% Gaussian/30% Lorenzian [GL(30)] was selected for all peaks apart from for C sp_2 peak. For C sp_2 peak an asymmetric line-shape was chosen [A(0.4, 0.38, 20)GL(20)]. FWHM was constrained to be the same for all peaks, apart from the pi-pi* peak and the water peak because these are

broad signals. The peak position for each bond was constrained to be the same in every spectrum, with a low ratio of variability. For the surface composition study the carbon spectra were deconvoluted in C=O, C-O, C-N and C sp^2 and sp^3. These peaks were constrained to have the same FWHM, apart from the C-N because it is the only peak not considering two functional groups. For the DOTA-GO samples and the multifunctionalization study, instead, almost every bond was considered individually in the carbon high resolution spectra, keeping into consideration the error due to the proximity of the binding energy (BE) values and proportional to the overlapping ratio. Only C-OH/C-N and C=OOR/C=ONR$_2$ were cumulated under the same peak due to the higher proximity of the BE values. For oxygen and nitrogen high resolution spectra all signals were assembled due to the high proximity of the BE values. Also with this approximation a certain degree of error should be taken in to account. In the table, the deconvolution constrains used are reported.

Table 6.1 BE values used for peak deconvolution in XPS data analysis.

C1s	C=C	C-C	C-OH, C-N	C-O-C	C=O	C=OOR, CHONR$_2$	Π- Π*
Peak (eV)	284.4 (±0.2)	285.2 (±0.1)	286.5 (±0.3)	287.1 (±0.2)	288.1 (±0.1)	289.1 (±0.1)	290 (±0.2)
FWHM (eV)	0.7-1.8						1-2.5

O1s	H$_2$O	C-O-C, C-OH, (C=O)OH	C=O, C=OOH, C=ONR$_2$
Peak (eV)	535.0 (±0.1)	532.8 (±0.1)	531.1 (±0.15)
FWHM (eV)	1-2.5	0.9-1.8	

N1s	C-NR$_2$, C=ONR$_2$	C-N$^+$R$_3$
Peak (eV)	399.8 (±0.2)	401.9 (±0.1)
FWHM (eV)	0.8-1.9	

Raman Spectroscopy - Raman spectroscopy was performed using a Renishaw inVia microRaman equipped with a Leica microscope. The spectra were recorded using 514 nm laser (5% laser power) and ×50 objective lens. The samples were prepared by drop casting water dispersions of the respective samples on Si window -E coated (Ø25.4 mm, 5 mm thick) substrates (ThorLabs), followed by drying at room temperature.

Solid-state MAS NMR - SS MAS NMR experiments were performed on an AVANCE 750 MHz wide bore spectrometer (BrukerTM) operating at a frequency of 188.5 MHz for ^{13}C and equipped with two different MAS probes: a double resonance MAS probe designed for 2.5 mm o.d. zirconia rotors (closed with Kel-F caps) and a triple resonance MAS probe designed for 3.2 mm zirconia rotors (also closed with Kel-F caps). The samples were spun either at 30 kHz spinning frequency (MAS 2.5) or 18 kHz (MAS 3.2).

2D ^{1}H-^{13}C HETCOR with FSLG irradiation during the evolution time[7] was obtained with the first CP step following the Adiabatic Passage through the Hartmann-Hahn (HH) conditions scheme[8]. The latter conditions were set to 97 kHz and 127 kHz B1 fields for ^{13}C and ^{1}H, respectively (when spinning at 30 kHz), and 90 kHz /108 kHz in the other case (MAS = 18 kHz). The ^{1}H RF field was swept from 107 to 147 kHz (MAS = 30 kHz) or from 93 kHz to 123 kHz (MAS = 18 kHz) through the HH condition using the tangential time dependence and defined by the shape angle $\phi = at_{cp}/2$ where a is the rate of angular,[9] ϕ and t_{cp} (contact time) were set to 88° and 1.5 ms after optimization.[10] Proton decoupling during acquisition was obtained by using SPINAL-64[11], while the recycle time was set to 1 s. The duration of the successive FSLG pulses was 3.57 µs and the magic-angle pulse length was 1.34 µs. A number of 192 complex data points were acquired in the ^{1}H indirect dimension and for each t1 increment 2048 scans were accumulated leading to a time resolution of 6.3361 ms for ^{1}H and 12.2880 ms for ^{13}C. Prior to Fourier transformation, a Lorentzian line broadening of 150 Hz was applied in the direct dimension, while the proton dimension apodization was done with a 90° shifted squared sine-bell function.

1D ^{13}C{^{1}H} CP/MAS spectra were recorded with the same spectral parameters than 2D spectra. But, owing to the spectral wide lines and in order to get undistorted line-shapes, we used and improved CP experiment version that perform Hahn's echo prior to FID acquisition.[12] The latter echo had to be

synchronized with the rotation (echo time = n rotation periods) and was kept identical for all ^{13}C spectra and equal to two rotation periods. The total echo time was 66.67 µs (MAS = 30 kHz) and 111.11 µs (MAS = 18 kHz).

Quantitative 1D $^{13}C\{^{1}H\}$ DP spectra were acquired directly with the original Hahn's echo sequence[12], with a recycling delay set to 30 s to ensure reliable quantitation (total experimental time was 24 h per spectrum).

Filtration - For filtration workup PTFE membranes from Millipore MWCO were used.

Dialysis - For dialysis purification MWCO 12000-14000 Da membrane tubes purchased from Spectrum laboratories were employed. For dialysis milliQ water was used and the water was changed three times a day.

HPLC - Reversed phase high-performance liquid chromatography analyses (RP-$HPLC_{anal}$) were performed on a Waters Alliance e2695 instrument, with integrated autosampler and a Waters 2998 PDA detector, using a Macherey–Nagel Nucleosil 100–5 C 18 column 4.6x125 mm (gradient: 20-80% B and 1-31% in 20 min at 1.2 mL/min flow rate). The purifications by preparative RP-HPLC were performed on a Beckman instrument equipped with a System Gold 166 NMP detector with a Macherey–Nagel Nucleodur 100–16 C18 column (gradient: 20–80% B in 20 min at 6 mL/min flow rate; λ = 220 nm). Eluent for both analytical and preparative RP-HPLC: A = H_2O+0.1% TFA, eluent B = MeCN+0.08% TFA.

Sonication – Sonication was done with a Elmasonic P (Elma) (20 W, 40 kHz). For PG-polymerization Branson 5510J-MT sonicator has been used, with water cooling system stabilized at 20°C.

Dynamic Light Scattering - DLS was performed on a Nanotrac UPA EX150 (Nikkiso Co. Ltd.) and a Nanostar from Wyatt Technology equipped with a 100 mW laser using disposable plastic cells for particles with radii in the 1 nm to 1000 nm range. Data taken on Nanostar were analyzed with DYNAMICS® Software. Data taken on Nanotrac were analyzed with MICROTRAC Software.

Centrifugation - For PG-polymerization Avanti J-E (Beckman Coulter, Inc, 21000 rpm=50400 g) was used.

Xylenol Orange Test - Preparation of acetate buffer (pH 5.8) and xylenol orange (XO) solution according to Contrast Med. Mol. Imaging 2006, 184.

Preparation of different concentrations of Gd solutions: use Gd perchlorate 50% in water (→ c = 1.1 M) and prepare 1/100 dilution (→c = 11 mM); 1/100 dilution of 11 mM solution (→c = 110 µM); 1/10 dilution of 110 µM solution (→c = 11 µM).

[Gd] (µM)	Gd solution (µL)	H_2O(µL)
50	46 (110 µM)	54
25	23(110 µM)	77
11	100 (11 µM)	0
5	46(11 µM)	54
2.5	23(11 µM)	77
0	0	100

- UV/Vis Spectroscopy

To 1 mL of the XO solution, add 100 µL of the different concentration solutions of Gd.

Shake and run UV/Vis spectra.

- Calibration curve
Ratio A(573 nm)/A(433 nm)

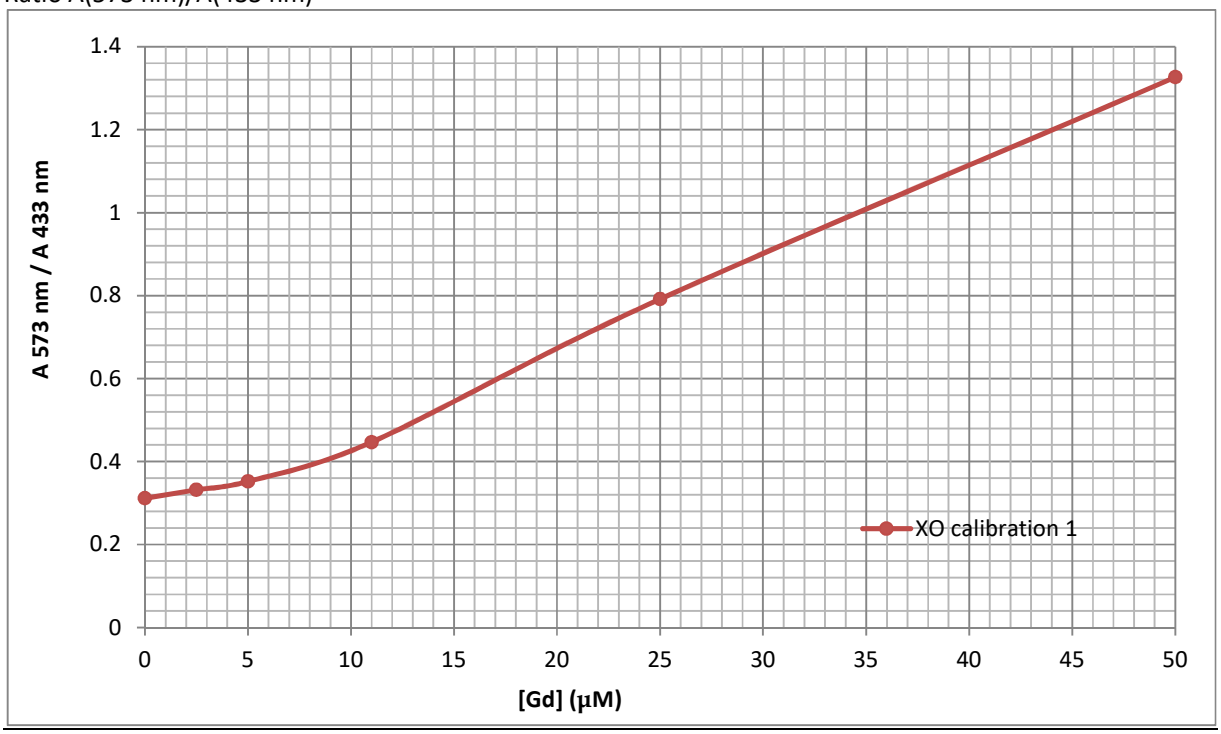

6.2 Methods

6.2.1 Chemical synthesis

COMPOUND 1 - C1

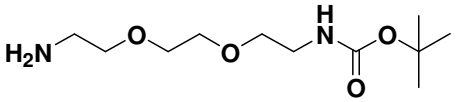

To a solution of 2,2'-(ethylenedioxy)bis(ethylamine) (9.85 ml, 67.48 mmol) in CH_2Cl_2 (50 ml) in an ice bath, a solution of Boc_2O (2.9 g, 13.47 mmol) in CH_2Cl_2 (30 ml) was added dropwise over a period of 3 hours. The reaction mixture was stirred overnight at room temperature. The solvent was removed under reduced pressure and after dissolving the residue in H_2O (200 ml) the precipitate formed was filtered on celite. The filtrate was extracted with CH_2Cl_2 (100 ml x 3) and dried over Na_2SO_4. Evaporation of the solvent afforded **C1** as a colorless oil (2.4 g, 9.56 mmol, 71%).[1]H NMR spectroscopy showed a satisfactory purity; therefore the crude was used without purification. ^{1}H-NMR (300 MHz,$CDCl_3$): δ 5.13 (*bs*, 1H), 3.60 (*t*, 7.3 Hz, 4H), 3.53 (*t*, 5.1 Hz, 4H), 3.30 (*bt*, 2H), 2.89 (*t*, 5.1 Hz, 2H), 2.2 (*s*, 2H), 1.42 (*s*, 9H). ^{13}C-NMR (75MHz, $CDCl_3$): δ 155.9, 78.8, 73.1, 70.0, 41.5, 40.2, 28.3. ESI-MS: Found 249.1 $[M+H]^+$.
All structural assignments were in agreement with the data available from the literature.[13]

COMPOUND 2 - C2

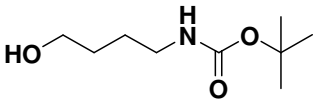

To a solution of 4-amino-1-butanol (4 g, 44.87 mmol) in CH_2Cl_2 (44 ml), a solution of Boc_2O (10.8 g, 49.48 mmol) in CH_2Cl_2 (44 ml) was added dropwise over a period of 3 h. The reaction mixture was stirred 3 h at

room temperature and monitored by TLC. The solvent was removed under reduced pressure and after dissolving the residue in H_2O the precipitate formed was filtered on celite.

The filtrate was extracted with CH_2Cl_2 (100 ml x 3) and the organic phase was dried over Na_2SO_4. Evaporation of the solvent afforded **C2** as a colorless oil (8.2 g, 43.54 mmol, 97%).

^{1}H-NMR (400 MHz, $CDCl_3$): δ 4.66 (*bs*, 1H), 3.67-3.63 (*m*, 2H), 3.14-3.13 (*m,* 2H), 1.86 (*bs*, 1H), 1.58-1.55 (*m*, 4H), 1.43 (*s*, 9H). ^{13}C-NMR (100 MHz, $CDCl_3$): δ 156.2, 79.1, 62.4, 40.3, 29.7, 28.4, 26.6. ESI-MS: Found 189.7 $[M]^+$.

COMPOUND 3 -C3

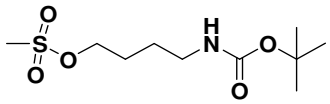

To a solution of **C2** (1 g, 5.29 mmol) in CH_2Cl_2 (53 ml) at 0°C were added triethylamine (0.81 ml, 5.82 mmol) and methanesulfonylchloride (0.45 ml, 5.82 mmol). The reaction mixture was stirred at room temperature for 1h. The reaction was monitored by TLC. Water was added to the solution and the aqueous phase was extracted 3 times with CH_2Cl_2. A yellow oil was obtained after evaporation and was immediately utilized.

COMPOUND 4 - C4

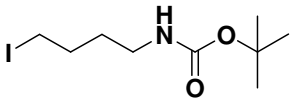

To a solution of **C3** (1.4 g, 5.29 mmol) in acetone (53 ml) was added sodium iodide (1.2 g, 8.00 mmol). The reaction was stirred for 17 h at 50° C and monitored by TLC. The solvent was removed under reduced pressure after dissolving the residue in H_2O the product was extracted with CH_2Cl_2 (x3), and washed with $Na_2S_2O_3$ solution (x3), brine (x3) and dried over Na_2SO_4. The solution was evaporated *in vacuo.* The residue was purified by chromatography on silica gel using 100% DCM as eluent. A yellow oil was obtained (0.9 g, 2.91 mmol, 55%).

^{1}H-NMR (400 MHz, $CDCl_3$): δ 4.52 (*bs*, 1H), 3.19 (*t*, 7 Hz, 2H), 3.14 (*bt*, 2H), 1.86 (*qt*, 7.2 Hz, 2H), 1.58 (*qt*, 7.2 Hz, 2H), 1.44 (*s*, 9H).^{13}C-NMR (100 MHz, $CDCl_3$): δ 155.9, 78.9, 39.5, 31.1, 30.7, 28.6, 6.2.

COMPOUND 5 - C5

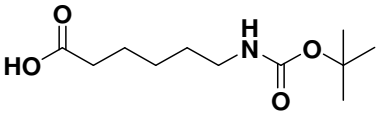

To a solution of aminoesanoic acid (0.96 ml, 7.6 mmol) in 1,4-dioxane (10 ml), a solution of Boc_2O (1.8 g, 8.4 mmol) in 1,4-dioxane (5 ml) was added dropwise over a period of 3 h. The reaction mixture was stirred 48 h at room temperature and monitored by TLC. The solvent was removed under reduced pressure and water was added to the residue. The product was then extracted with AcOEt (x 3) and dried over Na_2SO_4. The evaporation of the solvent afforded **C5** as a white solid (1.5 g, 6.4 mmol, 84%).

^{1}H-NMR (400 MHz, $CDCl_3$): δ 4.55 (*bs*, 1H), 3.11 (*bd*, 2H), 2.35 (*t*, 7.4 Hz, 2H), 1.65 (*qt*, 7.6 Hz, 2H), 1.53-1.46 (*m*, 2H), 1.44 (*s*, 9H), 1.40-1.35 (*m*, 2H). ^{13}C-NMR (100 MHz, $CDCl_3$): δ 177.7, 155.9, 78.7, 39.9, 33.6, 29.3, 28.1, 25.8, 24.2. ESI-MS: Found 132.0 attributed to Boc loss $[M-100]^+$.

All structural assignments were in agreement with the data available from the literature.[15]

COMPOUND 6 - C6

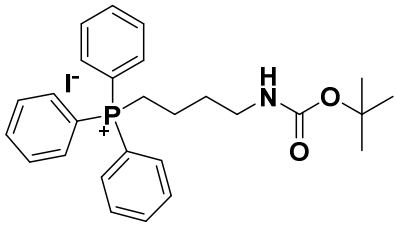

To a solution of **C4** (250 mg, 0.83 mmol) in acetonitrile (8.5 ml) was added triphenylphosphine (219 mg, 0.83 mmol). The reaction mixture was stirred at 80 °C for 24 h. EtOAc was then added to precipitate **C6**, the reaction mixture was sonicated and the supernatant removed with a Pasteur pipette. The crude was purified by chromatography on silica gel using DCM/MeOH (9.5:0.5) as eluent. A yellow oil was obtained (40 mg, 0.07 mmol, 9%).

^{1}H-NMR (400 MHz, $CDCl_3$): δ 7.89-7.75 (*m*, 15H), 5.1 (*bs*, 1H), 3.79-3.72 (*bt*, 2H), 3.2 (*q*, 6.4 Hz, 2H), 1.94-1.90 (*m*, 2H), 1.73-1.67(*m*, 2H), 1.36 (*s*, 9H). ESI-MS: Found 433.8 $[M-I]^+$.

COMPOUND 7 - C7

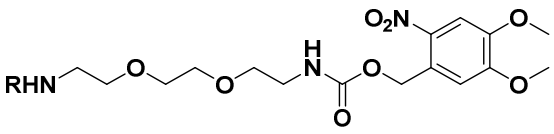

R=H, Boc (C1)

R=H: To a solution of 2,2'-(ethylenedioxy)bis(ethylamine) (1.5 g, 10.1 mmol) in 1,4-dioxane (10 ml) was added dropwise a solution of 4,5-dimethoxy-2-nitrobenzyl chloroformate (0.3 g, 1.01 mmol) in 1,4-dioxane (15 ml). The reaction mixture was stirred for 72h at room temperature and monitored by TLC. The solvent was removed under reduced pressure and water was added to the residue. The product was then extracted with DCM (x3) and dried over Na_2SO_4. The crude was purified by chromatography on silica gel using DCM/MeOH (9.5:0.5) as eluent. A yellow powder was obtained (154 mg of pure product, 0.4 mmol, 40%).[16]

^{1}H-NMR (400 MHz, $CDCl_3$): δ 7.69 (*s*, 1H), 7.26 (*s*, 1H), 5.86 (*bs*, 1H), 5.49 (*s*, 2H), 3.98 (*s*, 3H), 3.94 (*s*, 3H), 3.62-3.57 (*m*, 6H), 355-3.53 (*t*, 5.3 Hz, 2H), 3.42-3.38 (*q*, 5.4 Hz, 2H), 2.91-2.88 (*t*, 5.1 Hz, 2H), 2.39 (*bs*, 2H). ESI-MS: Found 388.2 $[M+H]^+$.

R=Boc: To a solution of **C1** (196 mg, 0.79 mmol) in DCM (4 ml) was added dropwise a solution of 4,5-dimethoxy-2-nitrobenzyl chloroformate (200 mg, 0.72 mmol) in DCM (4 ml). Afterwards *N*,*N*-diisopropylethylamine (0.15 ml, 0.86 mmol) was added. The reaction mixture was stirred for 24h at room temperature and monitored by TLC. The solvent was removed under reduced pressure and acid water (pH=4) was added to the residue. The product was then extracted with DCM (x3) and dried over Na_2SO_4. The crude was then purified by chromatography on silica gel using AcOEt/cyclohexane (8:2) as eluent. A yellow powder was obtained (240 mg, 0.49 mmol, 68%).

^{1}H-NMR (400 MHz, $CDCl_3$): δ 7.7 (*s*, 1H), 7.01 (*s*, 1H), 5.51 (*s*, 2H), 5.00 (*bs*, 1H), 3.97 (*s*, 3H), 3.95 (*s*, 3H), 3.61-3.57 (*m*, 6H), 355-3.53 (*t*, 5.3 Hz, 2H), 3.44-3.40 (*q*, 5.6 Hz, 2H), 3.31-3.30 (*bt*, 2H), 1.65 (*bs*, 2H), 1.42 (*s*, 9H). ESI-MS: Found 511 $[M+Na]^+$.

COMPOUND 8 - C8

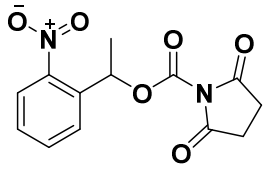

To a solution of 1-(2-nitrophenyl)ethanol (1 g, 5.98 mmol) in dry acetonitrile (9 ml) was added triethylamine (2 ml, 14,7 mmol) and di(*N*-succimidyl)carbonate (2.1 g, 8.24 mmol) under argon atmosphere. The reaction mixture was stirred for 2h at room temperature and monitored by TLC. The solvent was removed under reduced pressure. The crude was then purified by chromatography on silica gel using petroleum ether/EtOAc (7:3) as eluent. A pure product was obtained (1.5 g, 5.07 mmol, 85%).[17]

^{1}H-NMR (400 MHz, $CDCl_3$): δ 8.03-8.01 (*bd*, 1H), 7.76-7.70 (*m*, 2H), 7.52-7.48 (*m*, 1H), 6.42-6.37 (*q*, 6.5 Hz, 1H), 2.79 (*s*, 4H), 1.80-1.78 (*d*, 6.5 Hz, 3H). ^{13}C-NMR (400 MHz, $CDCl_3$): δ 168.43, 150.75, 147.33, 135.90, 134.35, 129.29, 127.01, 124.82, 76.02, 25.43, 22.15.

All structural assignments were in agreement with the data available from the literature.[17]

COMPOUND 9 - C9

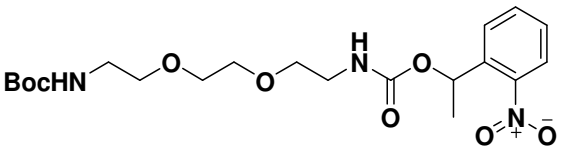

To a solution of **C1** (248 mg, 1 mmol) in DCM (2.5 ml) were added Et_3N (0.4 ml, 2.99 mmol) and dropwise a solution of **C8** (296 mg, 1 mmol) in DCM (2.5 ml). The reaction mixture was stirred for 5h at room temperature and monitored by TLC. The solvent was removed under reduced pressure and brine was added to the residue. The product was then extracted with DCM (x3) and dried over Na_2SO_4. The crude was then purified by chromatography on silica gel using petroleum ether/EtOAc (1:1) as eluent. The pure product was obtained (212 mg, 0.48 mmol, 48%).[17]

^{1}H-NMR (400 MHz, $CDCl_3$): δ 7.91-7.89 (*bd*, 1H), 7.64-7.57 (*m*, 2H), 7.41-7.37 (*m*, 1H), 6.25-6.20 (*q*, 6.6 Hz, 1H), 5.34 (*bs*, 1H), 5.04 (*bs*, 1H), 3.58-3.52 (*m*, 8H), 3.32-3.29 (*bt*, 4H), 1.61-1.59 (*d*, 6.6 Hz, 3H), 1.43 (*s*, 9H). ^{13}C-NMR (500 MHz, $CDCl_3$): δ 156.06, 155.41, 147.68, 138.83, 133.55, 128.19, 127.14, 124.40, 79.48, 70.25, 70.08, 68.60, 40.80, 40.39, 28.46, 22.27. ESI-MS: Found 464.3 $[M+Na]^+$.

PHOTOCLEAVAGE OF C9 - C9-PD

A solution of **C9** (10 mg, 23 µmol) in $CHCl_3$ (2.55 ml, 0.009 M) was exposed to irradiation at 365 nm (100 W, 15 cm distance, under a black tissue) for about 4-6h. The reaction was followed by TLC and HPLC (20-80 gradient).

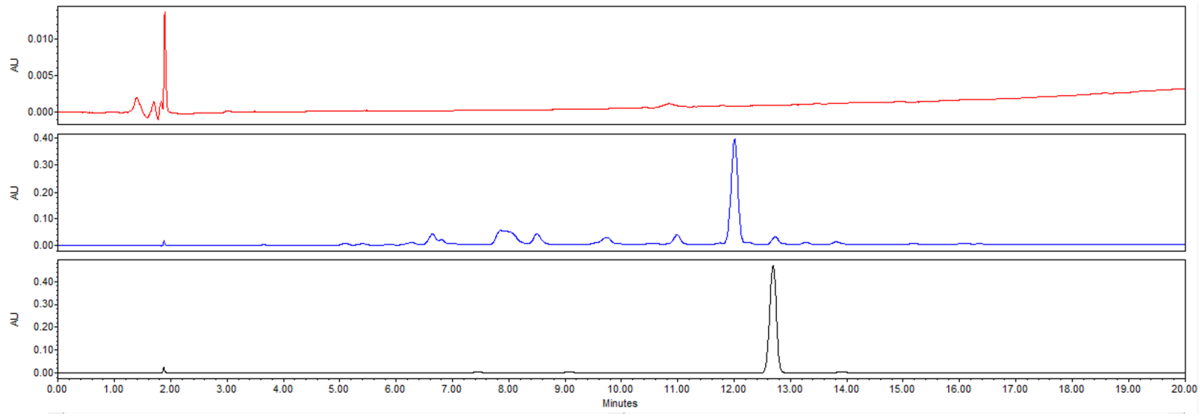

HPLC of **C1** in red, **C9-PD** in blue and **C9** in black.

COMPOUND 10 - C10

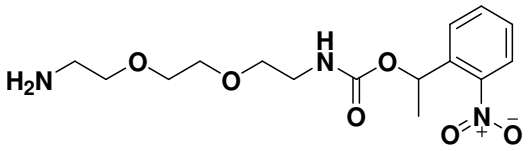

To a solution of 2,2'-(ethylenedioxy)bis(ethylamine) (1.5 g, 10.1 mmol) in DCM (25 ml) was added dropwise a solution of **C8** (0.3 g, 1.01 mmol) in 1,4-dioxane (25 ml). The reaction mixture was stirred for 7h at room temperature and monitored by TLC. The solvent was removed under reduced pressure and water was added to the residue. The product was then extracted with DCM (x3) and dried over Na_2SO_4. The crude was then purified by chromatography on silica gel using DCM/MeOH (9.5:0.5) as eluent. A yellow oily liquid was obtained (189 mg, 0.55 mmol, 55%).[17]

^{1}H-NMR (400 MHz, $CDCl_3$): δ 7.76-7.74 (*bd*, 1H), 7.52-7.46 (*m*, 2H), 7.28-7.24 (*m*, 1H), 6.10-6.06 (*q*, 6.6 Hz, 1H), 5.84 (*bs*, 1H), 3.46-3.37 (*m*, 8H), 3.20-3.10 (*bt*, 2H), 2.76-2.73 (*bt*, 2H), 2.11 (*bs*, 2H), 1.46-1.45 (*d*, 6.6 Hz, 3H). ^{13}C-NMR (500 MHz, $CDCl_3$): δ 155.69, 147.71, 138.79, 133.55, 128.19, 127.24, 124.62, 72.29, 70.28, 70.16, 70.03, 68.59, 41.35, 40.78, 22.31.

COMPOUND 11 - C11

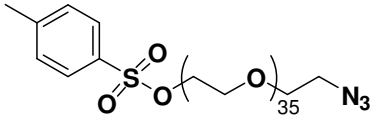

To a solution of HO-PEG_{36}-N_3 (25 mg, 0.0153 mmol) in DCM (306 µl) was added Et_3N (9.6 µl, 0.069 eq) and dropwise a solution of TsOCl (10 mg, 0.0534 mmol) in DCM (306 µl) at 0°C. The reaction mixture was stirred for 72h at room temperature and monitored by HPLC (20-80 gradient). The solvent was removed under reduced pressure. The product was purified by HPLC. A white powder was obtained (16 mg, 0.0092 mmol, 60%).

^{1}H-NMR (500 MHz, $CDCl_3$): δ 7.78-7.76 (*d*, 8.2 Hz, 2H), 7.33-7.32 (*d*, 8.2 Hz, 2H), 4.14-4.12 (*t* ,4.7 Hz, 2H), 3.69-3.58 (*m*, 136 H), 3.57 (*s*, 4H), 3.38-3.36 (*t*, 4.9 Hz, 2H), 2.43 (*s*, 3H). ^{13}C-NMR (500 MHz, $CDCl_3$): δ 144.92, 132.90, 129.94, 127.98, 70.68, 70.65, 70.55, 70.46, 70.40, 70.28, 70.03, 69.29, 68.68, 50.62, 21.67. ESI-MS: Found 1782 $[M+H]^+$.

All structural assignments were in agreement with the data available from the literature.[18]

COMPOUND 12 - C12

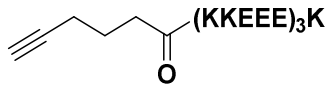

The peptide was synthesized in our laboratory using classical *N*-(fluorenyl)methoxycarbonyl solid-phase chemistry and purified by reversed-phase high performance liquid chromatography.[19]
FT-IR (cm^{-1}): 3296, 3067, 2962, 1647, 1543, 1425, 1259, 1197, 1182, 1131, 1088, 1015. ESI-MS: 2171.4 $[M]^+$.

COMPOUND 13 - C13

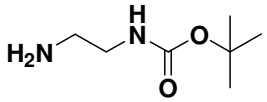

To a solution of 1,2-ethylenediamine (2.29 ml, 34 mmol) in CH_2Cl_2 (25 ml), a solution of Boc_2O (1.3 g, 6 mmol) in CH_2Cl_2 (25 ml) was added dropwise over a period of 2 h. The reaction mixture was stirred overnight at room temperature.
The solvent was removed under reduced pressure and the residue was dissolved in CH_2Cl_2 and H_2O. The product was extracted from H_2O three times with CH_2Cl_2 and the organic phase was dried over Na_2SO_4. The evaporation of the solvent afforded **C13** as a colorless oil (0.45 g, 2.81 mmol, 47%).
^{1}H-NMR (400 MHz, $CDCl_3$): δ 4.93 (*bs*, 1H), 3.16-3.12 (*m*, 2H), 2.77 (*t,* 5.8 Hz, 2H), 1.42 (*s*, 9H). ^{13}C-NMR (400 MHz, $CDCl_3$): δ 156.2, 81, 43.4, 41.9, 28.4.

COMPOUND 14 - C14

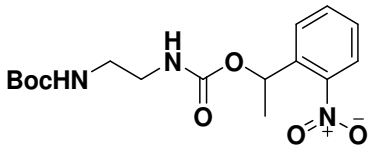

To a solution of **C13** (160 mg, 1 mmol) in DCM (2.5 ml) with Et_3N (0.42 ml, 3 mmol) a solution of **C8** (292 mg, 1 mmol) in DCM (2.5 ml) was added dropwise. The reaction mixture was stirred for 1 day at room temperature and monitored by TLC. The solvent was removed under reduced pressure and brine was added to the residue. The product was then extracted with DCM (x3) and dried over Na_2SO_4. The crude was then purified by chromatography on silica gel using DCM/MeOH (9.85:0.15) as eluent. The pure product was obtained (160 mg, 0.45 mmol, 45%).[17]
^{1}H-NMR (400 MHz, $CDCl_3$): δ 7.92-7.89 (*d*, 8.2 Hz, 1H), 7.61-7.60 (*m*, 2H), 7.42-7.38 (*m*, 1H), 6.25-6.20 (*q*, 6.4 Hz, 1H), 5.27 (*bs*, 1H), 4.84 (*bs*, 1H), 3.21 (*bs*, 4H), 1.61-1.59 (*d*, 6.5 Hz, 3H), 1.43 (*s*, 9H).

PHOTOCLEAVAGE OF C14 - C14-PD

Same procedure of **C9-PD** with a solution of **C14** (10 mg) in $CHCl_3$ (3.2 ml, 0.009 M) irradiated for 4.5 h. The reaction was monitored by HPLC (20-80 gradient).

6.2.2 Functionalization of graphene oxide

AMIDATION - GO1

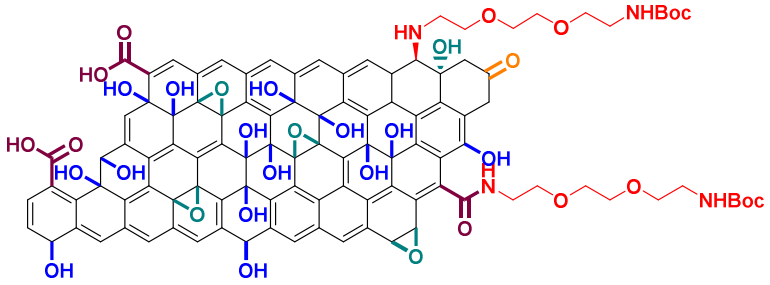

To a suspension of GO (20 mg) in dry DMF (20 ml), sonicated in a water bath for 10 min at 10°C, were added **C1** (80 mg, 0.32 mmol), HOBt (20 mg, 0.15 mmol) and EDC (30 mg, 0.19 mmol). The reaction mixture was stirred for 5 days at room temperature. GO was separated from the solvent through filtration (0.1 µm PTFE membrane). The recovered sample was dispersed in DMF, sonicated in a water bath for a few minutes and filtered. This workup sequence was repeated twice with DMF, twice with MeOH, and twice with DCM. Afterwards **GO1** was dialyzed in milliQ water for 4 days. **GO1** was obtained as a powder after freeze drying of the water suspension.[20]

Boc-DEPROTECTION - BD

To a solution of Boc protected-***f*-GO** (10 mg) in 1,4-dioxane (5 ml), sonicated in a water bath for 10 min, was added a solution of 4M HCl in 1,4-dioxane (5 ml). The reaction mixture was stirred overnight. After filtration (0.1 µm PTFE membrane) the precipitate was dispersed in DMF, sonicated in a water bath for few minutes and filtered. This workup sequence was repeated twice with DMF, twice with MeOH and twice with DCM. The precipitate was dried under vacuum to obtain Boc-deprotected ***f*-GO**.

OPENING OF EPOXIDE - GO2

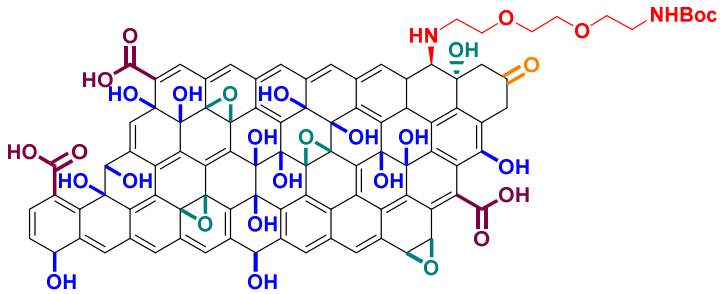

To a suspension of GO (20 mg) in dry DMF (20 ml) sonicated in a water bath for 10 min, **C1** (80 mg, 0.32 mmol) was added. The reaction mixture was stirred for 5 days. GO was separated from the solvent through filtration (0.1 µm PTFE membrane). The recovered sample was dispersed in DMF, sonicated in a water bath for a few minutes and filtrated. This work-up sequence was repeated twice with DMF, twice with MeOH, and twice with DCM. Afterwards, **GO2** was dialyzed in milliQ water for 4 days. **GO2** was obtained as a powder after freeze drying of the water suspension.[20]

CONTROL REACTION OF GO1-GO2 and GO4 - GO2_CONT

A suspension of GO (20 mg) in dry DMF (20 ml) was sonicated in a water bath for 10 min and stirred for 5 days. GO was separated from the solvent through filtration (0.1 µm PTFE membrane). The recovered sample was dispersed in DMF, sonicated in a water bath for a few minutes and filtered. This work-up sequence was repeated twice with DMF, twice with MeOH, and twice with DCM. Afterwards **GO2_CONT** was dialyzed in milliQ water for 4 days. **GO2_CONT** was obtained as a powder after freeze drying of the water suspension.[20]

ESTERIFICATION REACTION ON CARBOXYLIC ACID - GO3

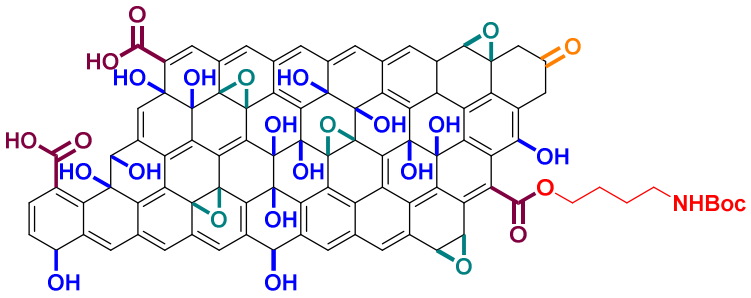

To a suspension of GO (10 mg) in dry DMF (10 ml), sonicated in a water bath for 10 min, were added EDC (15 mg, 0.10 mmol), DMAP (20 mg, 0.16 mmol) and **C2** (31 mg, 0.16 mmol). The reaction mixture was stirred for 2 days at room temperature. GO was separated from the solvent through filtration (0.1 µm PTFE membrane). The recovered sample was dispersed in DMF, sonicated in a water bath for a few minutes and filtered. This workup sequence was repeated twice with DMF, twice with MeOH, and twice with DCM. Afterwards **GO3** was dialyzed in milliQ water for 4 days. **GO3** was obtained as a powder after freeze drying of the water suspension.

OPENING OF EPOXIDE WITH LONG PEG CHAIN - GO4

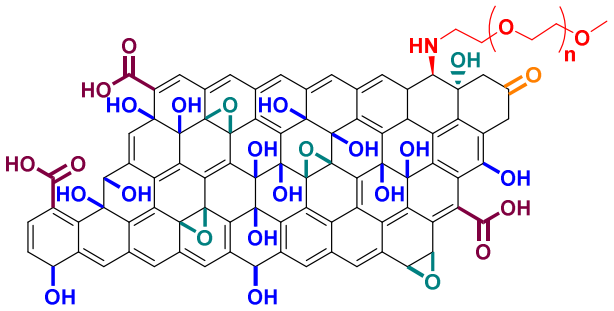

To a suspension of GO (10 mg) in dry DMF (10 ml), sonicated in a water bath for 10 min, aminopolyethylene glycol monomethyl ether was added (40 mg, average MW 1,000). The reaction mixture was stirred for 5 days at room temperature. GO was separated from the solvent through filtration (0.1 µm PTFE membrane). The recovered sample was dispersed in DMF, sonicated in a water bath for a few minutes and filtered. This workup sequence was repeated twice with DMF, twice with MeOH, and twice with DCM. Afterwards **GO4** was dialyzed in milliQ water for 4 days. **GO4** was obtained as a powder after freeze drying of the water suspension.[20]

ADSORPTION CONTROL FOR GO3 - GO5

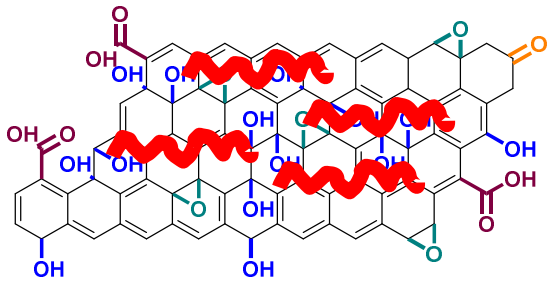

To a suspension of GO (10 mg) in dry DMF (10 ml), sonicated in a water bath for 10 min, poly(ethylene glycol) dimethyl ether was added (40 mg, average MW 1,000). The reaction mixture was stirred for 5 days at room temperature. GO was separated from the solvent through filtration (0.1 µm PTFE membrane). The recovered sample was dispersed in DMF, sonicated in a water bath for a few minutes and filtered. This workup sequence was repeated twice with DMF, twice with MeOH, and twice with DCM. Afterwards **GO5** was dialyzed in milliQ water for 4 days. **GO5** was obtained as a powder after freeze drying of the water suspension.[20]

WILLIAMSON REACTION - GO6

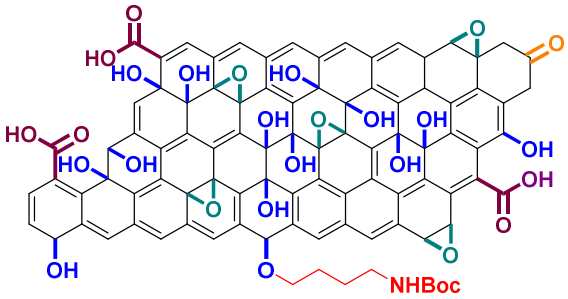

To a suspension of GO (20 mg) in dry DMF (20 ml), sonicated for 10 min in a water bath, were added K_2CO_3 (400 mg, 2.89 mmol) and **C4** (237 mg, 0.79 mmol). The reaction mixture was stirred under argon atmosphere for 2 days and then the solvent was separated by filtration (0.1 µm PTFE membrane). The recovered sample was dispersed in milliQ H_2O, sonicated in a water bath until thorough dispersion of GO and filtered. This sequence was repeated twice with milliQ H_2O, twice with DMF, twice with MeOH and twice with DCM. Afterwards **GO6** was dialyzed in milliQ water for 4 days. **GO6** was obtained as a powder after freeze drying of the water suspension.

To optimize the reaction conditions this reaction has been performed at different temperatures:

- **GO6-80**: at 80°C.
- **GO6-60**: at 60°C.
- **GO6-40**: at 40°C.
- **GO6-RT**: at room temperature.
-**GO6-RT2**: at room temperature adding Cs_2CO_3 (938.36 mg, 2.88 mmol).[21]

CONTROL REACTION OF GO6 - GO6_CONT1

This control reaction was performed in the same condition as **GO6**, without adding **C4**.

CONTROL REACTION OF GO6 - GO6_CONT2

This control reaction was performed in the same condition as **GO6**, without adding the base.

ESTERIFICATION REACTION ON HYDROXYL GROUP - GO7

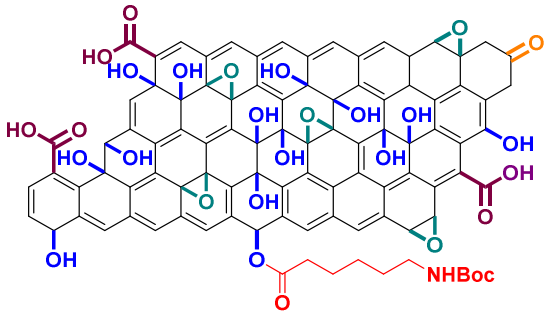

To a suspension of GO (10 mg) in dry DMF (10 ml), sonicated in a water bath for 10 min, were added **C5** (37 mg, 0.16 mmol), EDC (15 mg, 0.1 mmol) and DMAP (6 mg, 0.05 mmol). The reaction mixture was stirred for 2 days at room temperature. GO was separated from the solvent through filtration (0.1 µm PTFE membrane). The recovered sample was dispersed in DMF, sonicated in a water bath for a few minutes and filtered. This workup sequence was repeated twice with DMF, twice with MeOH, and twice with DCM. Afterwards **GO7** was dialyzed in milliQ water for 4 days. **GO7** was obtained as a powder after freeze drying of the water suspension.

CONTROL REACTION OF GO7- GO7_CONT

This control reaction has been performed in the same condition as **GO7**, without adding the coupling agents (EDC and DMAP).

WITTIG REACTION - GO8

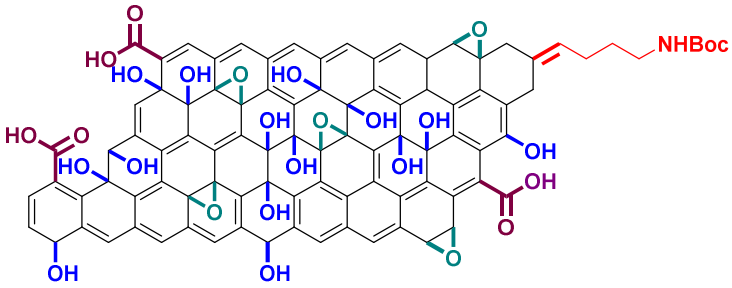

KHMDS 0.7 M in THF (50 µl, 0.032 mmol) was added to a solution of **C6** (20 mg, 0.036 mmol) in dry THF (2.5 ml) under argon atmosphere at 0° C and stirred for 30 min at RT. After a 10 min sonication process in a water bath a suspension of GO (10 mg) in dry THF (2.5 ml) under argon was added to the solution of **C6** and KHMDS at 0° C. The reaction mixture was sonicated for 10 min in a water bath at 0° C and then stirred in an ice bath letting it slowly return to RT. The reaction was stirred for 24 h. The reaction was diluted with 6 ml of a milliQ H_2O/MeOH mixture (1:5). The solvent was separated through filtration (0.1 µm PTFE membrane). The recovered sample was dispersed in DMF, sonicated in a water bath until thorough dispersion of GO and filtrated. This sequence was repeated twice with DMF, twice with MeOH and once with DCM. Afterwards **GO8** was dialyzed in milliQ water for 4 days. **GO8** was obtained as a powder after freeze drying of the water suspension.

CONTROL REACTION OF GO8 - GO8_CONT

This control reaction has been performed in the same condition as **GO8**, without adding **C6**.

OPENING OF EPOXIDE WITH NH_2-PEG_4-DOTA - GO9

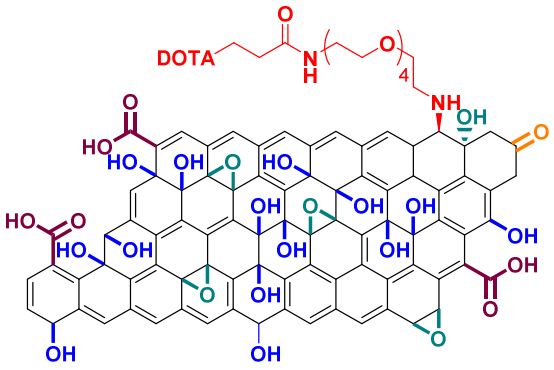

To an aqueous suspension of GO (9 mg; 1 mg/ml) NH_2-PEG_4-DOTA (9 mg, 0.0129 mmol) was added. The reaction mixture was stirred for 2 days. **GO9** was directly dialyzed in milliQ water for 4 days. **GO9** was stored in water without further treatment.

OPENING OF EPOXIDE WITH C10 - GO10

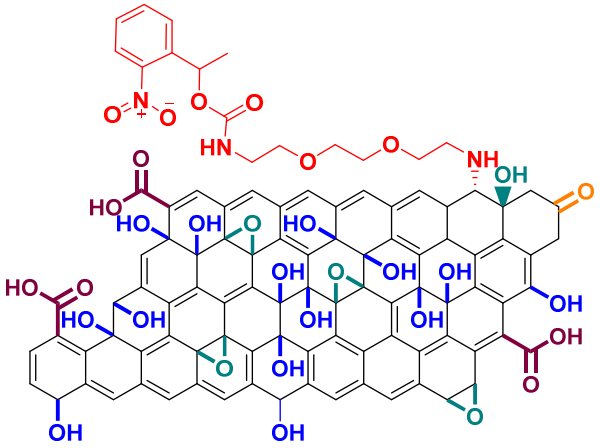

To a suspension of GO (10 mg) in dry DMF (10 ml) sonicated in a water bath for 5 min, **C10** (54.7 mg, 0.16 mmol) was added. The reaction mixture was stirred for 4 days protected from light. GO was separated from the solvent through filtration (0.1 µm PTFE membrane). The recovered sample was dispersed in DMF, sonicated in a water bath for a few minutes and filtered. This work-up sequence was repeated twice with DMF, twice with MeOH, and twice with DCM. Afterwards **GO10** was dialyzed in milliQ water for 4 days. **GO10** was obtained as a powder after freeze drying of the water suspension. (Control reaction is **GO2_CONT**)

PHOTOCLEAVAGE OF GO10 - GO11

A suspension of GO (2 mg) in $CHCl_3$ (2 ml) sonicated in a water bath for 5 min, was exposed to UV irradiation (UV lamp, 100 W, hν 365 nm, 15 cm of distance from lamp) for 6h. The reaction was monitored by HPLC (analysis of the supernatant, 20-80 gradient). GO was separated from the solvent through filtration (0.1 µm PTFE membrane). The recovered sample was dispersed in DMF, sonicated in a water bath for a few minutes and filtered. This work-up sequence was repeated twice with DMF, twice with MeOH, and twice with DCM. Afterwards **GO11** was dialyzed in milliQ water for 4 days. **GO11** was obtained as a powder after freeze drying of the water suspension.

PHOTOCLEAVAGE ADSORPTION CONTROL- GO11_CONT

To **C14-PD** solution after irradiation, was added GO (2 mg). The control mixture was stirred for 1h. Then the supernatant was recovered by centrifugation (3500 rpm, 14°C) and analyzed through HPLC (20-80 gradient).

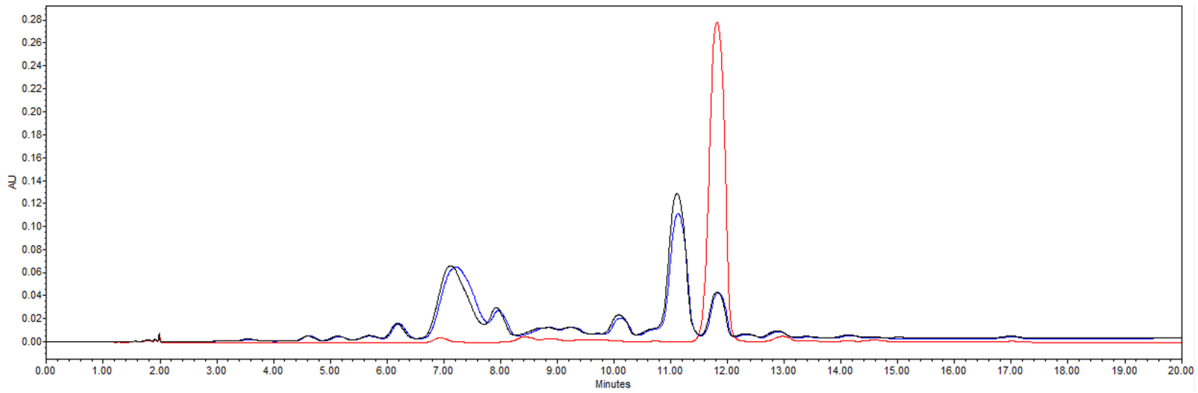

HPLC of **C14** in red, **C14-PD** in blue and **GO11-CONT** in black.

OPENING OF EPOXIDE FOR DOUBLE FUNCTIONALIZATION - GO12

Followed the same procedure as for **GO2.**

CONTROL REACTION FOR GO12 - GO12_CONT

Performed in the same conditions used for **GO2_CONT**.

WILLIAMSON REACTION ON GO12 - GO13

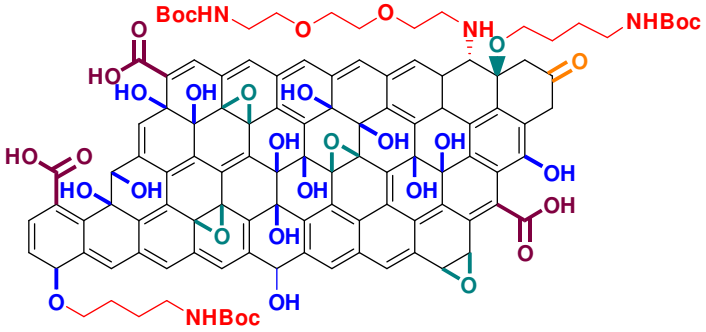

To a suspension of **GO12** (4 mg) in dry DMF (4 ml), sonicated for 5 min in a water bath, were added K_2CO_3 (80 mg, 0.578 mmol) and **C4** (48 mg, 0.16 mmol). The reaction mixture was stirred under argon atmosphere for 2 days and then the solvent was separated by filtration (0.1 µm PTFE membrane). The recovered sample was dispersed in milliQ H_2O, sonicated in a water bath until thorough dispersion of GO and filtered. This sequence was repeated twice with milliQ H_2O, twice with DMF, twice with MeOH and twice with DCM. Afterwards **GO13** was dialyzed in milliQ water for 4 days. **GO13** was obtained as a powder after freeze drying of the water suspension.

CONTROL FOR GO13 - GO13_CONT

Performed in the same conditions than **GO13** using **GO12_CONT** as starting material and without adding **C4**.

OPENING OF EPOXIDE WITH HEAVY DIAMINO-CHAIN - GO14

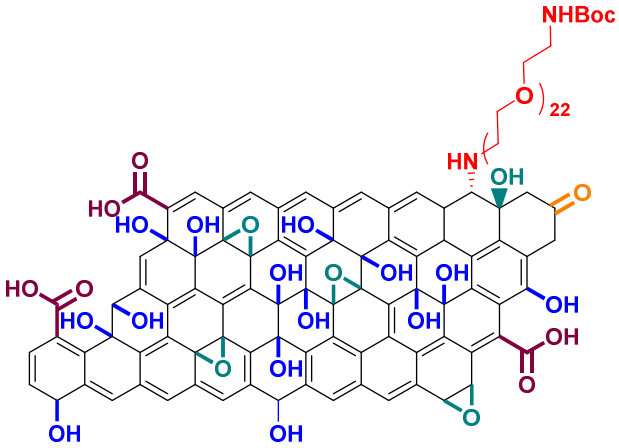

To a suspension of GO (30 mg) in dry DMF (30 ml) sonicated in a water bath for 5 min, NH_2-PEG_{23}-NHBoc (15.8 mg, 0.0135 mmol) was added. The reaction mixture was stirred for 4 days. GO was separated from the solvent through filtration (0.1 µm PTFE membrane). The recovered sample was dispersed in DMF, sonicated in a water bath for a few minutes and filtered. This work-up sequence was repeated twice with DMF, twice with MeOH, and twice with DCM. Afterwards **GO14** was dialyzed in milliQ water for 4 days. **GO14** was obtained as a powder after freeze drying of the water suspension. (Control reaction is **GO2_CONT**)

WILLIAMSON REACTION WITH TsO-PEG_{36}-N_3 - GO15

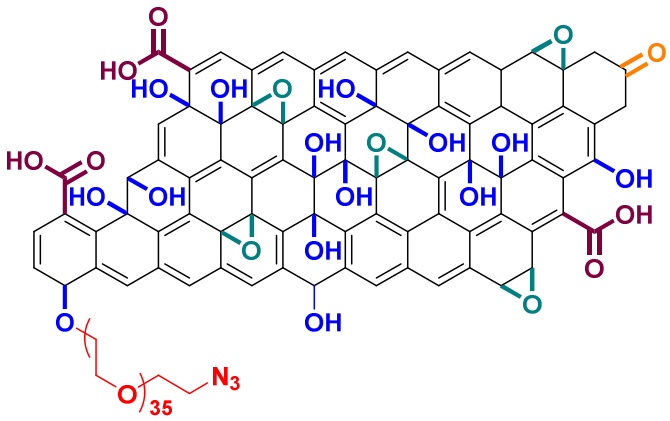

To a suspension of GO (7 mg) in dry DMF (7 ml), sonicated for 5 min in a water bath, were added K_2CO_3 (140 mg, 1.01 mmol) and **C11** (5.6 mg, 0.00314 mmol). The reaction mixture was stirred under argon atmosphere for 2 days and then the solvent was separated by filtration (0.1 µm PTFE membrane). The recovered sample was dispersed in milliQ H_2O, sonicated in a water bath until thorough dispersion of GO and filtered. This sequence was repeated twice with milliQ H_2O, twice with DMF, twice with MeOH and twice with DCM. Afterwards **GO15** was dialyzed in milliQ water for 4 days. **GO15** was obtained as a powder after freeze drying of the water suspension. (Control reaction is **GO6_CONT1**)

ONE POT DOUBLE FUNCTIONALIZATION - GO16

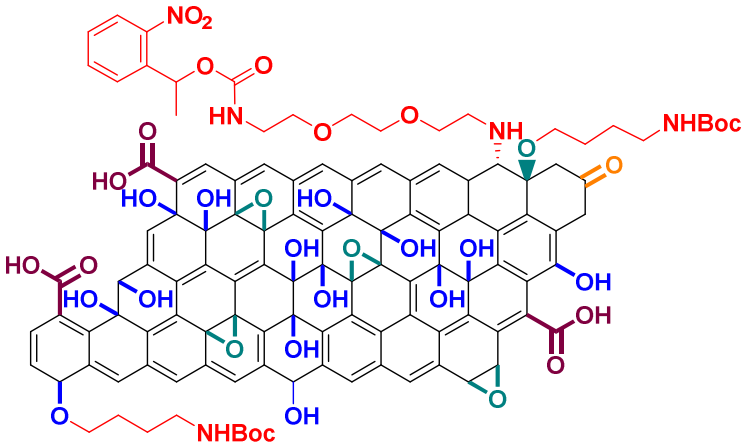

To a suspension of GO (20 mg) in dry DMF (20 ml), sonicated for 5 min in a water bath, was added **C10** (109 mg, 0.32 mmol). The reaction mixture was stirred under argon atmosphere and protected from light for 24h. To the reaction mixture K_2CO_3 (400 mg, 2.89 mmol) and a solution of **C4** (290 mg, 0.97) in dry DMF (2 ml) were added. The reaction mixture was stirred under argon atmosphere and protected from light for other 2 days. Then the solvent was separated by filtration (0.1 µm PTFE membrane). The recovered sample was dispersed in milliQ H_2O, sonicated in a water bath until thorough dispersion of GO and centrifuged. This sequence was repeated twice with milliQ H_2O, twice with DMF, twice with MeOH and twice with DCM. Afterwards **GO16** was dialyzed in milliQ water for 4 days. **GO16** was obtained as a powder after freeze drying of the water suspension.

CONTROL FOR GO16 - GO16_CONT

Performed in the same conditions than **GO16** without adding **C10** and **C4**.

PHOTOCLEAVAGE OF GO16 - GO16_PD

Performed in the same conditions as **GO11**.

WILLIAMSON REACTION FOR DOUBLE FUNCTIONALIZATION - GO17

Followed the same procedure as for **GO6.**

CONTROL REACTION FOR GO17 - GO17_CONT

Performed in the same conditions used for **GO6_CONT1**.

OPENING OF EPOXIDE ON GO17 - GO18

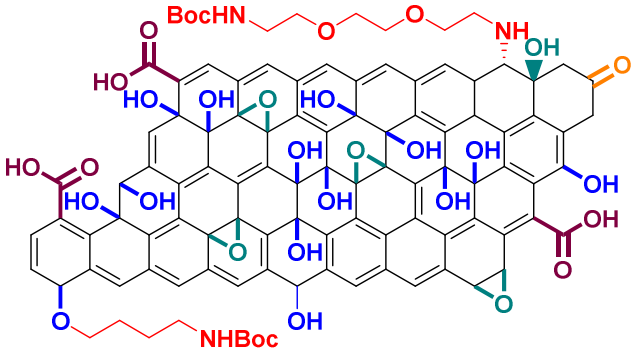

To a suspension of **GO17** (10 mg) in dry DMF (10 ml) sonicated in a water bath for 5 min, **C1** (40 mg, 0.16 mmol) was added. The reaction mixture was stirred for 2 days. GO was separated from the solvent through filtration (0.1 µm PTFE membrane). The recovered sample was dispersed in DMF, sonicated in a water bath for a few minutes and filtered. This work-up sequence was repeated twice with DMF, twice with MeOH, and twice with DCM. Afterwards **GO18** was dialyzed in milliQ water for 4 days. **GO18** was obtained as a powder after freeze drying of the water suspension.

CONTROL FOR GO18 - GO18_CONT

Performed in the same conditions than **GO18** using **GO17_CONT** as starting material and without adding **C1**.

OPENING OF EPOXIDE FOR DOUBLE FUNCTIONALIZATION - GO19

Followed the same procedure as for **GO2.**

CONTROL REACTION FOR GO19 - GO19_CONT

Performed in the same conditions used for **GO2_CONT**.

ESTERIFICATION REACTION ON GO19 - GO20

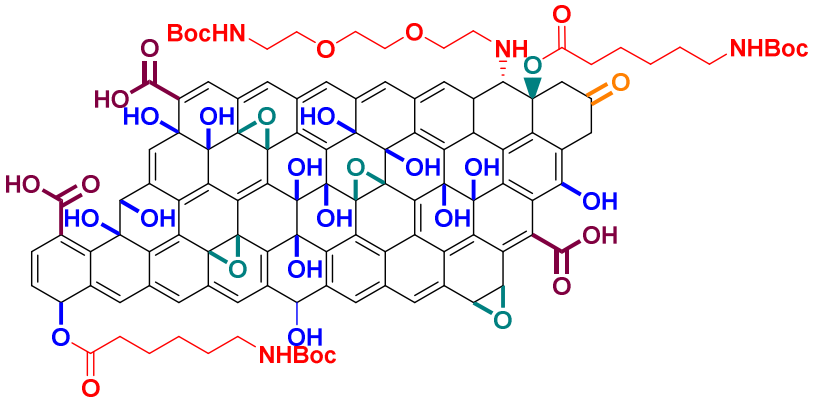

To a suspension of **GO19** (10 mg) in dry DMF (10 ml), sonicated in a water bath for 5 min, were added **C5** (37.2 mg, 0.16 mmol), EDC (15 mg, 0.1 mmol) and DMAP (6 mg, 0.05 mmol). The reaction mixture was stirred for 2 days at room temperature. GO was separated from the solvent through filtration (0.1 µm PTFE membrane). The recovered sample was dispersed in DMF, sonicated in a water bath for a few minutes and filtered. This workup sequence was repeated twice with DMF, twice with MeOH, and twice with DCM. Afterwards **GO20** was dialyzed in milliQ water for 4 days. **GO20** was obtained as a powder after freeze drying of the water suspension.

CONTROL FOR GO20 - GO20_CONT

Performed in the same conditions than **GO20** using **GO19_CONT** as starting material and without adding the coupling agents.

GLYCIDOL POLYMERIZATION ON GO - GO21

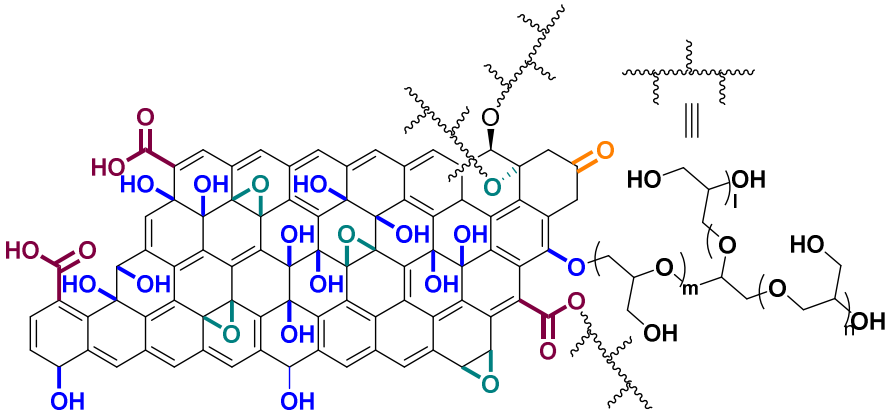

To GO (10 mg) glycidol (20 ml) was added. The mixture was sonicated in a water bath for 5 min, and stirred for 2 days. GO was separated from the solvent through centrifugation (GO-NI: 21000 rpm, 10min, 15°C; GO-Jp: 110000 rpm, 30 min, 4°C). The recovered sample was dispersed in milliQ water, sonicated in a water bath until re-dispersion and centrifuged. This workup sequence was repeated five times. Afterwards **GO21** was dialyzed in milliQ water for 4 days. **GO21** was kept in solution and obtained as a powder after freeze drying only for characterization.

To optimize the reaction conditions the reaction has been performed:

- **GO21-a**: at 140°C.
- **GO21-b**: at 80°C.
- **GO21-c:** at room temperature.
- **GO21-d**: at room temperature adding NaOH (287 mg, 7.2 mmol) in 0.5 ml of milliQ H_2O.[22]
  (Care has to be taken because of an explosion risk by adding a base)
- **GO21-e**: at room temperature adding Et_3N (220 mg, 2.2 mmol) in 0.2 ml of milliQ H_2O. [22,23]
  (Care has to be taken because of an explosion risk by adding a base)
- **GO21-f**: at room temperature adding Et_3N (728 mg, 7.2 mmol) in 1 ml of milliQ H_2O.[22,23]
  (Care has to be taken because of an explosion risk by adding a base)

Control reactions (Name_CONT) were done in the same conditions only with glycerol (20 ml) in place of glycidol.

TOSYLATION OF GO21 - GO22

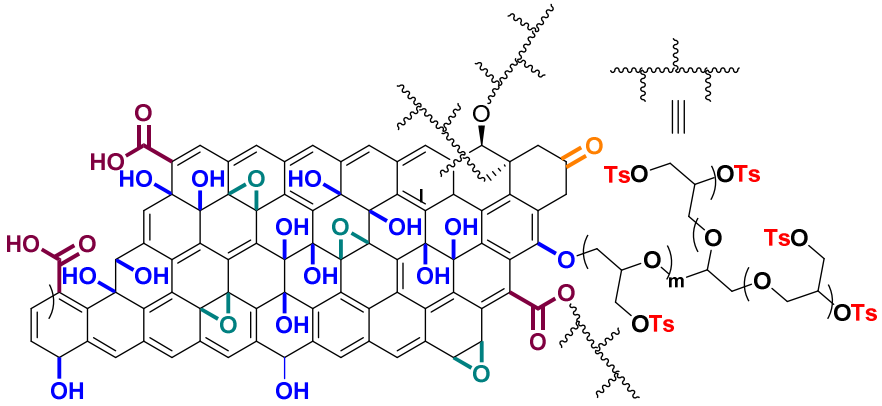

GO21-b (30 mg) water suspension was exchanged to pyridine through centrifugation (GO-NI: 21000 rpm, 10min, 15°C; GO-J: 110000 rpm, 30 min, 4°C) three times. To **GO21-b** in pyridine a solution of TsCl (45 mg, 0.24 mmol) in pyridine (0.5 ml) was added dropwise at 0°C. The mixture was stirred for 12h. GO was separated from the solvent through centrifugation (GO-NI: 21000 rpm, 10min, 15°C; GO-Jp: 110000 rpm, 30 min, 4°C). The recovered sample was dispersed in DMF, sonicated in a water bath until re-dispersion and centrifuged. This workup sequence was repeated five times. Afterwards **GO22** was kept in solution and obtained as a powder after freeze drying only for characterization.[24,25]

CONTROL FOR GO22 - GO22_CONT

Performed in the same conditions than **GO22** using **GO21-b_CONT** as starting material and without adding TsOCl.

AZIDATION OF GO22 - GO23

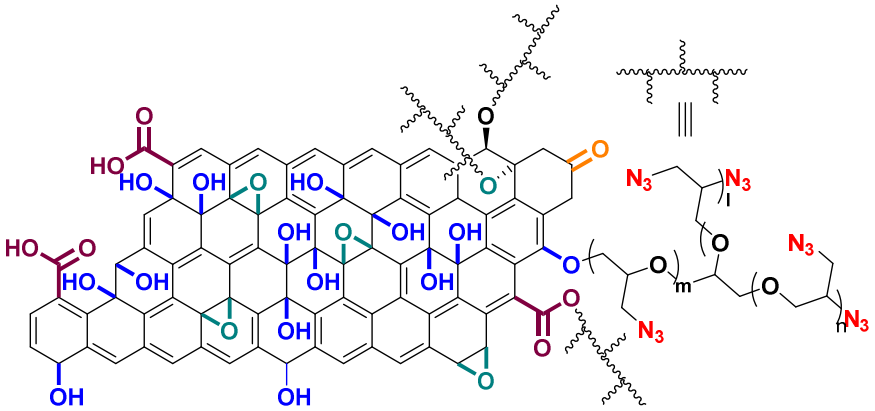

To **GO22** (20 mg) in DMF a solution of NaN_3 (40 mg, 0.61 mmol) in milliQ H_2O (0.5 ml) was added dropwise at room temperature. The mixture was stirred for 24h at 80°C. GO was separated from the solvent through centrifugation (GO-NI: 21000 rpm, 10min, 15°C; GO-Jp: 110000 rpm, 30 min, 4°C). The recovered sample was dispersed in DMF/milliQ H_2O (5:1), sonicated in a water bath until re-dispersion and centrifuged. This workup sequence was repeated five times. Afterwards **GO23** was kept in solution and obtained as a powder after freeze drying only for characterization.[24,25]

CONTROL FOR GO23 - GO23_CONT

Performed in the same conditions than **GO23** using **GO22_CONT** as starting material and without adding NaN_3.

CLICK REACTION ON GO23 - GO24

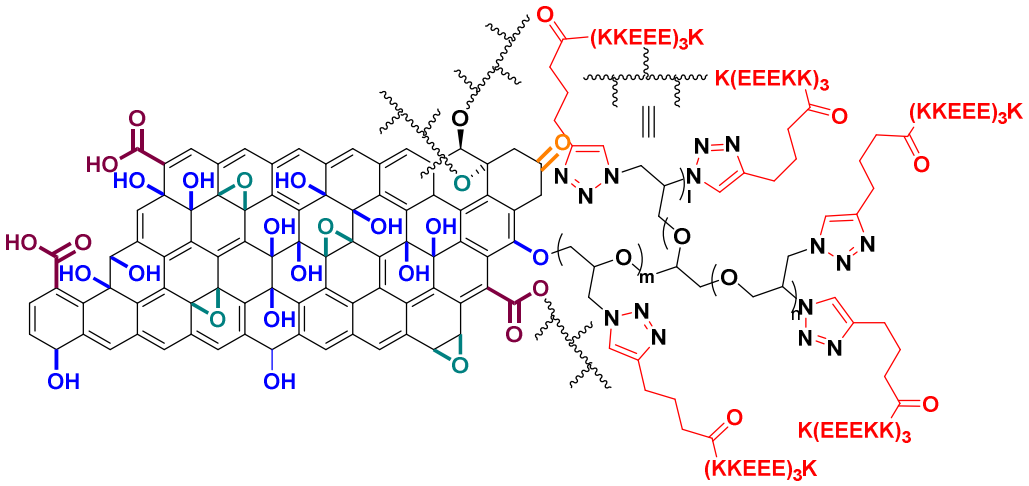

To **GO23** (2.4 mg) in milliQ H_2O (0.15 ml) under argon a solution of **C12** (3.1 mg, 1.44 µmol) in milliQ H_2O-*t*BuOH (2:1, 2.4 ml) was added. Afterwards $CuSO_4$ (92 µg, 0.576 µmol) and sodium ascorbate (0.1 mg, 0.57 µmol) were added. The reaction mixture was stirred for 24h at room temperature. The reaction was monitored through HPLC (analysis of the surnatant, 1-31 gradient). To **GO24,** milliQ water was added and the sample was dialyzed in milliQ water for 4 days. **GO24** was kept in solution and obtained as a powder after freeze drying only for characterization.

CONTROL REACTION OF GO20 - GO20_CONT

Performed in the same conditions of **GO24** on **GO23** as starting material, without adding sodium ascorbate and $CuSO_4$.

6.3 Bibliography

1. Ménard-Moyon C, Fabbro C, Prato M, Bianco A. One-Pot Triple Functionalization of Carbon Nanotubes. Chem – Eur J 2011;17(11):3222–3227.

2. M. C. Biesinger. X-ray Photoelectron Spectroscopy (XPS) database [Internet]. X-Ray PHotoelectron Spectrosc. XPS Ref. Pages. [cited 2017 Jun 28];Available from: http://www.xpsfitting.com/

3. Xue Y, Liu Y, Lu F, Qu J, Chen H, Dai L. Functionalization of Graphene Oxide with Polyhedral Oligomeric Silsesquioxane (POSS) for Multifunctional Applications. J Phys Chem Lett 2012;3(12):1607–12.

4. Navaee A, Salimi A. Efficient amine functionalization of graphene oxide through the Bucherer reaction: an extraordinary metal-free electrocatalyst for the oxygen reduction reaction. RSC Adv 2015;5(74):59874–80.

5. Tong W, Zhang Y, Zhang Q, et al. Achieving significantly enhanced dielectric performance of reduced graphene oxide/polymer composite by covalent modification of graphene oxide surface. Carbon 2015;94:590–8.

6. Ejigu Andinet, Edwards Matthew, Walsh Darren A. Synergistic Catalyst-Support Interactions in a Graphene-Mn3O4 Electrocatalyst for Vanadium Redox Flow Batteries. ACS Catal 2015;5(12):7122–30.

7. B.-J. Rossum, H. Förster, H.J.M. de Groot. High-Field and High-Speed CP-MAS13C NMR Heteronuclear Dipolar-Correlation Spectroscopy of Solids with Frequency-Switched Lee–Goldburg Homonuclear Decoupling. J Magn Reson 1997;124(2):516–9.

8. Egorova-Zachernyuk T, van Rossum B, Erkelens C, de Groot H. Characterisation of uniformly 13C, 15N labelled bacteriochlorophyll a and bacteriopheophytin a in solution and in solid state: complete assignment of the 13C, 1H and 15N chemical shifts. Magn Reson Chem MRC 2008;46(11):1074–83.

9. S. Hediger, B.H. Meier, Narayanan D. Kurur, Geoffrew Bodenhausen, R.R. Ernst. NMR cross polarization by adiabatic passage through the Hartmann—Hahn condition (APHH). Chem Phys Lett 1994;223(4):283–8.

10. Jésus Raya, Barbara Perrone, Jérôme Hirschinger. Chemical shift powder spectra enhanced by multiple-contact cross-polarization under slow magic-angle spinning. J Magn Reson 2013;227:93–102.

11. B. M. Fung, A. K. Khitrin, Konstantin Ermolaev. An Improved Broadband Decoupling Sequence for Liquid Crystals and Solids. J Magn Reson 2000;142(1):97–101.

12. Hahn EL. Spin Echoes. Phys Rev 1950;80(4):580–94.

13. Vacchi IA, Spinato C, Raya J, Bianco A, Ménard-Moyon C. Chemical reactivity of graphene oxide towards amines elucidated by solid-state NMR. Nanoscale 2016;8(28):13714–21.

14. Pastorin G, Wu W, Wieckowski S, et al. Double functionalisation of carbon nanotubes for multimodal drug delivery. Chem Commun 2006;(11):1182–4.

15. Singh P, Lamanna G, Ménard-Moyon C, et al. Formation of Efficient Catalytic Silver Nanoparticles on Carbon Nanotubes by Adenine Functionalization. Angew Chem Int Ed 2011;50(42):9893–9897.

16. Park S, Yousaf MN. An Interfacial Oxime Reaction To Immobilize Ligands and Cells in Patterns and Gradients to Photoactive Surfaces. Langmuir 2008;24(12):6201–7.

17. Junzhou Wu, Xinjing Tang. Synthesis and enzymatic incorporation of photolabile dUTP analogues into DNA and their applications for DNA labeling. Bioorg Med Chem 2013;21(20):6205–11.

18. Bader SL, Luescher MU, Gademann K. Synthesis of maculalactone A and derivatives for environmental fate tracking studies. Org Biomol Chem 2014;13(1):199–206.

19. Janzer M, Larbig G, Kübelbeck A, Wischnjow A, Haberkorn U, Mier W. Drug Conjugation Affects Pharmacokinetics and Specificity of Kidney-Targeted Peptide Carriers. Bioconjug Chem 2016;27(10):2441–9.

20. Vacchi IA, Spinato C, Raya J, Bianco A, Ménard-Moyon C. Chemical reactivity of graphene oxide towards amines elucidated by solid-state NMR. Nanoscale 2016;8(28):13714–21.

21. Parrish JP, Sudaresan B, Jung KW. Improved Cs2Co3 Promoted O-Alkylation of Phenols. Synth Commun 1999;29(24):4423–31.

22. Sandler SR, Berg FR. Room temperature polymerization of glycidol. J Polym Sci [A1] 1966;4(5):1253–9.

23. Das M, Datir SR, Singh RP, Jain S. Augmented Anticancer Activity of a Targeted, Intracellularly Activatable, Theranostic Nanomedicine Based on Fluorescent and Radiolabeled, Methotrexate-Folic Acid-Multiwalled Carbon Nanotube Conjugate. Mol Pharm 2013;10(7):2543–57.

24. Zhao L, Xu Y-H, Qin H, et al. Platinum on Nanodiamond: A Promising Prodrug Conjugated with Stealth Polyglycerol, Targeting Peptide and Acid-Responsive Antitumor Drug. Adv Funct Mater 2014;24(34):5348–57.

25. Zhao L, Xu Y-H, Akasaka T, et al. Polyglycerol-coated nanodiamond as a macrophage-evading platform for selective drug delivery in cancer cells. Biomaterials 2014;35(20):5393–406.

List of publications and communications

Publications

- Rajendra Kurapati, Laura Muzi, Aritz Perez Ruiz de Garibay, Julie Russier, Damien Voiry, Isabella A Vacchi, Manish Chhowalla, Alberto Bianco, "**Enzymatic Biodegradability of Pristine and Functionalized Transition Metal Dichalcogenide MoS_2 Nanosheets**", Advanced Functional Materials, 2017, DOI: 10.1002/adfm.201605176.

- Ngoc Do Quyen Chau, Giacomo Reina, Jésus Raya, Isabella A. Vacchi, Cécilia Ménard-Moyon, Yuta Nishina, Alberto Bianco, "**Elucidation of siRNA complexation efficiency by graphene oxide and reduced graphene oxide**", Carbon, 2017, 643-652.

- Isabella A. Vacchi, Cinzia Spinato, Jésus Raya, Alberto Bianco, Cécilia Ménard-Moyon, "**Chemical reactivity of graphene oxide towards amines elucidated by solid-state NMR**", Nanoscale, 8, 2016, 13714-13721.

- Eijiro Miyako, Benoit P. Pichon, Cécilia Ménard-Moyon, Isabella A. Vacchi, Christophe Lefèvre, Sylvie Bégin-Colin, Alberto Bianco, "**Design, synthesis, characterization and properties of magnetic nanoparticle- nanocarbon hybrids**", Carbon, 96, 2016, 49-56.

Book chapter

- Isabella A. Vacchi, Cécilia Ménard-Moyon, Alberto Bianco, "**Chemical Functionalization of Graphene Family Members**", Chemistry of Carbon Nanostructures, Eds. K. Müllen, X. Feng, De Gruyter, Berlin, 2017.

Communications

Oral presentations:

- **Colloque Francophone du Carbone 2015 du Groupe Francophone d'Etude des Carbones (GFEC)**, 18th -21st Mai 2015, Les Karellis, France. Isabella Anna Vacchi, Cinzia Spinato, Jésus Raya, Cécilia Ménard-Moyon, Alberto Bianco; "*Strategies for the selective chemical functionalization of graphene oxide*".

- **International meeting on the chemistry of graphene and carbon nanotubes: ChemOnTubes 2016**, 3rd -7th April 2016 Bruxelles, Belgium. Isabella Anna Vacchi, Jésus Raya, Cécilia Ménard-Moyon, Alberto Bianco; "*Chemical investigation of graphene oxide reactivity through covalent functionalization*".

- **52nd Fullerenes-Nanotubes-Graphene General symposium (FNTG52)**, 28th February 2017, Tokyo, Japan. Isabella Anna Vacchi, Jésus Raya, Cécilia Ménard-Moyon, Alberto Bianco; "*Graphene oxide: Chemical investigation of its surface composition through covalent functionalization*".

Poster presentations:

- **Graphene Study 2016**, 17th -22nd January 2016, Les Houches, France. Isabella Anna Vacchi, Cinzia Spinato, Jésus Raya, Cécilia Ménard-Moyon, Alberto Bianco; "*Graphene oxide: an insight on its surface composition through covalent functionalization*".

- **Ecole thematique XPS: from measurements to scientific answers**, 26th -30th September 2016, Roscoff, France. Isabella Anna Vacchi, Jésus Raya, Cécilia Ménard-Moyon, Alberto Bianco; "*Graphene oxide: Chemical and analytical investigation of its surface composition*".

- **1st European Conference on Chemistry of Two-Dimensional Materials (Chem2DMat)**, 22nd -26th August 2017, Strasbourg, France. Isabella Anna Vacchi, Jésus Raya, Cécilia Ménard-Moyon, Naoki Komatsu, Alberto Bianco; "*Understanding graphene oxide: an all-around study of its surface composition and functionalization*".